

UNIVERSITY OF NAPLES FEDERICO II

*Department of Structures  
for Engineering and Architecture*

PH.D. PROGRAMME IN  
MATERIALS ENGINEERING AND STRUCTURES  
COORDINATOR PROF. GIUSEPPE MENSITIERI  
XXV CYCLE



COSTANTINO MENNA

PH.D. THESIS

**MULTISCALE DAMAGE MODELING OF ADVANCED  
COMPOSITE MATERIALS**

TUTORS: PROF. DR. ANDREA PROTA  
PROF. DR. CHARLES E. BAKIS  
CO-TUTOR: DR. DOMENICO ASPRONE

**2013**



*“The process of scientific discovery is, in effect,  
a continual flight from wonder”*

***Albert Einstein***



# *Acknowledgements*

At the end of this PhD programme, there are many people who deserve gratitude for giving me the possibility to conduct valuable research, acquire new engineering skills, make this work possible and broaden my horizons of knowledge.

Sincere and deep gratitude goes to my advisor Prof. Andrea Prota who, three years ago, motivated me to join the Department of Structures for Engineering and Architecture. I would like to sincerely thank him for giving me guidance during these three years and particularly for his sincere and precious advices to take up fruitful and valuable scientific experiences; without him, I wouldn't have started this “journey”. Special thanks go also to Prof. Gaetano Manfredi for making this department a very motivating place with exceptional people.

Very special thanks go to Prof. Charles E. Bakis, firstly for the hospitality and the incomparable willingness he has shown me during my visiting research period at the department of Engineering Science and Mechanics of the Pennsylvania State University. His scientific guidance and motivation encouraged me to enthusiastically work on valuable research topics, contributing to increase my love for materials engineering. I am also grateful to Prof. Auricchio, for his precious advices in conducting valuable research activities.

My deepest appreciation goes to my co-tutor, Dr. Domenico Asprone for his invaluable guidance, patience, support and encouragement throughout the course of this research. Through these years Mimmo has become firstly a good friend and a source of precious teachings throughout the wide range of activity conducted during this programme. I really thank him for making things easier than they are!

I would like to also thank all colleagues and roommates at the Department of Structures for Engineering and Architecture who have contributed in many ways to make this period an enjoyable one.

Finally, there is also a “non-academic” part that deserves sincere gratitude for supporting and motivating my choices. Special thanks go to my closer Italian, Canadian and American friends for valuable advices they gave me during these three years. I can never give enough thanks to my parents and my sister whose unconditional love and encouragement never left me during this journey. Lastly, special thanks go particularly to Valeria, for her love, patience on my lack of time on many occasions and especially for the wonderful moments we shared in US during this experience.

Naples, April 2013



# ***ABSTRACT***

The use of composite materials has spread over the years throughout the engineering areas of structures. The technological progress in this field has recently expanded, resulting in the design of new composite configurations, including multilayered composite materials and multifunctional nanostructured materials. Even though traditional and emerging composite materials offer wide potentialities for engineering, a significant challenge is still open with respect to damage phenomena. Driven by safety requirements and cost-effective optimization needs, damage modeling has gained a fundamental role for composite engineering. It represents a strong motivation to support design procedures by means of numerical methods, such as finite element analyses. Recently, multiscale computational analyses effectively gained a major role within the challenging task of damage prediction. Particularly, by bridging physical phenomena occurring at different scales, i.e. macro, meso, micro and even nano, damage evolution can be accurately predicted.

The present work is collocated within this scenario with the aim of exploring and addressing different critical issues related to the failure mechanisms acting at different length scales of different composite systems. The multiscale procedures, proposed to evaluate the damage behavior of such materials, involved experimental, analytical and numerical tools. In detail, damage modeling has been performed for different case studies: *i*) GFRP composite laminates, *ii*) phenolic impregnated skins/honeycomb Nomex core sandwich structures, *iii*) Carbon Nanotube/Nanofiber modified S2-Glass/epoxy composites.

For the case study *i*), the activity concerned the damage occurred in case of low-velocity impact tests, carried out on glass fabric/epoxy laminates. In this case, the multiscale modeling was implemented to account for both intralaminar and interlaminar levels of damage occurring within the composite laminate. This allowed to characterize the critical parameters acting at the smaller (interlaminar) scale which affect the macroscopic impact response of the composite laminate.

With reference to honeycomb sandwich structures of case *ii*), due to their hierarchical structure, a multiscale approach was necessary in order to suitably capture damage mechanisms occurring to the composite skins and honeycomb core. The study was firstly aimed at accurately addressing the out-of-plane compressive response; particularly, in order to evaluate the influence of imperfection variability on the buckling and crushing behavior, a statistics-based approach was proposed and applied to a detailed finite element model of a single representative honeycomb cell. Furthermore, the impact was also investigated. Finite element numerical models, based on the sandwich assembly structure, were progressively validated through experimental tests, both static and dynamic, performed from the coupon to the sandwich assembly length scale.

In the case study *iii*) the multiscale damage modeling procedure was focused on some issues related to the Carbon Nanotube/Nanofiber length scale, including nanotube length and orientation characterization, stress transfer to the matrix and nanotube toughening mechanisms. A micromechanical model, taking into account CNT length and orientation distribution, was implemented in order to model mode I interlaminar fracture toughness of multiscale CNT/CNF S2-Glass/epoxy composites.

For all the investigated case studies the adopted multiscale based strategies revealed to be mostly effective in capturing the most significant damage-related parameters at the lower scales, influencing the structural mechanisms, acting at the structure/component scale.

# *Contents*

<b>CONTENTS</b> .....	I
<b>LIST OF FIGURES</b> .....	IV
<b>LIST OF TABLES</b> .....	IX
<b>CHAPTER I</b> .....	1
<b>INTRODUCTION</b> .....	1
1.1. INTRODUCTION .....	1
1.2. HISTORICAL OVERVIEW AND MULTISCALE DAMAGE ANALYSIS.....	3
1.3. RESEARCH PURPOSES AND OUTLINE .....	6
<b>CHAPTER II</b> .....	11
<b>IMPACT BEHAVIOR OF GFRP COMPOSITE LAMINATES</b> .....	11
2.1. INTRODUCTION TO FRAMEWORK .....	11
2.2. LITERATURE OVERVIEW: IMPACT ON COMPOSITE LAMINATES.....	12
2.3. IMPACT MODELING .....	15
2.4. MATERIALS AND EXPERIMENTAL METHODS .....	16
2.5. EXPERIMENTAL RESULTS AND DISCUSSION .....	17
2.6. NUMERICAL ANALYSIS .....	22
2.6.1. MODEL FEATURES .....	22
2.6.2. DELAMINATION MODELING .....	25
2.7. ASSESSMENT OF THE MODEL .....	27
2.7.1. CALIBRATION ANALYSIS.....	28
2.7.2. FORCE-DISPLACEMENT CURVES .....	31
2.7.3. DAMAGE ASSESSMENT.....	35
2.8. CLOSING REMARKS .....	37

REFERENCES.....	38
<b>CHAPTER III</b> .....	43
<b>OUT OF PLANE COMPRESSIVE BEHAVIOR OF HONEYCOMB SANDWICH STRUCTURES</b> .....	43
3.1. INTRODUCTION TO FRAMEWORK .....	43
3.2. LITERATURE OVERVIEW.....	44
3.2.1. SANDWICH STRUCTURES: INTRODUCTION .....	44
3.2.2. SANDWICH FAILURE MODE: SKIN FAILURE .....	47
3.2.3. SANDWICH FAILURE MODE: CORE FAILURE.....	48
3.2.4. SANDWICH FAILURE MODE: FAILURE MAP.....	49
3.2.5. HONEYCOMB OUT OF PLANE PROPERTIES .....	50
3.2.6. IMPERFECTIONS – CLASSIFICATION AND MODELING.....	55
3.3. MATERIALS AND METHODS.....	59
3.3.1. MODEL FEATURES .....	60
3.3.2. APPROACH VALIDATION .....	64
3.4. RESULT DISCUSSION .....	66
3.4.1. EXPERIMENTAL BEHAVIOR .....	66
3.4.2. NUMERICAL RESULTS: BUCKLING FAILURE MODE .....	69
3.4.3. NUMERICAL RESULTS: CRUSHING.....	84
3.5. CLOSING REMARKS .....	87
REFERENCES.....	88

**CHAPTER IV**..... 93

**IMPACT BEHAVIOR OF HONEYCOMB SANDWICH STRUCTURES**

93

4.1. INTRODUCTION TO FRAMEWORK .....	93
4.2. LITERATURE OVERVIEW: IMPACT ON SANDWICH STRUCTURES.....	94
4.3. MATERIALS AND METHODS.....	96
4.4. SANDWICH MATERIAL MODELING .....	97
4.4.1. E-GLASS PHENOLIC SKINS.....	98

4.4.2. NOMEX CORE .....	101
4.5. CALIBRATION AND NUMERICAL SIMULATION .....	102
4.5.1. E-GLASS PHENOLIC SKINS – STATIC TESTS .....	103
4.5.2. NOMEX CORE – STATIC TESTS.....	107
4.5.3. SANDWICH ASSEMBLY – FOUR POINT BENDING TEST.....	108
4.6. SANDWICH ASSEMBLY – INDENTATION TEST .....	110
4.7. IMPACT ANALYSIS .....	112
4.7.1. DAMAGE ASSESSMENT.....	119
4.8. CLOSING REMARKS .....	121
<b>CHAPTER V .....</b>	<b>125</b>
<b>FRACTURE TOUGHNESS OF MULTISCALE CARBON NANOTUBE REINFORCED COMPOSITES .....</b>	<b>125</b>
5.1. INTRODUCTION TO FRAMEWORK .....	125
5.2. CARBON NANOTUBES – BACKGROUND AND INTRODUCTION 127	
5.2.1. CNT LENGTH CHARACTERIZATION .....	128
5.2.2. CNT ORIENTATION.....	137
5.2.3. CNT WAVINESS.....	143
5.2.4. CNT-POLYMER INTERFACIAL SHEAR STRESS (LOAD TRANSFER) .....	145
5.3. ON NANOCOMPOSITE TOUGHNESS.....	148
5.3.1. CNT FRACTURE TOUGHNESS MODELING.....	154
5.4. CURRENT CNT PULLOUT MODEL.....	163
5.4.1. EXPERIMENTAL VALIDATION .....	171
5.4.2. MATERIALS AND EXPERIMENTAL RESULTS [91] .....	172
5.4.3. CNT PULLOUT MODEL APPLICATION .....	177
5.5. CONCLUDING REMARKS.....	200
<b>CONCLUSIONS .....</b>	<b>213</b>

# List of figures

Figure 1.1: Multiscale procedure for the design and optimization of multilayered composite structures: a) increasing the scale levels of the composite component; b) type of tests and analyses to be performed as the length scale increases. ....5

Figure 1.2: Concept of *multiscale strategies* applied to nanostructures: a) [7]; multiscale simulation strategy for coarse-graining of surfactant molecules into beads b) [8].....6

Figure 2.3: Scheme of multiscale damage analysis for GFRP laminates adopted within the study..... 12

Figure 2.4: Typical impact damage in a composite laminate: a) failure due to fiber breakage [4]; b) intralaminar matrix shear cracks [5]; c) delaminations between adjacent plies [4]. ..... 14

Figure 2.5: Illustration of impact damage development: a) damaged area through the thickness of the composite laminate; matrix cracks (red) and delamination (blue) pattern for transverse impact b), c) [6]. ..... 15

Figure 2.6: Schematic representation of the GFRP stacking sequence with  $n=1$ , a) and  $n=2$ , b). ..... 17

Figure 2.7: Effect of the laminate thickness,  $t$ , on the  $F-d$  curves. .... 18

Figure 2.8: Effect of the energy level,  $U$ , on the  $F-d$  curves. Laminate thickness  $t=0.96\text{mm}$ . ... 19

Figure 2.9: Absorbed energy,  $U_d$ , vs impact energy,  $U$ . .... 19

Figure 2.10: Visible damaged area of an impacted panel. .... 20

Figure 2.11: Extent of ply-by-ply delaminated area,  $A_m$ . Panel thickness  $t=1.92\text{mm}$ ; impact energy  $U=20.0\text{ J}$ . .... 21

Figure 2.12: Characteristic dimension of projected delaminated area,  $d$ , vs impact energy,  $U$ . . 21

Figure 2.13: Projected delaminated area,  $A_p$ , vs impact energy,  $U$ . .... 22

Figure 2.14: Stress profile a) and damage evolution law b) of TieBreak contact [31]. .... 26

Figure 2.15: FE model set up adopted in the numerical analysis. .... 27

Figure 2.16: Comparison of experimental and numerical  $F-d$  curves for the 0.96 mm thick laminate; a)  $U=0.4\text{J}$ ; b)  $U=1.5\text{J}$ ; c)  $U=3.3\text{J}$ ; d)  $U=4.0\text{J}$ ; e)  $U=6.0\text{J}$ . .... 31

Figure 2.17: Comparison of experimental and numerical  $F-d$  curves for the 1.92 mm thick laminate; a)  $U=0.8\text{J}$ ; b)  $U=8.3\text{J}$ ; c)  $U=12.4\text{J}$ ; d)  $U=15.5\text{J}$ ; e)  $U=20.0\text{J}$ . .... 34

Figure 2.18: Comparison of: a) experimental, and, b) calculated delaminated area. Laminate thickness  $t=0.96\text{ mm}$ ; impact energy  $U=6.0\text{ J}$ . .... 36

Figure 2.19: Interlaminar damage of the 1.92 mm thick laminate impacted at  $U=15.5\text{J}$ : a) through the thickness shear failure; b) exploded laminate view depicting longitudinal tensile failure,  $X$  direction; c) bottom view of composite laminate, longitudinal tensile failure,  $X$  direction; d) post impact view. .... 37

Figure 3.20: Scheme of multiscale analysis performed for the investigated Nomex honeycomb structure. .... 44

Figure 3.21: Schematic representation of a sandwich structure..... 45

Figure 3.22: Skin failure modes: a) compressive failure; b) intra-cell buckling; c) wrinkling failure [20]. ..... 48

Figure 3.23: Core failure modes: a) shear failure; b) indentation failure [20]. ..... 49

Figure 3.24: Schematization of the plastic buckling of a honeycomb loaded in  $Z(3)$  direction a); work dissipated in the plastic hinge b). ..... 54

Figure 3.25: Expansion manufacturing process for honeycomb material [7]. ..... 55

Figure 3.26: Corrugated manufacturing process for honeycomb material [7]. ..... 56

Figure 3.27: a) in plane periodical honeycomb microstructure for hexagonal cells,  $W-L$  plane; b) single representative periodic cell; c) 3D finite element mesh rendering for a single Nomex honeycomb cell. .... 61

Figure 3.28: SEM photos of Nomex™ core. a) Transverse section; b) detail of a vertex of a hexagonal cell [40]...... 63

Figure 3.29: Schematic flow chart of the simulation strategy. .... 65

Figure 3.30: a) compressive stress – strain,  $\sigma_c$  vs  $\delta/h$ , response for HRH 10-1/8-3.0 hexagonal Nomex honeycomb; b) sequence of photographs of honeycomb cells at different stages of axial compressive strain. .... 68

Figure 3.31: a) compressive stress – strain,  $\sigma_c$  vs  $\delta/h$ , response for Hexcel Al-5052-H39 hexagonal aluminum honeycomb; b) focus on critical buckling load; c) focus on compressive strength; d) first (A), second (B) buckling mode and plasticized cell (C) as a result of the current approach..... 71

Figure 3.32: compressive stress – strain,  $\sigma_c$  vs  $\delta/h$ , response for HRH 10-1/8-3.0 hexagonal Nomex honeycomb up to folding with FE results of cell deformations corresponding to A=critical buckling limit, B=shape up to compressive strength, C1-C5=strain localization for the five cell samples, D=first fold of the cell. .... 72

Figure 3.33: Effect of thickness variability on  $\sigma_c$  vs  $\delta/h$  curves for a) CV=10%, b) CV=15%, c) CV=20%, d) CV=25% with the corresponding PDF and focusing on the peak of compressive strength; e) superposition of CV=10% and CV=25% cases..... 76

Figure 3.34: Effect of Young’s modulus variability on  $\sigma_c$  vs  $\delta/h$  curves for a) CV=10%, b) CV=15%, c) CV=20%, d) CV=25% with the corresponding PDF and focusing on the peak of compressive strength; e) superposition of CV=10% and CV=25% cases. .... 79

Figure 3.35: Effect of both thickness and Young’s modulus variability on  $\sigma_c$  vs  $\delta/h$  curves for a) CV=10%, b) CV=15%, c) CV=20%, d) CV=25% with the corresponding PDF and focusing on the peak of compressive strength; e) superposition of CV=10% and CV=25% cases. .... 82

Figure 3.36: a) average computed compressive strength vs CV adopted for Nomex properties; b) average computed Young’s modulus vs CV adopted for Nomex properties; c) CV on computed compressive strength vs CV adopted for Nomex properties. .... 84

Figure 3.37: Full Stress-Strain relationship for Nomex honeycomb material – experimental (grey) vs simulation (red) results. .... 85

Figure 3.38: Folding mechanism during Nomex crushing regime; a) first fold (point 2), b) first contact between walls (point 3), c) double contact between walls (point 5), d) final deformed shape. ....87

Figure 4.39: Scheme of multiscale damage analysis conducted on Honeycomb sandwich structure. .... 94

Figure 4.40: Shape geometry of hexagonal honeycomb core. .... 97

Figure 4.41: a) Stress vs Strain relationship for single element tensile test (direction 1) for different values of  $E_1T$ , b) correspondent damage variable  $\omega_1$  vs strain relationship. ....101

Figure 4.42: Stress vs Strain relationship for tensile a) warp, b) weft, c) in plane shear direction and corresponding damage variable,  $\omega$ , evolution ranging from 0 (blue) to 1 (red). ....106

Figure 4.43: Compressive Stress vs Strain curve for the Nomex core. ....107

Figure 4.44: Load vs Deflection curve for the four point bending test. ....109

Figure 4.45: Contour of a)  $LT$  stress in the Nomex core, b)  $L$  direction stress in the upper and lower skin. ....110

Figure 4.46: Load vs Deflection numerical and experimental curve for the static indentation test a); through the thickness stress distribution before b) and after c) Nomex crushing. ....111

Figure 4.47: a) Comparison of experimental and numerical  $F-d$  curves for  $t=1$  mm,  $d=12.7$  mm,  $v=4$  m/s with numbered sequence of sandwich damage mechanisms; b) corresponding energy displacement curve. ....114

Figure 4.48: Fringe level of strain rate in warp direction a) and distribution of effective strain rate on the upper skin ( $t=1$  mm,  $d=12.7$  mm,  $v=4$  m/s). ....115

Figure 4.49: Simulated damage sequence occurring in the E-glass phenolic sandwich with  $t=1$  mm,  $d=12.7$  mm,  $v=4$  m/s (contour of plastic strain): 1) Nomex crushing, 2) Top skin failure, 3) Shear failure in the Nomex core, 4) Plug formation, 5) Bottom skin failure, 5) Complete penetration. ....116

Figure 4.50: Comparison of experimental and numerical  $F-d$  curves for  $t=1$ mm,  $d=12.7$ mm,  $v=8$ m/s with evolution of damage variable  $\omega_1$  and  $\omega_{12}$ . ....118

Figure 4.51: Comparison of experimental and numerical  $F-d$  curves for a)  $t=2$  mm,  $d=12.7$  mm,  $v=1$  m/s and b)  $t=2$  mm,  $d=12.7$  mm,  $v=4$  m/s. ....118

Figure 4.52: Comparison of experimental and numerical  $F-d$  curves for  $t=1$  mm,  $d=20.0$  mm,  $v=8$  m/s and corresponding top view of impacted specimens. ....119

Figure 4.53: Comparison of experimental a) and numerical b) top residual damage for E-glass phenolic sandwich with  $t=1$  mm,  $d=12.7$  mm,  $v=8$  m/s. ....120

Figure 4.54: Comparison of experimental a) and numerical b), through the thickness residual damage for E-glass phenolic sandwich with  $t=2$ mm,  $d=12.7$ mm,  $v=1$ m/s. ....120

Figure 5.55: Illustration of multiscale framework of damage analysis for Mode I interlaminar fracture toughness of CNT/CNF-based composites. ....126

Figure 5.56: Schematic representation of the SWCNT and MWCNT structure: a) definition of chiral vectors and chiral angle  $[\chi]$ , b) three dimensional rendering. ....128

Figure 5.57: a) AFM analysis of dispersions of CNTs in 0.5% SDBS, b) simultaneous length and diameter measurements [23]. ..... 132

Figure 5.58: Comparison of length distributions before (pristine MWCNTs) and after processing of Nanocyl™ NC7000 a) and Baytube b) C150HP MWCNTs [31]. ..... 133

Figure 5.59: PDF for different scale and shape parameters: Lognormal a) and Weibull distribution b). ..... 136

Figure 5.60: Histogram of dispersed SWNT lengths [34]. ..... 137

Figure 5.61: Definition of Euler angles in SWNT nanocomposites [36]. ..... 138

Figure 5.62: Incident and scattered intensities on the SWNT and related angles in the polymer and laboratory frames [36]. ..... 141

Figure 5.63: The spring model of a curved CNT [56]. ..... 144

Figure 5.64: RVE for wavy CNT embedded in polymer matrix [59]. ..... 145

Figure 5.65: Detail of an MD model: a) cross-sectional view of the model, b) CNT pull-out from polymer matrix [74]. ..... 147

Figure 5.66: Schematic description of possible fracture mechanisms of CNTs [80]: (a) initial state of the CNT; (b) CNT pull-out due to CNT/matrix; (c) rupture of CNT ; (d) sword in sheath mechanism, i.e. fracture of the outer CNT layer and pull-out of the inner tube; (e) bridging and partial debonding of the interface. .... 150

Figure 5.67: TEM micrographs of MWCNTs bridging a matrix crack; the inset highlights MWCNT pullout from the matrix [81]. ..... 150

Figure 5.68: Schematic representation of a crack propagating in a composite: through a micro-fiber a) and a certain number of CNTs b) having total volume equivalent to the volume of the microfiber. .... 152

Figure 5.69: Schematic illustration of a single fiber pullout. .... 152

Figure 5.70: Relationship between the pull-out force and pull-out displacement for a MWCNT being pulled out from its surrounding matrix [85]. ..... 156

Figure 5.71: Pull-out force and displacement curve MWCNT sword in sheath mechanism [85]. ..... 156

Figure 5.72: Linear bridging law for pullout of CNTs [86].: ..... 157

Figure 5.73: Mathematical illustration of equations 5.21 and 5.22 (MWCNT pullout and sword in sheath mechanism) [86]. ..... 158

Figure 5.74: Schematic representation of CNF/CNT filled epoxy resin interlayer placed at the midplane of the composite laminate (highlighted in red); a) S2-glass fiber/epoxy laminated composite, b) focus on the nanofilled epoxy interlayer placed at the midplane of the laminate. .... 163

Figure 5.75: Illustration of the CNT-bridged Mode I IFT specimen, a); focus on the CNF/CNT bridging action during crack propagation, b). ..... 165

Figure 5.76: Scheme of CNT pullout problem: a) pullout of different CNTs within the resin interlayer; b) CNT pullout schematization where  $l$  is the CNT embedded length,  $\delta$  is the

crack opening displacement and $\theta$ is the CNT inclination angle with respect to the load direction, $P$ .....	167
Figure 5.77: PDF for CNT orientation distribution: equation 5.31 reported for different scale and shape parameters. ....	168
Figure 5.78: Increment of the onset of damage $G_{Io}$ for the mode I IFT test .....	175
Figure 5.79: SEM images of mode I fracture surfaces [91]: a) composite with a long GPS-CNT epoxy interlayer; b) long GPS-CNTs in the interlayer: cavities in circles were possibly created by CNT pull-out; c) composite with a GPS-CNF interlayer; d) GPS-CNFs with epoxy layers bonded to the CNF surface. ....	177
Figure 5.80: CNF details: a) 3D rendering; b) longitudinal section; c) TEM image and material characteristics - (from <i>Applied Sciences Inc. (Cedarville, OH)</i> <a href="http://apsci.com/?page_id=19">http://apsci.com/?page_id=19</a> ).....	178
Figure 5.81: UF-CNF length distribution after 1 and 4 hours of bath sonication dispersion time according to the length distribution of equation 5.28.....	179
Figure 5.82: <i>Short OH Functionalized material properties and Short OH TEM image; provided by</i> <a href="http://www.cheaptubesinc.com/shortohcnts.htm#ixzz2HkbOislo">http://www.cheaptubesinc.com/shortohcnts.htm#ixzz2HkbOislo</a> .....	180
Figure 5.83: <i>VGCNTs material properties and VGCNTs TEM image; provided by</i> <a href="http://www.cheaptubesinc.com/shortohcnts.htm#ixzz2HkbOislo">http://www.cheaptubesinc.com/shortohcnts.htm#ixzz2HkbOislo</a> .....	180
Figure 5.84: Probability density distribution of a-MWCNTs (i.e. VGCNTs) after 5 minutes of sonication in epoxide/acetone mixture [96]. ....	181
Figure 5.85: Increment of fracture energy ( $G_{Ionset}$ increment) as a function of interfacial shear strength $\tau$ . Case 1 (baseline material properties, Table 5.11).....	185
Figure 5.86: Increment of fracture energy ( $G_{Ionset}$ increment) as a function of interfacial shear strength $\tau$ . Case 1 (variation of $V_{CNF}$ ).....	186
Figure 5.87: Increment of fracture energy ( $G_{Ionset}$ increment) as a function of interfacial shear strength $\tau$ . Case 1 (variation of $L_C$ ). ....	187
Figure 5.88: Increment of fracture energy ( $G_{Ionset}$ increment) as a function of interfacial shear strength $\tau$ . case 1 (variation of $d_{CNT}$ ).....	188
Figure 5.89: Increment of fracture energy ( $G_{Ionset}$ increment) as a function of interfacial shear strength $\tau$ . case 1 (variation of $\theta_{CNT}$ ).....	188
Figure 5.90: Increment of fracture energy ( $G_{Ionset}$ increment) as a function of interfacial shear strength $\tau$ . case 1-2, comparison of Fu and Lauke model and Mirjalili model by assuming modified input material data. ....	191
Figure 5.91: Increment of fracture energy ( $G_{Ionset}$ increment) as a function of interfacial shear strength $\tau$ . Case 4 (baseline material properties, Table 5.12).....	193
Figure 5.92: Increment of fracture energy ( $G_{Ionset}$ increment) as a function of interfacial shear strength $\tau$ . Case 4 (variation of $V_{CNF}$ ).....	193
Figure 5.93: Increment of fracture energy ( $G_{Ionset}$ increment) as a function of interfacial shear strength $\tau$ . Case 4 (variation of $L_C$ ). ....	194

Figure 5.94: Increment of fracture energy ( $G_{I_{onset}}$  increment) as a function of interfacial shear strength  $\tau$ . Case 4 (variation of  $d_{CNT}$ ) ..... 195

Figure 5.95: Increment of fracture energy ( $G_{I_{onset}}$  increment) as a function of interfacial shear strength  $\tau$ . Case 4 (variation of  $\theta_{CNT}$ ) ..... 195

Figure 5.96: Increment of fracture energy ( $G_{I_{onset}}$  increment) as a function of interfacial shear strength  $\tau$ . Case 4, comparison of the Fu and Lauke model and the Mirjalili model by assuming modified input material data. .... 197

Figure 5.97: Increment of fracture energy ( $G_{I_{onset}}$  increment) as a function of interfacial shear strength  $\tau$ . Case 3, comparison of Fu and Lauke model and Mirjalili model by assuming modified input material data. .... 199

Figure 5.98: Increment of fracture energy  $G_{I_{onset}}$  as a function of average CNT length,  $L_{average}$ : Case 3, comparison of the Fu and Lauke model varying interfacial shear strength,  $\tau$ , values. .... 200

Figure 5.99: a) MD initial system for CNT pullout at an angle  $\theta$  from an epoxy matrix; b) three dimensional rendering. .... 202

## **List of tables**

Table 2.1: Mechanical properties of the calibrated model ..... 28

Table 3.2: Failure equation for three-point bending configuration [20]. ..... 50

Table 3.3: Mechanical properties of Nomex Honeycomb – experimental results. .... 67

Table 4.4: Test methods involved in the mechanical characterization of skin materials. .... 104

Table 4.5: Mechanical properties of composite skins derived by experimental tests and calibrated parameters (in parenthesis)..... 104

Table 5.6: Comparison of toughness mechanisms of micro- and nano-reinforced polymer matrix composites [79]. ..... 149

Table 5.7: Functionalized nanofillers used for making multi-scale reinforced composites ..... 173

Table 5.8: Multiscale nanofiler-composite composition and sonication time ..... 173

Table 5.9: Mode I IFT test results ..... 175

Table 5.10: Mechanical properties of CNTs used within the present study ..... 181

Table 5.11: Input material data for case 1, 0.5 wt% UF-CNF epoxy, baseline material properties. .... 184

Table 5.12: Input material data for case 4, 0.25 wt% long GPS-CNTs epoxy, baseline material properties. .... 192

Table 5.13: Input material data for case 3, 0.5 wt% short GPS-CNTs epoxy, baseline material properties. .... 198



## **Chapter I**

# **INTRODUCTION**

### **1.1. Introduction**

Composite systems, such as fiber reinforced polymers, have increasingly advanced since early developments in the 1970s up to date, gaining the leadership in the lightweight structure engineering field. The aeronautics industry is certainly one of the major recipients of engineering and technological progresses of composite materials; in fact, today, aircrafts such as Boeing 787 and Airbus A380 represent the demonstration of such developments. The use of composite materials has over the years expanded beyond the aerospace applications to other areas of structures. Typical and emerging applications of composite materials include automotive, naval and wind energy sectors, whose future challenges are related to cost effectiveness, multiaxial fatigue resistance, long term durability and structural safety.

The concept of composite systems has expanded over the years resulting in the design of new composite configurations. For instance, the demand for light-weight efficient and high-stiffness structures led to the introduction of multilayered composite configuration, such as sandwich structures. Sandwich structures experienced a wide expansion over the years, still active up to date, especially for applications requiring high stiffness-to-weight ratios; the exclusive properties of core materials, such as honeycomb and foam materials, as well as the high mechanical properties of fiber reinforced composite facesheets, can be suitably tailored and combined to produce cost-effective lightweight components of complex geometries, offering varied physical

and mechanical performances (e.g. energy absorption and stiffness optimization, thermal insulation, acoustic damping).

In early 1990s, the development of nanotechnologies pushed research and engineering community to investigate the high potentialities of multifunctional nanostructured materials. In this way, the concept of “*composite*” material experienced a further evolution, with the possibility to incorporate nanofillers (e.g. carbon nanotubes, nanoparticles, nanoclay) to conventional composite systems, broadening the typical engineering applications of composites. However, the main concern related to these promisingly applications is associated with the small dimensional scale of the filler (the order of magnitude is between 5 and hundreds nm) that need great attention in order to have fully control of such type of innovative materials.

Even though positive aspects related to the use of composite materials offer wide perspectives for engineering, a significant challenge is still open with respect to damage phenomena; these represent a source of complexity due to significant heterogeneities and interactions between composite constituents. In fact, it is well known that the characterization of failure behavior of composite structures depends on a very large number of variables. For instance, the possibility of having interacting failure modes in a composite laminate constraints the damage analysis to properly characterize intralaminar and interlaminar damage, in order to assess the composite damage behavior. Moreover, with regard to the behavior of sandwich structures, the specific morphology of a sandwich configuration shall be taken into account. The assessment of the global behavior and local stress fields of sandwich structures depends on the material properties of the constituents (skins, core, and adhesive if involved), geometric dimensions, and type of loading. On the contrary, an exhaustive comprehension of damage mechanisms occurring at nanoscale, is the key step for the future effective development and control of nanocomposites systems.

In the light of these considerations, it appears that the modeling of damage and fracture plays an important role for composite engineering development affecting both design stages (to prevent in service damage) and the implementation of structural health monitoring systems (to predict the residual lifetime of structures). Therefore, the main challenge in any computational design procedure is to accurately incorporate damage and its effects on composite structure. In this context, the progress consists in taking advantages of properly modeling damage into computational design procedures with the final aim to reduce the cost of certification requirements and design safer and cost effective structures.

## **1.2. Historical overview and multiscale damage analysis**

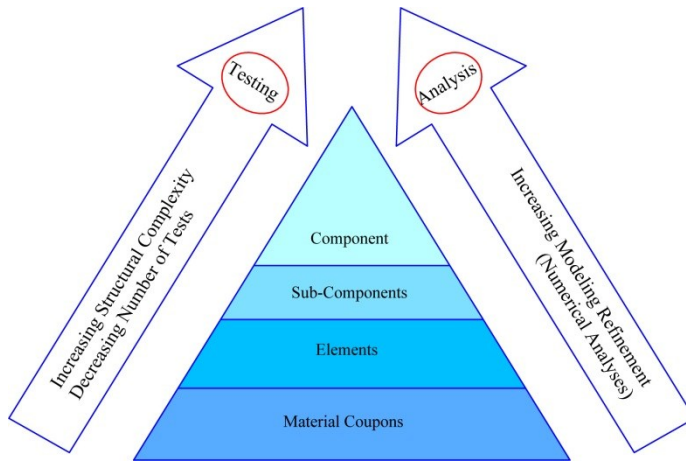
The mechanisms of damage taking place in a composite system and their effects on mechanical response represent the main challenging concern in the field of composite damage analysis and modeling. These issues developed starting in the 1980s. Before 1980s, the composite failure analysis was mostly based on the continuum mechanics approach extended by previous theories valid for metals. In the 1980s the need to consider the heterogeneous nature of composite materials led to the introduction of micromechanics and continuum damage mechanics theories which were firstly applied to multiple cracking observed in composite materials. The first pioneering work in this field was provided by Aveston et al. [1] who evaluated the role of composite constituent properties, i.e. fibers and matrix properties, relative volume fractions and fiber diameter in resisting multiple cracks in steel fibers reinforced cement composites. From these concepts, two main advancements were subsequently presented in the approach, namely micro damage mechanics [2] (investigating local ply stress fields to evaluate the overall stiffness degradation) and macro damage mechanics [3] (investigating internal material discontinuities through the definition of a damage scalar variable). Homogenization techniques were then applied to composite materials [4]; according to this approach, the reinforcement in a composite is treated as a part of the microstructure and is homogenized in a representative volume element as an anisotropic medium in which damage entities are considered. Many further developments have taken place up to the current knowledge in composite material damage field. Clearly, complex structural geometries, composite configurations and load conditions require numerical structural analysis. However the analysis of composite damage behavior, obtained by means of numerical approaches, is rather difficult due to the intrinsic complexity of the interaction of failure modes, damage development and multilayered configurations.

Recently, the advancements achieved in the field of numerical methodologies as well as computational efficiency, have motivated the rise of the so called “*multiscale*” computational analysis. The key concept is that physical phenomena occurring at lower length scale control the material response at higher length scales. The heterogeneous nature of composite systems makes multiscale modeling methodologies optimal candidates for these materials. By formulating models at different scales, i.e. macro, meso, micro and even nano, damage evolution can be accurately predicted. A wide literature on multiscale modeling exists providing a wide range of results which point out the critical role of multiscale methods in achieving feasible and accurate

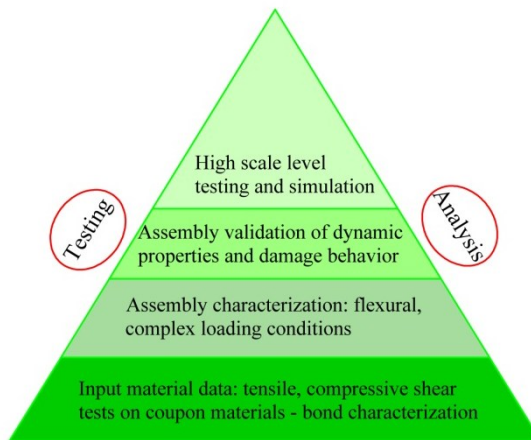
descriptions of the behavior of many complex systems [5-7].

In industrial sectors, such as the aerospace industry, the issue of structural modeling, including static strength prediction, durability analysis and damage tolerance of composite and sandwich materials, is often addressed through a multiscale method based on a complex mix of testing and analysis. This process is also named *building block* approach or *virtual testing* which develops according to the flow chart reported in Figure 1.1a,b. Tests and numerical analyses are performed progressively at various levels of structural complexity, starting from small material coupons and moving through structural elements, sub-components, components, and, finally, up to the complete full-scale product. Each level uses the experimental/numerical outcomes gained at the previous level of analysis in order to generate composite material properties and appropriate analysis methods. For instance, in case of sandwich structures, the first level of analysis has the objective to characterize of basic material properties (including skins and core materials) to be used as input data at the assembly level of analysis. Then, tests and analyses performed at the element level are used to investigate and validate of both analytical and numerical predictions, with particular emphasis on the failure modes; at the sub-component level, tests and failure analysis are implemented to deal with specific geometrical, loading, and environmental conditions (e.g. fatigue, impact loading, hygrothermal aging). Finally, at the highest level of structural complexity, tests are used to validate the analysis methods developed during the previous levels. As the structural complexity rises up, testing costs increase as well, but the number of tests decreases and more reliable numerical simulations are validated.

Recently, other features of multiscale approach have emerged in case nanocomposite systems. Nanofillers, thanks to their exceptional properties, offer the possibility to achieve outstanding improvements if added to polymer matrices at much lower concentrations than traditional (micro-sized) fillers. The resulting physical and chemical properties of nanocomposites can be related to the hierarchical structure of this kind of materials. Moreover, nanomodified polymers can be used for the development of nano-modified composite laminates achieving higher performance materials. The engineering progress in the field of nanocomposites requires models capable of accounting for their multiscale structure ranging from the nano to the macro length scales.



a)



b)

**Figure 1.1: Multiscale procedure for the design and optimization of multilayered composite structures: a) increasing the scale levels of the composite component; b) type of tests and analyses to be performed as the length scale increases.**

In this way, characteristic phenomena acting at each length-scale could be taken into account and their effects bridged from the smaller scale to the macroscale. By accounting for these features, an effective modeling can be achieved. Quaresimin et al. [7] proposed a classification of the multiscale modeling strategies in the field of nanocomposites, as reported in Figure 1.2:

- *Micromechanical* modeling strategies, based on micromechanical models only. The matrix and the nanofiller are described by means of continuum mechanics without accounting for interfacial interactions and nanostructure.

- *Nanostructural* modeling strategies, making use of both micromechanical models and nanostructural models. These methods account for the effects of the inherent nanostructure on the overall macroscopic properties, but chemical–physical interactions are not taken into account.
- *Molecular modeling* strategies, making a combined use of all the above mentioned models. Intermolecular and supramolecular interactions are accounted for by means of discrete methodologies at the actual nanoscale level.

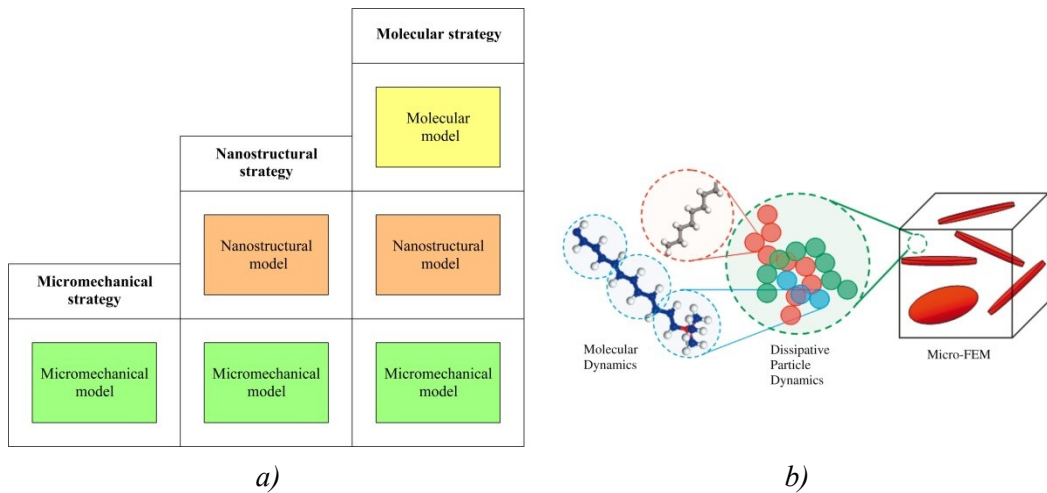


**Figure 1.2:** Concept of *multiscale strategies* applied to nanostructures: a) [7]; multiscale simulation strategy for coarse-graining of surfactant molecules into beads b) [8].

### 1.3. Research purposes and outline

In the present work, different critical issues, related to damage assessment and modeling of advanced composite structures, are addressed through the analysis of different case studies in a multiscale procedure. Hereafter, an outline including each case study is presented.

The activity presented in *Chapter II* is aimed at simulating the response of clamped circular GFRP plates of two different thickness values, struck at low-velocity by a rigid hemispherical projectile. The design of advanced composite structures or components subjected to impact loadings requires a deep understanding of the damage and degradation mechanisms occurring within the composite material. The multiscale

numerical analysis proposed in *Chapter II* is aimed at properly including the possible modes of failure of the GFRP composite laminates and quantify the energy dissipated by different mechanisms. Through the definition of suitable finite element models for both composite plies and interlaminar connections two levels of composite damage analysis are taken into account:

- *intralaminar* level, related to the damage occurring to the matrix and fibers within a composite ply;
- *interlaminar* level, related to the damage occurring within the matrix layer between two adjacent plies.

This numerical approach allows to characterize the critical parameters acting at the smaller (interlaminar) scale, which affect the whole impact response of the composite laminate, at the larger scale. In this way, the energy absorbed by the composite laminate during impact (that is measurable at the larger scale) is related to damage mechanisms occurring within the laminate (that are analyzed at the smaller scale).

The activities presented in *Chapter II* and *Chapter III* have the objective to model the mechanical behavior of E-glass phenolic skins/Nomex honeycomb core sandwich structures, particularly focusing on out of plane compressive properties (including buckling and crushing) and impact behavior. In detail, the damage analysis conducted in *Chapter III* focuses on the buckling and crushing behavior of hexagonal honeycomb structures; the multiscale numerical analysis moves from the meso scale level, focusing on Nomex paper material properties, including the sensitivity to material defects. Then, the numerical analyses are performed on a representative honeycomb cell enabling to transfer mechanical properties, predicted at the meso scale, to the macroscale of the whole sandwich structure, with the final aim of predicting the compressive strength and folding mechanism during the Nomex cell crushing. The key aspect proposed in the study is the inclusion of imperfections in terms of both material (elastic modulus variability) and geometrical (thickness variability) defects through a stochastic approach: random sampling at each element of the FE mesh are performed assuming different Young's modulus values and different thickness properties, according to a pre-defined statistical distribution. The modeled cell is used to address several aspects of the compressive response, particularly focusing on the onset of buckling, the collapse limit and the crushing behavior.

The damage analysis conducted in *Chapter IV* moves to the scale length of the sandwich assembly aimed at modeling the impact behavior of Nomex honeycomb core combined with E-glass phenolic facesheets. Since the impact damage occurring in composite sandwich structures affects both skins and core materials, the multiscale

approach involves the detailed (static and dynamic) modeling of both skin and core material properties. The adopted multiscale virtual testing procedure is based on the progressive validation of the composite facesheet and orthotropic honeycomb material models on the basis of experimental tests, ranging from coupon tests (for E-glass phenolic skins and Nomex core) to sandwich assembly tests. This allows to verify the capability of the model to take into account the main damage mechanisms taking place during impact. The dynamic impact behavior is then validated through different impact conditions; some important issues on the strain rate sensitiveness affecting the investigated materials are addressed, along with the assessment of energy absorption and damage mechanisms.

*Chapter V* investigates the main issues related to the multiscale modeling of nanocomposite properties. In detail, the activity focuses on multiscale modeling of Mode I interlaminar fracture toughness of S2-glass fiber/epoxy laminated composite modified using nanofillers (Carbon NanoTubes, CNTs, and Carbon NanoFibers, CNFs) with/without surface functional groups and with different ranges of aspect ratio.

The smaller scale of the analysis takes into account the toughening mechanisms acting at the nanoscale. A suitable analytical model describing the CNT pullout mechanism is then presented accounting for the CNTs properties within the matrix at the nanoscale, i.e. length and orientation distribution and stress transfer. Then, the result of this modeling is used to calibrate fracture energy models at the macroscale, by means of Mode I interlaminar fracture toughness tests on nanofilled S2-glass fiber/epoxy laminated composites. Some important issues are discussed, including interfacial shear stress determination, CNT/CNT volume fraction as well as CNT critical length definition.

## **References**

1. Aveston, J., G.A. Cooper, and A. Kelly, *Single and multiple fracture*. In: The Properties of Fiber Composites (Surrey, UK: IPC Science and Technology Press, National Physical Laboratory), 1971: p. 15-26.
2. Hashin, Z., *Analysis of cracked laminates: a variational approach*. Mechanics of Materials, 1985. **4**(2): p. 121-136.
3. Kachanov, L.M., *Rupture time under creep conditions*. Izv Akad Nauk SSSR Otd Tekhn Nauk [in Russian], 1958. **8**: p. 26-31.

4. Talreja, R., *Transverse cracking and stiffness reduction in composite laminates*. Journal of Composite Materials, 1985. **19**: p. 355-375.
5. Zinno, A., E. Fusco, A. Prota, and G. Manfredi, *Multiscale approach for the design of composite sandwich structures for train application*. Composite Structures, 2010. **92**(9): p. 2208-2219.
6. Feraboli, P., F. Deleo, et al., *Predictive modeling of an energy-absorbing sandwich structural concept using the building block approach*. Composites Part a-Applied Science and Manufacturing, 2010. **41**(6): p. 774-786.
7. Quaresimin, M., M. Salviato, and M. Zappalorto, *Strategies for the assessment of nanocomposite mechanical properties*. Composites Part B-Engineering, 2012. **43**(5 ): p. 2290-2297.
8. Fermeglia, M. and S. Pricl, *Multiscale molecular modeling in nanostructured material design and process system engineering*. Computers & Chemical Engineering, 2009. **33**(10): p. 1701-1710.



## **Chapter II**

# ***IMPACT BEHAVIOR OF GFRP COMPOSITE LAMINATES***

### **2.1. Introduction to framework**

The design of advanced composite structures or components subjected to impact loadings requires a deep understanding of the damage and degradation mechanisms occurring within the composite material. Despite years of extensive research around the world, a complete and validated methodology for predicting the behavior of composite structures, including the effects of damage, has not yet been fully achieved. This is largely due to the complexity of the physical phenomena involved, requiring an effective modeling of dynamic effects, material-projectile contact, failure modes development and interaction within the laminate, yet taking into account the influence of impactor geometry, velocity, and mass, and target geometry, constraint conditions, and lay-up.

Damage in a composite laminate generally involves two levels of analysis:

- *intralaminar* level, related to the damage occurring to the matrix and fibers within a composite ply;
- *interlaminar* level, related to the damage occurring within the matrix layer between two adjacent plies.

This peculiarity makes suitable a multiscale approach aimed at properly including the possible modes of failure of the laminate and quantifying the energy dissipated by the different mechanisms. The multiscale modeling approach presented in *Chapter II* is conducted including both levels of damage analysis through the definition of suitable

finite element models for the composite plies and interlaminar connections, as depicted in Figure 2.3.

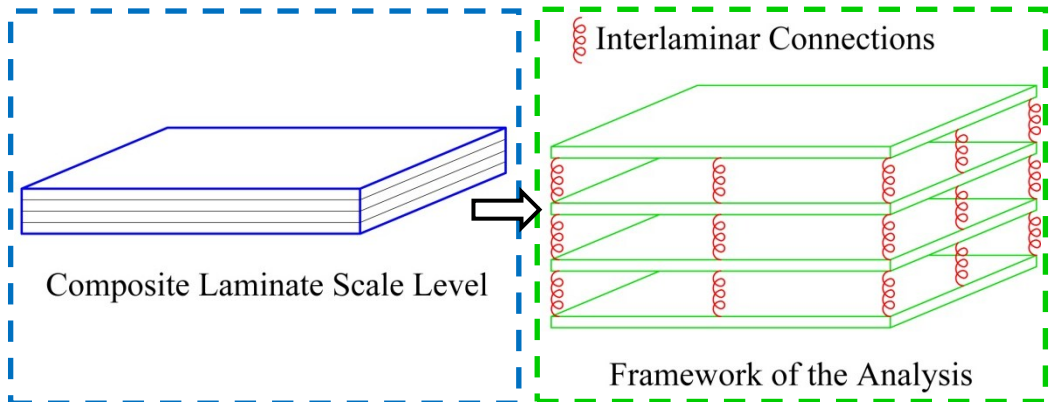


**Figure 2.3: Scheme of multiscale damage analysis for GFRP laminates adopted within the study.**

By using this approach, the composite impact behavior is studied at two scales. This allows to characterize the critical parameters acting at the smaller (interlaminar) scale and affecting the whole impact response of the composite laminate at the larger scale. The energy absorbed by the composite laminate during impact (that is measurable at the larger scale) is related to damage mechanisms occurring within the laminate (that are analyzed at the smaller scale).

In details, the present activity is aimed at simulating the response of clamped circular GFRP plates of two different thickness values, struck at low-velocity by a rigid hemispherical projectile. A finite element model, based on the commercial tool LS-DYNA, is built and calibrated using the information gathered from a minimum of experimental data. Solid finite elements combined with orthotropic failure criteria are used to model the composite failure and stress based contact failure between plies are adopted to model the delamination mechanism.

## 2.2. Literature overview: impact on composite laminates

The use of fiber-reinforced composite materials has increased over the last decades, due to their advantageous specific mechanical properties and corrosion resistance. Advanced composites have been used in many different engineering applications encompassing military, automotive and naval industry, and especially in aerospace, where weight reduction is one of the most important design parameters.

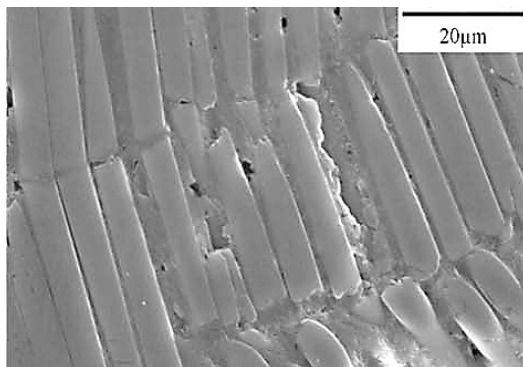
Although these materials offer very attractive properties, their application is often restricted by their vulnerability to transverse impact [1], forcing the adoption of large safety factors and resulting in significantly over-designed structures.

Aeronautical components are prone during service to foreign object impact events [1], varying in the range of low to high velocities and impacting masses, consisting of dropping tools during production, repair or maintenance operations, ice particles or runway debris, bird strikes. At high velocity, the structural response is dominated by the stress wave propagation through the thickness of the laminate, and the resultant damage is quite localized. On the contrary, in a low-velocity impact the contact duration is long enough to excite the global structural response, leading to a more diffuse damage [2, 3].

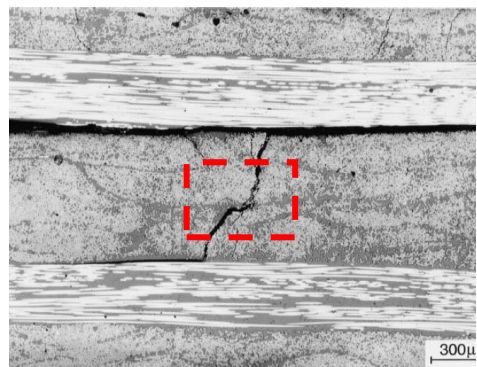
The damage suffered by a composite laminate subjected to impact loading can affect the composite material within each lamina of the laminate, i.e. intralaminar damage, or it can develop between adjacent plies, i.e. interlaminar damage. Within this distinction, the damage can be divided into four distinct groups:

- *matrix cracking*, where cracking occurs parallel to the fibers due to tension, compression or shear;
- *delamination* between adjacent plies which is produced by interlaminar stresses;
- *fiber breakage* due to tension fiber breakage and compression fiber buckling;
- *perforation*, where the impactor completely perforates the impacted surface.

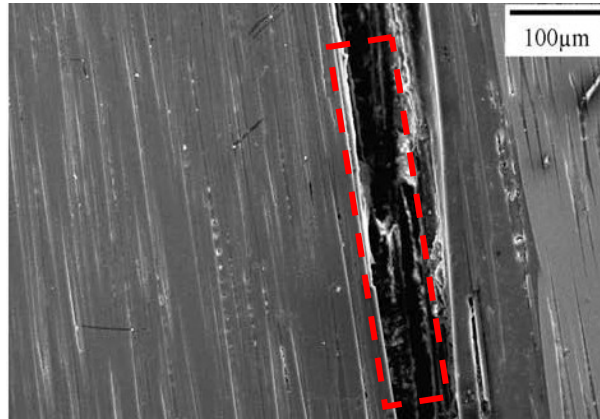
Such order corresponds to the damage sequence occurring for increasing impact energies. Figure 2.4 reports SEM images depicting the typical damage occurring in a composite laminate as a consequence of impact, referring to fiber breakage (a), matrix cracking (b) and delamination (c), respectively.



a)



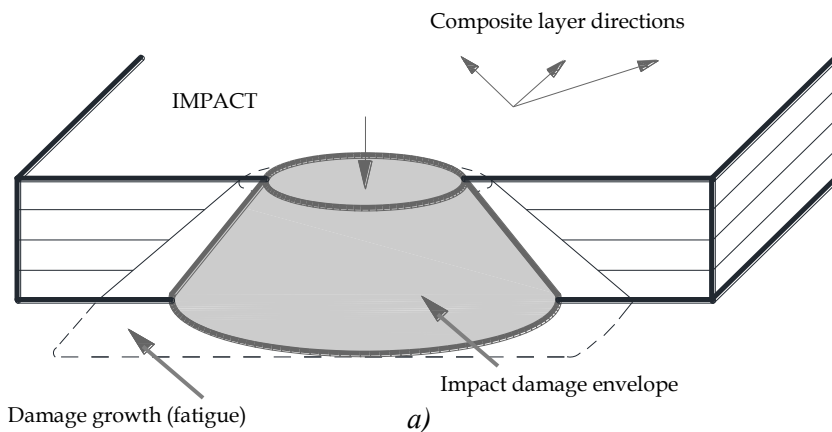
b)



c)

**Figure 2.4: Typical impact damage in a composite laminate: a) failure due to fiber breakage [4]; b) intralaminar matrix shear cracks [5]; c) delaminations between adjacent plies [4].**

If the impact energy increases, the damage pattern develops as truncated conical shape with wider damage taking place at the bottom of the panel (Figure 2.5a). Matrix damage is the first type of failure that occurs during transverse low-velocity impact; it typically takes the form of matrix cracking but also debonding between fiber and matrix within the lamina. Matrix cracks take place due to property mismatching between the fiber and matrix, and are usually oriented in planes parallel to the fiber direction in unidirectional layers. Joshi and Sun [6] provided a typical shear (red), flexural (green) matrix crack and delamination pattern (blue), as shown in Figure 2.5b and c.



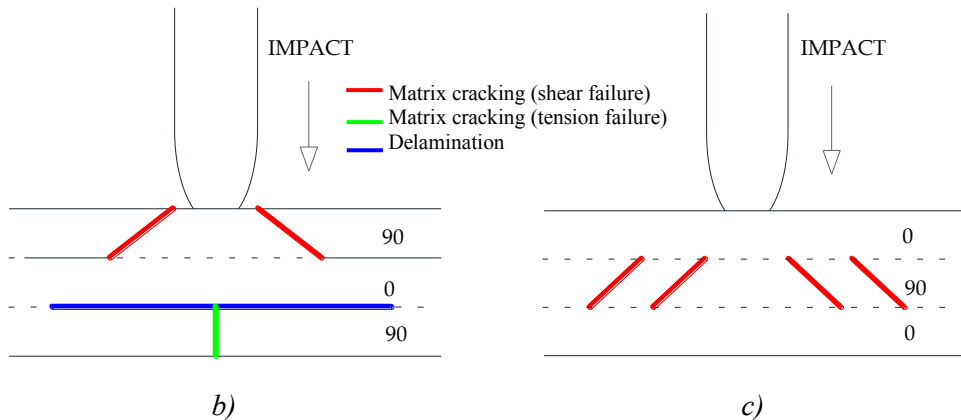


**Figure 2.5: Illustration of impact damage development: a) damaged area through the thickness of the composite laminate; matrix cracks (red) and delamination (blue) pattern for transverse impact b), c) [6].**

Delamination, occurring at moderately low energy levels, deserves serious considerations, being able to cause a significant decrease in the static material compression strength, or growing under cyclic loads leading to a gradual loss in strength and stiffness [7].

### 2.3. Impact modeling

The impact response of composite laminates has been widely treated in the literature by experimental research works, analytical formulations and numerical implementations, with the objectives of understanding the tip-material interaction [8, 9], predicting the extent of induced damage [10, 11], and estimating the residual properties of the structure [7, 12, 13]. In particular, many research efforts have been spent to model impact history. To this aim, quite simple closed-form solutions [14], easy to use and effective, but restricted to simple impact cases due to the underlying simplifying assumptions [10, 14, 15], have been often employed.

In the last decades, an alternative to the analytical formulations has been offered by the numerical methodologies based on Finite Element (FE) approach. Since the onset of damage in a composite does not usually lead to ultimate failure, the ability of FE in simulating an impact event is critically dependent on its capacity to represent the sequence of damage modes, the conditions for delamination propagation, as well as the stiffness and strength degradation associated with the various damage states. FE simulation works available in the literature are based on different theoretical

formulations including failure criteria, plasticity theory, fracture mechanics, and damage mechanics. The main drawback of the failure criteria approach [16], initially adopted for unidirectional composites and developed for the static regime, is related to the impossibility to locate the position of the crack and to predict the crack sizes. Moreover, the progressive degradation of stiffness material properties cannot be taken into account. Plasticity approach can be appropriate for composites exhibiting ductile behavior (e.g. thermoplastic composites), in combination with the failure criteria approach for damage prediction [17]. For such materials, a generalized anisotropic model in large strains, based on the classical isotropic plasticity theory, was presented by Car et al. [18]. The fracture mechanics approach [19] is based on the comparison of the strain energy at a crack front of known size with critical values of strain energy release rate. Zerbst et al. [20] applied this approach to predict residual compression strength and delamination growth in composites, showing appreciable results. The main disadvantage of fracture mechanics analysis is that it requires the definition of a pre-existing crack region in the numerical model. The Continuum Damage Mechanics (CDM) approach, initially introduced by Kachanov [21] and Rabotnov [22], has grown considerably in the past twenty years. According to CDM, damage is considered as a deterioration process of the material, introduced as part of the material definition. Using CDM concept, Matzenmiller et al. [23] developed a mathematical model for damage of composite materials, connecting the damage level to the degraded elastic properties of the material, in turn depending on the particular damage mechanism (fiber breakage, fiber microbuckling, matrix cracking, etc.). This approach has been implemented in many research works [24-27], demonstrating promising results in predicting the impact response and damage extent.

## 2.4. Materials and experimental methods

The GFRP panels considered in this work were obtained from prepreg layers made of E-glass plain-weave fabric, 295 g/m<sup>2</sup> in areal weight, and Cycom 7701 epoxy resin. An overview of the mechanical properties of the ply material, drawn from the manufacturer's technical data sheet, is given in Tab. I (values in parentheses).

Two laminates, having stacking sequence [(0,90)<sub>n</sub>/(+45,-45)<sub>n</sub>]<sub>s</sub>, with  $n=1,2$  as depicted in Figure 2.6a and b, respectively, were obtained and press cured for 2 hours at 120°C temperature and 0.1 MPa pressure. The nominal thickness  $t$  was 0.96 mm and 1.92 mm for  $n=1$  and  $n=2$ , respectively.

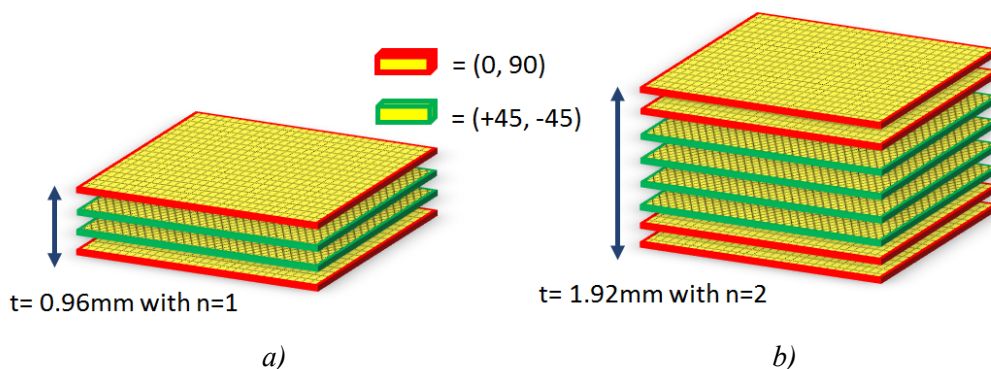


**Figure 2.6:** Schematic representation of the GFRP stacking sequence with  $n=1$ , a) and  $n=2$ , b).

From the laminates, square specimens 70 mm in side were cut, and subjected to low-velocity impact tests using a Ceast MK4 instrumented testing machine, equipped with a DAS 4000 digital acquisition system. The samples were clamped on a steel plate with a circular opening 50 mm in diameter, and struck at their center using a hemispherical steel impactor, 16 mm in diameter and 3.6 kg in mass. Various energy levels  $U$ , in the range 0.4 to 20 J were adopted, appropriately setting the tup height. For each impact energy level, three experimental tests were performed.

Thanks to the translucent appearance of GFRP, the projected damage area  $A_p$  of selected impacted samples was highlighted by an intense light source located at their back side, photographed, and the  $A_p$  extent was measured through an image analyzer. Then, the specimens were immersed in a blue ink bath, until  $A_p$  was fully darkened; after that, they were carefully depled with the help of moderate heating, and the extent of the delaminated areas found in correspondence of each interface was computed as the average measures of upper and lower delaminated areas of each ply,  $A_m$ ; the total delaminated area,  $A_d$ , was computed as the sum of the delaminated surfaces in correspondence of each interface.

## 2.5. Experimental results and discussion

Typical  $F-d$  curves recorded during the impact tests, obtained for the two panel thicknesses, are collected in Figure 2.7. At low displacement, the material behavior is substantially elastic, and disturbed by dynamic oscillations, more marked for the thicker panel. As discussed in previous works [28, 29], the curvature affecting the

thinner laminate during this step is due to membrane effects. Beyond a given load threshold, dependent on the target thickness, sudden load drops appear in the  $F-d$  curves, indicating damage beginning and propagation. Nevertheless, the general trend of the contact force increases further up to the maximum load, where a dramatic load drop, suggesting major damage, is observed. After that, the  $F-d$  curves flatten out until the maximum displacement, corresponding to a zero velocity, is achieved. During rebound, the elastic portion of the energy stored into the material is transferred back to the impactor, whereas another portion (represented by the area enclosed in the  $F-d$  curve) is irreversibly absorbed through material damage, heat, and vibrations.

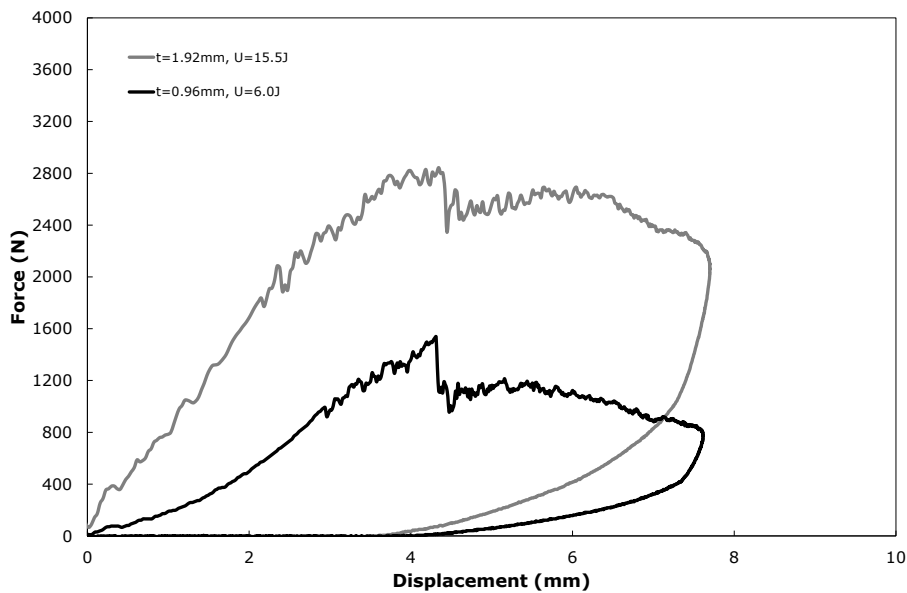


**Figure 2.7:** Effect of the laminate thickness,  $t$ , on the  $F-d$  curves.

As previously specified, the different energy levels in the tests were obtained by suitably setting the drop height of the impactor, i.e. using different impact velocities. In Figure 2.8, different  $F-d$  curves, deriving from impact tests performed at increasing energy levels, are superposed. Despite some obvious differences, attributable to the experimental scatter, the superposition is good. This indicates that, within the experimental conditions adopted in the present tests, the material response is not sensitive to velocity, so that energy is the true parameter affecting its response. In Figure 2.9, the irreversibly absorbed energy  $U_a$ , measured as the area enclosed within the  $F-d$  curve, is plotted against  $U$  (full symbols). As also found by other researchers

[29], the trend is sensibly linear, with a slightly higher rate characterizing the thinner laminate.

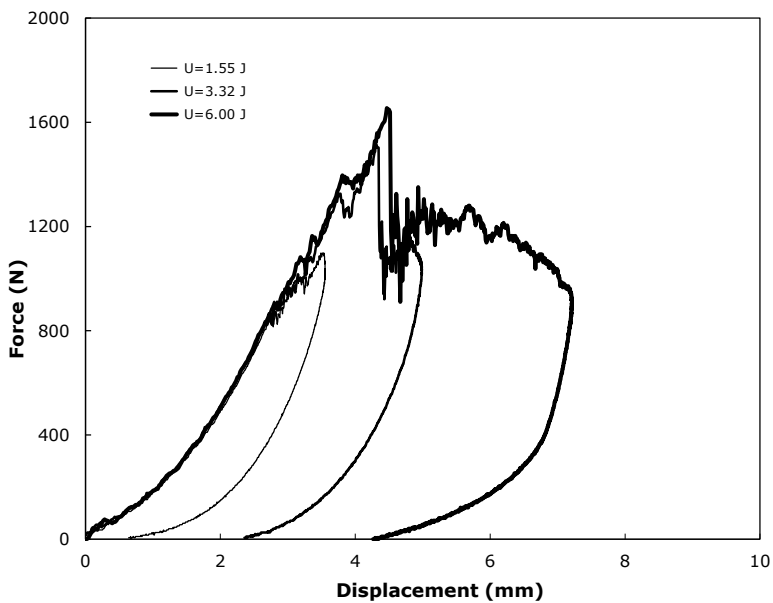


Figure 2.8: Effect of the energy level,  $U$ , on the  $F-d$  curves. Laminate thickness  $t=0.96\text{mm}$ .

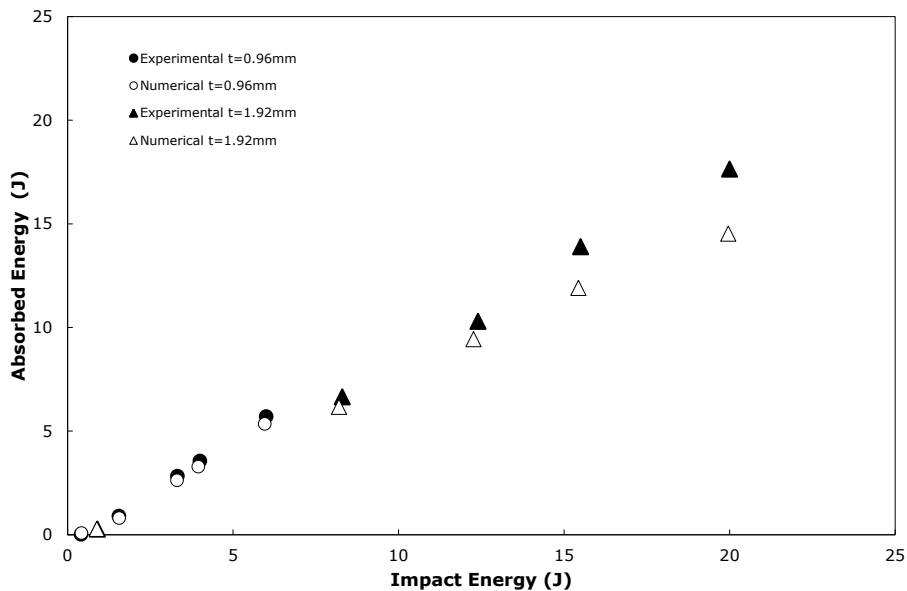
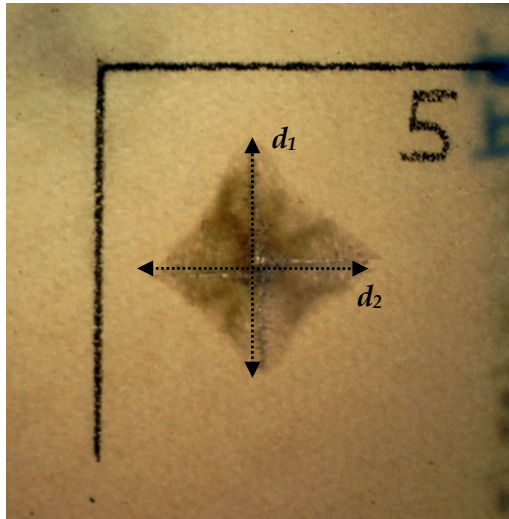


Figure 2.9: Absorbed energy,  $U_{ab}$ , vs impact energy,  $U$ .

The visible delaminated area (Figure 2.10) was diamond-shaped, with the principal axes coinciding with the warp-weft directions of the surface fabric layers (horizontal and vertical directions in the figure), along which fiber fracture was found.



**Figure 2.10: Visible damaged area of an impacted panel.**

Apparently, delamination extent of the impacted specimens was larger when observed by the back face of the panel. This feature was confirmed by the measurements carried out after deplying, which also revealed fiber fractures, developing along the warp-weft directions, in the internal layers. However, for  $t=1.92$  mm, delamination took place also between layers with the same orientation located at the mid-plane of the laminate, as shown by the black symbols in Figure 2.11, where the extent of ply-by-ply delaminated area  $A_m$  is diagrammed for  $U=20.0$  J. In particular, the average measured delaminated area was  $251.53 \text{ mm}^2$  and  $482.80 \text{ mm}^2$  for the interface between layers  $(0;90)/(-45;+45)$  and  $(-45;+45)/(0;90)$  respectively, with the latter  $\approx 92\%$  larger than the former. This damage was expected since the interfaces between layers having different orientations are more prone to delamination, with the largest delaminated area located near the back face of the panel as often found in several impact studies [3, 11, 30]. Nevertheless, should be remarked that the amount of damage occurred at the mid-plane of the laminate, i.e. between layers with the same orientation  $(-45;+45)/(-45;+45)$ , although smaller than the others ( $105.83 \text{ mm}^2$ ), is of the same order of magnitude compared with the other delaminated interfaces.

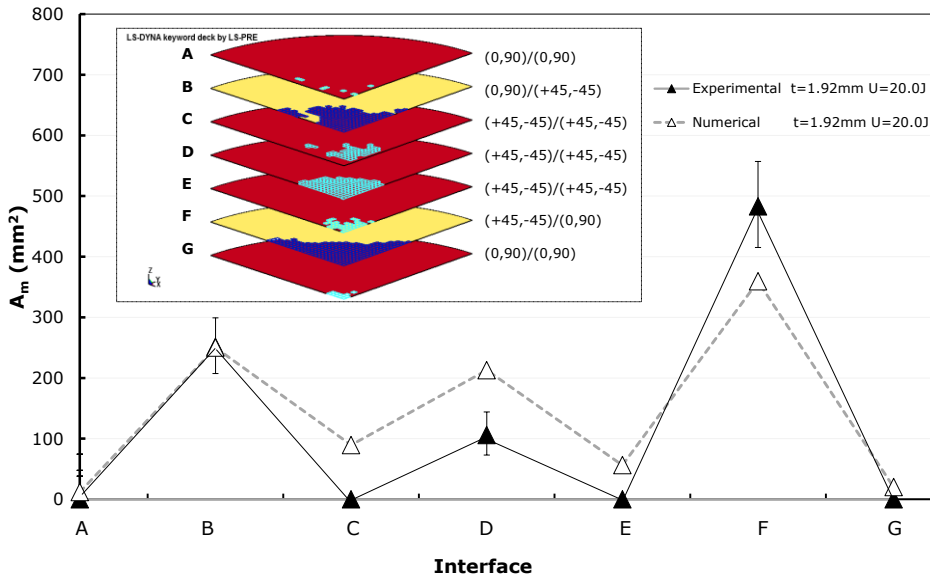


Figure 2.11: Extent of ply-by-ply delaminated area,  $A_m$ . Panel thickness  $t=1.92\text{mm}$ ; impact energy  $U=20.0\text{ J}$ .

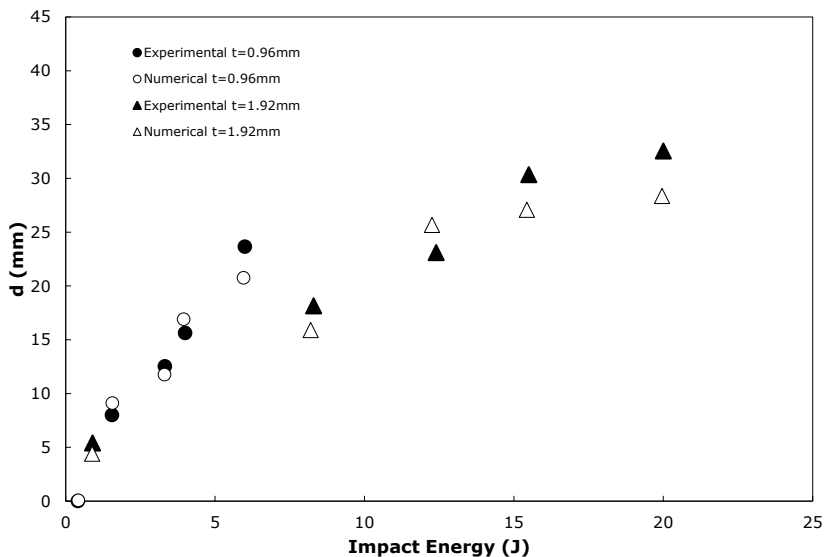


Figure 2.12: Characteristic dimension of projected delaminated area,  $d$ , vs impact energy,  $U$ .

Of course, damage extent increased monotonically with increasing impact energy. This is shown in Figure 2.12 and Figure 2.13 (full symbols), where the mean value  $d$  of the

axes indicated by  $d_1$ ,  $d_2$  in Figure 2.10, and the extent of projected delaminated area,  $A_p$ , are plotted, respectively, against  $U$ .

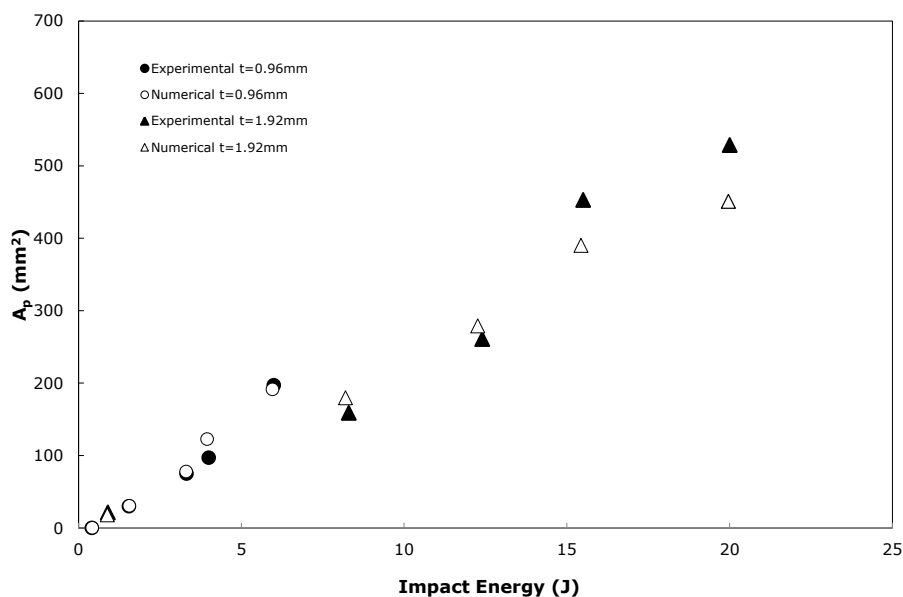


Figure 2.13: Projected delaminated area,  $A_p$ , vs impact energy,  $U$ .

## 2.6. Numerical analysis

### 2.6.1. Model features

The impact tests were simulated using the commercial finite element code LS-DYNA Version 971, and were run in double precision mode. Since one of the scopes of the analysis was the prediction of damage development, a 3D model of the ply was selected, to obtain a more accurate description of the stress distribution along the ply thickness. Each ply was modeled through a single layer of three-dimensional eight nodes finite elements, whereas the bond between adjacent plies was simulated through distributed spring connections. The whole laminate model consists of 4 (for  $t=0.96\text{mm}$  laminate) and 8 ( $t=1.92\text{mm}$ ) discrete circular plates 50 mm in diameter, representing each single fabric ply arranged according to the fixed lay-up sequence. The elements had an edge length along the thickness corresponding to the thickness of a single ply, i.e. 0.24 mm. A parametric study was carried out, investigating the influence of the

plane element lengths showing a mesh dependency. Specifically, the composite material failure behavior is influenced by the element size affecting the absorbed energy which varies with the element length and converges for small elements dimensions. Moreover, since the impact of the rigid hemisphere is very localized, a very fine mesh is required in order to achieve an accurate mechanical behaviour and a correct working of the contact algorithm. The selected in-plane element edge lengths were approximately 0.657 mm and the 90% of elements had an aspect ratio of 3:1 or less.

Among the lamina constitutive models available in LS-DYNA, the Mat Composite Failure Option Model (Mat 059, Option = Solid) [31], able to model the progressive damage of the material on the basis of a three-dimensional stress-based failure criterion, was chosen in this work. Although the selection of MAT59 in shell formulation has been discussed in several applications available in literature [32], works or detailed descriptions investigating its behavior in 3D formulations are scarce and only few information can be found from informal documentation available from Livermore Software Technology Corp. (LSTC); nevertheless authors verified the behavior of the constitutive model through single element analysis. In particular, the composite failure model MAT059 simulates the 3-dimensional behavior of an orthotropic composite material and its progressive failure due to any of several failure criteria. The 3-D constitutive model is based on orthotropic elasticity up to failure, according to the following equation:

$$[C] \cdot \{\sigma\} = \{\varepsilon\} \tag{2.1}$$

being:

$$[C] = \begin{bmatrix} \frac{1}{E_{11}} & -\frac{\nu_{12}}{E_{22}} & -\frac{\nu_{13}}{E_{33}} & 0 & 0 & 0 \\ -\frac{\nu_{21}}{E_{11}} & \frac{1}{E_{22}} & -\frac{\nu_{23}}{E_{33}} & 0 & 0 & 0 \\ -\frac{\nu_{31}}{E_{11}} & -\frac{\nu_{32}}{E_{22}} & \frac{1}{E_{33}} & 0 & 0 & 0 \\ 0 & 0 & 0 & \frac{1}{G_{23}} & 0 & 0 \\ 0 & 0 & 0 & 0 & \frac{1}{G_{31}} & 0 \\ 0 & 0 & 0 & 0 & 0 & \frac{1}{G_{12}} \end{bmatrix}$$

the compliance matrix, where 1 and 2 are the in plane directions, and

$$\{\boldsymbol{\sigma}\} = \begin{Bmatrix} \sigma_{11} \\ \sigma_{22} \\ \sigma_{33} \\ \sigma_{23} \\ \sigma_{31} \\ \sigma_{12} \end{Bmatrix}, \{\boldsymbol{\varepsilon}\} = \begin{Bmatrix} \varepsilon_{11} \\ \varepsilon_{22} \\ \varepsilon_{33} \\ \gamma_{23} \\ \gamma_{31} \\ \gamma_{12} \end{Bmatrix}$$

the six stress and strain components respectively.

The presented material model implements a stress based failure criterion for solid elements derived by the Tsai-Wu theory [33], able to predict the onset of the major failure modes, including:

- Longitudinal and transverse tensile failure ( $\sigma_{11}>0, \sigma_{22}>0$ ):

$$\left(\frac{\sigma_{11}}{X_t}\right)^2 + \left(\frac{\sigma_{12}}{S_{12}}\right)^2 + \left(\frac{\sigma_{13}}{S_{13}}\right)^2 \geq 1 \quad (2.2)$$

$$\left(\frac{\sigma_{22}}{Y_t}\right)^2 + \left(\frac{\sigma_{12}}{S_{12}}\right)^2 + \left(\frac{\sigma_{23}}{S_{23}}\right)^2 \geq 1 \quad (2.3)$$

- longitudinal and transverse compressive failure ( $\sigma_{11}<0, \sigma_{22}<0$ ):

$$\left(\frac{\sigma_{11}}{X_c}\right)^2 \geq 1 \quad (2.4)$$

$$\left(\frac{\sigma_{22}}{S_{12} + S_{23}}\right)^2 + \left[\left(\frac{Z_c}{S_{13} + S_{23}}\right)^2 - 1\right] \frac{\sigma_{33}}{|Z_c|} + \left(\frac{\sigma_{13}}{S_{13}}\right)^2 + \left(\frac{\sigma_{23}}{S_{23}}\right)^2 \geq 1 \quad (2.5)$$

- through the thickness compressive failure ( $\sigma_{33}<0$ ):

$$\left(\frac{\sigma_{33}}{S_{12} + S_{23}}\right)^2 + \left[\left(\frac{Y_c}{S_{12} + S_{23}}\right)^2 - 1\right] \frac{\sigma_{22}}{|Y_c|} + \left(\frac{\sigma_{12}}{S_{12}}\right)^2 + \left(\frac{\sigma_{23}}{S_{23}}\right)^2 \geq 1 \quad (2.6)$$

- longitudinal and transverse through the thickness shear failure ( $\sigma_{11}>0, \sigma_{22}>0$ ):

$$\left(\frac{\sigma_{11}}{X_t}\right)^2 + \left(\frac{\sigma_{13}}{S_{13}}\right)^2 \geq 1 \quad (2.7)$$

$$\left(\frac{\sigma_{22}}{Y_t}\right)^2 + \left(\frac{\sigma_{23}}{S_{23}}\right)^2 \geq 1 \quad (2.8)$$

being  $(\sigma_{11}, \sigma_{22}, \sigma_{33})$ , the longitudinal/transverse/normal stress components, respectively,  $\sigma_{12}$  and  $(\sigma_{13}, \sigma_{23})$  the in plane shear and out of plane shear stress components, respectively and  $X_{tc}, Y_{tc}, Z_c, S_{12}, S_{23}$  and  $S_{13}$  the corresponding strength

values. In example, the longitudinal tensile failure is reached when the following relationship is fulfilled (equation 2.2):

$$\left(\frac{\sigma_{11}}{X_t}\right)^2 + \left(\frac{\sigma_{12}}{S_{12}}\right)^2 + \left(\frac{\sigma_{13}}{S_{13}}\right)^2 \geq 1$$

When the criterion is satisfied, the corresponding stiffness (and consequently the load carrying capability of the material in that direction) is degraded to zero over a small computational time, corresponding to a rapid decay of the stress-strain relationship; hence, the compliance matrix progressively reduces to:

$$[\mathbf{C}] = \begin{bmatrix} 0 & 0 & 0 & 0 & 0 & 0 \\ 0 & \frac{1}{E_{22}} & 0 & 0 & 0 & 0 \\ 0 & 0 & \frac{1}{E_{33}} & 0 & 0 & 0 \\ 0 & 0 & 0 & 0 & 0 & 0 \\ 0 & 0 & 0 & 0 & 0 & 0 \\ 0 & 0 & 0 & 0 & 0 & 0 \end{bmatrix}$$

The other failure modes act similarly according to threshold stress criteria, as that introduced in equation (2.2). Failure criteria act independently contributing to an ultimate failure of the composite system, that is, once a failure criterion is attained, degradation occurs only in the corresponding direction without affecting the other stress criteria computation. Element is removed from the calculation when the failure is attained in all the directions and can no longer carry any load. The input parameters needed for this material formulation are the orthotropic elastic parameters and the threshold values of the critical stresses for failure criteria.

### **2.6.2. Delamination modeling**

Delamination damage was implemented in the simulation model through the use of a surface-to-surface tiebreak contact algorithm based on the knowledge of the interlaminar properties of the material in terms of normal and shear strengths. Among the different formulations available in LS-DYNA, the penalty contact formulation contact-automatic-one-way-surface-to-surface-tiebreak with failure law *option 6* [31] was adopted between separate solid elements modeling solid plies. Using this approach, each ply is modeled as a solid layer of elements, but the nodes between plies

initially in contact are tied together, inhibiting sliding motions, until a failure criterion is reached, corresponding to delamination onset. In particular, the nodal stress is monitored throughout the analysis and implemented in the interface strength-based failure criterion:

$$\left(\frac{|\sigma_n|}{NFLS}\right)^2 + \left(\frac{|\sigma_s|}{SFSL}\right)^2 \geq 1 \quad (2.9)$$

where  $\sigma_n$  and  $\sigma_s$  are the current normal and shear stresses, respectively, and  $NFLS$ ,  $SFSL$  the normal and shear interlaminar strengths to be set in the contact definition. When equation 2.9 is fulfilled, contact stress is linearly reduced to zero (Figure 2.14a) as a function of the distance between two points initially in contact. As soon as a defined critical crack opening ( $CCRIT$ ) is reached, the tie contact definition for those nodes is released (Figure 2.14b). Once the tie component of the contact definition is deleted, the contact for those nodes converts into a standard surface-to-surface definition preventing interpenetration.

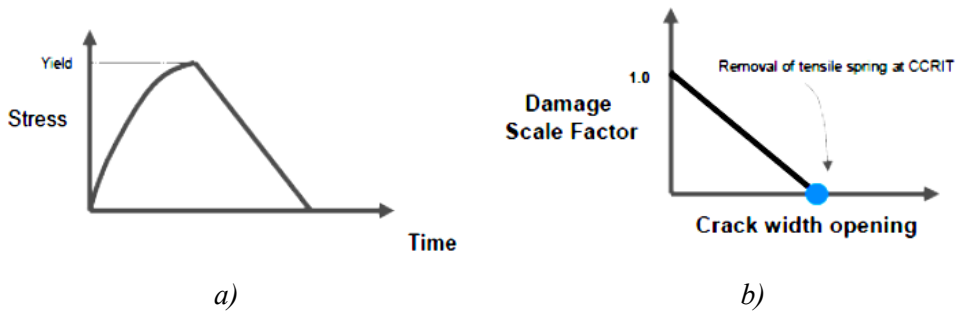


**Figure 2.14: Stress profile a) and damage evolution law b) of TieBreak contact [31].**

The impactor was modeled as a hemispherical rigid body with rigid LS-DYNA material model (MAT-RIGID). Its initial velocity and mass were set depending on the energy level considered. Contact between the impactor and the whole laminate was simulated using the AUTOMATIC-SURFACE-TO-SURFACE penalty based contact algorithm.

Ply element deleting criterion was added by using ADD-EROSION card, which allows elements to be deleted from the calculation if a certain condition based on values of stress, strain, pressure, etc. is met; in particular, a strain condition was set as a deleting criterion on the basis of reasonable maximum principal strain and shear

strain values occurring at fiber and matrix failure, in order to avoid excessive distortion of failed elements and consequent instabilities of the finite elements. A stiffness-based hourglass control was employed to improve the deformation behavior of the elements. The outer boundaries of the plates were considered to be clamped. Geometric and material symmetry allowed the analysis of one-quarter of the impactor and of the plate, as depicted in Figure 2.15.

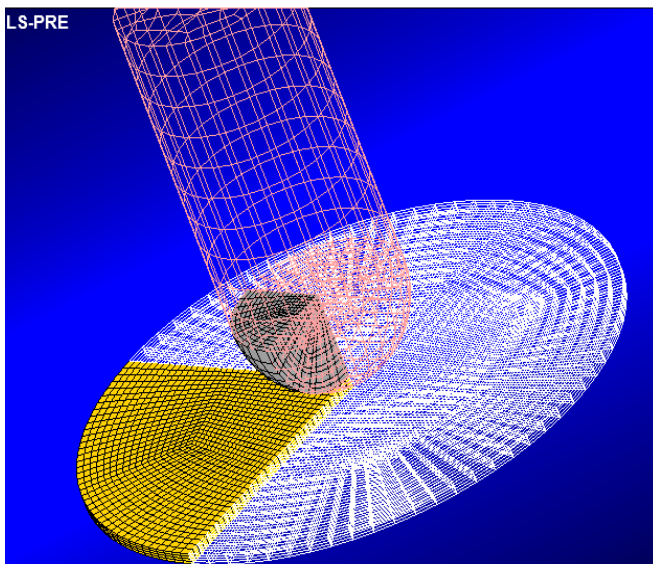


**Figure 2.15:** FE model set up adopted in the numerical analysis.

## **2.7. Assessment of the model**

The mechanical properties needed for MAT059 concern elastic moduli along the three principal directions, in-plane tensile, compressive and shear strength values, and interlaminar failure stresses ( $NFLS$ ,  $SFLS$ ). Only some of the input parameters requested for the numerical analysis were available from the manufacturer's data sheet (values in parentheses in Table 2.1), so that a calibration procedure was followed to assign the unknown properties. In this section, first, some details on the calibration stage are given; then, the main topics of the work, i.e. predicting the  $F-d$  curve, and calculating the shape and extent of delaminated zone, are addressed separately.

**Table 2.1: Mechanical properties of the calibrated model.**

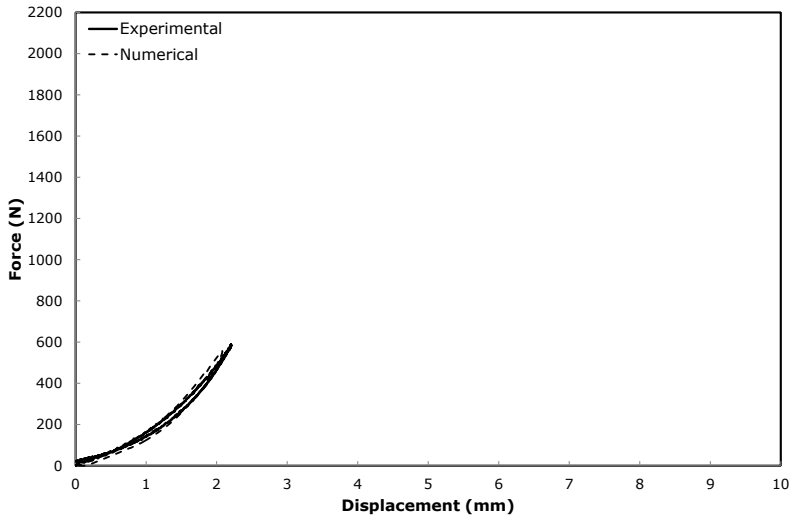
Elastic Moduli	(GPa)	Shear Moduli	(GPa)	Poisson ratios	(-)
$E_1$	26 (26)	$G_{12}$	3.8	$\nu_{12}$	0.1
$E_2$	26 (26)	$G_{23}$	2.8	$\nu_{13}$	0.25
$E_3$	8	$G_{13}$	2.8	$\nu_{23}$	0.25
<i>Tensile strengths</i>	(MPa)	<i>Compressive strengths</i>	(MPa)	<i>Shear strengths</i>	(MPa)
$X_T$	850 (414)	$X_C$	720 (458)	$S_{12}$	105
$Y_T$	850 (414)	$Y_C$	720 (458)	$S_{13}$	65 (65)
$Z_T$	120	$Z_C$	500	$S_{23}$	65 (65)
Interlaminar Normal Failure Stress	(MPa)		Interlaminar Shear Failure Stress	(MPa)	
$NFLS$	35		$SFLS$	65 (65)	

### 2.7.1. Calibration analysis

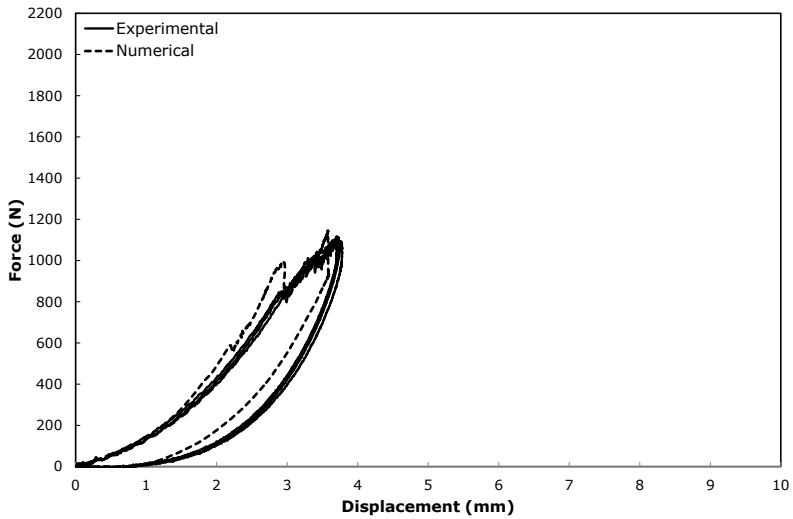
A sensitivity analysis showed that, within a quite large range of values, the influence of the Poisson’s ratios on the elastic response of the panels is negligible. Typical values, deriving from those adopted in [34, 35], were then employed in the calculations. The structural response was more sensitive to the through-the-thickness Young’s modulus,  $E_3$ , as well as to the shear moduli. To find reasonable values for these parameters, the  $F-d$  curve recorded for  $U=0.41$  J,  $t=0.96$  mm (Fig. 10a), developing in the elastic range, was considered, and the constants  $E_3$ ,  $G_{12}$ ,  $G_{13}=G_{23}$  were calibrated requiring a satisfactory superposition of the predicted to the experimental curve.

The sensitivity analysis also revealed that the compression strengths  $X_C=Y_C$  do not sensibly affect the trend of the  $F-d$  curve. On the contrary, the first failure point (signaled by an evident load drop in the  $F-d$  curve) is critically dependent on  $X_T=Y_T$ ,  $S_{12}$ , and  $NFLS$ . Assuming a value similar to the one adopted in [30] for  $S_{12}$ ,  $X_T$  and  $NFLS$  were determined from the  $F-d$  curves concerning  $U=1.55$  J,  $t=0.96$  mm (Figure 2.16b), imposing that: a) the experimental displacement in correspondence of which

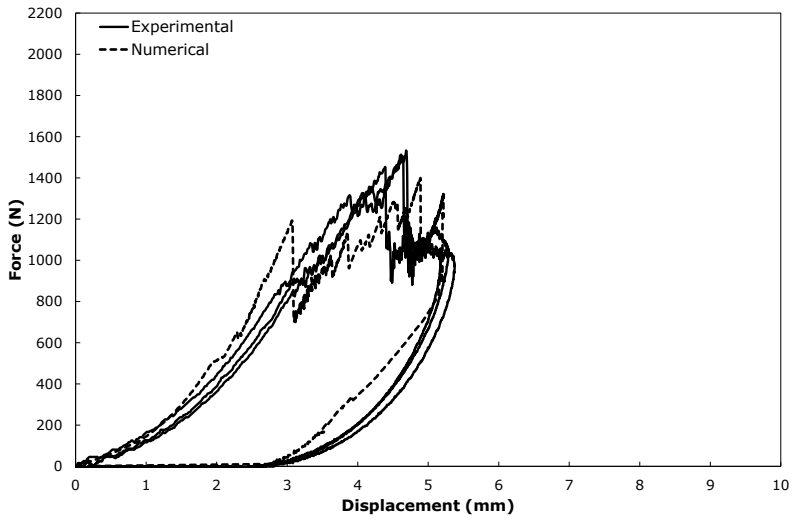
first failure was found would be coincident with the numerical one; b) after load drop at first failure, the trend of the calculated and actual curve would overlap.



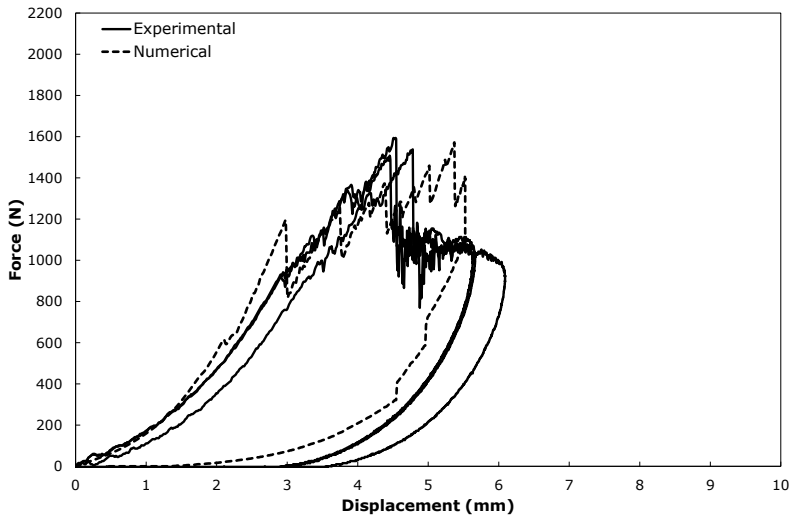
a)



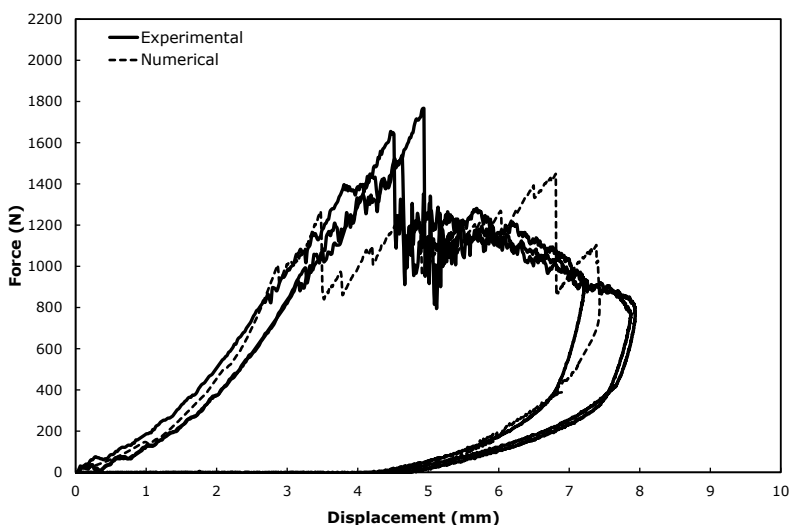
b)



c)



d)



e)

**Figure 2.16: Comparison of experimental and numerical  $F-d$  curves for the 0.96 mm thick laminate; a)  $U=0.4J$ ; b)  $U=1.5J$ ; c)  $U=3.3J$ ; d)  $U=4.0J$ ; e)  $U=6.0J$ .**

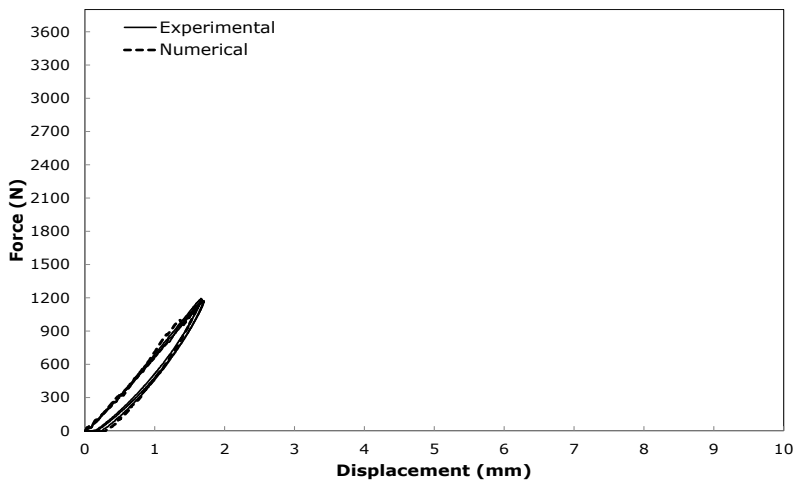
The calibrated values used in the numerical model are reported Table 2.1. Comparing them with the properties drawn from the producer’s data sheet (in parentheses in the Table 2.1),  $X_T=Y_T$  is more than doubled. This is somehow anticipated, since the strength of GFRP is particularly sensitive to loading rate. Caprino et al. [36], conducting low-velocity impact tests on glass-polyester plates, noted a 70% increase in the maximum contact force with respect to static loading. Sims [37] reported an increase in flexural strength for glass mat/polyester laminates in the speed range 10-6 to 10-1  $ms^{-1}$ , while Asprone et al. [38] recorded an improvement in tensile mechanical properties in pultruded glass-polyester composites at strain rates ranging from 1  $s^{-1}$  to 700  $s^{-1}$ .

### 2.7.2. Force-displacement curves

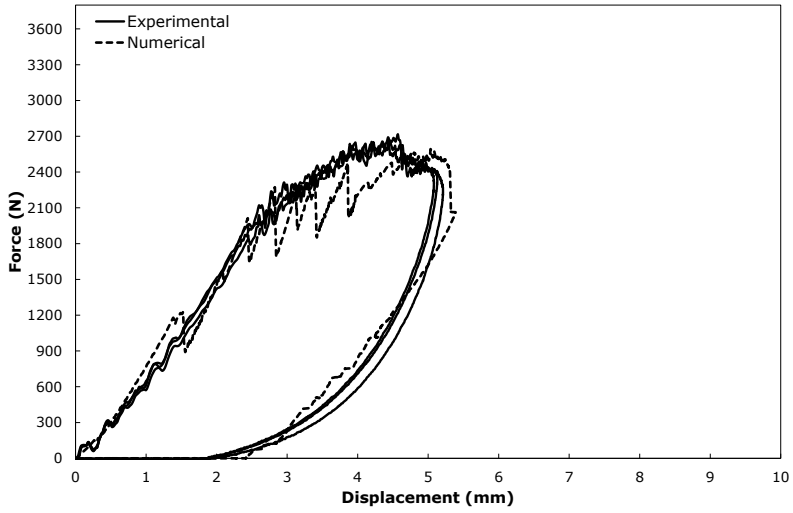
In Figure 2.16 and Figure 2.17, the experimental  $F-d$  curves (continuous lines) recorded at different impact energy levels are compared with those obtained by numerical analysis (dashed lines) for  $t=0.96$  mm and  $t=1.92$  mm, respectively. The agreement between experiments and FE in Figure 2.16a, b in the loading phase is obvious, since some information gathered from these curves was used to calibrate the

numerical model. However, the general trend of all other (completely unknown) curves is reasonably well captured by FE, not only in the loading, but also in the unloading stage of contact history. In particular, the elastic response of the thicker laminate (Figure 2.17a) is predicted with excellent accuracy.

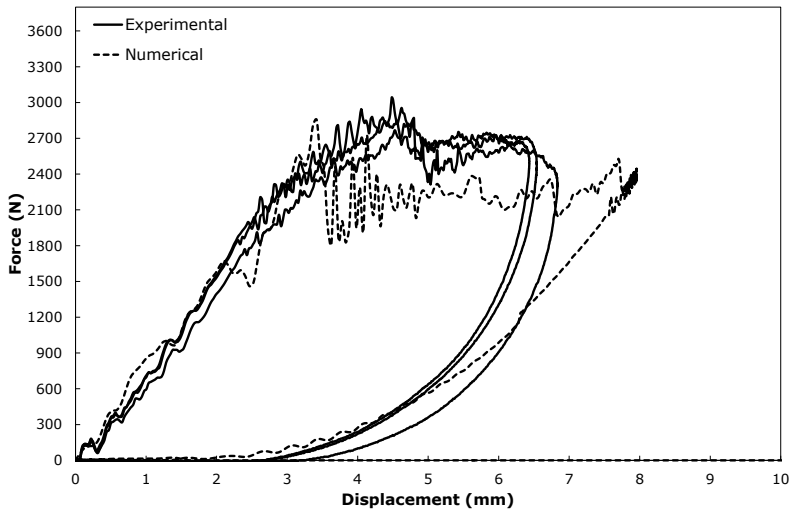
Indeed, two major phenomena, evident when the thicker laminate is considered (Figure 2.17), distinguished the numerical solutions from the actual cases: the oscillations pertaining to the elastic phase are not accurately described, and the predicted sudden load drops deriving from failures are much larger than observed. The first event is anticipated: since the  $F-d$  curve was verified to be substantially insensitive to velocity (Figure 2.8), the initial impact velocity  $V$  was held constant in the FE model ( $V=50$  mm/s), and energy was set by suitably selecting the impactor mass. Consequently, the main features correlated with impact dynamics were lost. The entity of sudden load drops in the numerical  $F-d$  curve, determined by damage propagation, is critically dependent on the ability to effectively model the progressive damage within the ply, as well as the laminate response after equation 2.9 has been fulfilled. Probably, a more sophisticated law describing the behavior of tiebreak elements would be required to better reproduce the actual material behavior.



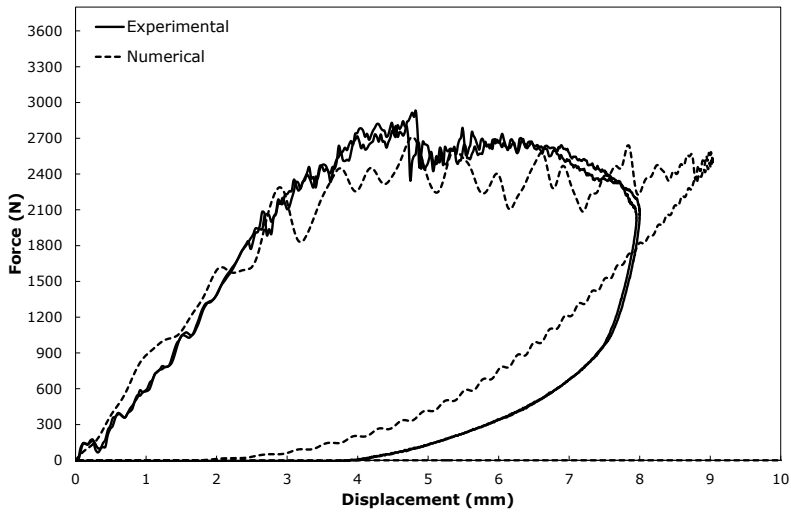
a)



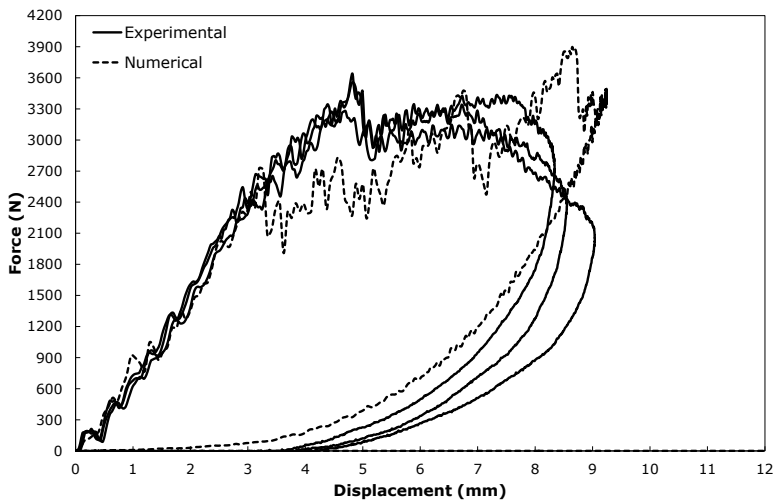
b)



c)



d)



e)

**Figure 2.17: Comparison of experimental and numerical  $F-d$  curves for the 1.92 mm thick laminate; a)  $U=0.8\text{J}$ ; b)  $U=8.3\text{J}$ ; c)  $U=12.4\text{J}$ ; d)  $U=15.5\text{J}$ ; e)  $U=20.0\text{J}$ .**

The open symbols in Figure 2.9 represent the absorbed energy provided by FE analysis. The numerical values match satisfactorily the experimental data (full symbols), especially for small energy values. In particular, the FE simulations reproduce well both the linear dependence of  $U_d$  on impact energy and the effect of the

thickness on the slope of the straight line. With increasing  $U$ , the FE predictions tend to underestimate  $U_d$ . Of course, this reflects the approximations implicit in the modeling of material behavior during progressive damage.

### **2.7.3. Damage assessment**

As previously specified, the simulation results indicate where interlaminar failures occur in terms of nodal restraint failures. In particular, once the failure criterion is reached, the force in contact restraint is linearly scaled down to zero. Then, nodal connection fails completely and nodal restraint is removed. Through the identification of the released node restraints, the delamination mapping can be defined for each laminate interface, in order to quantify interlaminar damage.

The open symbols in Figure 2.12 represent the characteristic length  $d$  of the delaminated area provided by FE. Indeed, the numerical values are very close to the experimental ones (full symbols), confirming the reliability of FE model. Similar conclusions can be drawn from Figure 2.13, where the comparison between FE and measured values is carried out referring to the projected delaminated area,  $A_p$ .

Further support to the numerical results is given in Figure 2.18, where a view of the bottom face of a damaged plate is illustrated (Figure 2.18a). In Figure 2.18b, the FE mesh of the portion enclosed within the dashed line in Figure 2.18a is shown; the bright area represents delamination, as predicted by the FE model. Clearly, not only the dimensions, but also the overall shape of delaminated area is well predicted by FE. In order to more deeply evaluate the capability of the model to estimate delamination, a comparison between the extent of experimentally determined and predicted ply-by-ply delaminated areas was carried out. An example of the results obtained is shown in Figure 2.11, where the open symbols refer to FE.

The general trend of delamination development within the laminate is well reproduced by the numerical analysis. In particular, as often found in impact studies [3,8,35], the interfaces between layers having different orientations are recognized to be more prone to delamination, with the largest delaminated area located near the back face of the panel. Further, in agreement with the experimental observations, FE indicates that the critical conditions for delamination are also reached at interfaces between laminae with the same orientation. Among the latter, the mid-plane is correctly predicted to suffer the most extensive propagation.

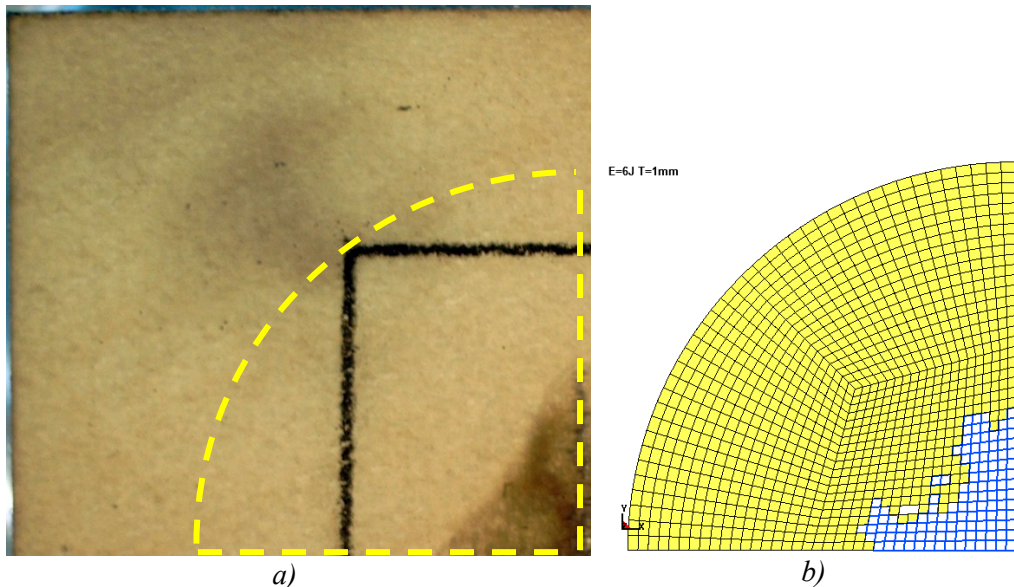


**Figure 2.18: Comparison of: a) experimental, and, b) calculated delaminated area. Laminate thickness  $t=0.96$  mm; impact energy  $U=6.0$  J.**

It is interesting to note that, when interlaminar surfaces between layers having the same orientation are concerned, the delamination extent calculated by FE is larger than its actual counterpart (Figure 2.11). A possible explanation is in the fact that, in the numerical analysis, the same interlaminar strength was assigned to all the interlayers. Probably, better agreement between experiments and calculated values could be achieved by assuming the normal and shear failure stresses at the interfaces as dependent on the relative orientations of the adjacent laminae.

Figure 2.19 reports some representative images of intralaminar damage. Figure 2.19a refers to the through the thickness shear failure that affects the matrix within the ply in case of 1.92 mm thick laminate impacted at  $U=15.5$  J. The contour of the image (blue) highlights the elements which failed due to the through the thickness failure criterion (equation 2.7). It can be observed that the elements under the impactor undergo very high levels of through the thickness deformation, leading to localized matrix failure. Figure 2.19b and Figure 2.19c depict the exploded view and the bottom view of the 1.92 mm thick laminate impacted at  $U=15.5$  J, respectively. The tensile damage along the  $X$  direction is highlighted in blue and represents the longitudinal failure according to the criterion expressed by equation 2.2. It can be observed that this type of damage is mainly concentrated at the bottom layers with  $(0,90)$  orientation. The extension of the tensile failure roughly corresponds to the tensile fiber breakage

occurred within the laminate, as reported in Figure 2.10. **Figure 2.19d** reports the 1.92 mm thick laminate impacted at  $U=15.5$  J after the impact simulation.

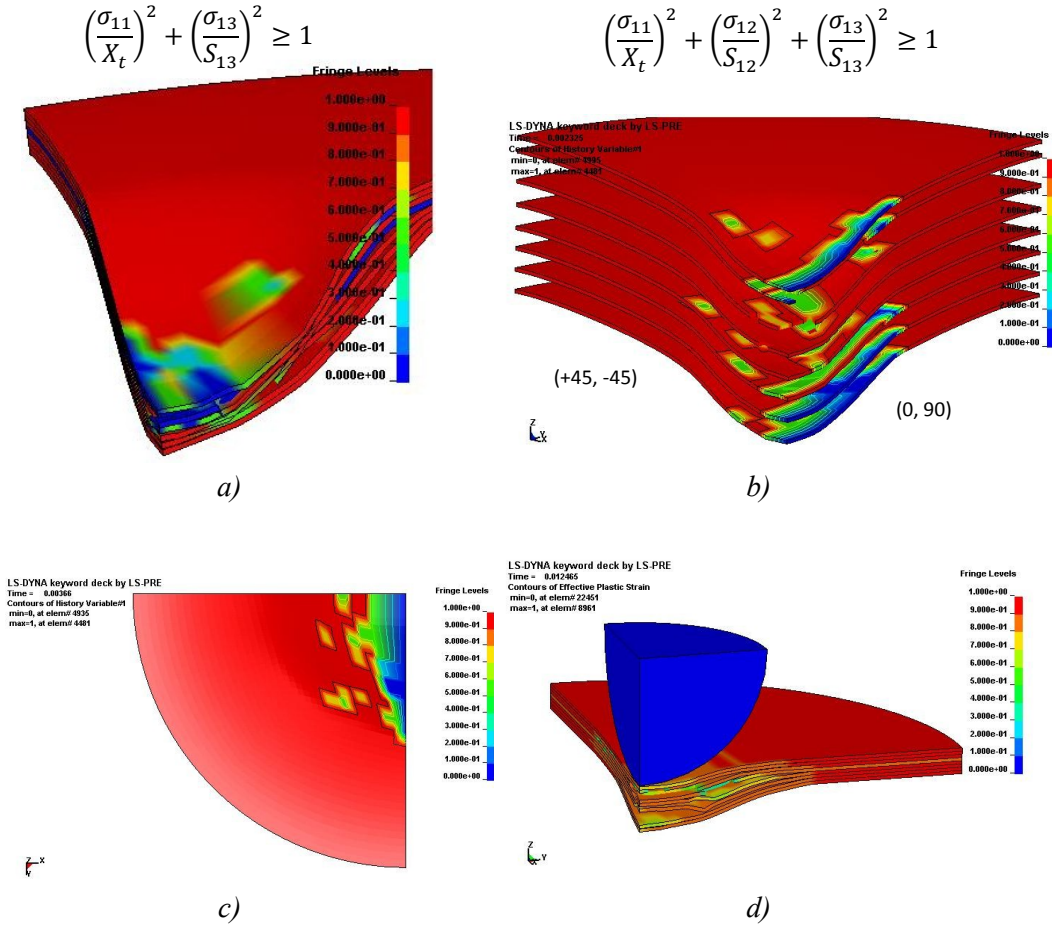


**Figure 2.19:** Interlaminar damage of the 1.92 mm thick laminate impacted at  $U=15.5$ J: a) through the thickness shear failure; b) exploded laminate view depicting longitudinal tensile failure, X direction; c) bottom view of composite laminate, longitudinal tensile failure, X direction; d) post impact view.

## 2.8. Closing remarks

Low-velocity impact tests were carried out on glass fabric/epoxy laminates, adopting two panel thicknesses and different impact energies. The experimental tests were modeled through the explicit FE software LS-DYNA.

From the results obtained, FE estimated with sufficient accuracy the overall force-displacement curve during the loading and rebound phases, as well as the irreversibly absorbed energy. Satisfactory agreement between numerical predictions and experiments was also verified with reference to the extent and shape of projected and ply-by-ply delaminated areas. In particular, as confirmed by the “post-mortem” analysis of the impacted panels, FE calculated considerable delamination at the interface located at the mid-plane of the specimens, characterized by two layers having same orientation. In general, the predicted delamination extent between laminae of identical orientation was larger than the actual one. Probably, this depends on the interlaminar strengths assigned in the calculations, which were assumed independent of the relative orientations of adjacent plies. Satisfactory agreement with test results was also found in terms of extension of extent of fiber breakage. However, when the impact energy was closer to penetration limit the predicted absorbed energy was slightly underestimated; in this case constitutive models based on damage accumulation will be desirable for future numerical analysis.

### References

1. Abrate, S., *Impact on composite structures*. Cambridge University Press, 1998.
2. Sjoblom, P.O., J.T. Hartness, and T.M. Cordell, *On Low-Velocity Impact Testing of Composite-Materials*. Journal of Composite Materials, 1988. **22**(1): p. 30-52.
3. Richardson, M.O.W. and M.J. Wisheart, *Review of low-velocity impact properties of composite materials*. Composites Part A-Applied Science and Manufacturing, 1996. **27**(12): p. 1123-1131.
4. Burks, B.M., D.L. Armentrout, M. Baldwin, J. Buckley, and M. Kumosa, *Hybrid composite rods subjected to excessive bending loads*. Composites Science and Technology, 2009. **69**(15-16): p. 2625-2632.
5. Diao, X.X., L. Ye, and Y.W. Mai, *Fatigue behaviour of CF/PEEK composite laminates made from commingled prepreg .1. Experimental studies*. Composites Part a-Applied Science and Manufacturing, 1997. **28**(8): p. 739-747.
6. Joshi, S.P. and C.T. Sun, *Impact Induced Fracture in a Laminated Composite*. Journal of Composite Materials, 1985. **19**(1): p. 51-66.

7. Shim, V.P.W. and L.M. Yang, *Characterization of the residual mechanical properties of woven fabric reinforced composites after low-velocity impact*. International Journal of Mechanical Sciences, 2005. **47**(4-5): p. 647-665.
8. Chen, J.K. and C.T. Sun, *Dynamic Large Deflection Response of Composite Laminates Subjected to Impact*. Composite Structures, 1985. **4**(1): p. 59-73.
9. Caprino, G., A. Langella, and V. Lopresto, *Elastic behaviour of circular composite plates transversely loaded at the centre*. Composites Part a-Applied Science and Manufacturing, 2002. **33**(9): p. 1191-1197.
10. Olsson, R., *Analytical prediction of large mass impact damage in composite laminates*. Composites Part A-Applied Science and Manufacturing, 2001. **32**(9): p. 1207-1215.
11. Naik, N.K., Y.C. Sekher, and S. Meduri, *Damage in woven-fabric composites subjected to low-velocity impact*. Composites Science and Technology, 2000. **60**(5): p. 731-744.
12. Sutherland, L.S. and C.G. Soares, *Effect of laminate thickness and of matrix resin on the impact of low fibre-volume, woven roving E-glass composites*. Composites Science and Technology, 2004. **64**(10-11): p. 1691-1700.
13. Zhou, G., *The use of experimentally-determined impact force as a damage measure in impact damage resistance and tolerance of composite structures*. Composite Structures, 1998. **42**(4): p. 375-382.
14. Abrate, S., *Modeling of impacts on composite structures*. Composite Structures, 2001. **51**(2): p. 129-138.
15. Olsson, R., M.V. Donadon, and B.G. Falzon, *Delamination threshold load for dynamic impact on plates*. International Journal of Solids and Structures, 2006. **43**(10): p. 3124-3141.
16. Jones, R., *Mechanics of composite materials*. 2nd ed, Taylor and Francis, 1999.
17. Olsson MD, V.R., Anderson DL, *Damage in composites: a plasticity approach*. Journal of Composite Materials, 1992. **44** p. 103-116.
18. Car, E., S. Oller, and E. Onate, *A large strain plasticity model for anisotropic materials - composite material application*. International Journal of Plasticity, 2001. **17**(11): p. 1437-1463.

19. Garg, A.C., *Delamination - a Damage Mode in Composite Structures*. Engineering Fracture Mechanics, 1988. **29**(5): p. 557-584.
20. Zerbst, U., M. Heinemann, C.D. Donne, and D. Steglich, *Fracture and damage mechanics modelling of thin-walled structures - An overview*. Engineering Fracture Mechanics, 2009. **76**(1): p. 5-43.
21. Kachanov, L.M., *Rupture time under creep conditions*. Izv Akad Nauk SSSR Otd Tekhn Nauk [in Russian], 1958. **8**: p. 26-31.
22. Rabotnov, Y.N., *Creep problems in structural members*. Amsterdam: North-Holland, 1969: p. 822.
23. Matzenmiller, A., J. Lubliner, and R.L. Taylor, *A Constitutive Model for Anisotropic Damage in Fiber-Composites*. Mechanics of Materials, 1995. **20**(2): p. 125-152.
24. Williams, K.V., R. Vaziri, and A. Poursartip, *A physically based continuum damage mechanics model for thin laminated composite structures*. International Journal of Solids and Structures, 2003. **40**(9): p. 2267-2300.
25. Iannucci, L., *Progressive failure modelling of woven carbon composite under impact*. International Journal of Impact Engineering, 2006. **32**(6): p. 1013-1043.
26. Donadon, M.V., L. Iannucci, B.G. Falzon, J.M. Hodgkinson, and S.F.M. de Almeida, *A progressive failure model for composite laminates subjected to low velocity impact damage*. Computers & Structures, 2008. **86**(11-12): p. 1232-1252.
27. Lopes, C.S., P.P. Camanho, Z. Gurdal, P. Maimi, and E.V. Gonzalez, *Low-velocity impact damage on dispersed stacking sequence laminates. Part II: Numerical simulations*. Composites Science and Technology, 2009. **69**(7-8): p. 937-947.
28. Shivakumar, K.N., W. Elber, and W. Illg, *Prediction of Impact Force and Duration Due to Low-Velocity Impact on Circular Composite Laminates*. Journal of Applied Mechanics-Transactions of the Asme, 1985. **52**(3): p. 674-680.
29. Sutherland, L.S. and C.G. Soares, *Impact characterisation of low fibre-volume glass reinforced polyester circular laminated plates*. International Journal of Impact Engineering, 2005. **31**(1): p. 1-23.

30. Wu, H.Y.T. and G.S. Springer, *Measurements of matrix cracking and delamination caused by impact on composite plates*. Journal of Composite Materials, 1988. **22**: p. 518-532.
31. Zhu, Y., *Carbon nanofiller modified multifunctional glass/fiber epoxy laminated composites*. PhD dissertation - Penn State University, 2011.
32. Schweizerhof, K., *Crashworthiness analysis with enhanced composite material models in LS-DYNA – merits and limits*. LS-DYNA World Conference, Detroit, Michigan, USA, 1998.
33. Tsai, S.W. and E.M. Wu, *A general theory of strength for anisotropic materials*. Journal of Composite Materials, 1971. **5** p. 58-80.
34. Gama BA, B.T., Gillespie JW Jr, *Progressive Damage Modeling of Plain-Weave Composites using LS-Dyna Composite Damage Model MAT162*. 7th European LS-DYNA Conference **D-III-04**.
35. Sevkat, E., B. Liaw, F. Delale, and B.B. Raju, *Drop-weight impact of plain-woven hybrid glass-graphite/toughened epoxy composites*. Composites Part a- Applied Science and Manufacturing, 2009. **40**(8): p. 1090-1110.
36. Caprino G, C.V.I., Di Ilio A, *Composite material response under low velocity impact*. Composite Structures, 1984. **2**: p. 261-271.
37. Sims, G.D., *Understanding Charpy impact testing of composite laminates*. Proc. 6th Int. Conf. on Composite Materials, Imperial College, London 1988: p. 3494-3507.
38. Asprone, D., E. Cadoni, A. Prota, and G. Manfredi, *Strain-rate sensitiveness of a pultruded e-glass/polyester composite*. Journal of Composites for Construction, 2009;. **13**: p. 558-564.



## **Chapter III**

# ***OUT OF PLANE COMPRESSIVE BEHAVIOR OF HONEYCOMB SANDWICH STRUCTURES***

### **3.1. Introduction to framework**

The use of honeycomb structures as core material in sandwich panels is widely diffused in many engineering applications, especially where high mechanical performances and low density are requested. The main key performance factors of honeycombs are represented by the capability to withstand through the thickness compression and to absorb energy by plastic deformation of the cell walls. Given the heterogeneous nature of honeycomb sandwich structures, damage may affect both composite skins and honeycomb core. Due to this hierarchical structure, a multiscale approach appears suitable in order to capture damage mechanisms in case of out of plane compressive loading conditions. In particular, the damage analysis may include the whole structure (macro scale) or the honeycomb-skins structures (meso scale).

With the scope to move from the meso scale level, the analyses presented in *Chapter III* are aimed at accurately modeling the buckling and crushing behavior of hexagonal honeycomb structures. The damage analysis moves from the modeling of the honeycomb material properties, including the sensitivity to material defects, as depicted in Figure 3.20. Owing these damage characterizations, the numerical analyses are performed on a representative honeycomb cell enabling to transfer mechanical properties, predicted at the meso scale, to the macroscale of the whole sandwich structure, in order to predict the compressive strength and folding mechanism during the crushing.

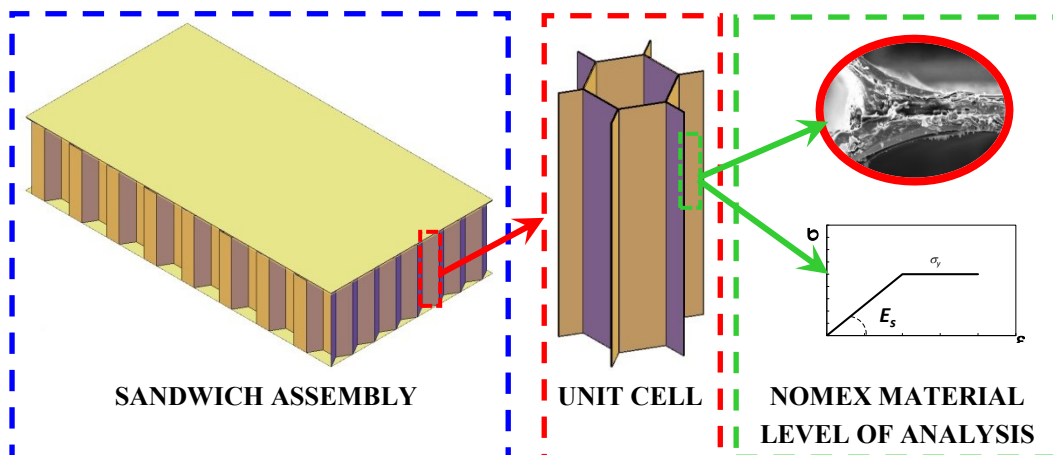


**Figure 3.20: Scheme of multiscale analysis performed for the investigated Nomex honeycomb structure.**

The following sections firstly deal with the main theoretical concepts related to the out of plane compressive properties of hexagonal honeycomb core materials. Thus, a statistical-based method to include imperfections in the simulation is presented and applied to predict the compressive behavior of hexagonal Nomex honeycomb structure. A shell model of a representative single cell made of expanded Nomex has been created using the ABAQUS FE code (Simulia, Dassault Systèmes, Providence, RI, USA). The key aspect proposed in the study is the inclusion of imperfections in terms of both material (elastic modulus variability) and geometrical (thickness variability) defects. To do this, a stochastic approach is proposed by performing random sampling at each element of the FE mesh, assuming different Young’s modulus values and different thickness properties, according to a pre-defined statistical distribution. The modeled cell is used to address several aspects of the compressive response, particularly focusing on the onset of buckling, the collapse limit and the crushing behavior.

## 3.2. Literature overview

### 3.2.1. Sandwich structures: introduction

Nowadays composite sandwich structures are widely used in many different engineering fields especially in the aerospace and mass transport industry where

weight reduction is one of the most significant design parameters. These materials offer many advantageous specific mechanical properties, such as stiffness-to-weight ratio, which make them suitable for component construction including secondary structural parts like flaps, wing-body fairings, engine cowls, spoilers, nacelles, radomes, etc. [1-3]. Sandwich structures are generally made of two thin and stiff skins, separated by a thick, lightweight core, which increases the inertia of the resulting section without significantly increasing the mass (Figure 3.21). The skins primarily carry tensile and compressive loads whereas the core carries transverse shear loads and gives the panel high specific bending stiffness. In addition, the core influences the out-of-plane compressive behavior and the energy absorbing capability of the sandwich structure by its failure mechanisms.

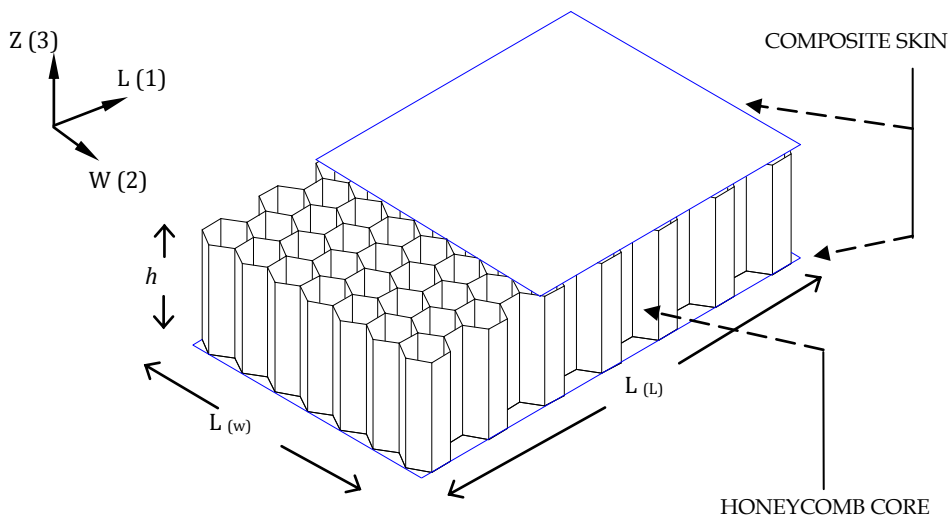


**Figure 3.21: Schematic representation of a sandwich structure**

The skins are regularly made of lightweight materials such as aluminum or fiber reinforced composite laminates. Different types of sandwich core structures are commonly used in the aerospace and transportation industry including foam/solid core (ships, aircrafts), honeycomb (aircrafts, satellites), truss core (buildings, bridges), and web core [1, 2], which can be manufactured by using a variety of base materials, e.g., metal foils, plastic foils, or resin impregnated paper-like materials made of synthetic or natural fibers.

The use of honeycomb is highly diffused in many engineering applications due to the high density-specific performances they can offer. The main key performance factors of honeycombs are represented by the ability to withstand through-thickness

compression and to absorb energy by plastic deformation of the cells. Generally, in the aerospace industry honeycomb structures are made of aluminum foils, phenolic-impregnated Nomex® paper or carbon honeycomb, given their superior weight-specific mechanical properties in terms of stiffness and structural weight reduction [4-6]. Furthermore they offer design versatility and cost-efficient manufacturing [7]. However, the closed structure of honeycomb cells may lead to negative effects regarding condensed water trapped in the cells and trigger an increase in weight as well as a reduction of mechanical properties. To overcome this issue, new configurations for core structures, such as folded cores [8], have been recently introduced. In particular, the manufacturing process is described in [9] and a wide range of experimental results can be found in [10].

Most honeycomb structures show a similar mechanical behavior under out-of-plane (i.e., through-thickness direction) compression. In particular, they are characterized by: (i) an initial linear-elastic regime up to the buckling limit and a subsequent compressive strength reduction; (ii) a plateau of constant stress, named crush strength, corresponding to a progressive degradation of cell walls; (iii) a final segment of densification characterized by the compression of the cell wall itself. However, honeycomb structures can exhibit different features in their compressive out-of-plane behavior depending on the nature of the honeycomb core constituent material. In particular, when the critical compressive stress is reached, the cells begin to collapse by elastic buckling, plastic yielding or brittle fracture, depending on the wall material type. Hanel et al. [11] investigated the influence of the different paper materials, i.e., Kevlar and Nomex, on the structural properties of wedge-shaped folded cores, whereas other authors investigated the structural behavior of a honeycomb structure made of Nomex paper material, making comparison with a honeycomb core made of aluminum [12]. They report that Nomex material is much more brittle than aluminum foil during the progressive failure mechanism and the crushing regime.

In dealing with the modeling of flat-wise compressive behavior, several approaches have been proposed, encompassing analytical models [13, 14], macro mechanical finite element models adopting equivalent solid formulations [12], as well as meso-mechanical models focusing on the cellular honeycomb structure, both analytical and numerical [8, 15-18]. Nevertheless, the first two types of approaches present limiting drawbacks mainly related to the prediction of the shear behavior and the progressive collapse of the honeycomb cells. For these reasons, the problem is often tackled through detailed numerical models and/or through a virtual testing approach. In general, virtual testing consists of a step-by-step numerical procedure

where a detailed model is employed on the basis of experimental tests. Usually, this procedure begins from a small scale (as an example, from coupon material tests); once the mechanical behavior is properly calibrated at that scale, more complex tests can either be simulated or carried out scaling up to the scale of the component/assembly. As a consequence of this process, experimental tests can be limited to a preliminary stage supporting numerical implementations in subsequent steps. This procedure represents a key tool especially for composite materials exhibiting different behavior at different scales. In fact, by reproducing the exact shape of the core structure, this numerical technique gives the possibility to reproduce not only the elastic behavior prior to cell wall buckling but also the complex crushing behavior characterized by cell wall folding mechanisms at micro/meso scale, even though a large computational time may be required. Moreover, it allows to gather mechanical properties which are usually not available among experimental manufacturer databases. This kind of approach is usually pursued to model honeycomb or folded core materials by using different scales ranging from one single cell scale to large scale including the full honeycomb model. An example of this numerical approach can be found in recent studies performed by Heimbs and concerning virtual testing of sandwich panels manufactured with Nomex honeycomb and folded cores [8]. The author successfully simulated the cellular core behavior in different loading directions by adopting a very detailed finite element model and addressing numerical problems such as mesh and loading rate dependencies.

### **3.2.2. Sandwich failure mode: skin failure**

The sandwich beam failure due to the skin includes three main failure modes: face ultimate strength (both compressive and tensile), face wrinkling and intra-cellular buckling (Figure 3.22a,b and c, respectively). The maximum stress levels reached in the face sheets can be derived by sandwich beam theory and used to predict the skin failure threshold. In a symmetric beam, the stress is the same in the compression and tension faces. For composite skins, the critical face is usually the compressive face. The failure occurs when the axial stress in either of the skins,  $\sigma_f$ , reaches the in-plane ultimate strength,  $F_c$ .

$$\sigma_f = F_c \tag{3.1}$$

The wrinkling of the compression face takes place when the wavelength of the buckled face is of the same order as the thickness of the core. This problem may is

usually handled as the buckling of a beam (the face sheet) supported transversely by an elastic foundation (the core). With three-point bending, wrinkling of the top skin occurs in the vicinity of the central load. Allen [19] gave the critical compressive stress  $\sigma_{fw}$  that results in wrinkling:

$$\sigma_{fw} = B_1 E_f^{\frac{1}{3}} E_c^{\frac{2}{3}} \quad (3.2)$$

where:

$$B_1 = 3[12(3 - \nu_{cz})^2(1 + \nu_{cz})^2] \quad (3.3)$$

and  $\nu_{cz}$  and  $E_c$  are respectively the out-of-plane Poisson's ratio and Young's's modulus of the core.

When a honeycomb structure is used as core material within the sandwich structure, failure may arise by buckling of the face in a small region where it is unsupported by the walls of the honeycomb. The following expression has been proposed [20] for the in-plane stress  $\sigma_{fi}$  in the skin at which intra-cellular buckling occurs:

$$\sigma_{fi} = \frac{2E_f}{(1 - \nu_f^2)} \left(\frac{t}{R}\right)^2 \quad (3.4)$$

where  $R$  is the cell size of the honeycomb core.

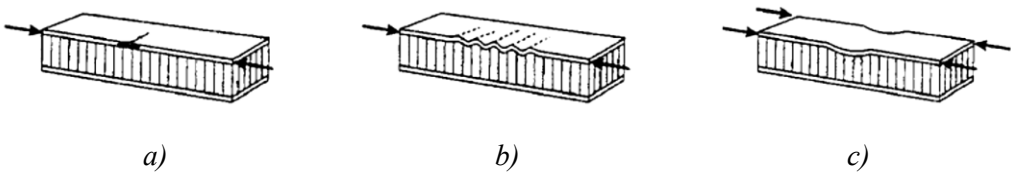


Figure 3.22: Skin failure modes: a) compressive failure; b) intra-cell buckling; c) wrinkling failure [20].

### 3.2.3. Sandwich failure mode: core failure

Sandwich structures loaded in bending can fail due to core failure. Related failure modes include: shear failure or indentation by local crushing in the vicinity of the loads application.

Shear failure (Figure 3.23a) occurs when the applied shear stress,  $\tau_c$ , equals the shear strength,  $\tau_{cu}$ , of the core:

$$\tau_c = \tau_{cu} \quad (3.5)$$

It should be pointed out that when honeycomb cores are used, two different values of the ultimate shear strength should be considered corresponding to shear strength in the two in-plane directions, depending on the direction of the honeycomb ribbon.

Indentation failure (Figure 3.23b) is predicted when the out-of-plane compressive stress,  $\sigma_z$ , equals the out-of-plane compressive strength,  $\sigma_{cc}$ , of the core. Knowing the length of contact,  $\delta$ , between the central loading bar and the top face sheet, it is assumed that the load is transferred uniformly to the core over this contact length. The out-of-plane compressive stress in the core is assumed to be given by:

$$\sigma_z = \frac{W}{b\delta} \quad (3.6)$$

To evaluate the core failure mechanism, stiffness and strength properties for the core structure are required. The data required for the failure analysis can be derived using the given relations between the properties of the core and its solid material reported in the following sections.



**Figure 3.23: Core failure modes: a) shear failure; b) indentation failure [20].**

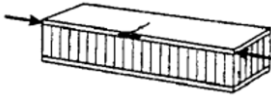
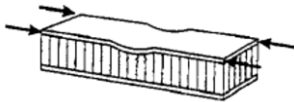
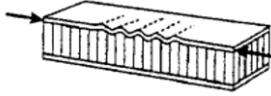
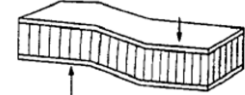
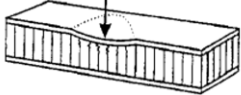
### 3.2.4. Sandwich failure mode: failure map

A failure mode map is a useful tool that can be used to predict the critical failure mode for a particular beam design. The map is constructed as follows. Since each of the failure equations depends on the beam width  $b$  and the core depth  $c$  in the same way, the transition from one failure mode to another can be expressed in terms of two variables: the ratio  $t/L$  of the face thickness to the beam span and the relative density  $\rho^*/\rho_s$  of the core. Moreover, the core shear properties can be expressed as function of the core relative density and solid characteristics, i.e. compressive strength  $\sigma_{sc}$ , elastic  $E_c$  and shear modulus  $G_c$ . These two beam design parameters are used as the

axes of the failure mode map; by equating pairs of failure equations in turn, the transitions between one failure mode and another can be plotted on the failure map.

Table 3.2 reports the failure equations in the case of a sandwich beam, with thin skins and weak core, loaded in three point bending. The equations of core failure are expressed as function of  $K_1$ ,  $n$ ,  $K_2$ , and  $m$  constants, which can be evaluated for both honeycomb and foam core on the basis of cellular structure and solid material.

**Table 3.2: Failure equation for three-point bending configuration [20].**

Skin compressive failure		$W_0 = 4dF_c \left( \frac{t}{L} \right)$
Intra-cell buckling		$W_0 = \frac{8dE_f}{1-\nu_f^2} \left( \frac{t}{R} \right)^2 \left( \frac{t}{L} \right)$
Face Wrinkling		$W_0 = 4dB_1E_f^{\frac{1}{3}}E_s^{\frac{2}{3}} \left( \frac{t}{L} \right) \left( \frac{\rho^*}{\rho_s} \right)^{\frac{2}{3}}$
Core shear		$W_0 = 2K_1E_s d \left( \frac{\rho^*}{\rho_s} \right)^n$
Indentation		$W_0 = K_2 b \delta \sigma_{sc} \left( \frac{\rho^*}{\rho_s} \right)^m$

### 3.2.5. Honeycomb out of plane properties

Honeycomb out-of-plane compressive properties are of interest for many applications since they influence the mechanical performance of the sandwich panel, such as local compression and impact resistance. For this reason, some of the most important results concerning out of plane honeycomb axial properties are summarized in the following paragraphs.

#### *Linear-Elastic deformation (Modulus)*

One of the main functions of honeycomb core is to carry normal and shear loads in planes containing the axis of the hexagonal prisms, i.e. the  $Z(3)$  direction in Figure 3.21. When a hexagonal honeycomb structure is loaded in this direction, the cell walls are extended or compressed (rather than bent) and the resulting elastic (compressive and tensile) moduli are much larger than those calculated for in plane loading. Assuming a low density hexagonal honeycomb core (such as Nomex), so that  $t \ll l$ , the linear elastic regime of the honeycomb cell is governed by the elastic modulus  $E^*_3$ . The theoretical prediction for the sandwich structure Young's's modulus  $E^*_3$ ; [20, 21] (reported in Equation 3.7), for normal loading into the through-the-thickness direction, simply reflects the cell material Young's's modulus  $E_s$ , scaled by the area of the load-bearing section:

$$\frac{E^*_3}{E_s} = \frac{\frac{h}{l} + 2}{2\left(\frac{h}{l} + \sin\alpha\right)\cos\alpha} \cdot \frac{t}{l} \quad (3.7)$$

for the honeycomb with uniform thickness ( $t$ ), and

$$\frac{E^*_3}{E_s} = \frac{2}{\cos\alpha(1 + \sin\alpha)} \cdot \frac{t}{l} = \frac{\rho}{\rho_s} \quad (3.8)$$

for the honeycomb with one third double thickness ( $2t$ ); where  $\alpha$  is the angle between the inclined walls and the  $W(2)$  direction and  $\rho$  and  $\rho_s$  are the density of the honeycomb structure and of the solid cell wall material, respectively. In the case of perfect hexagonal cells with  $\alpha = 30^\circ$  and  $c=l\sqrt{3}$ , and with one third double thickness ( $2t$ ), the relationship becomes:

$$\frac{E^*_3}{E_s} = \frac{8}{3} \cdot \frac{t}{c} = \frac{\rho}{\rho_s} \quad (3.9)$$

The ultimate strength of a honeycomb structure describes the maximum resistance under the compressive load. Generally, the compressive strength of such structures is correlated not only to the compressive strength of the solid cell wall materials, but also to the buckling behavior of the honeycomb cell walls. For instance, [20], reported that failure under out of plane compressive stresses occurs due to fracture of the cell walls or due to elastic or plastic buckling of the cell walls. For Nomex honeycombs, failure is due to a “crushing” mechanism, initiated by elastic

buckling and developing as a plastic buckling process [20]. For this reason, some important results concerning different modes of collapse under out of plane compressive loads are following reported.

**Non-linear elasticity: elastic buckling**

The honeycomb compressive behavior is intrinsically related to the cell wall buckling behavior under in-plane compression. Experimental tests showed that an elastomeric honeycomb, compressed in the Z(3) direction, will eventually buckle with the cell walls bulging in a periodic way. By assuming a perfect geometry of the honeycomb with uniform cell wall thickness  $t$ , the elastic buckling collapse stress was derived from the thin plate elastic in-plane compressive buckling theory (developed by Timoshenko) by Gibson and Ashby [22], representing the sum of the loads carried by the individual cell walls:

$$\frac{(\sigma_{el}^*)_3}{E_s} \approx \frac{2}{(1 - \nu_s^2)} \cdot \frac{\frac{h}{l} + 2}{\left(\frac{h}{l} + \sin\alpha\right) \cos\alpha} \cdot \left(\frac{t}{l}\right)^3 \tag{3. 10}$$

where  $\nu_s$  is the Poisson’s ratio of solid cell wall material. Zhang and Ashby [21] also developed the elastic buckling strength for the honeycomb with one third  $2t$  cell walls:

$$\frac{(\sigma_{el}^*)_3}{E_s} \approx \frac{5K}{(1 - \nu_s^2)(1 + \sin\alpha) \cos\alpha} \cdot \left(\frac{t}{l}\right)^3 \tag{3. 11}$$

where  $K$  is a constant depending of the boundary constraint applied to the walls. For instance,  $K=5.73$  and  $K=3.29$  in case the four boundaries of any single cell wall are fully clamped and for the condition of simply supported boundaries, respectively. It should be pointed out that in honeycombs the cell wall is neither completely free nor rigid clamped. For this reason a mean value  $K=4$  is often used.

**Plastic collapse**

If the net section stress in the plane of honeycomb cell wall exceeds the yield strength  $\sigma_{ys}$  of the cell wall material, then the cell walls will yield axially [22]. This collapse mechanism mainly exists for honeycombs made of rigid-plastic materials. The upper limit for the plastic collapse strength of the honeycombs is:

$$\frac{(\sigma_{pl}^*)_3}{\sigma_{ys}} = \frac{\frac{h}{l} + 2}{2\left(\frac{h}{l} + \sin\alpha\right) \cos\alpha} \cdot \frac{t}{l} = \frac{\rho}{\rho_s} \quad (3.12)$$

This equation properly describes the axial strength in tension whereas in compression this limit is reached only if plastic buckling does not occur first. Wierzbicky [23] treated the axial collapse of hexagonal honeycombs by plastic buckling. He stated that the cells progressively fold with a wavelength  $\lambda$  which usually is equal to the cell side length  $l$  Figure 3.24a. The geometry of collapse is characterized by very little extension or tension and large bending of the cell wall. By equating the plastic work per unit depth of cell wall to the work done by the force  $P$  per cell in a displacement of  $(\lambda/2 - 2t)$  it is possible to give an estimation of the plastic buckling stress:

$$\frac{(\sigma_{pl}^*)_3}{\sigma_{ys}} \approx \frac{\pi}{4} \cdot \frac{\frac{h}{l} + 2}{\left(\frac{h}{l} + \sin\alpha\right) \cos\alpha} \cdot \left(\frac{t}{l}\right)^2 \quad (3.13)$$

which, for regular hexagons, reduces to:

$$\frac{(\sigma_{pl}^*)_3}{\sigma_{ys}} \approx 2 \cdot \left(\frac{t}{l}\right)^2 \quad (3.14)$$

Since this was a simplified calculation, Wierzbicky identified a compatible collapse mode which requires additional plastic hinges and limited amount of cell wall extension at the cell corners (Figure 3.24b).

By minimizing the collapse load with respect to the wavelength  $\lambda$ , Wierzbicky's method provided the stress limit for collapse caused by plastic buckling, as:

$$\frac{(\sigma_{pl}^*)_3}{\sigma_{ys}} \approx 5.6 \cdot \left(\frac{t}{l}\right)^{\frac{5}{3}} \quad (3.15)$$

In case of hexagonal honeycomb with uniform thickness  $t$ , and

$$\frac{(\sigma_{pl}^*)_3}{\sigma_{ys}} \approx 6.6 \cdot \left(\frac{t}{l}\right)^{\frac{5}{3}} \rightarrow (\sigma_{pl}^*)_3 = 3.25\sigma_{ys} \left(\frac{\rho}{\rho_s}\right)^{\frac{5}{3}} \quad (3.16)$$

for honeycombs with two of the six cell walls having double thickness,  $2t$ . The stress for collapse by plastic buckling provided by these equations may be less than that for simple plastic compression (equation 3.12) when  $t/l < 0.1$  leading to a compressive collapse mode by plastic buckling.

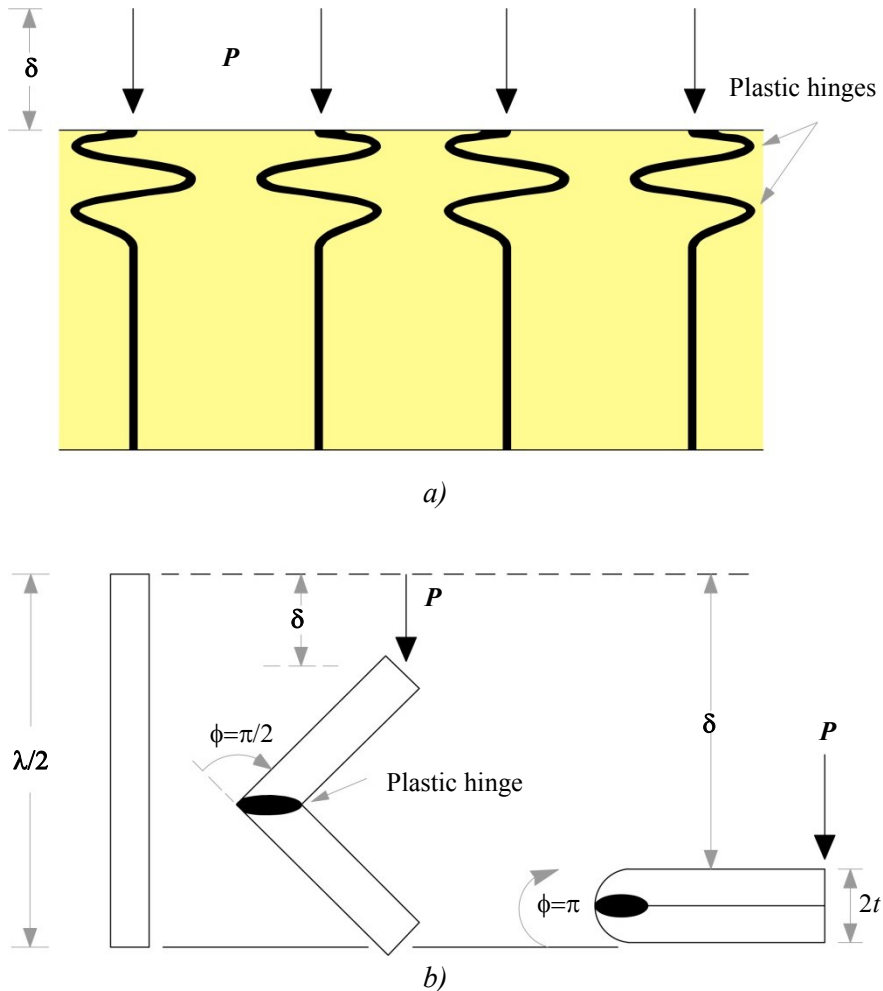


Figure 3.24: Schematization of the plastic buckling of a honeycomb loaded in  $Z(3)$  direction a); work dissipated in the plastic hinge b).

### ***Brittle failure***

The strength of brittle honeycombs is important both for bearing loads and under temperature gradient conditions. If the net section stress in the plane normal to

$Z(3)$  exceeds the tensile fracture strength (approximately  $\sigma_{ts}$ ) of the cell wall material, a brittle honeycomb will fail in tension. The upper limit for tensile strength is then:

$$\frac{(\sigma_T^*)_3}{\sigma_{Ts}} = \frac{\frac{h}{l} + 2}{2 \left( \frac{h}{l} + \sin\alpha \right) \cos\alpha} \cdot \left( \frac{t}{l} \right) = \frac{\rho}{\rho_s} \quad (3.17)$$

This is an upper limit because it describes a defect-free condition; in fact, if the honeycomb contains a kind of defect it may fail at lower stresses. For brittle honeycomb under compression, the fracture strength of the cell wall solid material under compression should be used instead.

### 3.2.6. Imperfections – classification and modeling

The knowledge of core constituent material properties and the sensitivity of such structures to different sources of defects represent a fundamental concern for the development of a cellular- based finite element (FE) model able to capture the behavior of such structures, including the buckling limit and the folding mechanism occurring during the crushing mode.

Generally, the usual source of material imperfections is the manufacturing process of honeycomb structures. The most common manufacturing method is the adhesive bonding followed by an expansion process [7], reported in Figure 3.25: honeycomb starts out as flat strips of material, or ribbons. Strips of adhesive are placed on the ribbons in a staggered pattern; for metallic cores, a corrosive resistant coating is applied to foil sheets before printing the adhesive lines.

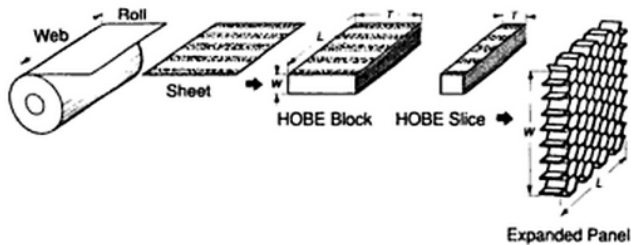
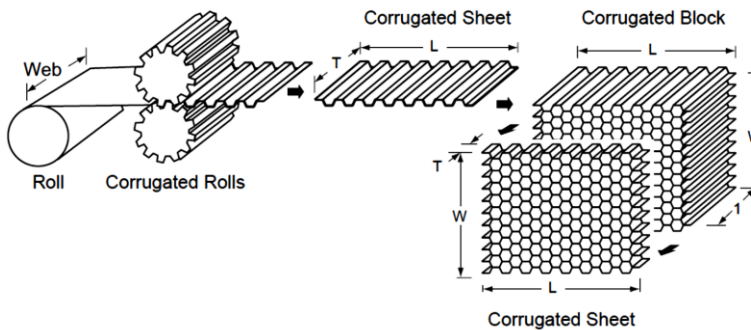


Figure 3.25: Expansion manufacturing process for honeycomb material [7].

The sheets are cut to the required thickness and stacked, and the adhesive is cured under pressure at elevated temperature. Once cured, the blocks are cut to the desired thickness, and then the ribbons are pulled apart or expanded to form honeycomb. Fully expanded honeycomb forms the classical hexagon shape whereas if the expansion is stopped before or after the hexagons are fully formed, an under-expanded or an over-expanded core can be obtained, respectively. When metallic cores are expanded, the sheets yield plastically and the node free wall joints thereby retain their expanded geometric shape. The procedure for nonmetallic honeycomb is slightly different. Here the honeycomb does not retain its shape after expansion and must be held in a rack. The block web material contains a small amount of resin which is heat-set in an oven. Most paper cores will retain their expanded shape. Then, the honeycomb block is dipped in liquid resin (usually phenolic or polyamide) and oven cured. The dipping curing cycle is repeated until the block is at the desired density. The corrugated process of honeycomb manufacture is typically used to produce products in the higher density values. This process starts with the application of the adhesive to the corrugated nodes; then, the corrugated sheets are stacked into blocks and the node adhesive cured. Sheets of honeycomb material are cut from these blocks to the required core thickness (Figure 3.26).



**Figure 3.26: Corrugated manufacturing process for honeycomb material [7].**

The different types of imperfections and irregularities which characterize these materials may affect the ideal structure of a cellular honeycomb core and modify its mechanical behavior. These are inevitably generated by the manufacturing process and/or loading conditions. A general classification of imperfections can be provided as follows [10, 24, 25]:

- *Geometrical imperfections*: i.e., shape defects, curvatures, non-perfect angular corners, surface roughness, wall thickness variability, uneven cells (global imperfections);
- *Material imperfections*: i.e., variability of the material properties, for example due to the heterogeneity of the adopted composite system (e.g., Nomex paper or CFRP), resin accumulation in cell wall corners, pores, variation of fibre volume fraction (local imperfections);
- *Initial imperfections*: i.e., prestress and prestrain conditions;
- *Loading imperfections*: i.e., load misalignment, variation of loads.

Typically, the actual case originates as a combination of the kinds of imperfections listed above.

Defects are responsible for the initiation of damage and subsequent degradation (damage propagation, folding phase, tearing of the edges etc.) and, therefore, greatly influence the global and local mechanical response of the structure. Several studies have been conducted addressing this issue. An ideal model without imperfections tends to overestimate the mechanical properties, in particular critical buckling load and initial stiffness [26, 27]. Combescure [24] reported some results showing how initial shape imperfections, thickness defects, and boundary condition imperfections can lead to a drastic decrease of the load carrying capacity of a structure under compression. Baranger et al. [26] analyzed the influence of geometrical defects in folded cores and their consequences on buckling behavior with the final aim of performing a numerical optimization of the core geometry. They reported that geometrical defects may play a major role in the response of the structure in terms of stability problem involving both local and global buckling.

In this context the modeling of imperfections represents a critical issue in the simulation process of cellular-based honeycomb structures. As a consequence of the variety of imperfections characterizing the manufactured core, different methods have been implemented to include imperfections into meso-scale honeycomb FE models for virtual testing simulations. Usually, FE analysis includes 2 main approaches: linear elastic buckling analysis (i.e. eigenvalue problem) and non-linear analysis (i.e. geometric-non-linear). The linear buckling analysis predicts the critical load that triggers the structure to buckle according to a certain shape of deformation for an ideal geometry of the structure. The result of this analysis is a bifurcation point in the load (e.g. compressive load) history of the structure dividing a first perfect elastic state to a secondary loading path of a quasi-equilibrium state. The linear buckling problem is formulated as the following eigenvalue problem:

$$K\Phi_i = \lambda_i M\Phi_i \quad (3.18)$$

where  $K$  is the global element stiffness matrix,  $\lambda_i$  is the  $i$ th eigenvalue or buckling load factor,  $\Phi_i$  is the  $i$ th eigenvector or buckling mode vector of the displacement,  $M$  is the global geometric stiffness matrix which is also known as the initial stress stiffness matrix. However, a structure as honeycomb usually undergoes geometric non-linear behavior due to the existence of different sources of imperfections. Geometrical imperfections can be implemented on the basis of experimental observations or by the geometric scanning of the actual shape of a manufactured core [24, 27]. In addition, geometrical imperfections can be created in a model by performing random deviations from the ideal shape of nodal positions according to a fixed range of variability. This approach is generally called node shaking and is available in most of the commercial FE codes. Baranger [26] proposed a new method which differs from the aforementioned procedures, based on the modeling of the manufacturing folding process in order to reproduce physical defects, such as the out-of-straightness of the edges. Li et al. [28] studied honeycomb cell structures having irregular cell shapes and non-uniform cell wall thickness by using a Voronoi tessellation technique and the FE method. The effect of cell wall corrugation, curvature and missing cell walls was investigated by [29-31]. Moreover, Fan [32] investigated thermoplastic hexagonal honeycombs considering only that the vertical walls of the honeycombs were not perfectly straight (cell wall tilting angle of  $0.2^\circ$  from vertical position) for the non-linear simulation of flat-wise compression test, obtaining a slightly overestimated final strength.

Another technique used to model imperfections is to consider global modes of the cell on the basis of linear buckling analysis [33, 34]. More in detail, the ideal initial geometry (mesh) of the cell is distorted according to one of the computed global buckling modes (or eigenmodes) with amplitude scaled down of about 1-5% of the wall thickness. Xue and Hutchinson [35] generated eigenmodes by quasi-static buckling analysis with ABAQUS/Standard and applied them to perturb the perfect geometry of square metal honeycomb and initiate cell wall buckling. Other examples can be found in [33, 34], where hexagonal honeycomb cores are investigated by means of ABAQUS/Standard and LS Dyna (LSTC, Livermore, CA, USA) FE codes. In all cases it is reported that the eigenmodes had a strong influence on the resulting compressive stress-strain curve with particular emphasis on the nonlinear part of the curve. The choice of one of the dominant modes and the magnitude of the scale factor

may affect the global mechanical response, which sometimes can also be affected by the user's sensibility. In particular, different imperfections corresponding to different buckling modes may lead to different collapse modes, affecting the effectiveness in determining the initial stiffness and the compressive peak load [26, 35]. Moreover, the use of the first buckling mode not necessarily allows to describe all types of defects and it may be not appropriate when constituent cell materials are not homogeneous.

### **3.3. Materials and methods**

The honeycomb sandwich material investigated within the present work is a 48 kg/m<sup>3</sup> hexagonal honeycomb core with a nominal cell size of 3.175 mm, made of Nomex phenolic resin-impregnated aramid paper. The trade name is HRH 10-1/8-3.0 and it is manufactured by Hexcel [36]. Hexcel manufactures aramid-fiber reinforced honeycomb from three types of para-aramid substrates, including Nomex®, Kevlar®, and KOREX® materials. The analyzed honeycomb consists of Dupont's Nomex aramid-fiber paper dipped in a heat-resistant phenolic resin to achieve the final density. It provides high strength, toughness and fire resistance properties in a small cell size. It is widely used as core material for sandwich panels throughout the aerospace industry and also in several other commercial areas. According to the datasheet of the manufacturer, the code name is referred to its geometrical and mechanical features: HRH 10 indicates the product type, 1/8 is the cell size in fractions of an inch and 3.0 is the nominal density in pounds per cubic foot.

In Figure 3.21 and Figure 3.27a,b the geometry of the honeycomb is illustrated. All the honeycomb specimens considered in the following activities have been assembled with the  $L(1)$  direction of the honeycomb core along the primary direction. The Out-of-plane crushing behavior of Nomex honeycomb has been investigated by flat-wise stabilized compressive tests according to ASTM C365M standard. The tests were run on 60x60x32.2 mm Nomex core coupons (five) bonded between two 1-mm-thick E-glass fiber reinforced phenolic resin skins (with a cured ply thickness of 0.25 mm), with a constant cross head velocity of 0.5 mm/min. The specimens were laminated with external skins in order to prevent local crushing at the edges of the honeycomb cores. Compressive modulus of the elastic phase, stabilized compressive strength and strain, crush strength, fully compacted compressive modulus and strain values at which densification occurs have been derived by these tests.

### 3.3.1. Model features

The elastic and failure behavior of the honeycomb structure is strongly influenced by cell wall mechanical properties and their modeling represents a crucial factor for the development of the FE honeycomb model. The manufacturing process generates an orthotropic material where aramid fibers embedded in the layers are oriented almost randomly. The material is characterized by two principal directions, called machine direction and cross direction. The principal material direction corresponds to the thickness direction  $T$  of the honeycomb structure.

Foil thickness can be highly variable whereas porosity and lack of matrix can affect the ideal smoothness of the foil. The overall thickness is very difficult to estimate and can be detected directly from micrographics or SEM images. It should be mentioned that it is not straightforward to gather experimental data of such paper material due to the thin configuration of the specimen. Mechanical characterization of Nomex paper material can be found in experimental works performed by Tsujii et al. [37] as well as Foo et al. [5] while Fisher et al. [38] performed experimental tensile and compressive tests on Kevlar based paper material used for folded cores showing a mechanical performance similar to the Nomex paper. These experimental tests (including tension, compression, and bending) provided stress-strain curves as well as stiffness and strength values reporting a nonlinear behavior that can be estimated by a bilinear elasto-perfectly plastic material law in compression. Moreover, differences in the material constitutive behavior were found in different loading directions, machine, and cross direction.

The development of the Nomex honeycomb FE model is based on the definition of representative cell geometry, its meshing, the definition of boundary and loading conditions, and the assignment of proper constitutive material laws including the implementation of imperfections. The periodicity of the idealized hexagonal microstructure allows to consider one representative hexagonal unit cell to simulate the buckling and compressive/crushing response of Nomex honeycomb observed in the experiments by assigning appropriate boundary conditions. The cell is extracted from the periodic microstructure of the honeycomb as highlighted in Figure 3.27a (dashed line). Residual stresses deriving from the mechanical expansion process through which the honeycomb is manufactured are assumed to be negligible. Additionally, the small rounding of the corners of the actual cells is not taken into account. The final idealized cell geometry is shown in Figure 3.27b in the  $L-W$  plane and it is depicted in a three-

dimensional rendering in Figure 3.27c. The representative cell is represented by a perfect hexagonal cell of diameter =  $l\sqrt{3}$ , paper thickness  $t$  and height  $h$ .

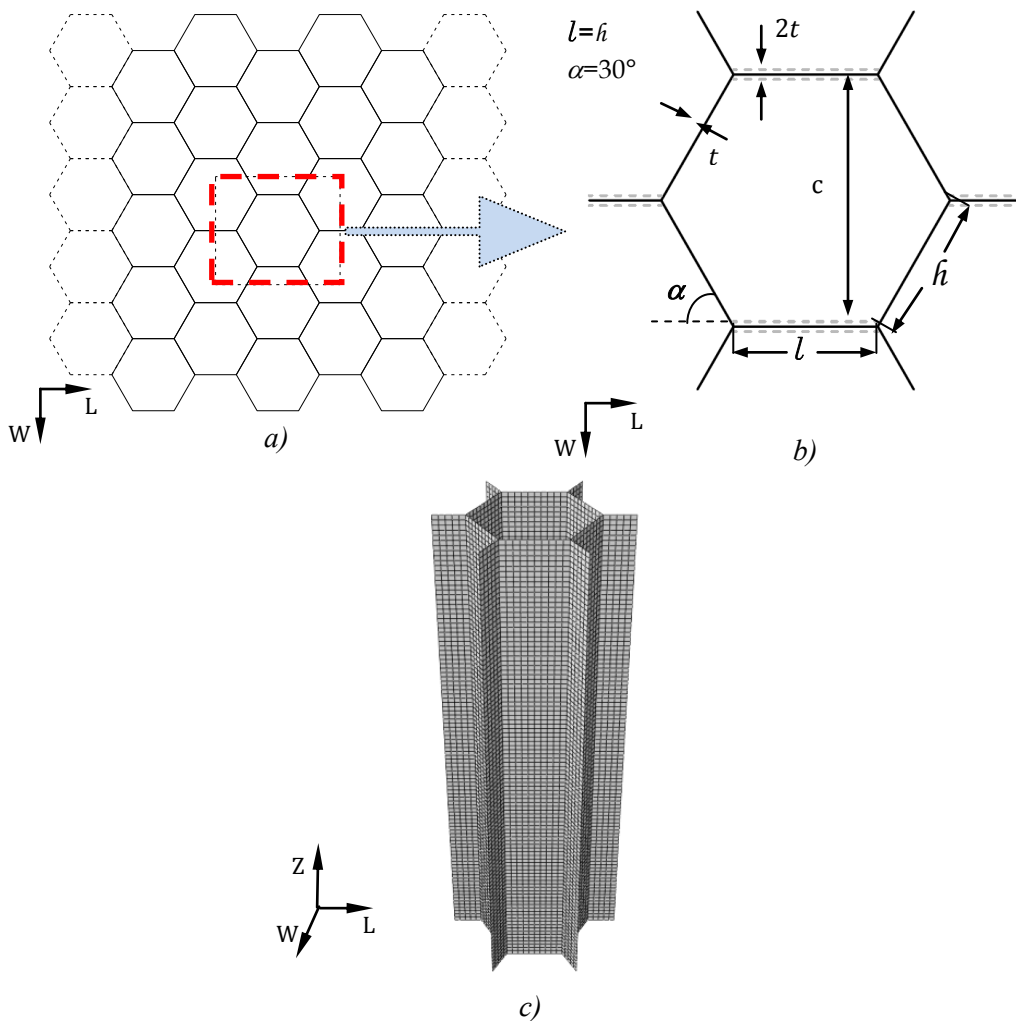


**Figure 3.27: a) in plane periodical honeycomb microstructure for hexagonal cells,  $W$ - $L$  plane; b) single representative periodic cell; c) 3D finite element mesh rendering for a single Nomex honeycomb cell.**

The corresponding projected area is equal to  $\left(\frac{3}{2}\sqrt{3}l\right) \times (3l)$ , i.e. the two cell dimensions in the  $W$  and  $L$  direction, respectively. The double wall thickness of both sides in the  $L$  direction is due to the manufacturing process (adhesive between strips)

and a monolithic thickness of  $2t$  is assumed in the model neglecting the bonding of the two walls. The hexagonal unit cell is discretized within the nonlinear FE code ABAQUS using 9000 S4 shell elements. The bottom edges of the unit cell are assumed to be fixed while the nodes of the top edges can only translate in the  $Z$  direction. To enforce periodicity, for the six lateral edges of the unit cell only displacements in the plane perpendicular to the wall direction and rotations around the radial direction are allowed. The cell is loaded by incrementally prescribing the  $Z$  displacement of the top surface, indicated as  $\delta$ .

According to the manufacturer, the cell walls are made of a 0.051 mm thick Nomex® T412 aramid paper with an additional phenolic resin coating, resulting in a total average wall thickness of roughly 0.063 mm. This value has been taken as a reference for the single wall thickness  $t$  in the honeycomb single cell model. The constitutive behavior of the implemented material model was assumed to be isotropic and linearly elasto-perfectly plastic until failure, on the basis of available experimental results for Nomex paper material [5, 37].

As previously mentioned the actual cellular structure of a honeycomb core is non-uniform in geometry and characterized by imperfections and irregularities. This feature inevitably affects the critical buckling load of the single cell and the overall strength of the honeycomb structure which would be overestimated in a model without imperfections. In Nomex® honeycomb cores both global and local imperfections are present arising from the manufacturing process, i.e., the expansion of the hexagonal cells and the dipping into phenolic resin.

In the present work, since impregnated aramid-paper exhibits mainly variations in the material properties and paper thickness, two different sources of imperfections were investigated in the FE model of the Nomex cell:

- foil thickness variability,
- in-plane Young's modulus variability.

In fact, there are significant variations in the material properties and paper thickness, especially in case of impregnated aramid paper. In particular, experimental tensile tests on aramid-impregnated paper revealed, through observations by optical strain measurement, that there was a strongly varying in-plane strain distribution over the paper area. This was attributed to the variation of paper thickness, fiber dispensation within the phenolic matrix, rough surfaces, resin accumulation [39]. In addition, Fisher et al. [38] observed displacements varying over the paper area as well, and microscopic analysis revealed irregular properties of paper thickness, fiber distribution/orientation

with the presence of a quantity of voids in the phenolic resin. This evidence is important since the weakest or thinnest areas of a cell wall may initiate the global buckling, triggering damages. Other types of imperfections described in the previous sections are not handled for the development of the model. In Figure 3.28 two examples of imperfections are illustrated by means of SEM images. In Figure 3.28a it can be observed that within the same Nomex paper wall, the highlighted thicknesses (yellow and red markers) appear different whereas in Figure 3.28b some amount of glue appear collected on the surface of the paper Nomex material.

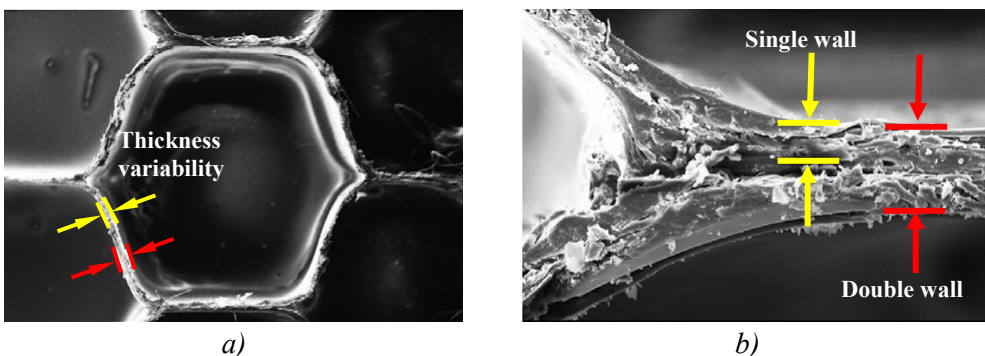


**Figure 3.28: SEM photos of Nomex™ core. a) Transverse section; b) detail of a vertex of a hexagonal cell [40].**

According to the current approach, the properties of Nomex paper are modified in terms of wall thickness and material constitutive properties by stochastically distributing thickness and elastic modulus values over the finite elements of the numerical model. Values of thickness and elastic modulus were chosen according to a uniform distribution, defined by the average value and the coefficient of variation (CV). In detail, the average values have been assumed equal to 0.063 mm and 3.50 GPa for the thickness and the Young's modulus, respectively. In dealing with the CV, four different values have been considered, i.e., 10%, 15%, 20%, and 25%. All the adopted distributions are presented in combination with the results of the analysis (Figure 3.33 to Figure 3.35).

This approach has been implemented through a model generation tool by extracting, for each finite element, a value for the thickness and the elastic modulus according to the adopted distribution.

Through this approach, three cases have been analyzed, using: a) only thickness variation; b) only Young's modulus variation; c) a variation of both parameters. Moreover, for each case five numerical samples have been generated. It should be specified that some configurations of the samples did not reach convergence in the analysis; in those cases, new extractions were made until convergence was attained. In Figure 3.29, a flowchart illustrates the adopted methodology depicting the final single cell with randomly assigned material properties in a three dimensional rendering.

### **3.3.2. Approach validation**

The proposed approach has been validated on the basis of the out of plane compressive/crushing experiments and analyses performed by Wilbert et al. [33] on Hexcel Al-5052-H39 (aluminum) honeycomb having nominal cell size  $c$  of 9.53 mm, wall thickness  $t$  of 95  $\mu\text{m}$  and height  $h$  of 15.9 mm. This case allowed to compare the current approach with a standard one where the critical buckling load was calculated by means of a linear buckling analysis, and post-buckling response (up to folding) was obtained by including some imperfections in the geometrical model according to the first buckling mode with a fixed amplitude of the displacement field. The buckling and post-buckling analyses performed by Wilbert et al. revealed that the out of plane mechanical response is initially stiff and linear elastic up to a level of stress close to 2.95 MPa. From this limit, the plate-like walls of the cell buckle into the first mode characterized by three half waves along the height of the cell and symmetric about mid-height. This generates a bifurcation in the elastic response that develops, at slightly higher stress, with the second buckling mode characterized by an anti-symmetric shape about mid-height with four half waves along the height of the cell. Further compression gives rise to plasticization in the cell wall concentrated around the cell middle height and, as a consequence, the compressive collapse load/stress of the structure is reached; particularly, in that case, it is equal to 4.93 MPa.

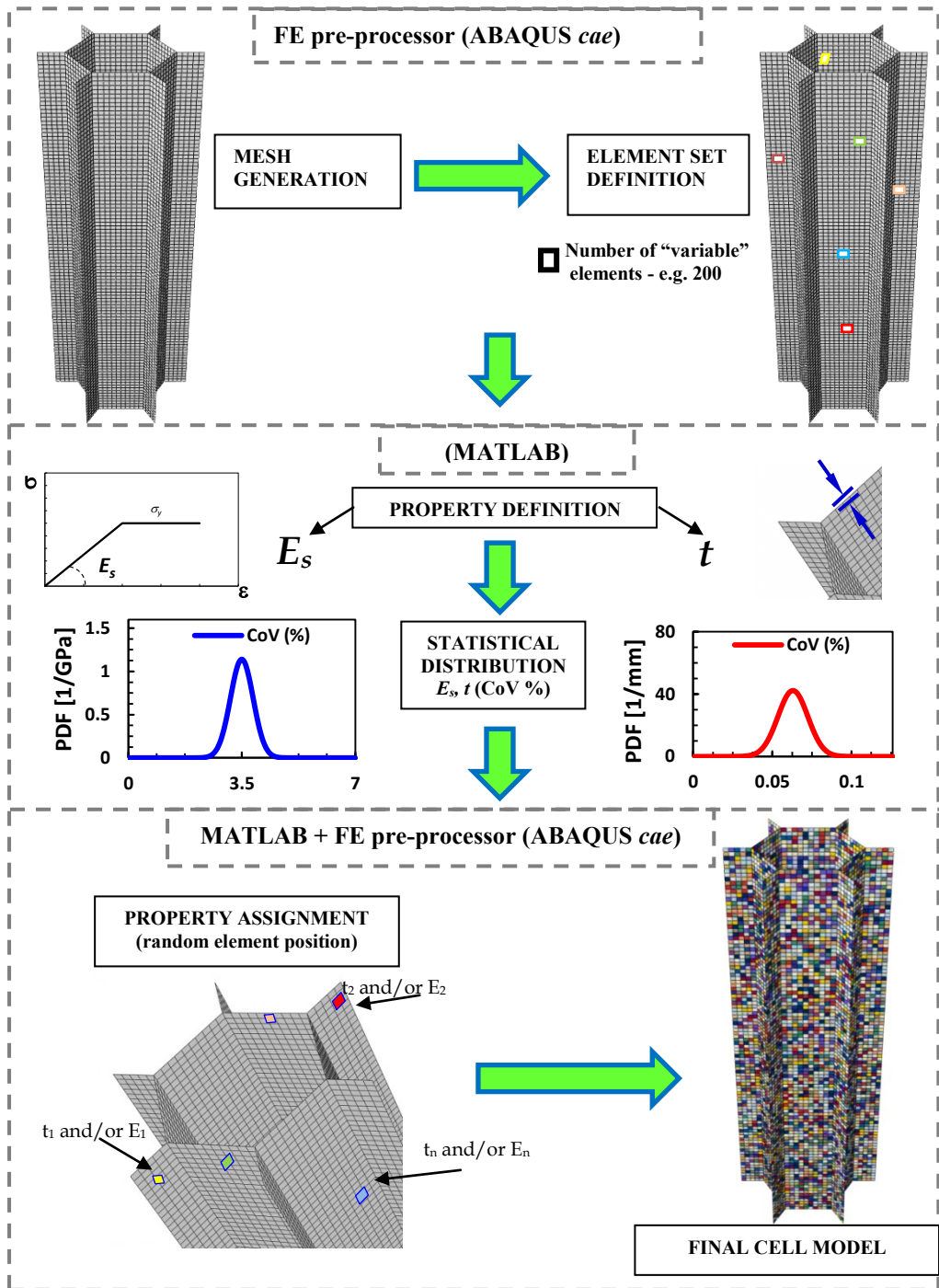


Figure 3.29: Schematic flow chart of the simulation strategy.

The authors noticed that the predicted value of collapse stress was higher than the average value measured in the experiments, i.e., 3.72 MPa, and, for this reason, they performed imperfection sensitivity studies aimed at investigating various sources of imperfections which tend to reduce the collapse load.

Within the present approach, the mechanical properties of the honeycomb Al-5052-H39 foil were assigned on the basis of the experimental results gathered in that work. Accordingly, an isotropic and linearly elasto-perfectly plastic until failure constitutive behavior has been adopted for the aluminum foil, with elastic modulus equal to 69 GPa, and yield stress as 248 MPa. The cell model was then generated considering only thickness variation and only Young's Modulus variation into two limit cases for each one, corresponding to values of CV equal to 5%, and 20% (five samples for each case).

## 3.4. Result discussion

### 3.4.1. Experimental behavior

The compressive stress-strain relationship (Figure 3.30a) of the Nomex honeycomb core has been gained through an out-of-plane flat-wise compressive test previously illustrated. The nominal compressive stress has been derived as the reordered force divided by the projected area of the honeycomb specimen, i.e.,  $L \times W$  dimensions. The constitutive behavior consists of three stages: the elastic regime up to the stabilized compressive strength ( $\sigma_c$ ), the crushing regime at nearly constant plateau stress (crush strength,  $\sigma_{crush}$ ), and finally the densification regime, where the cellular structure is fully compacted resulting in a steep stress increase. Figure 3.30a reports the mean curve of five replicate specimens, where the three characteristic deformation stages are noticeable. The average values of the compressive elastic modulus, compressive strength, crushing strength, and densification strain computed on five specimens are reported in Table 3.3 with the corresponding coefficient of variation.

Figure 3.30b depicts some highlights (points A-E) on the deformation phases undergone by the Nomex structure under compressive stress. In detail, after the initial linear elastic phase (with an average compressive elastic modulus of  $E_c=137.7$  MPa), the axial deformation develops into different waves along the total height of the cells for a short range of deformation values, leading to a short non-linear elastic regime (an

instability failure) that is not easy to capture in the experiment. In fact, for Nomex honeycombs, failure is due to a crushing mechanism, initiated by elastic buckling and developing as a plastic buckling process [20, 21].

**Table 3.3: Mechanical properties of Nomex Honeycomb – experimental results.**

<i>Compressive behavior</i>	Average	Coefficient of Variation (%)
Young's Modulus (MPa)	137.7	7.74
Compressive Strength (MPa)	2.08	4.46
Crush Strength (MPa)	1.31	2.27
Densification strain (-)	0.76	1.63

By proceeding with axial deformation, the previous phase is rapidly followed by the localization of the deformation in correspondence to a certain number of cells of the honeycomb and at different positions along the height of the cells, that triggers the attainment of the compressive collapse limit of the honeycomb,  $\sigma_c$ ; the experimental average value (computed on five specimens) is equal to  $\sigma_c = 2.08$  MPa with a coefficient of variation  $CV_{exp} = 4.46\%$ . It can be highlighted that the deformation does not localize into equal waves for all the cells of the honeycomb and does not develop symmetrically about the mid height of the cell. On the contrary, from Figure 3.30b point B, it can be seen that the waves develop with different shapes and the collapse takes place randomly along the height of different cells of the specimen where the local stress concentration is attained. The collapse is due to the failure of the deformed foils of the cell which is represented by a drop in the compressive load carrying capacity approximately equal to one third of the collapse stress value. The load slightly increases after reaching the minimum of the stress due to the resistance offered by the deformed cells that start to fold on the plasticized points along the cell height. The folding process develops consecutive folds with small in length, rapidly collapsing one on each other. Within this stage the stress is not able to step up and is kept almost at the constant value of the crush strength,  $\sigma_{crush} = 1.31$  MPa. When folding is completed throughout all the height of the cell, the densification regime takes place at an average value of strain of  $\varepsilon_d = 0.76$ . At this phase, the compressive resistance is offered by the compacted material leading to a step increase in the stress (point E Figure 3.30 2b). It should be noticed that the free edge of the specimen may play a major role in the position of the concentration of the strain.

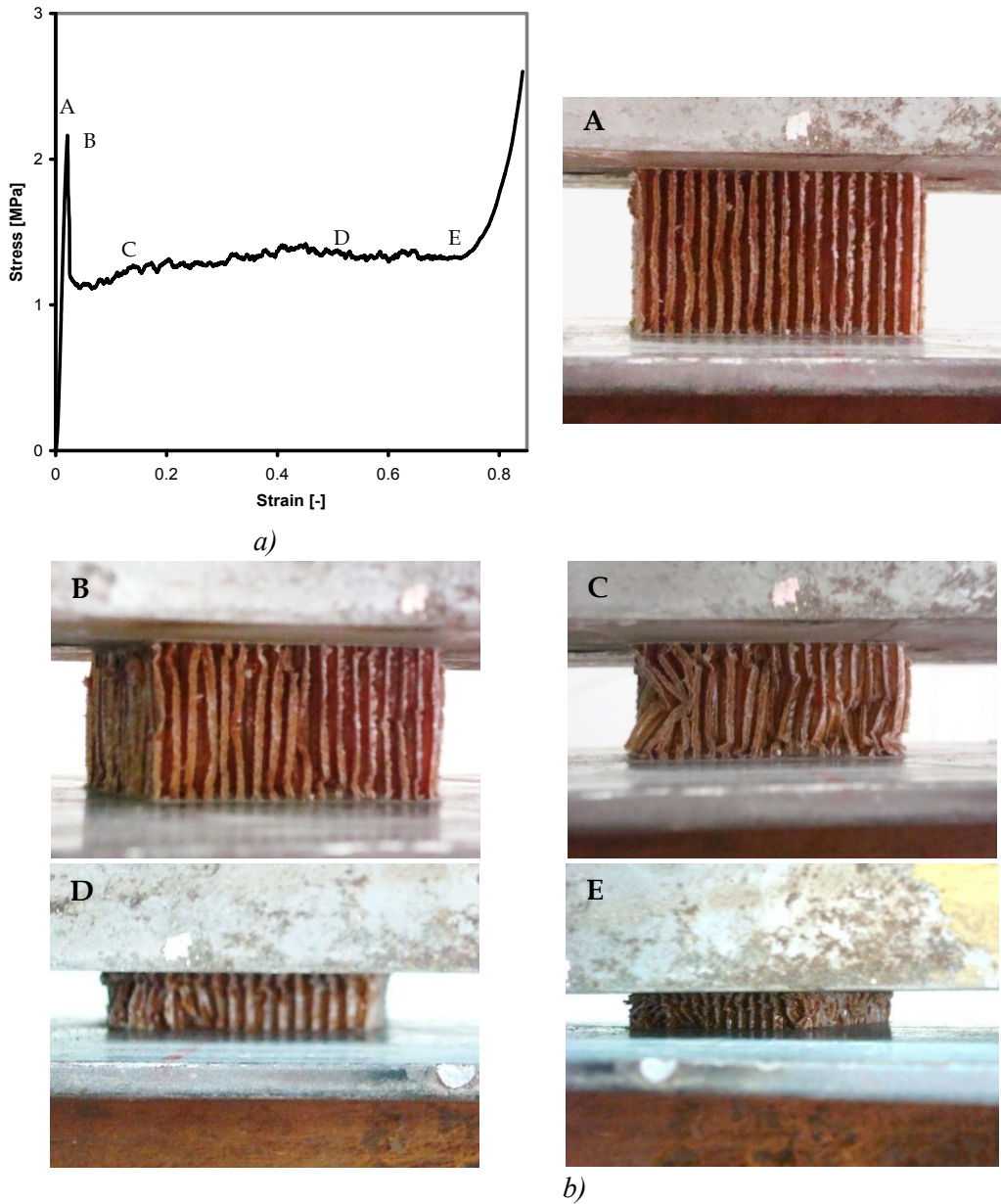
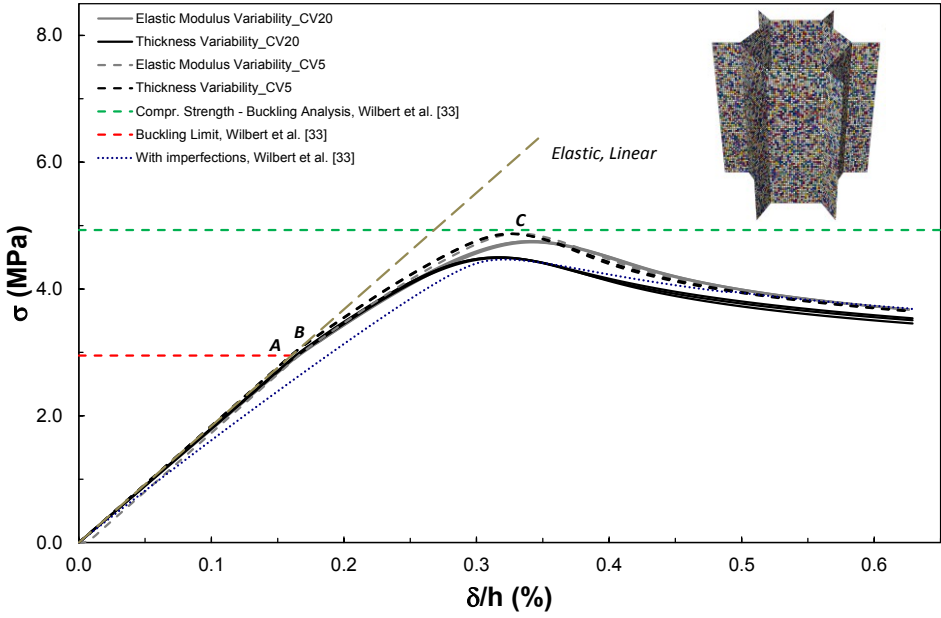


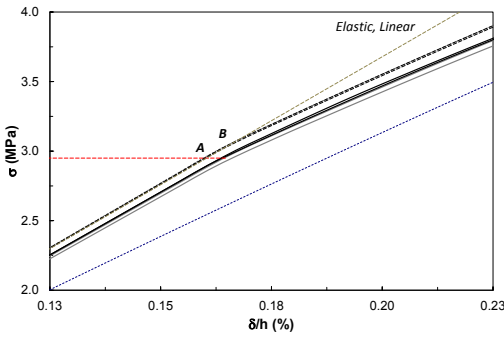
Figure 3.30: a) compressive stress – strain,  $\sigma_c$  vs  $\delta/h$ , response for HRH 10-1/8-3.0 hexagonal Nomex honeycomb; b) sequence of photographs of honeycomb cells at different stages of axial compressive strain.

### **3.4.2. Numerical results: buckling failure mode**

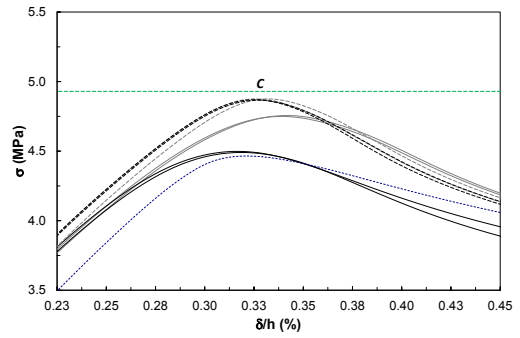
The results of the implicit analysis conducted with ABAQUS/Standard on the aluminum honeycomb cell are compared in terms of experimental and estimated values of compressive strength, buckling limit and modes obtained by Wilbert et al. [33]. Figure 3.31a reports the compressive stress vs  $\delta/h$  for the different cases whereas the inset in the same figure depicts the aluminum cell with variable material properties represented by different colors. Due to high repeatability in the results, only 2 of the 5 sample curves have been reported in the graph. Dashed and solid lines correspond to CV equal to 5% and 20% respectively, whereas grey and black lines correspond to elastic modulus and thickness variability, respectively. Horizontal lines correspond to Wilbert's result in terms of elastic buckling limit and compressive strength values from buckling analysis. The variation of elastic modulus and thickness with CV equal to 5% generates approximately the same compressive response, with a compressive strength value reaching approximately 4.87 MPa. On the contrary, in case of CV equal to 20%, the thickness variation is characterized by a critical compressive stress lower than the one obtained with the elastic modulus variation: 4.50 and 4.73 MPa, respectively. In all cases, the elastic stiffness, for both linear and nonlinear parts, is approximately the same since the curves appear almost superposed. Moreover, the response is characterized by an elastic critical buckling limit at a stress level of 3.0 MPa (A point in Figure 3.31a,b), that is very close to the one obtained by Wilbert et al. [33] by means of elastic buckling simulation. At this point, a bifurcation takes place and a deformation shape corresponding to the first buckling mode (with three waves) shows up (point A in Figure 3.31a,b); due to bifurcation, the post-buckling regime is held with a nonlinear trend, as found by Wilbert et al. [33] by adding shape imperfections to the cell. By slightly increasing the stress values, the cell deforms according to the second mode (with four waves point B in Figure 3.31a,b) and the deformation continues with this shape up to the plasticization of the cell wall around middle height (point C in Figure 3.31a,c). In Figure 3a, the dashed blue line represents the response of an imperfect version of the unit cell obtained by Wilbert et al. [33] by assigning an initial deformation according to the first buckling mode with the point of maximum transverse deflection of amplitude equal to the cell thickness,  $t$ . In this case, the peak of the maximum compressive stress approximately corresponds to the one obtained in case of CV equal to 20% for thickness variation, whereas the elastic stiffness is not affected by a reduction as it happens in case of first buckling mode imperfection.



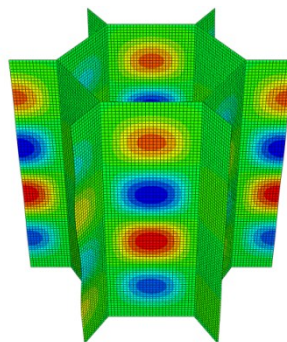
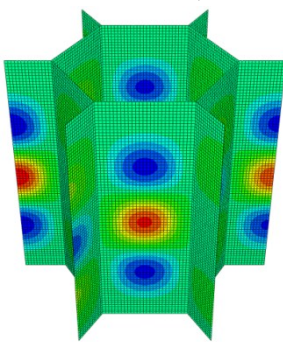
a)



b)



c)



d)

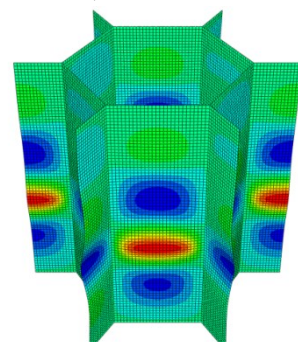


**Figure 3.31: a) compressive stress – strain,  $\sigma_c$  vs  $\delta/h$ , response for Hexcel Al-5052-H39 hexagonal aluminum honeycomb; b) focus on critical buckling load; c) focus on compressive strength; d) first (A), second (B) buckling mode and plasticized cell (C) as a result of the current approach.**

The results of the implicit analysis on the Nomex honeycomb cell are presented in the following in terms of compressive stress  $\sigma_c$  vs  $\delta/h$  curves for the different implemented imperfections: thickness variability, elastic modulus variability, and both thickness and elastic modulus variability. All the analysis have been run up to contact between cell walls, as a consequence of the folding process, i.e., approximately at a  $\delta/h$  value equal to 4-5%. Each of the three cases of imperfection has been applied to the five samples, considering four different coefficients of variation, namely, CV= 10%, 15%, 20%, 25% (cf. Figure 3.33 to Figure 3.35). For each graph, the corresponding probability density functions (PDF, black line in the figures) are reported for the variability of thickness only, elastic modulus only, as well as of both thickness and elastic modulus. Moreover, the region of the graph corresponding to the attainment of the peak of compressive stress is highlighted in Figure 3.33 to Figure 3.35 within the experimental statistical values (dashed lines in the figures), computed as:

$$\sigma_c^{min} = \sigma_c^{exp}(1 - CV_{exp}) \quad \text{and} \quad \sigma_c^{max} = \sigma_c^{exp}(1 + CV_{exp}) \quad (3.19)$$

where  $\sigma_c^{exp}$  and  $CV_{exp}$  are the average experimental compressive strength and the corresponding experimental coefficient of variation, respectively. The compressive behavior reproduced by the analysis is practically the same for the investigated cases. For this reason, the detailed description of the  $\sigma_c$  vs  $\delta/h$  curve is conducted only for the case of both elastic modulus and thickness variability with CV=10%, as depicted in Figure 3.32. The five samples generated within the above-mentioned imperfections, are characterized by a very similar compressive behavior with small differences in the values of the peak of compressive stress. The linear elastic regime of the honeycomb cell is governed by the elastic modulus  $E_3^*$ .

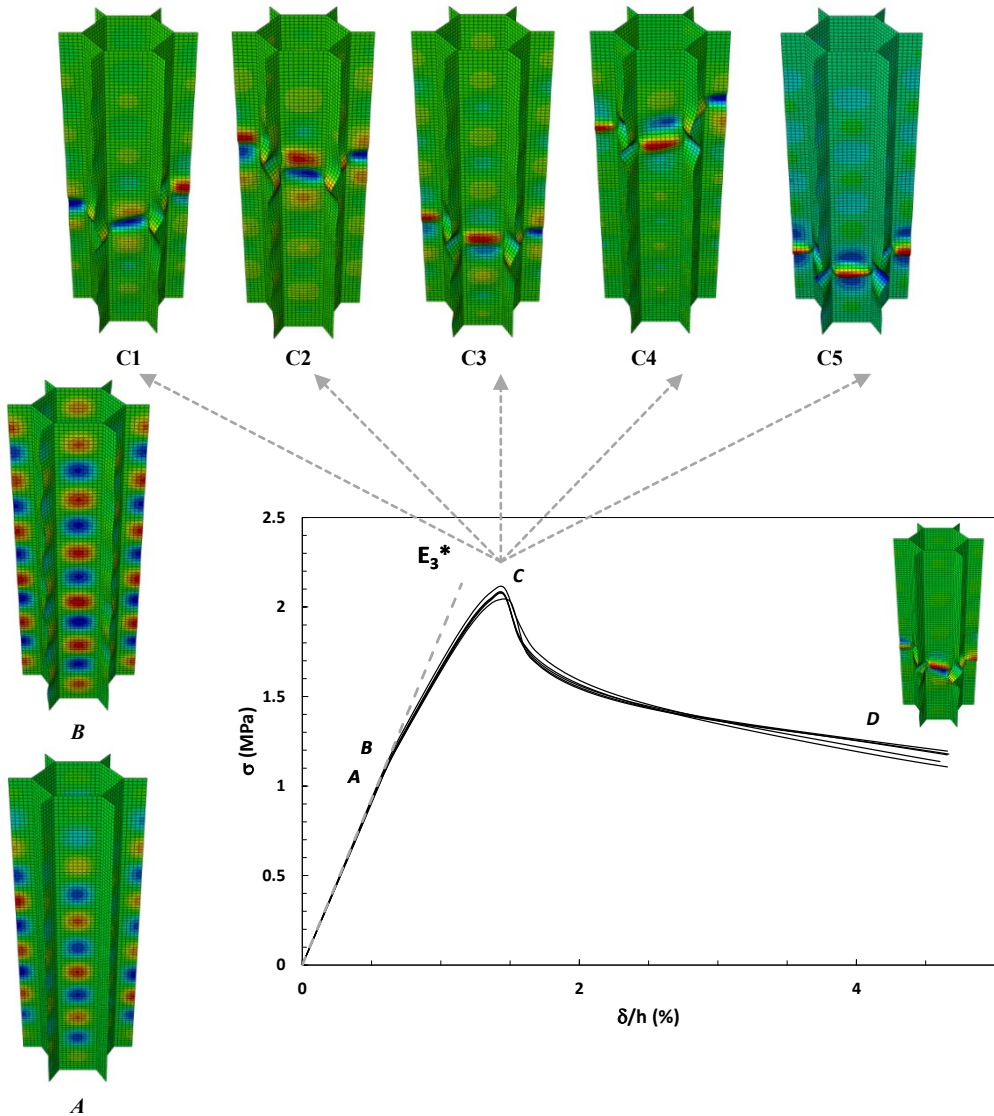


Figure 3.32: compressive stress – strain,  $\sigma_c$  vs  $\delta/h$ , response for HRH 10-1/8-3.0 hexagonal Nomex honeycomb up to folding with FE results of cell deformations corresponding to A=critical buckling limit, B=shape up to compressive strength, C1-C5=strain localization for the five cell samples, D=first fold of the cell.

The theoretical prediction for the sandwich structure Young's modulus  $E_3^*$  [20, 21] reported in Figure 3.32, for normal loading into the through-the-thickness direction, simply reflects the cell material Young's modulus  $E_s$  scaled by the area of the load-bearing section (see also section 3.2.4):

$$\frac{E_3^*}{E_s} = \frac{2}{\cos\alpha(1 + \sin\alpha)} \cdot \frac{t}{l} = \frac{\rho}{\rho_s} \quad (3.20)$$

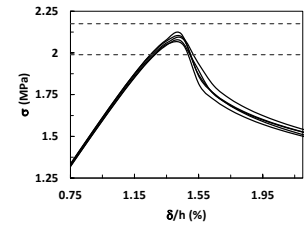
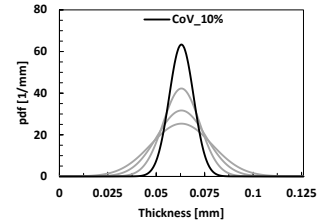
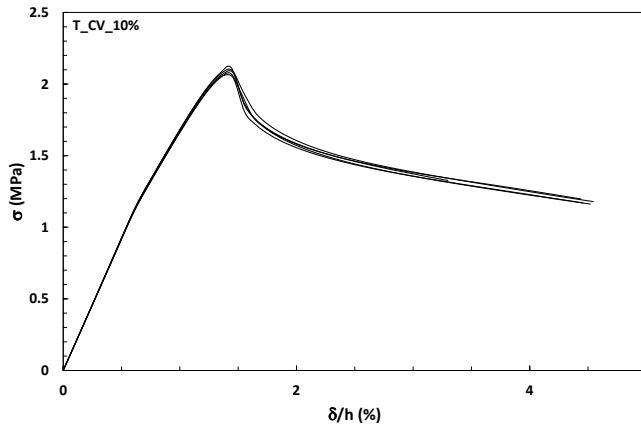
where  $\alpha$  is the angle between the inclined walls and the  $W$  direction and  $\rho$  and  $\rho_s$  are the density of the honeycomb structure and of the solid cell wall material, respectively. In the case of perfect hexagonal cells with  $\alpha = 30^\circ$  and  $c = l\sqrt{3}$ , the relationship becomes:

$$\frac{E_3^*}{E_s} = \frac{8}{3} \cdot \frac{t}{c} = \frac{\rho}{\rho_s} \quad (3.21)$$

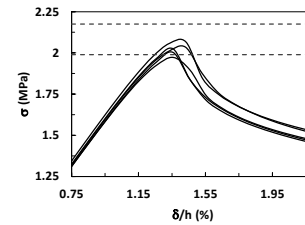
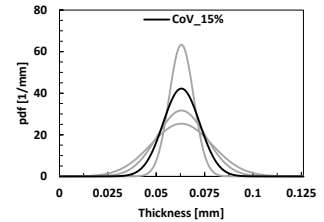
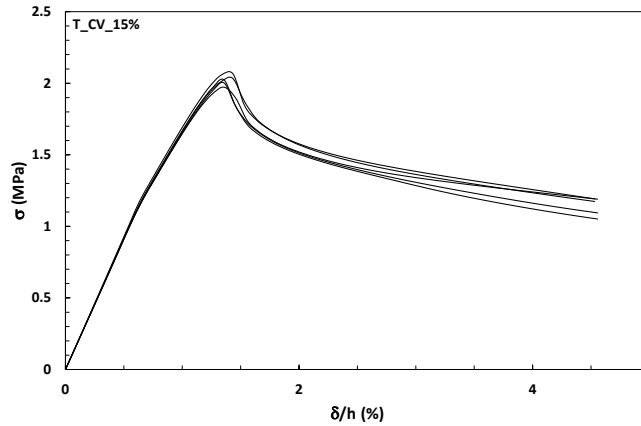
The linear elastic regime terminates when the cell walls of the honeycomb buckle elastically at a value of compressive stress of approximately 1.20 MPa (Figure 3.32-A). After reaching the critical buckling load a bifurcation takes place in the  $\sigma$  vs  $\delta/h$  curve giving rise to the non-linear post buckling regime. At this point the cell bulges in a periodic way according to the shape depicted in Figure 3.32-B that evolves in a different manner at slightly higher level of stress. This is a common behavior among honeycomb structures; generally, the linear-elastic regime terminates when the cell walls of the honeycombs buckle elastically, or bend plastically, or fracture in a brittle manner [21], depending on the relative density  $\frac{\rho}{\rho_s}$ : in low density flexible structural honeycombs it is usually elastic buckling that first leads to nonlinear behavior, although it is found that in intermediate and high density honeycombs, fracture can occur under compression into the through-the-thickness direction.

Commonly, the initiation of elastic buckling does not make the honeycomb lose all of its stiffness and load-carrying capacity; failure of structural plates is typically defined by the ultimate strength, considering post buckling strength [21]. The configuration at point B is kept unchanged up to the attainment of the compressive peak of stress  $\sigma_c$  where yielding is reached in some elements of the mesh along the height of the cell leading to a sudden drop in the compressive stress. In terms of physical behavior, the sampling generation having different values of  $E_s$  and  $t$  within a statistical range of variation, is mainly reflected through different compressive strength values and different positions at which plasticization occurs rather than through different buckling mode sequences. Figure 3.32-C depicts five cells corresponding to the five different samples at the collapse deformation. It can be noticed that the position along the height at which compressive strain localizes is different for the five

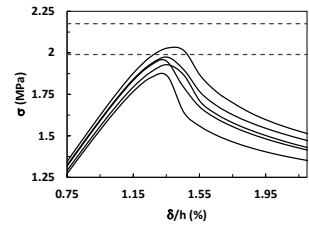
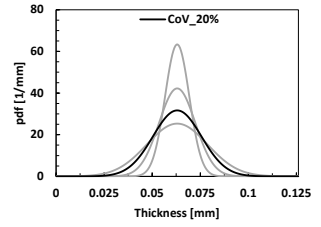
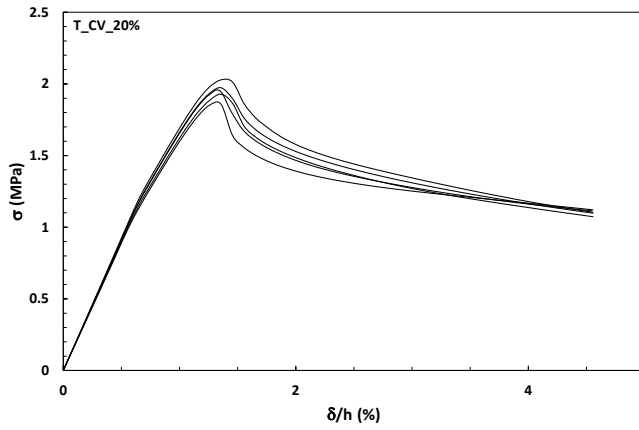
cases as well as the initial direction of folding that can be even inclined with respect to the  $L$  direction. The folding mechanism begins from that point along the height of the cell, while the compressive stress slightly changes from case to case due the residual resistance offered by the deformed cells. The implicit analysis terminates when cell walls collapse one on each other due to progressive folding.



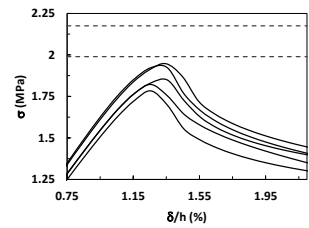
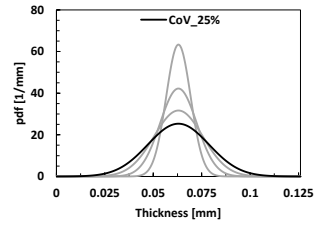
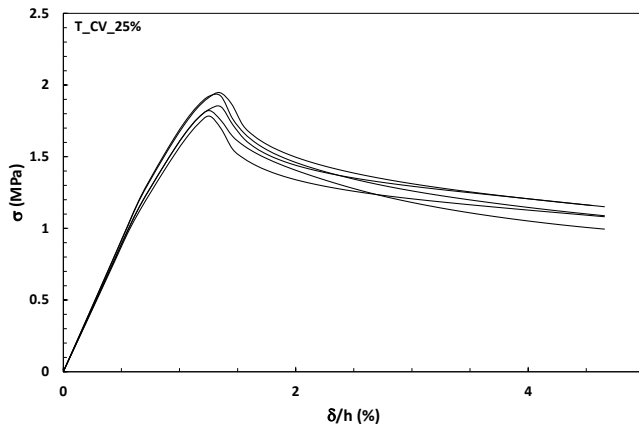
a)



b)



c)



d)

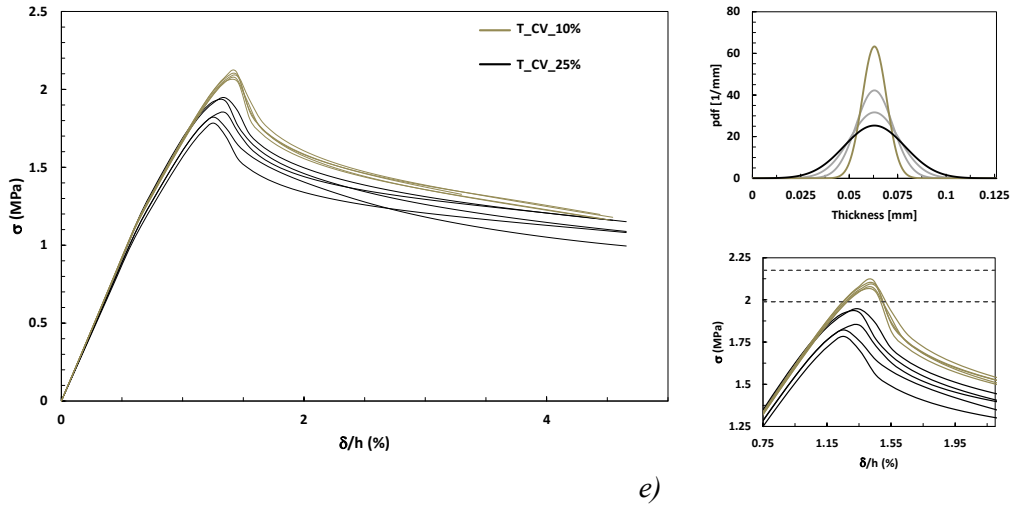
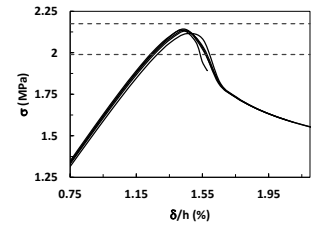
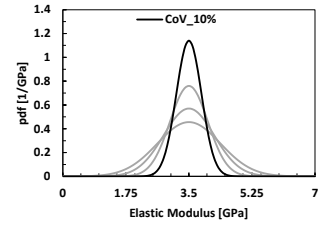
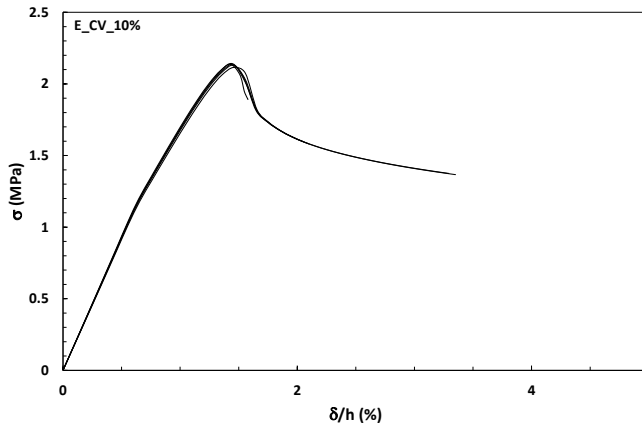
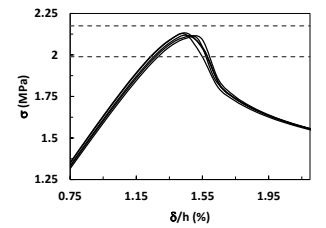
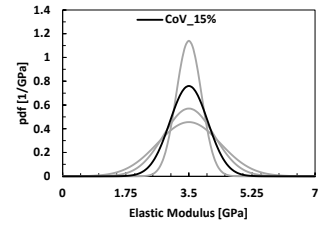
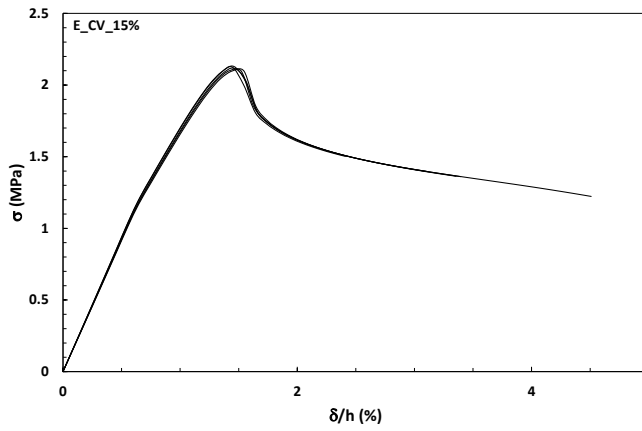


**Figure 3.33: Effect of thickness variability on  $\sigma_c$  vs  $\delta/h$  curves for a) CV=10%, b) CV=15%, c) CV=20%, d) CV=25% with the corresponding PDF and focusing on the peak of compressive strength; e) superposition of CV=10% and CV=25% cases.**

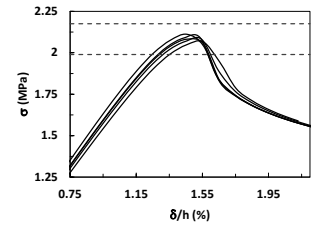
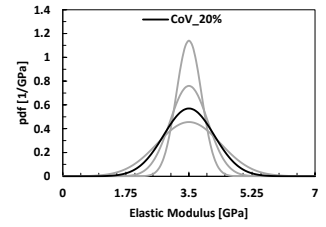
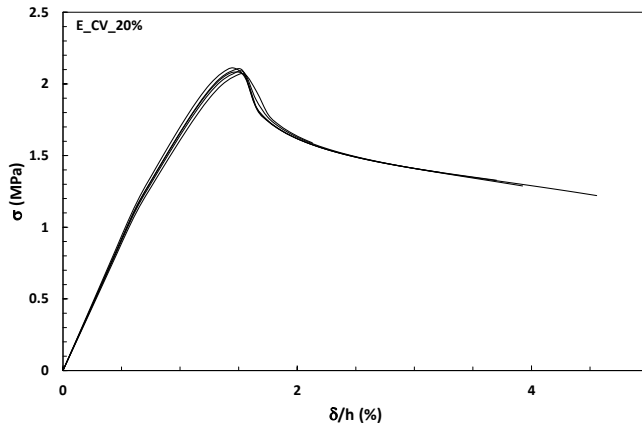
In dealing with the three cases of imperfections, the cell wall thickness variability generates a compressive response that is very similar among the five samples in case of CV=10% with an average compressive strength  $\sigma_c$  equal to 2.084 MPa, that is well represented in the experimental range defined by  $\sigma_c^{min}$ ,  $\sigma_c^{max}$  (Figure 3.33a). By increasing the thickness variability CV, the average compressive strength (computed on 5 samples) decreases almost linearly up to a value of 1.864 MPa corresponding to the case of CV=25% (Figure 3.33b-d); in this case the  $\sigma_c$  vs  $\delta/h$  curves for the five samples appear very different each other. In detail, from Figure 3.33e, where the cases CV=10% and CV=25% are superposed, it appears that a significant variation of  $t$  reduces the compressive strength values, the slope of nonlinear elastic regime, and the residual stress after collapse.



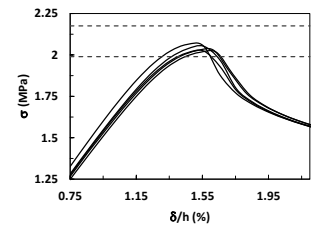
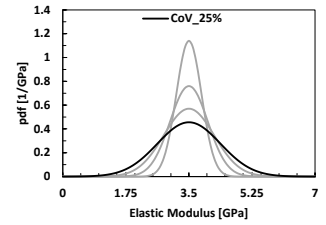
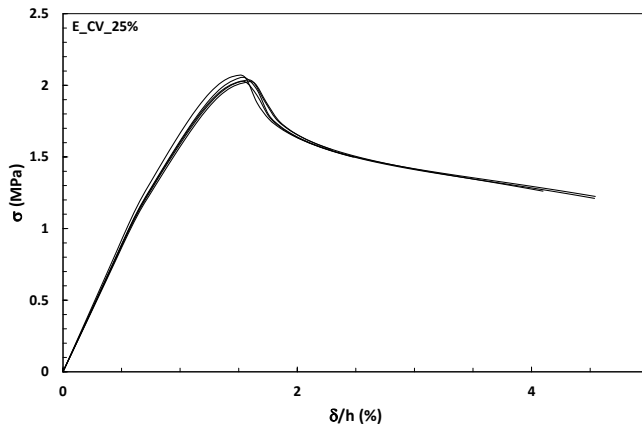
a)



b)



c)



d)

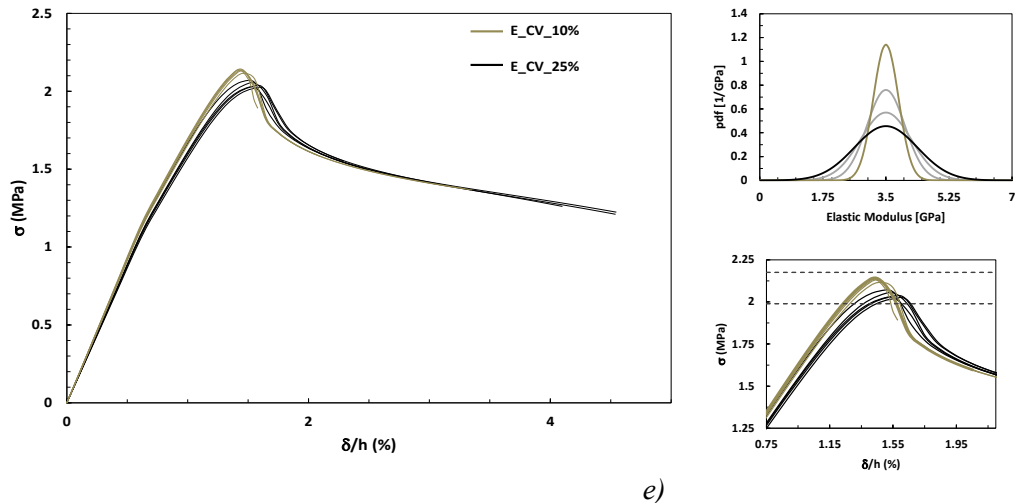
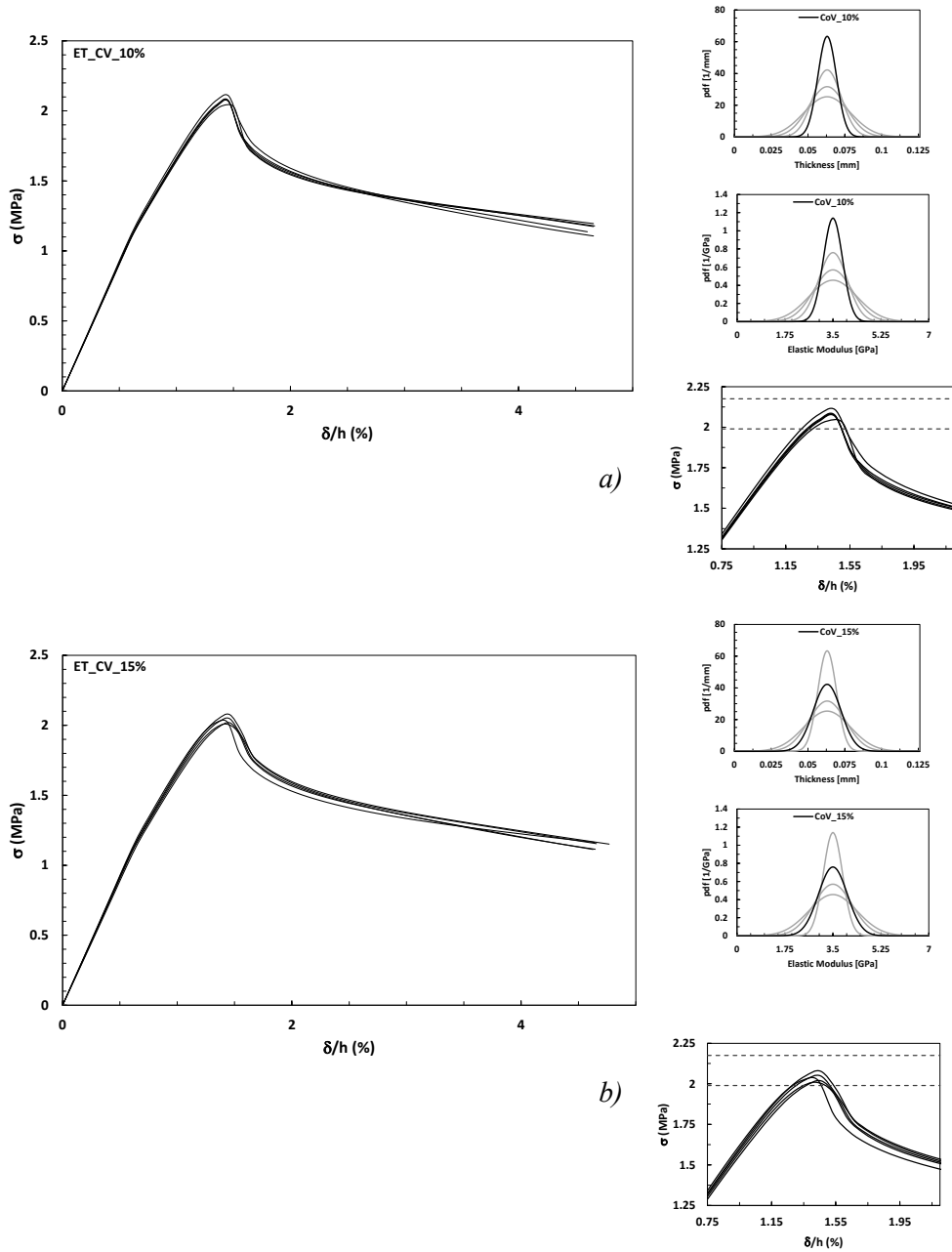


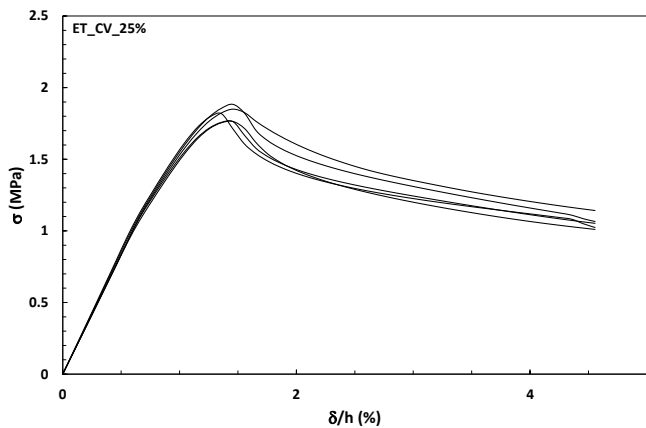
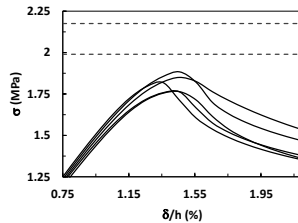
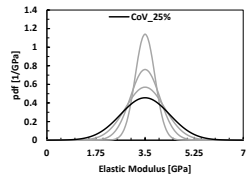
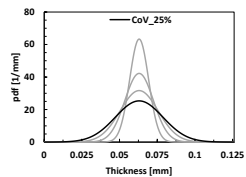
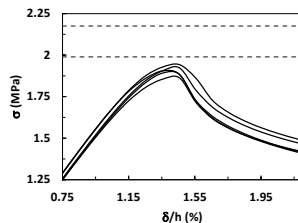
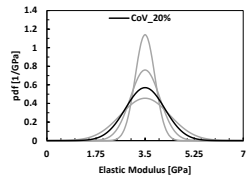
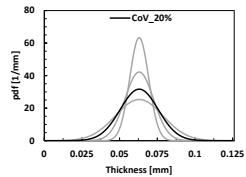
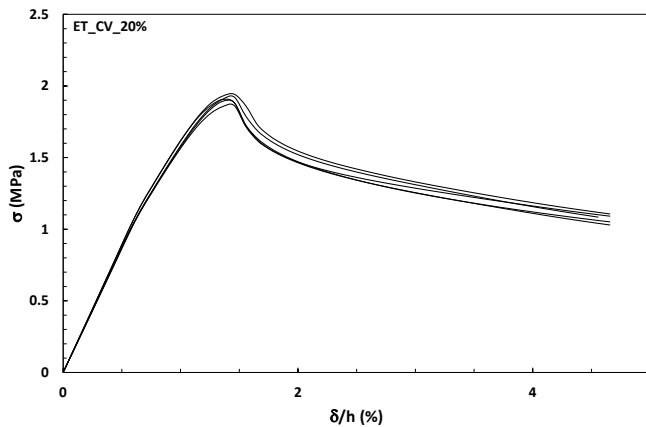
**Figure 3.34: Effect of Young's modulus variability on  $\sigma_c$  vs  $\delta/h$  curves for a) CV=10%, b) CV=15%, c) CV=20%, d) CV=25% with the corresponding PDF and focusing on the peak of compressive strength; e) superposition of CV=10% and CV=25% cases.**

A Young's modulus variability gives rise to a compressive response that is very similar among the five samples and for all the CV adopted within the analysis. In particular, when the adopted Young's modulus has a lower variability with respect to the initial one (i.e., 3.50 GPa), the five curves appear well superposed with an average compressive stress equal to 2.135 MPa that is slightly overestimated with respect to the average experimental one, but still within the experimental range defined by  $\sigma_c^{min}$ ,  $\sigma_c^{max}$  (Figure 3.34b and Figure 3.34c). By increasing the CV of Young's modulus (Figure 3.34c and Figure 3.34d), the average compressive strength decreases almost linearly up to the value of 2.036 MPa in case of CV=25% that is still characterized by small statistical variation. The nonlinear elastic regime is stiffer in case of little variability whereas the post peak behavior is not affected by the different CV (see Figure 3.34e).

When both foil thickness and Young's modulus variability are used to model imperfection in the honeycomb cell, the average compressive strength decreases in a nonlinear manner from 2.072 MPa to 1.815 MPa for CV=10% to CV=25%, respectively (see Figure 3.35a-e). From Figure 3.36a it can be highlighted that, when the variability in the material properties is high, the effect of both types of imperfections is amplified and a greater loss in the compressive load carrying capacity is experienced (with respect to the previous cases). Moreover, in case of CV = 25%,

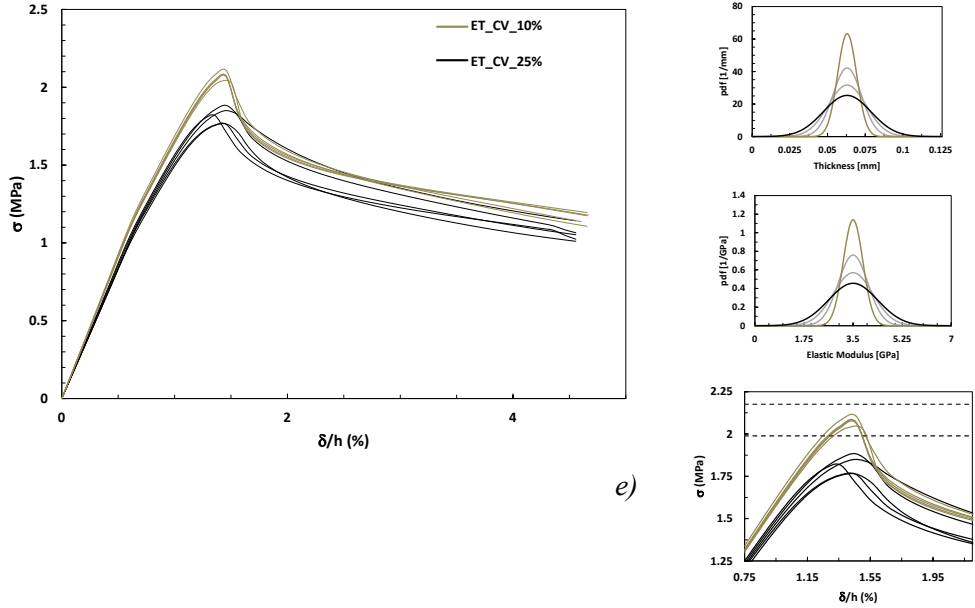
the  $\sigma$  vs  $\delta/h$  curves show significant deviations for the five samples in terms of compressive strength and post peak behavior with a significant lower stiffness in the nonlinear elastic regime with respect to the case of CV=10%.





c)

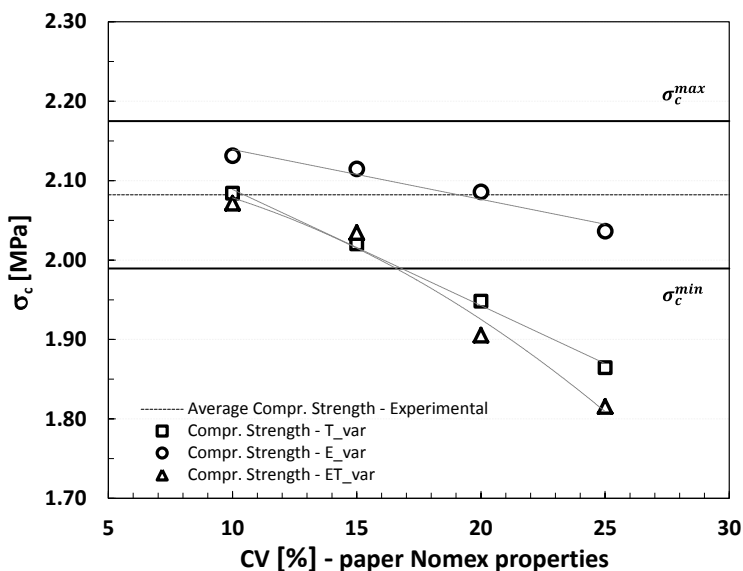
d)



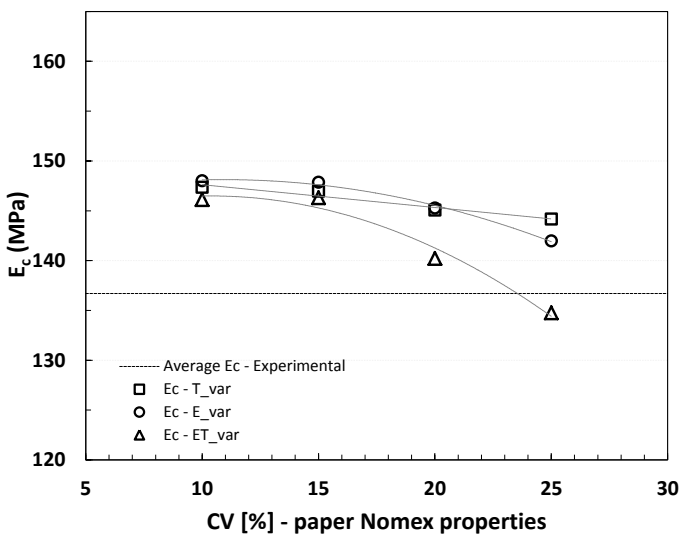
**Figure 3.35: Effect of both thickness and Young’s modulus variability on  $\sigma_c$  vs  $\delta/h$  curves for a) CV=10%, b) CV=15%, c) CV=20%, d) CV=25% with the corresponding PDF and focusing on the peak of compressive strength; e) superposition of CV=10% and CV=25% cases.**

Figure 3.36 summarizes the results of the analysis in terms of average compressive strength  $\sigma_c$  (a), and average Young’s modulus  $E_c$  (b). The increase of CV on thickness variability and Young’s modulus triggers a linear decrease of the average compressive strength that is much more noticeable in case of thickness variability. In fact, in the range of CV=10 and 25%, the compressive strength varies between 2.03 and 2.13 MPa when imperfection on Young’s modulus are included in the model; on the contrary, the compressive strength decreases up to 1.86 MPa when an high level of statistical deviation is considered for the thickness variability. The combination of both types of imperfections gives rise to a nonlinear decrease of compressive strength with increasing CV, with a sensible underestimation in case of CV=25%, i.e.,  $\sigma_c = 1.81$  MPa that is out of the experimental limits. It is interesting to notice (Figure 3.36c) that only thickness variability leads to a wide range of statistical deviation on the computed compressive strength: between 1% and 4% values of CV. On the contrary, the Young’s modulus variability of the Nomex paper produces samples very close to each other in

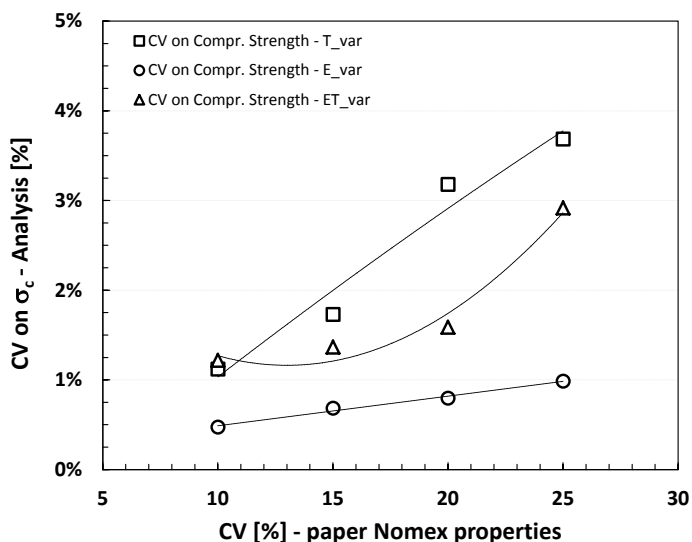
terms of compressive behavior, with a CV on the computed compressive strength always less than 1%.



a)



b)



c)

**Figure 3.36:** a) average computed compressive strength vs CV adopted for Nomex properties; b) average computed Young's modulus vs CV adopted for Nomex properties; c) CV on computed compressive strength vs CV adopted for Nomex properties.

The compressive elastic modulus of the honeycomb structure (Figure 3.36b) appears slightly dependent on the CV when thickness and Young's modulus imperfections are individually implemented in the cell model. However, in these cases the computed value of compressive elastic modulus of the honeycomb structure is overestimated compared to the experimental one. On the contrary, the combination of the two types of imperfections sensibly affects the compressive elastic modulus, especially in case of high CV.

### 3.4.3. Numerical results: Crushing

Honeycomb crushing regime takes place after reaching the maximum compressive load. This stage is characterized by severe local bending and contact between the folding walls. Thus, in contrast to the prebuckling and initial postbuckling calculations illustrated in Section 3.3.1, crushing was performed using ABAQUS/Explicit due to the computational efficiency that it affords, especially for contact issues. The numerical analysis involved the characteristic cell shown in Figure 3.27d with a mesh of 5850 S4 elements and the periodicity conditions described in section 3.3.1. For this

analysis, the cell configuration corresponding to CV=15% of thickness variation was chosen. The bottom edges were fixed whereas the top nodes were prescribed a downward displacement of 12 mm in the Z(3)-direction. Since crushing involves contact between folds of adjacent cell walls as well as self-contact, both sides of the cell walls were considered for self-contact in ABAQUS. The introduction of contact surfaces, along with the wide number of different elements with different properties, provides major contribution to the total computation time of the simulation.

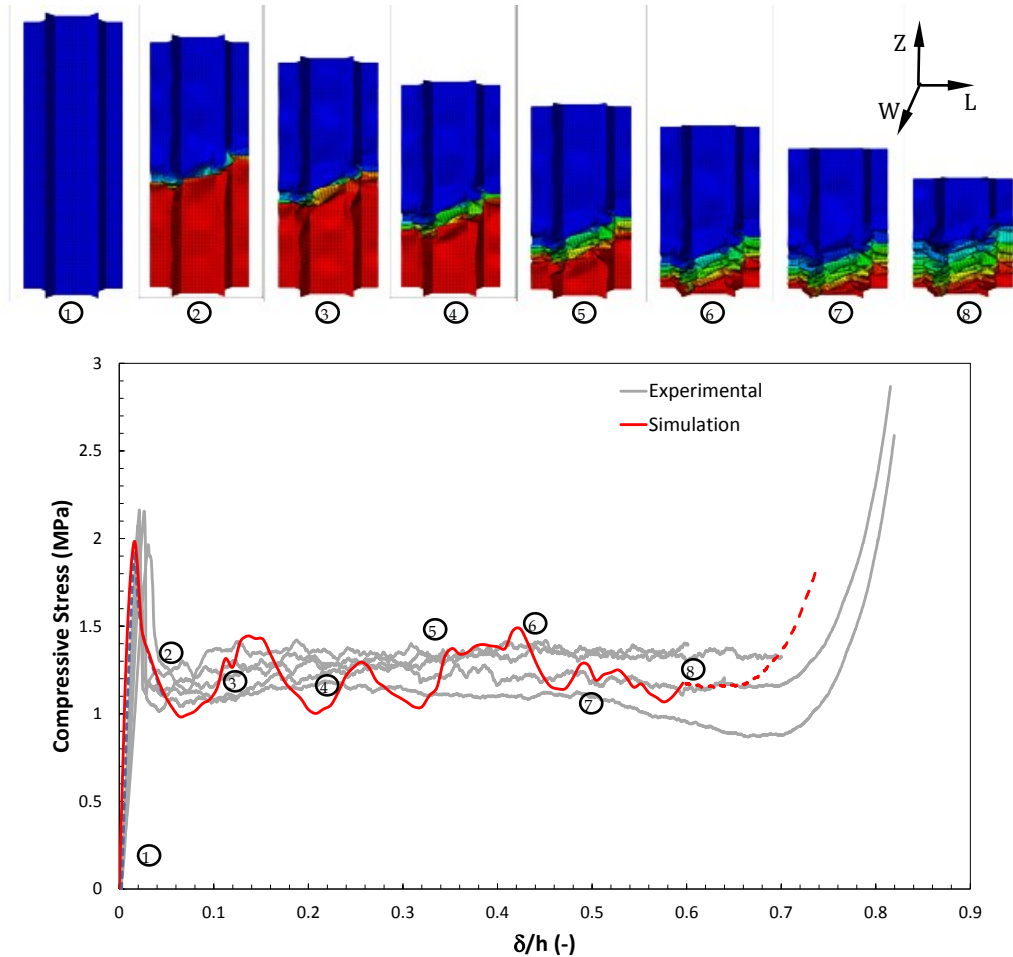


**Figure 3.37: Full Stress-Strain relationship for Nomex honeycomb material – experimental (grey) vs simulation (red) results.**

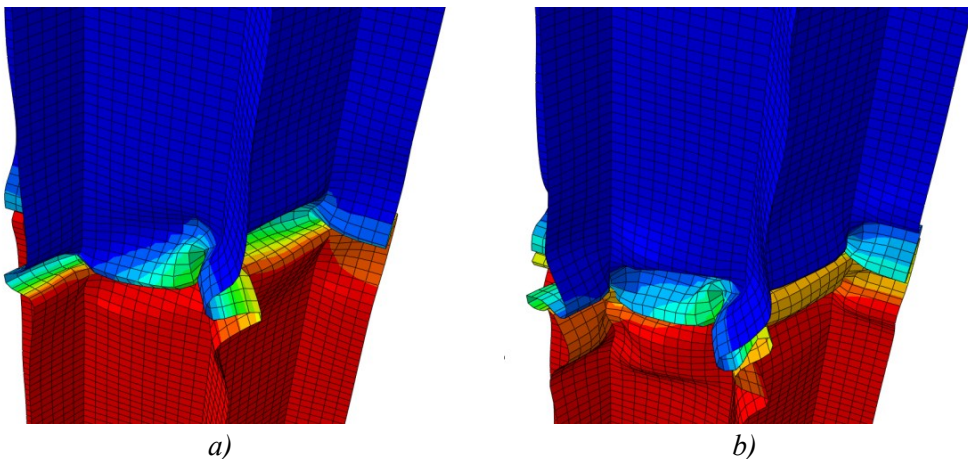
Figure 3.37 shows the simulated crushing response (red line) along with four typical experimental responses (grey lines). The same figure reports the views of the

initial and a set of 7 deformed configurations of the unit cell corresponding to the numbered bullets marked on the graph.

It should be pointed out that in this simulation no initial shape imperfection (e.g. corresponding to the first buckling mode) was adopted, but only thickness variability with CV=15% was considered. Within this approach, as specified in section 3.4.2, the initial mode of collapse localizes in correspondence of a random point along the total height of the cell. Configuration 2, corresponds to the first descending part of the compressive response, showing localized deformation approximately about the mid-height of the cell; this is associated with the initial stages of collapse of the cell.

The collapse continues with a folding mechanism that follows the local buckling shape; in this stage the compressive load reduces until a stress value of approximately 1 MPa. In the region of configuration 2, contact between folds in adjacent walls develops for the first time Figure 3.38a; this is reflected with the lowest value of compressive stress in the  $\sigma_c - \delta h$  curve after the initial cell collapse. After the stabilization of the self-contact in the folds, the compressive load starts an upward trend due to the resistance provided by the bent wall and the contact mechanism. The increasing load terminates when the intact part of the upper half of the cell gets a new destabilization (local collapse) leading to a second fold initiation.

The folding mechanism continues with the same increasing/decreasing trend forming a total of six folds before densification. In fact, at higher strain, the opposing cell walls are folded on each other and further deformation compresses the resulting packed configuration Figure 3.38d. This final configuration approximately agrees with the experiment one, for which, a slightly higher number of folds appeared at the end of the test.



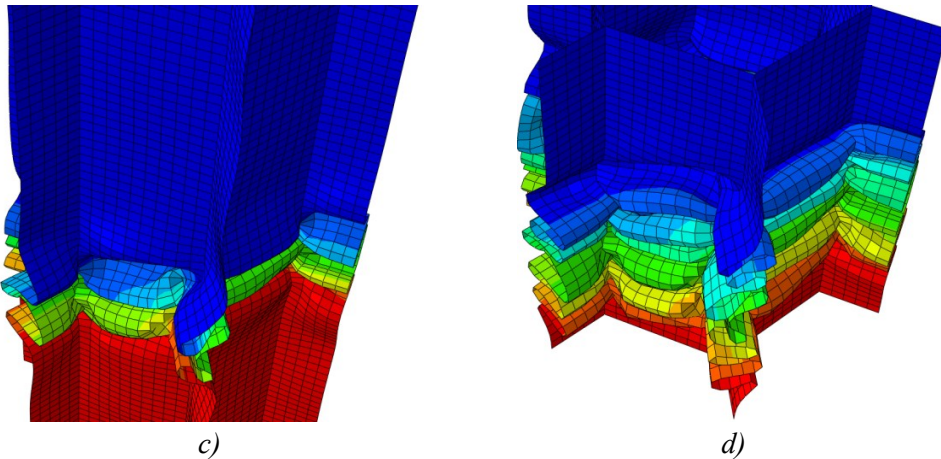


**Figure 3.38: Folding mechanism during Nomex crushing regime; a) first fold (point 2), b) first contact between walls (point 3), c) double contact between walls (point 5), d) final deformed shape.**

Globally, the simulated crushing response reproduces reasonably the experimental one, with an average crushing stress of 1.20 MPa. It should be pointed out that the pronounced flattening behavior exhibited by the simulated cell throughout the crushing regime, somewhat disagrees with the nearly constant stress found in the experimental test. This can be attributed to the elastic-plastic constitutive law assigned to the cell wall material that is most probably more brittle in the actual case. In fact, plasticized walls provided a stiffer contribution to the compressive load (due to the plastic stress capability) leading to a higher peak before each progressive buckling collapse. Finally, it should be specified that in the experiments some debonding of double walls was observed at this stage. Wall separation was precluded in this model and this omission is expected to introduce some minor differences between the calculated and measured responses.

### **3.5. Closing remarks**

In the present activity, a statistics-based method for virtual testing of cellular sandwich core structures using FE simulations has been conducted. An hexagonal honeycomb core made of Nomex material has been investigated in order to cover some important aspects related to its out-of-plane compressive response, such as linear elastic response, onset of instability, collapse limit (and its localization and progressive folding). The proposed method deals with the random sampling of the elements of the

mesh in a FE numerical analysis on the basis of a normal distribution for thickness and Young's modulus of the cell wall material. This allowed to incorporate material imperfections in the model and evaluate the influence of imperfection variability on the compressive response of Nomex honeycomb cells. All the simulations have been run through both ABAQUS/Standard and ABAQUS/Explicit. The analysis have revealed that the compressive behavior of the Nomex honeycomb is more sensitive to thickness imperfections rather than Young's modulus variation: a large CV on wall thickness tends to underestimate the compressive strength of the honeycomb if compared to the experimental values, whereas the Young's modulus variation (within all the adopted CV) gives rise to compressive strength values always in the range of the experimental ones, even though the statistical variation on the numerical results is very limited. In general, when both the imperfections are included in the model in the range of CV=10-15% a very good correlation to experimental results can be achieved with respect to compressive stress–strain relationships. Moreover, the detailed representation of the cell also allows for a deep investigation of the cell wall deformation patterns and failure modes to get a better understanding of the structural behavior, which can be expensive and sometimes difficult to study using only experimental observations. The present method can be potentially useful for the complete characterization of the mechanical behavior of honeycomb structures accounting for the influence of physical imperfections, especially when experimental characterization is not straightforward, such as in the case of tension and shear loading in both in-plane and out-of- plane directions.

Finally, we would like to emphasize that the approach could also be successfully extended and applied to other mechanical problems where different sources of imperfections play a major role, as well as when experimental testing is difficult and a virtual testing analysis is desirable.

### ***References***

1. Sandwich structures 7: advancing with sandwich structures and materials. In: Proceedings of the 7th international conference on sandwich structures. Aalborg, Denmark: Aalborg University, 2005.
2. Vinson, J.R., *Behavior of Sandwich Structures*. Crc Press Inc, University of Delaware, Newark, USA, 1999.

3. BDM-6700, *Introduction to sandwich structures*. Boeing design manual 01 APR 1989.
4. S. Mistou, M.S., M. Karama, *Experimental and Numerical Simulations of the Static and Dynamic Behavior of Sandwich Plates*. European Congress on Computational Methods in Applied Sciences and Engineering, Barcelona, Spain, 2000.
5. Foo, C.C., G.B. Chai, and L.K. Seah, *Mechanical properties of Nomex material and Nomex honeycomb structure*. *Composite Structures*, 2007. **80**(4): p. 588-594.
6. Allegri, G., U. Lecci, M. Marchetti, and F. Poscente, *FEM simulation of the mechanical behaviour of sandwich materials for aerospace structures*. *Experimental Techniques and Design in Composite Materials* 5, 2002. **221-2**: p. 209-220.
7. Bitzer, T., *Honeycomb technology, materials, design, manufacturing, applications and testing*. Chapman & Hall, ISBN-13: 9780412540509, 1997.
8. Heimbs, S., *Virtual testing of sandwich core structures using dynamic finite element simulations*. *Computational Materials Science*, 2009. **45**(2): p. 205-216.
9. Drechsler, K. and R. Kehrle, *Manufacturing of Folded Core-Structures for Technical Applications*. 25th International SAMPE Europe Conference, Paris, 2004: p. 508-513.
10. Nguyen, M.Q., S.S. Jacombs, R.S. Thomson, D. Hachenberg, and M.L. Scott, *Simulation of impact on sandwich structures*. *Composite Structures*, 2005. **67**(2): p. 217-227.
11. Hahnel, F., K. Wolf, A. Hauffe, K.A. Alekseev, and I.M. Zakirov, *Wedge-shaped folded sandwich cores for aircraft applications: from design and manufacturing process to experimental structure validation*. *CEAS Aeronautic Journal*, 2011. **2**: p. 203-212.
12. Aktay, L., A.F. Johnson, and B.H. Kroplin, *Numerical modelling of honeycomb core crush behaviour*. *Engineering Fracture Mechanics*, 2008. **75**(9): p. 2616-2630.
13. Aktay, L., A.F. Johnson, and M. Holzapfel, *Prediction of impact damage on sandwich composite panels*. *Computational Materials Science*, 2005. **32**(3-4): p. 252-260.

14. Fatt, M.S.H. and K.S. Park, *Perforation of honeycomb sandwich plates by projectiles*. Composites Part a-Applied Science and Manufacturing, 2000. **31**(8): p. 889-899.
15. Aminanda, Y., B. Castanie, J.J. Barrau, and P. Thevenet, *Experimental analysis and modeling of the crushing of honeycomb cores*. Applied Composite Materials, 2005. **12**(3-4): p. 213-227.
16. Castanie, B., C. Bouvet, Y. Aminanda, J.J. Barrau, and P. Thevenet, *Modelling of low-energy/low-velocity impact on Nomex honeycomb sandwich structures with metallic skins*. International Journal of Impact Engineering, 2008. **35**(7): p. 620-634.
17. Yamashita, M. and M. Gotoh, *Impact behavior of honeycomb structures with various cell specifications - numerical simulation and experiment*. International Journal of Impact Engineering, 2005. **32**(1-4): p. 618-630.
18. Hohe, J. and W. Becker, *Effective stress-strain relations for two-dimensional cellular sandwich cores: Homogenization, material models, and properties*. Applied Mechanics Reviews, 2002. **55**(1): p. 61.
19. Allen, H., *Analysis and design of structural sandwich panels*. Pergamon Press, 1969.
20. Petras, A. and M.P.F. Sutcliffe, *Failure mode maps for honeycomb sandwich panels*. Composite Structures, 1999. **44**(4): p. 237-252.
21. Zhang, J. and M.F. Ashby, *The out-of-Plane Properties of Honeycombs*. International Journal of Mechanical Sciences, 1992. **34**(6): p. 475-&.
22. Gibson, L. and M. Ashby, *Cellular Solids*. Cambridge University Press, 1999.
23. Wierzbicki, T., *Crushing analysis of metal honeycombs*. International Journal of Impact Engineering 1983. **1**: p. 157-174.
24. Combescure, A., *Influence of initial imperfections on the collapse of thin walled structures*. Advanced methods in materials processing defects. Edited by Predeleanu, Gilormini, Elsevier.
25. Z. Bazant, L.C., *Stability of structures: elastic, inelastic, fracture and damage theories*. New York: Oxford University Press [ISBN:0- 486-42568-1], 1991: p. 1011p.

26. Baranger, E., P.A. Guidault, and C. Cluzel, *Numerical modeling of the geometrical defects of an origami-like sandwich core*. Composite Structures, 2011. **93**(10): p. 2504-2510.
27. Yang, M.Y., J.S. Huang, and J.W. Hu, *Elastic buckling of hexagonal honeycombs with dual imperfections*. Composite Structures, 2008. **82**(3): p. 326-335.
28. Li, K., X.L. Gao, and J. Wang, *Dynamic crushing behavior of honeycomb structures with irregular cell shapes and non-uniform cell wall thickness*. International Journal of Solids and Structures, 2007. **44**(14-15): p. 5003-5026.
29. Simone, A.E. and L.J. Gibson, *The effects of cell face curvature and corrugations on the stiffness and strength of metallic foams*. Acta Materialia, 1998. **46**(11): p. 3929-3935.
30. Kress, G. and M. Winkler, *Honeycomb sandwich residual stress deformation pattern*. Composite Structures, 2009. **89**(2): p. 294-302.
31. Markaki, A.E. and T.W. Clyne, *The effect of cell wall microstructure on the deformation and fracture of aluminium-based foams*. Acta Materialia, 2001. **49**(9): p. 1677-1686.
32. Fan, X., *Investigation on Processing and Mechanical Properties of the Continuously Produced Thermoplastic Honeycomb*. PhD Thesis, Katholieke Universiteit Leuven, Belgium, 2006.
33. Wilbert, A., W.Y. Jang, S. Kyriakides, and J.F. Floccari, *Buckling and progressive crushing of laterally loaded honeycomb*. International Journal of Solids and Structures, 2011. **48**(5): p. 803-816.
34. Craig, K.J. and W.J. Roux, *On the investigation of shell buckling due to random geometrical imperfections implemented using Karhunen-Loeve expansions*. International Journal for Numerical Methods in Engineering, 2008. **73**(12): p. 1715-1726.
35. Xue, Z.Y. and J.W. Hutchinson, *Crush dynamics of square honeycomb sandwich cores*. International Journal for Numerical Methods in Engineering, 2006. **65**(13): p. 2221-2245.
36. HexWeb-HRH-10, *Aramid Fibre/Phenolic Honeycomb, Product Data*. Hexcell Corporation.

37. Tsujii, Y., K. Tanaka, and Y. Nishida, *Analysis of Mechanical Properties of Aramid Honeycomb Core*. Transactions of the Japan Society for Mechanical Engineers, 1995. **61**: p. 1608-1614.
38. Fischer, S., K. Drechsler, S. Kilchert, and A. Johnson, *Mechanical tests for foldcore base material properties*. Composites Part a-Applied Science and Manufacturing, 2009. **40**(12): p. 1941-1952.
39. Heimbs, S., P. Middendorf, S. Kilchert, A.F. Johnson, and M. Maier, *Experimental and numerical analysis of composite folded sandwich core structures under compression*. Applied Composite Materials, 2007. **14**(5-6): p. 363-377.
40. Giglio, M., A. Manes, and A. Gilioli, *Investigations on sandwich core properties through an experimental-numerical approach*. Composites Part B-Engineering, 2012. **43**(2): p. 361-374.

## **Chapter IV**

# ***IMPACT BEHAVIOR OF HONEYCOMB SANDWICH STRUCTURES***

### **4.1. Introduction to framework**

Composite sandwich structures are widely used in the high-performance applications, especially where weight reduction is one of the most desirable design objectives. However, structural sandwich components have low resistance to out-of-plane impact due to the thin outer composite skins and the highly deformable cores, which make them vulnerable to transverse impact phenomena. Impact damage occurring in composite sandwich structures affects both skins and core materials. The higher scale level of the impact damage analysis is the sandwich assembly which includes all constituent sandwich materials. In order to evaluate the overall impact sandwich behavior, the multiscale approach has to involve the detailed (static and dynamic) modeling of both skin and core material. The activity presented in *Chapter IV* deals with a numerical strategy aimed at simulating the dynamic behavior of Nomex core sandwich structures combined with E-glass phenolic facesheet under impact load, through the finite element code LS-DYNA. The honeycomb core structure and the composite skins are modeled by means of solid and shell elements, respectively. It is pointed out that, unlike previous modeling strategy, presented in *Chapter III*, in this case the honeycomb has not been modeled up to the cell scale, since it would have led to large computational efforts. The adopted procedure is based on a multiscale virtual testing approach by means of the progressive validation of the composite facesheet and orthotropic honeycomb material models on the basis of experimental tests, ranging

from coupon tests (for E-glass phenolic skins and Nomex core material) to sandwich assembly tests, as illustrated in Figure 4.39.

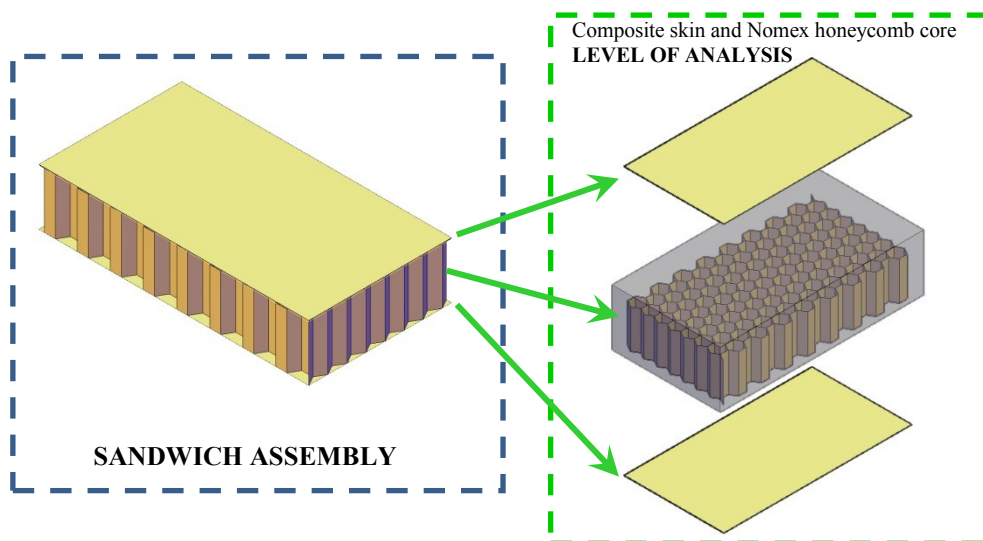


**Figure 4.39: Scheme of multiscale damage analysis conducted on Honeycomb sandwich structure.**

This allows to verify the capability of the model to take into account the main damage mechanisms taking place during penetration. Finally, the dynamic impact behavior is modeled on this basis and validated through different impact conditions, emphasizing important issues on the strain rate sensitiveness affecting the investigated materials. The main outcomes in terms of force displacement curves, energy absorption and damage mechanisms are assessed and compared to the experimental results.

## 4.2. Literature overview: impact on sandwich structures

Due to their advantageous specific mechanical properties (in terms of stiffness-to-weight ratio) and corrosion resistance, composite sandwich structures are becoming an attractive alternative to metals in many different engineering applications, especially for mass transport applications where weight reduction is one of the most important design parameter. Although the peculiar morphology of sandwich structures offer very attractive properties, their application is often restricted by their vulnerability to transverse impact [1].

Structural sandwich components generally exhibit a low resistance to out-of-plane impact due to the thin outer composite skins and the highly deformable cores. When

localized transverse loading is applied to a sandwich structure, the facesheet locally deflects up to failure and the core crushes, leading to a damage ranging from permanent indentation to complete penetration [1, 2]. The loss of load carrying capability they suffer as a consequence of impact events can be light or significantly injurious depending on the failure mechanisms which irreversibly have taken place. Hence in order to reliably predict the structural behavior and guarantee structural safety of composite sandwich structures, a deep understanding of the impact behavior (e.g. impact and penetration damage varying in the range of low to high velocities and impacting masses) has become essential. Available literature offers a wide range of studies on low velocity/energy impact response of sandwich structures in terms of experimental research, analytical formulations and numerical implementations [3-8].

Depending on the initial impact energy, impacts can induce damage of different entity to the skins, the core material, and the core-facing interface. However, the impact performance and the damage extent of sandwich composites depend on several factors (e.g. skin and core materials, geometries, boundary conditions [3]). Furthermore, the different damage mechanisms may take place individually or interact. In the case of low-energy impacts, the response of sandwich panels may be governed by bending and little damage occurs if the kinetic energy of the impacting object is absorbed elastically by the panel. For high-energy impacts, a failure condition is reached when local contact stress exceeds local strength triggering a damage sequence given by the laminate bending failure, core/skin interface delamination, core compression failure and its plastic deformation up to complete penetration [1]. Core deformation and failure represent therefore crucial factors for the energy absorption capability and impact behavior of sandwich panels [5].

Experimental and analytical studies have been conducted to understand the mechanical response of honeycomb sandwich structures composed by different skins and core materials under various loadings [6-10]. Numerical methodologies based on finite element (FE) approach represent a standard tool in the development process of composite and sandwich application industries allowing time and test-prototyping cost savings. The main source of complexity associated with FE impact modelling of sandwich structures is related to the adequate material constitutive models, proper prediction of the damage level in each sandwich constituent, and the definition of interaction laws for various damage mechanisms. Several strategies have been developed in the FE simulation environment for this class of structural materials. A combination of testing and numerical analysis is provided by the multiscale approach [11], where various levels of structural complexity are progressively validated

numerically through associated experimental tests up to a complete prediction of the full scale product behavior. Especially for cellular based, folded core materials, virtual testing FE strategies are often developed. According to this approach, specific material properties of cellular cores with complex geometries are achieved with detailed FE simulation models on a parametric basis, overcoming the lack of experimental databases [12, 13].

Furthermore, the design of sandwich panels for high dynamic loads requires to have information about the sandwich dynamic structural behavior and in particular on the influence of loading rate on the material properties. In case of high loading rate an increase in material stiffness and strength compared to the static behavior may occur. When this effect is neglected, dynamic FE simulations based on static material data often disagree with experimental dynamic results and therefore attention should be paid when design approaches are based on static data. Strain rate effects can affect both skins and core material. For former material types, especially when rate sensitive materials are used, a dynamic increase factor (DIF) may be characterized [14-16]. Concerning core materials, strain rate effects on axial behavior of both aluminum [17, 18] and Nomex [19, 20] honeycomb structures have been experimentally investigated through dynamic compressive tests performed with different techniques (i.e. drop weight, gas gun, and split Hopkinson bar). These results reported that dynamic loading leads to a marginal increase of the initial stiffness and peak compressive strength, a significant increase of the crush strength and a reduction of the deformation for the fully compacted final region.

### **4.3. Materials and methods**

In the present study the impact behavior of phenolic-impregnated sandwich structures has been investigated. The composite skins were obtained from pre-impregnated satin-weave E-glass fiber reinforced phenolic resin skins with a cured ply thickness of 0.25 mm. The sandwich core is made of 48 kg/m<sup>3</sup> Nomex hexagonal honeycomb with a nominal cell size of 3.18 mm and made of phenolic resin-impregnated aramid paper. Since the skins are pre-impregnated, there is no additional adhesive used to bond the skins to the core. The materials were laminated in an autoclave at a temperature of 135°C, a vacuum pressure of 2.5 bar and a curing time of 90 min. All the sandwich specimens considered in the following experimental activities have been assembled with the *L* direction of the honeycomb core (Figure 4.40) along

the primary direction and different configurations (in terms of size and thickness) for skins and Nomex core are handled in the present study. Different experimental tests were performed in order to characterize the static and dynamic behavior of the examined sandwich structures. The results are used to get the basic information to build up the numerical sandwich model and to validate it. Further details about the experimental activity, which are not presented hereafter, are available in [21]. The experimental tests concern the sandwich constituent level (in plane mechanical characterization of the phenolic skins, compressive behavior of Nomex core) and the sandwich assembly (four point bending tests, indentation tests).

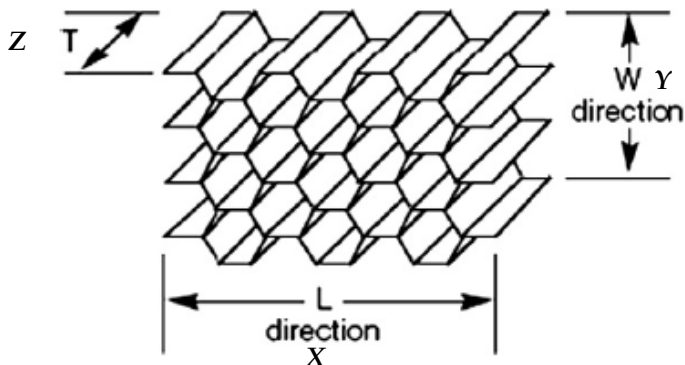


**Figure 4.40: Shape geometry of hexagonal honeycomb core.**

The numerical simulation of these tests allows to calibrate the constitutive models adopted for the sandwich materials at different scale level and to validate the capability of the model to predict the occurrence of damage mechanisms. The dynamic impact behavior is finally investigated through the simulation of the drop weight tests performed at different initial impact conditions. In the following sections, first the characteristics of the adopted material models are presented and afterwards, the details of the experimental tests and the numerical models are illustrated for each type of test.

#### **4.4. Sandwich material modeling**

A finite element model has been built up through the commercial FE code LS DYNA (Version 971) in order to model the sandwich impact behavior. The FE sandwich model consists of two different sandwich materials including solids and shell elements. Particularly, in order to save computational time and avoid instabilities (due

to large deformations) homogeneous equivalent solid elements have been adopted for the Nomex honeycomb core, shell elements for the phenolic facesheets and solid elements for the rigid steel impactor. A failure based nodal connection has been used to model the bonding between the Nomex core and the phenolic facesheets. The material models adopted for the sandwich materials are described in the following sections.

#### **4.4.1. E-Glass phenolic skins**

In order to adequately model the complete process of penetration in a sandwich structure, the energy absorbing capability and the damage behavior of both skin and core material need to be known. During impact on sandwich structures, one of the significant mode of absorbing energy is given by the perforations of the composite material skins (upper and lower) where a set of intralaminar, interlaminar failure modes can take place with increasing the impact energy, such as matrix cracking, delamination between adjacent plies, fiber breakage, ply failure etc. Therefore, a reliable model for the composite skin is required to study in depth the perforation stages. Since the onset of damage in a composite does not usually lead to ultimate failure, the ability of FE models in simulating an impact event is critically dependent on its capacity to represent the sequence of damage modes, the conditions for delamination propagation, the stiffness and strength degradation associated with the various damage states, as well as the residual composite properties. FE simulation works available in the literature are based on different theoretical formulations including failure criteria, plasticity theory, fracture mechanics, and damage mechanics. In the available commercial FE codes, several constitutive composite material models are adopted including shell and solid formulations. Generally they comprise progressive failure and continuum damage mechanics (CDM) based approaches [22, 23]. In both cases the composite behavior is modeled as orthotropic linear elastic materials until a certain onset given by a criterion-based failure surface. Different failure criteria can be implemented in the numerical models for laminated composites, by means of strength, strain or mixed based criteria such as Tsai-Wu, Hashin, and Chang–Chang [23]. Beyond failure, elastic properties are degraded according to degradation laws given by the material model.

In the present study, the composite skins, made by phenolic impregnated glass laminates, are modeled using shell elements combined with a continuum damage mechanics framework. In particular, the

MAT\_LAMINATE\_COMPOSITE\_FABRIC\_058 material model was selected in the LS DYNA Code which implements a CDM model derived from the constitutive theory of anisotropic damage introduced by Matzenmiller–Lubliner–Taylor (MLT) [22]. This model allows to describe the anisotropic mechanical properties and the progressive failure mechanisms affecting the composite skins during the impact event.

In detail, the composite elastic properties are described by four independent elastic constants,  $E_{11}$ ,  $E_{22}$ ,  $G_{12}$  and  $\nu_{12}$  (where  $E$ ,  $G$ ,  $\nu$ , stand for Young’s modulus, shear modulus and Poisson’s modulus, respectively), defined in the lamina plane, where the subscript 1 and 2 denotes parallel and transverse alignment with the fiber direction respectively. A damage level is related to the degraded elastic properties of the material, depending on the particular damage mechanism (fiber breakage, fiber microbuckling, matrix cracking, etc.). In the present model, three nonnegative internal variables are assumed to describe the evolution of the damage state caused by different failure mechanisms which lead to a progressive degradation of the material stiffness. In particular, five failure criteria for the composite material are used: tensile and compressive failure in the two normal directions, as well as in-plane shear failure; the corresponding damage is quantified by three damage variable ( $\omega_1$ ,  $\omega_2$  and  $\omega_{12}$ , where the subscript 1 and 2 denotes parallel and transverse alignment with the fiber direction respectively). The damage parameters  $\omega$  vary from 0.0 to 1.0 values, corresponding to an undamaged state to a completely damaged state respectively. The in plane stress–strain constitutive law for a damaged material is described as follow:

$$\begin{bmatrix} \sigma_{11} \\ \sigma_{22} \\ \tau_{12} \end{bmatrix} = \frac{1}{D} \cdot \begin{bmatrix} (1 - \omega_{11})E_{11} & (1 - \omega_{11})(1 - \omega_{21})\nu_{21}E_{22} & 0 \\ (1 - \omega_{11})(1 - \omega_{22})\nu_{12}E_{11} & (1 - \omega_{22})E_{22} & 0 \\ 0 & 0 & (1 - \omega_{12})G_{12} \end{bmatrix} \begin{bmatrix} \varepsilon_{11} \\ \varepsilon_{22} \\ \gamma_{12} \end{bmatrix} \quad (4.1)$$

where,  $D = 1 - (1 - \omega_{11})(1 - \omega_{22})\nu_{12}\nu_{21}$

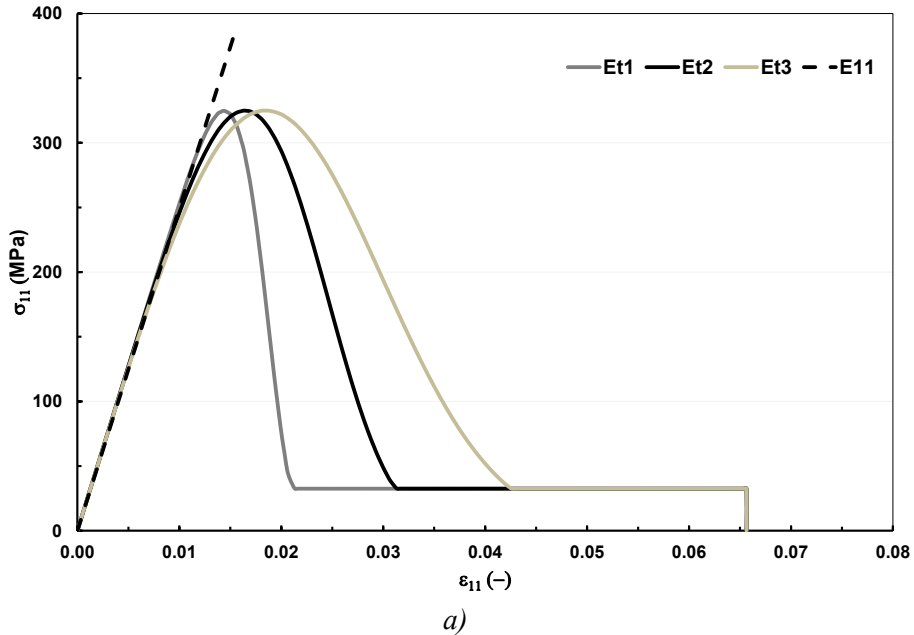
The exponential damage evolution law can be expressed by [26]:

$$\omega_i = \exp\left[-\frac{1}{m_i} e \left(\frac{\varepsilon}{\varepsilon_{fi}}\right)^{m_i}\right] \quad (4.2)$$

where the index  $i$  represents tension and compression in 1 and 2 direction, and shear respectively,  $\varepsilon_{fi}$  are the corresponding failure strains,  $m$  is a Weibull shape parameter and  $e$  is the Napierian logarithm base. After the onset of damage, the damage

degradation law is implemented in MAT058 through two sets of parameters  $E_iC,T,S$  and  $SLIM_iC,T,S$  (C=Compression, T=Tension, S=Shear) [27].  $E_iC,T,S$  is defined as the strain at the maximum stress response and  $SLIM_iC,T,S$  as the minimum residual stress of the damaged material up to the deletion of the element from the calculation.

Figure 4.41a represents the stress-strain responses of the adopted material model (in the uniaxial tensile loading case) whereas the corresponding evolution of the damage parameter  $\omega_l$  is given in Figure 4.41b varying the values of  $E_{iT}$  (with  $E_{iT_a} < E_{iT_b} < E_{iT_c}$ ) at a fixed value of  $SLIM_{iT}$  (i.e. 0.1).



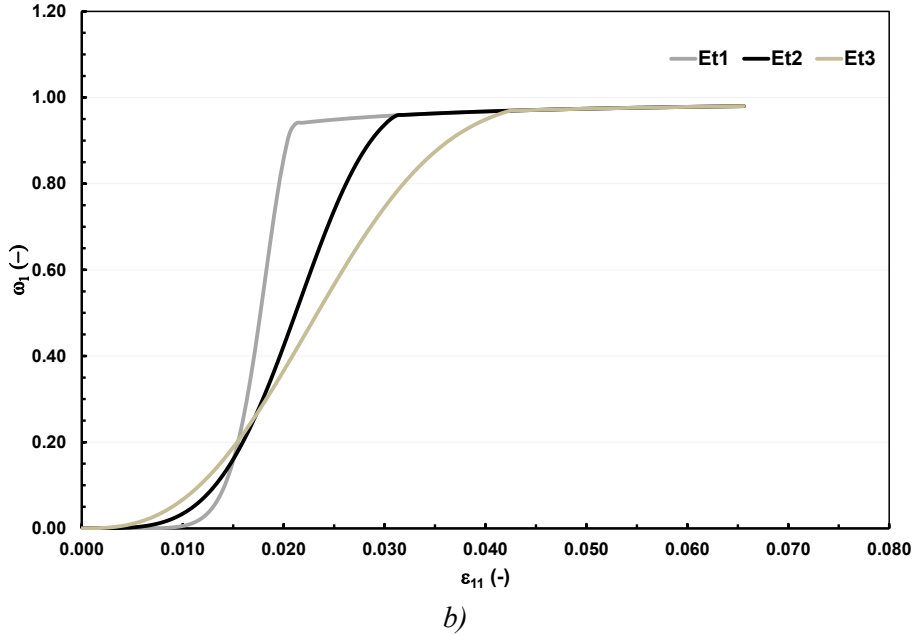


**Figure 4.41: a) Stress vs Strain relationship for single element tensile test (direction 1) for different values of  $E_i T$ , b) correspondent damage variable  $\omega_i$  vs strain relationship.**

The post-peak behavior and the corresponding damage parameter is affected by these two sets of values:  $E_i C, T, S$  controls both the onset of the loading and the slope of the post-peak response, whereas  $SLIM_i C, T, S$  sets the residual strength and the damage variable level  $\omega_i$  at which the final slope is achieved. In this way, the area underneath the stress strain constitutive curve can be modeled, representing the energy required to completely damage the finite element.

The material model allows also to choose between three different failure surfaces [23]. Among them, the uncoupled failure surface is adopted in the current study (option  $FS=-1$ ) since it appears more suitable in modeling fabric composite materials. In fact, in this case a nonlinear stress strain curve for the shear behavior can be also set within the model providing the appropriate couple  $\tau_i, \gamma_i$  representing the stress and strain limit respectively of the first slightly nonlinear part of the shear stress versus shear strain curve.

#### 4.4.2. Nomex core

The typical feature of the Nomex honeycomb structure under transverse compressive load is given by the initial linear elastic behavior up to crushing limit,

volumetric crushing and final phase of hardening to full compaction. Almost all energy absorption is done in the volumetric crushing zone and this is true also in the impact cases. However, the interaction of the core failure modes (including transverse shear) within the sandwich structure should be carefully analyzed. Different numerical modeling strategies can be used for hexagonal honeycomb cores, encompassing analytical formulations [6], or in a FE framework, by using shell models for honeycomb cells [12, 24], homogeneous equivalent solid material [5], Smoothed Particle Hydrodynamics (SPH) [25]. Sometimes these strategies are limited and/or require material properties for paper/sheet materials [10, 26] which are not easy to achieve or need the definition of numerical parameters with no physical meaning; in addition, modeling of real cells structures of honeycomb cores requires also a characterization of manufacturing defects and reduction of instabilities due to large deflections.

In the present study, the cellular Nomex honeycomb core structure is treated as a homogeneous solid material and material model MAT126 (MAT\_MODIFIED\_HONEYCOMB) has been adopted in LS DYNA in combination with co-rotational solid element type. The material model has an orthotropic nonlinear elasto-plastic constitutive behavior based on the experimentally determined stress strain curves which are defined separately for all normal and shear stresses. The components of the stress tensor are considered to be fully uncoupled ( $\nu = 0$ ). The elastic moduli, from their initial values to the fully compacted values, depend linearly on the relative volume [23]. Failure is reached when the element's stress components under load exceed the allowable values dictated by the empirical load–displacement curves. Strain rate effect can be introduced in the model as a scale factor versus effective strain rate, (which is the Euclidean norm of the deviatoric strain rate tensor), scaling all the stress curves.

## 4.5. Calibration and numerical simulation

Since composite material models adopted in a FE analysis require the definition of a set of parameters, an appropriate calibration is needed for a specific sandwich model in order to assign the unknown properties related to the definition of: (i) failure criterion; (ii) onset and propagation of damage through a degradation process; (iii) strain rate dependent materials. In the present study, the constitutive behavior of the materials involved in the sandwich impact simulation (phenolic E-glass skins and

Nomex core) is calibrated and validated through a set of experimental tests in the static case. The calibrations cover different steps going through the constituent sandwich materials to the sandwich assembly. The calibrated material properties are then used to simulate the impact behavior of a reference configuration of the examined sandwich (with 1 mm and 11 mm of thickness for phenolic skins and Nomex core respectively) and considerations on the strain rate effects are then addressed. The validation refers to both other different impact conditions and damage assessment. In the following sections, first the experimental procedure is illustrated and then the numerical model and calibration is presented for each step of the numerical analysis.

#### **4.5.1. E-Glass phenolic skins – Static tests**

In the present section, mechanical characterizations of glass phenolic skins are described in order to define the in-plane properties and validate the numerical composite model for the E-Glass phenolic skins.

In detail, uniaxial tensile tests are conducted on composite laminate to determine the following properties: longitudinal and transverse Young's moduli, Poisson's ratios, longitudinal and transverse tensile strengths, longitudinal and transverse ultimate tensile strains. A full characterization of composite material in two dimensions requires also the determination of lamina properties under in-plane shear parallel to the fibers, that is, shear modulus, shear strength, and ultimate shear strain. A full description of the test specifications and adopted procedures is reported in Table 4.4. All laminate tests were run on a 10 kN universal test frame controlled by an electronic control unit which allows monitoring the applied load and the stroke of the top cross head. Strain signals were acquired by a digital data acquisition system. For both in plane tensile and shear characterization, tests were conducted at a constant cross head velocity of 2 mm/min and three strain gauges were applied to each coupon, in order to monitor the longitudinal and transverse strain and the possible bending due to misalignment of the specimens.

Compressive mechanical parameters of selected composite skin are evaluated as 90% of the tensile values, according to the manufacture's suggestion. The compressive values have been compared by means of flexural tests on sandwich specimens in accordance with the ASTM C393 standard. Table 4.5 provides all the mechanical properties derived by the described tests.

**Table 4.4: Test methods involved in the mechanical characterization of skin materials.**

Loading Configuration	Test (ASTM Standard)	Lt [mm]	Lg [mm]	L [mm]	w [mm]	t [mm]
	Tensile test in warp direction (D3039) Stacking Sequence: All    loading direction	30	190	250	15	1
	Tensile test in fill direction (D3039) Stacking Sequence: all ⊥ loading direction	30	190	250	15	1
	In plane shear tests by tensile loading (D3518) Stacking Sequence: [+45°/-45°] <sub>2s</sub>	30	190	250	25	2

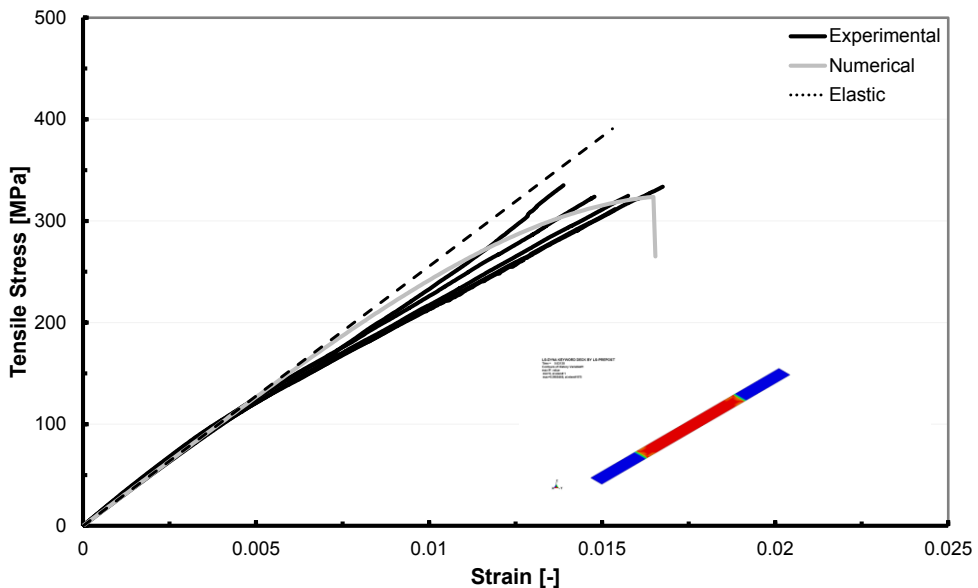
**Table 4.5: Mechanical properties of composite skins derived by experimental tests and calibrated parameters (in parenthesis)**

	E <sub>1</sub>	E <sub>2</sub>	G <sub>12</sub>	F <sub>1t</sub>	F <sub>2t</sub>	F <sub>6</sub>	ε <sup>u</sup> <sub>1t</sub>	ε <sup>u</sup> <sub>2t</sub>	γ <sup>u</sup>	v <sub>12</sub>	τ <sub>1</sub>	γ <sub>1</sub>
	[GPa]	[GPa]	[GPa]	[MPa]	[MPa]	[MPa]	[-]	[-]	[-]	[-]	[MPa]	[-]
<b>E-Glass Phenolic fabric</b>	25.54	22.97	3.41	325.77	288.21	45.30	1.53 (1.73)	1.56 (1.76)	7.67	0.15	(41.0)	(0.0285)

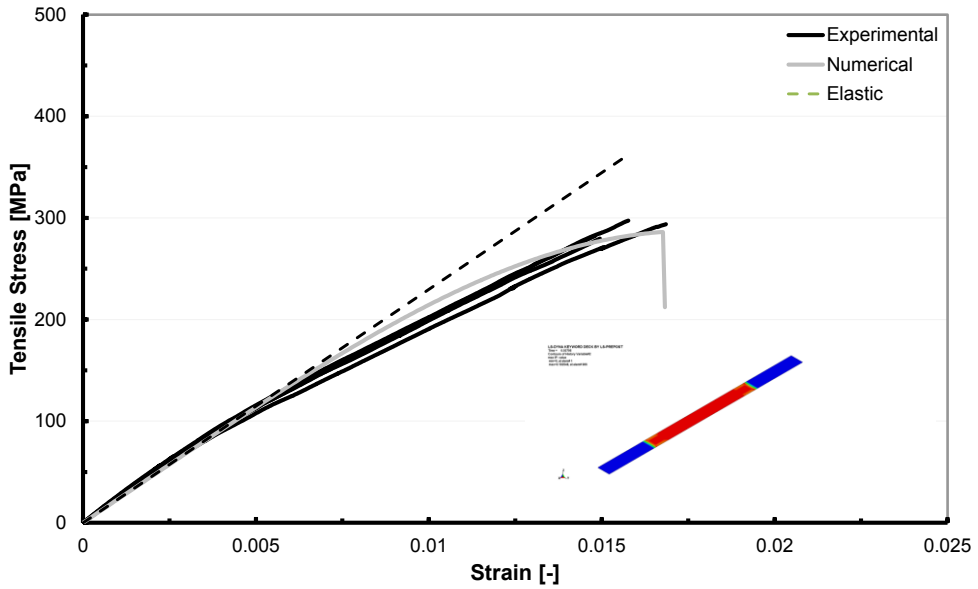
The outcomes of these experimental tests have been used to define the in plane properties of the material model adopted for the glass phenolic skin. However, in order to match the non linear tensile (in warp and weft direction) and shear behavior, exhibited by the facesheets, a calibration of the material parameters according to the constitutive material model has been needed. To do that, the static tensile and static

shear test for the phenolic laminates has been run numerically in LS DYNA explicit mode (Version 971). The numerical model of the specimens consists of one shell layer having dimensions of 250 mm(250 mm)x15 mm(25 mm) and 1 mm(2 mm) of thickness for the tensile(shear) tests. Two integration points have been assigned for each lamina (having 0.25 mm of thickness) in the composite laminates and the stacking sequence has been defined through the orientation of each integration point. The mesh size has been fixed with 2 mmx2 mm squared shell elements clumped at one and the analysis has been run with displacement control as reported in the experimental tests setup. Hence the values of  $E_iC,T,S$ ,  $SLIM_iC,T,S$ ,  $\tau_l$ ,  $\gamma_l$  for tensile and shear constitutive behavior respectively have been derived.

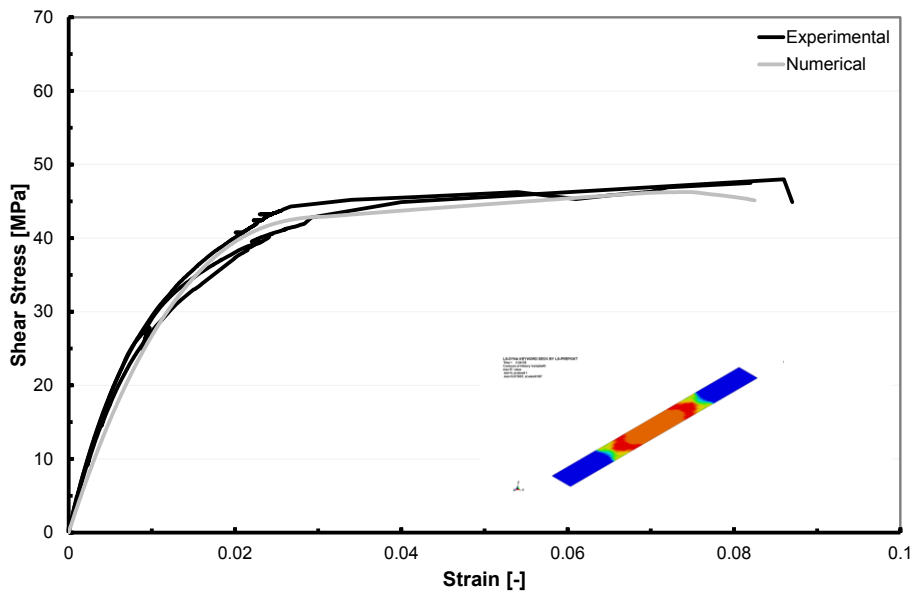
The calibration revealed that the final values for  $E_iT,S$  are slightly higher (in parenthesis in the Table 4.5) than the experimental strain to failure since the fabric behavior deviates from the pure elastic behavior (Figure 4.42). The highlighted pictures in the Figure 4.42 represent the fringe level of the corresponding damage variables for the specific loading case. The final residual value of  $E_iT,S$  has been chosen 0.1 as recommended [23, 27] and as resulted in the experiments.



a)



b)



c)

Figure 4.42: Stress vs Strain relationship for tensile a) warp, b) weft, c) in plane shear direction and corresponding damage variable,  $\omega$ , evolution ranging from 0 (blue) to 1 (red).

#### 4.5.2. Nomex Core – Static tests

The input parameters requested for the Nomex honeycomb material model concern the stress-engineering strain curves defined in all directions, including both uncompacted and compacted material properties. The compressive stress engineering strain curve was derived from the experimental test whereas the remaining curves from the data sheet and experimental results reported in [28, 29]. Out-of-plane crushing behavior of Nomex honeycomb has been investigated by flat-wise stabilized compressive tests according to ASTM C365M standard. The tests were run on 60x60x32.2 mm Nomex core coupons with a constant cross head velocity of 0.5 mm/min. Compressive modulus of the elastic phase, stabilized compressive strength and strain, crush strength, fully compacted compressive modulus and strain values at which densification occurs have been derived by these tests. In order to validate the model with the experimentally based properties, the honeycomb out-of-plane crushing test is reproduced numerically in LS-DYNA, using 6 mm x 6 mm x 4mm brick elements (Figure 4.43) without the introduction of any strain rate scale factor. The loading plate is modeled using solid elements with rigid properties in contact with the Nomex core through *automatic\_surface\_to\_surface* contact type.

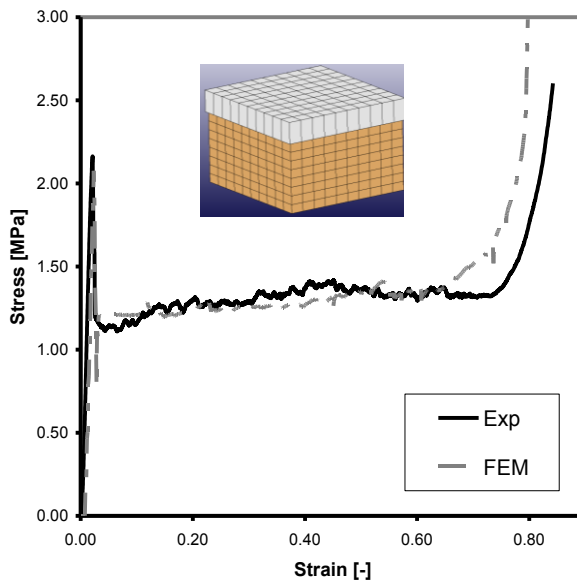


Figure 4.43: Compressive Stress vs Strain curve for the Nomex core.

The numerical results showed a good agreement with the experimental stress-strain curve and all the stages of the characteristic compressive behavior are well captured by the FE, Figure 4.43: the elastic regime up to the stabilized compressive strength, the crushing regime at nearly constant plateau stress (crush strength), and finally the densification regime, where the cellular structure is fully compacted resulting in a steep stress increase.

### 4.5.3. Sandwich assembly – four point bending test

The sandwich assembly, with the calibrated static constitutive material properties, has been build up through the use of tiebreak connection (*contact\_one\_way\_surface\_to\_surface\_tiebreak*) between shell skin and Nomex core solid elements on the basis of interlaminar properties derived from [28, 30]. Apart from the skin penetration, the failure mechanisms taking place during the transversal impact of Nomex core sandwich structures, are represented by shear in the transverse plane and compressive transverse failure, including crushing [1, 17]. These failure mechanisms have been investigated experimentally and numerically through 4 points bending tests, uniaxial compressive tests (reported in the previous section) and static indentation test respectively.

Four-point bending tests have been run on sandwich specimens obtained combining phenolic/E-glass sandwich skins (1mm thickness) with hexagonal Nomex core (21.5 mm thickness) and assembling with the  $L$  direction of the honeycomb core along the primary direction. The selected test fixture provides a support span of 420mm and a loading span of 140 mm. Specimen deformations were monitored by four longitudinally-oriented electrical resistance strain gauges; the tests were conducted in stroke control with a cross-head speed of 6 mm/min. The load was applied by a 25 mm wide flat steel blocks. The experimental results showed that flexural behavior of the examined sandwich structures is governed by the shear failure of the Nomex core which occurs before any debonding between the core and the facesheets (Figure 4.44).

The validation of this damage mechanism has been done through the FE assembly made up according to the selected test fixture, i.e. providing a support span of 420mm and a loading span of 140mm. The sandwich specimen is set up by 490 mm x 100 mm x 21.5 mm Nomex core between 1mm of E-glass phenolic skins. In detail, the Nomex core is modeled with solid brick elements (4mmx4mmx3.6mm) and the E-

glass phenolic skins with shell elements (4 mm x 4 mm) i.e. coincident with the in plane mesh density of the modeled core. The load/support span were modeled as solid elements with rigid material properties and an *automatic\_surface\_to\_surface\_contact* type is adopted for the contact between upper and lower steel span and the sandwich structure. The final assembly for the 4 point bending test is reported in Figure 4.44 where the superposition of the numerical load-deflection curve with the experimental ones (three) is reported. The initial rigidity is reproduced with satisfactory accuracy by the numerical simulation, as well as the onset of damage, caused by the Nomex shear failure in the *WT* plane for the attainment of the correspondent core shear strength. This numerical test validates also the performance of the connection between the two materials: no interface failure occurs in the numerical test. Figure 4.45a reports the core areas subjected to the *LT* shear during the loading phase, whereas the stress status in the skins at the onset of core failure (upper-compressive and lower-tensile) is illustrated in the Figure 4.45b where the onset of failure is not yet reached.

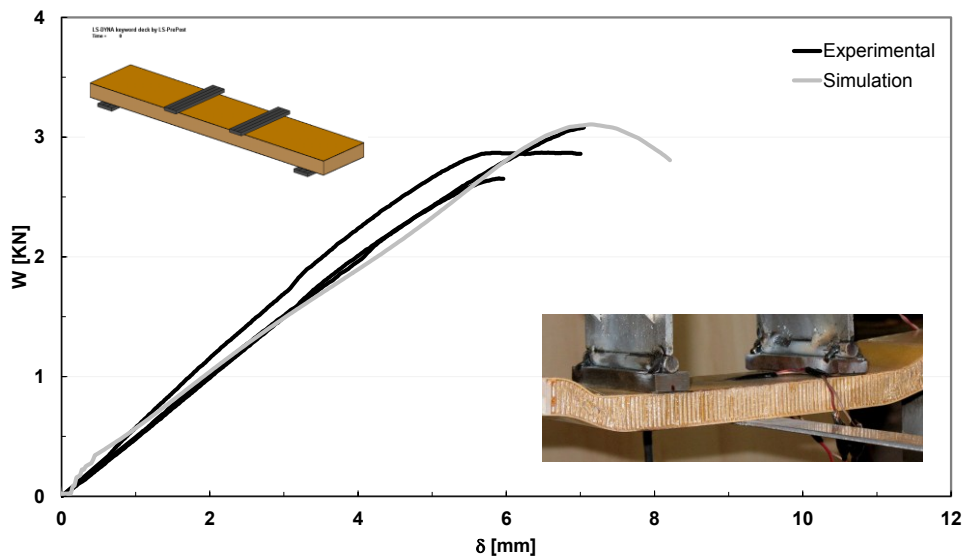


Figure 4.44: Load vs Deflection curve for the four point bending test.

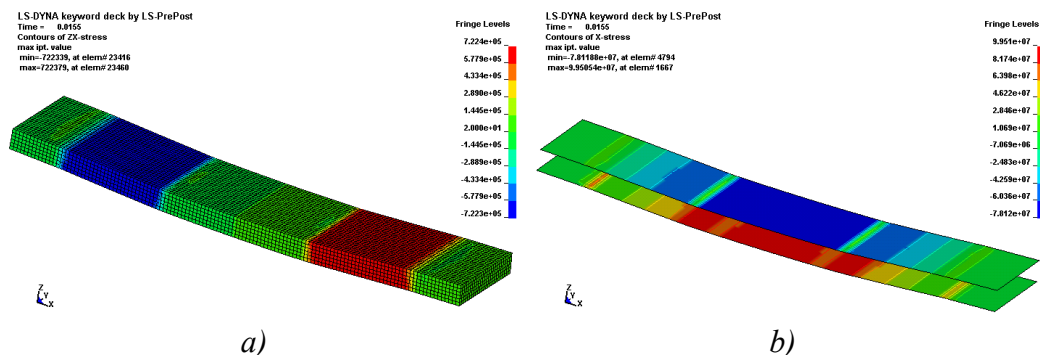
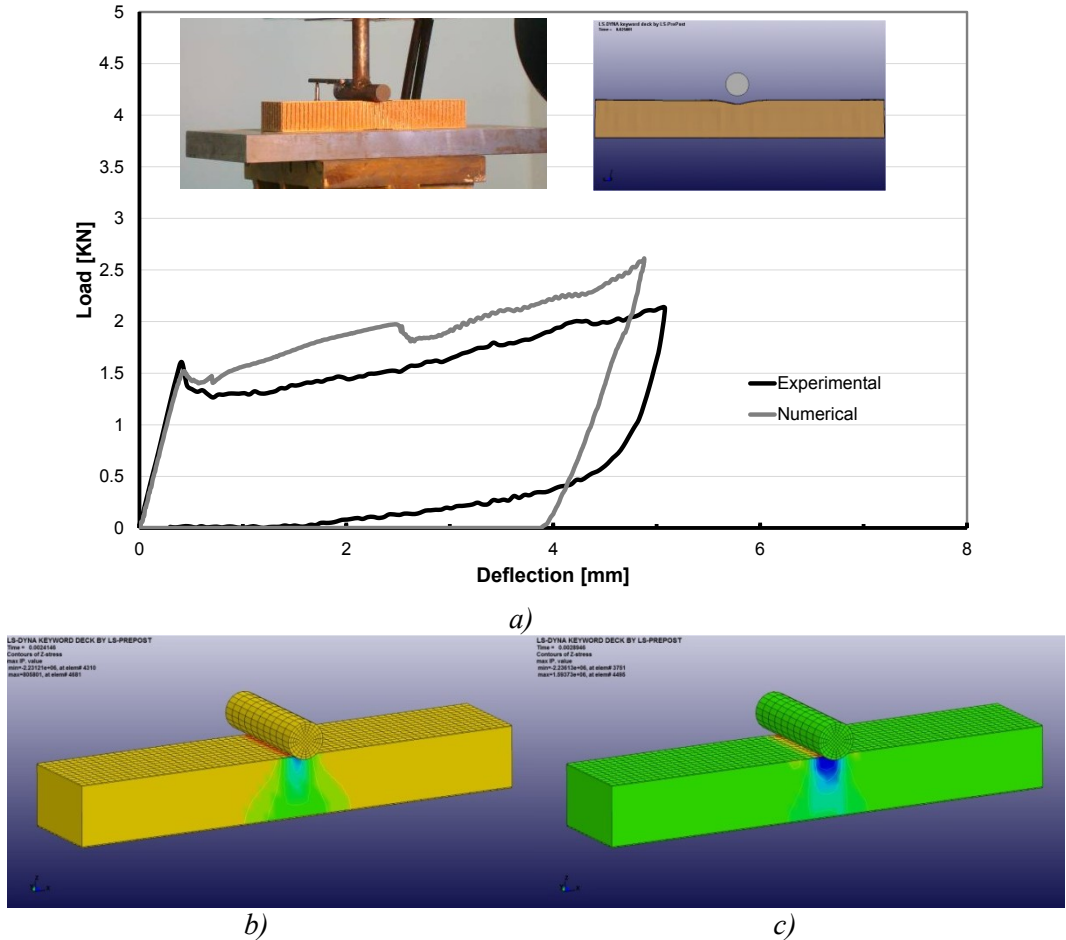


Figure 4.45: Contour of a)  $LT$  stress in the Nomex core, b)  $L$  direction stress in the upper and lower skin.

## 4.6. Sandwich Assembly – Indentation test

In order to predict the contact force history, the dynamics of both the projectile and the target must be modeled accurately, and local indentation effects must also be accounted for. The local crushing behavior has been investigated through static indentation tests. 250x50mm sandwich beam specimens composed by 32.2 mm-thick Nomex core between two 1 mm thick glass/phenolic skins were supported by a steel substrate in order to avoid overall bending of the specimen. The indentation load was applied through a steel cylinder (20 mm in diameter) across the whole width of the beam cross-section. The tests were carried out under displacement control at a loading rate of 2 mm/min and, after a fixed depth of the cylinder displacement, the load was released and the face sheet flexed back but did not recover completely its undeformed shape: thus, a residual facesheet dent remained revealing an irreversible absorbing energy mode of failure. The FE model has been constructed by using solid brick elements (4mmx4mmx3.6mm) for the Nomex core and shell elements (4mmx4mm) for the E-glass phenolic skins, i.e. coincident with the in plane mesh density of the modeled core. The bottom face of the sandwich is supported by constraining the  $Z(3)$  degree of freedom. In Figure 4.46a the comparison between load and displacement curve for the experimental and simulated test is reported. Both curves show a linear behavior up to the peak load, i.e. until when the transverse normal stress remains low, the core behaves elastically and the  $Z(3)$  stress is spread throughout all the thickness dimension (Figure 4.46b). In the experimental test, the emission of a cracking sound at

the end of the linear domain is believed to be associated with the onset of core crushing. This means that the core behaves elastically as long as the compressive stress in the core does not exceed the critical value of core compression strength.



**Figure 4.46: Load vs Deflection numerical and experimental curve for the static indentation test a); through the thickness stress distribution before b) and after c) Nomex crushing.**

After this stress level, the stress distribution becomes more concentrated under the indenter (Figure 4.46c) and the force–displacement curve becomes nonlinear with a decrease in the stiffness. The nonlinear behavior was due to the progressive honeycomb crushing in the area under the indenter which corresponds to a plastic volumetric compression in the solid elements of the core. The global behavior is well captured by the numerical simulation, especially for the load peak which is very close to the experimental one whereas a slight mismatch in the non linear part is observable

in the numerical curve with respect to the experimental one, probably due to the shear component of the material model [23]. After releasing the steel indenter, the numerical unloading curve reaches a slightly higher residual damage (residual dent) because there is no way to modify the unloading law and the elastic release of the deformed cells in the constitutive material model.

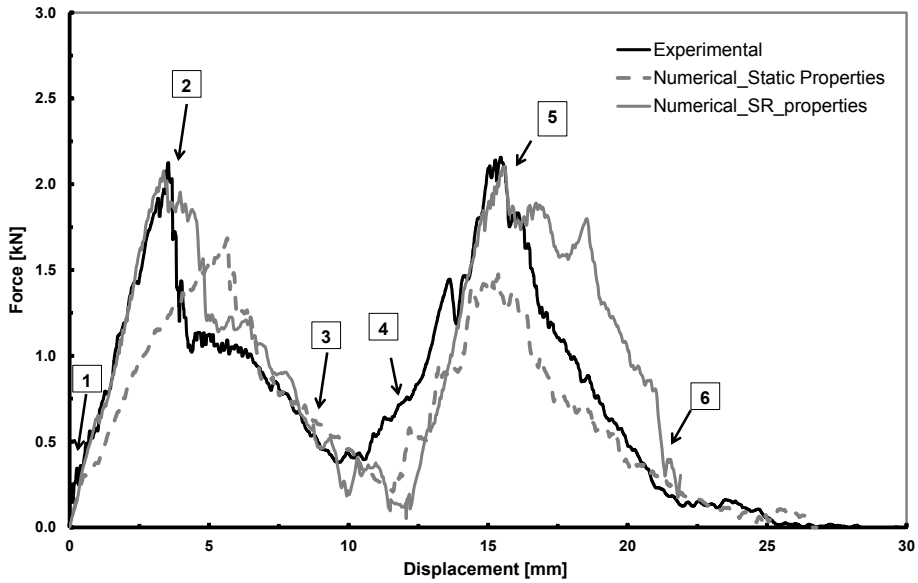
## 4.7. Impact analysis

A series of impact tests were carried out on specimens prepared with 11 mm-thick Nomex honeycomb and sandwiched between either  $t=1$  mm or  $t=2$  mm E-glass phenolic skins consisting of four or eight fabric plies, respectively. The specimens were clamped using cylindrical rings and impacted with a 16.8 kg mass at three different energy levels, achieved with three different velocities ( $v=1$  m/s,  $v=4$  m/s and  $v=8$  m/s). The selected impact velocities allowed to provide top skin damage ( $v=1$  m/s) and complete penetration ( $v=4$  m/s and  $v=8$  m/s). Moreover, two different hemispherical tips ( $d=12.7$  mm and  $d=20$  mm diameter) were adopted to provide their influences on the impact response. The variability of impact conditions has the principal aim of evaluating the effect of impact energy, skin thickness, impactor diameter, and impact velocity on the main outcomes of the impact tests, i.e. force-displacement history ( $F-d$ ) and impact damage (damaged area and through-thickness damage).

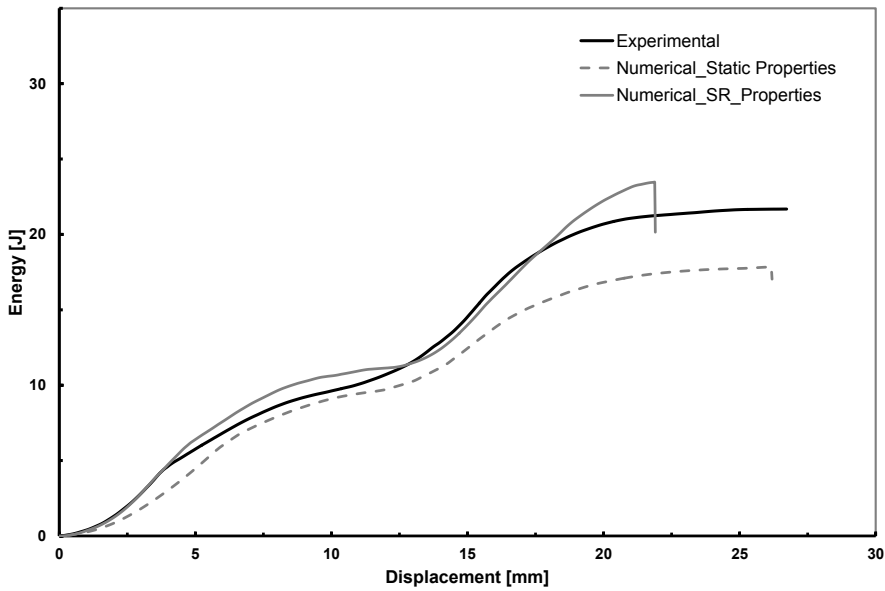
For the numerical simulation, the impact test involving 11 mm of thickness for Nomex core combined with 1 mm of E-glass phenolic skins and stroked by 12.7 mm impactor diameter at 4 m/s (leading to complete penetration) has been taken as a baseline reference in order to identify the sensitive parameters which affects the analysis and to calibrate the model. Model validation has been performed by mean of results of the other impact tests. The FE model consists of a solid cylinder having 40 mm of diameter and 11 mm of thickness to which the Nomex properties (defined in the previous sections) are assigned through MAT\_MODIFIED\_HONEYCOMB material type. The skins (upper and lower) are modelled as one or two circle shell in the case of  $t=1$  mm and  $t=2$  mm respectively, by assigning MAT058 material type and the corresponding calibrated static material properties whereas rigid properties have been assigned to the solid steel impactor. The clumped boundary conditions are achieved by fixing the outer edges of the sandwich constituents.

Within a quite large range of values, a sensitivity analysis showed significant influence of the following factors: (i) mesh size; (ii) values of  $SLIM_iT$ ; (iii) EROD values (principal strain level for element deletion for both skins and Nomex honeycomb); (iv) tensile skin material properties which control the stiffness and peak force of the  $F-d$  curves; (v) friction between impactor and target that slightly affects the shape of the  $f-d$  curve in the post peak phase. Convergence of results has been achieved by using approximately 1.2 mm squared elements for the shell skin elements and 1.2 mm x 1.2 mm x 1.6 mm solid elements for the Nomex core; whereas a more refined mesh may cause strain localization and a consequently reduction of absorbed energy [31]. Values for the erosion of the skins shell elements have been based on fiber ultimate failure strains for glass composites.

In Figure 4.47a the simulated  $F-d$  curve based on the derived static material properties is plotted with a dashed grey line for  $v=4$  m/s impact test and compared to the experimental one. Even though the global shape of the curve is captured by the FE simulation, the numerical response appears underestimated respect to the experimental one, in terms of both stiffness and peak force values. In the presented sandwich impact tests, the sandwich impact response is influenced by the strain rate sensitivity of the constituent sandwich materials which particularly affects the in plane facesheets material properties. In fact, by reporting the numerical fringe level of strain rate in warp direction for the upper skin next to first failure (Figure 4.48a), it can be observed that the in plane strain rate rises up to  $1000s^{-1}$  of order of magnitude leading to a possible modification of material properties. Considering the constituent sandwich materials adopted within the present study, Heimbs et al. [20] characterized the strain rate dependent material properties for E-glass phenolic composites reporting an average increase of almost 90% compared to the static values for tensile strength in warp and weft direction with a marginally increase of the elastic moduli and an increase of around 50% of strain to failure values; similar results were obtained by Barré et al. [14] on satin wave glass-phenolic composites. A possibility to include material strain rate dependence for the skins is to adopt `MAT_RATE_SENSITIVE_COMPOSITE_FABRIC_158` with a viscous stress tensor formulation based on an isotropic Maxwell model; however, this material model works reasonably well if the stress increases due to rate affects are up to 15% of the total stress [23] and consequently a calibration of strain rate dependent material properties was performed for the E-glass phenolic skins on the basis of the cited results.



a)



b)

Figure 4.47: a) Comparison of experimental and numerical  $F-d$  curves for  $t=1$  mm,  $d=12.7$  mm,  $v=4$  m/s with numbered sequence of sandwich damage mechanisms; b) corresponding energy displacement curve.

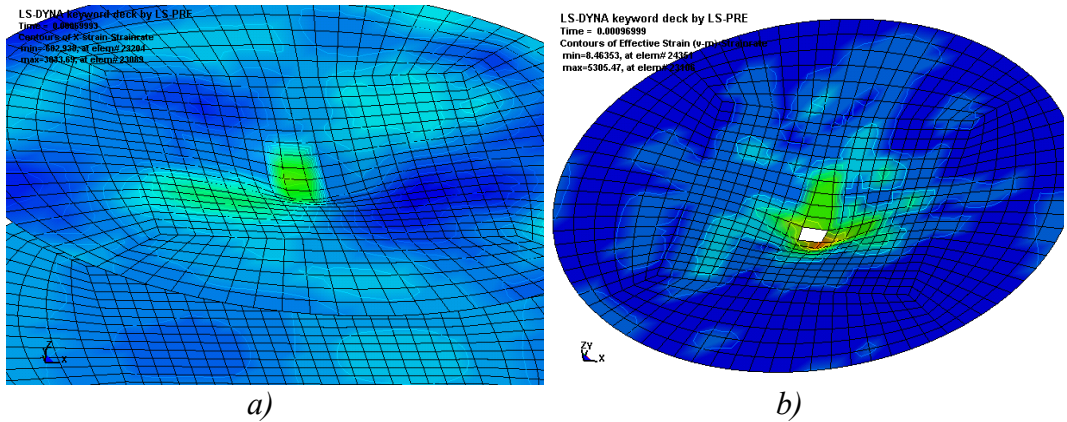


**Figure 4.48: Fringe level of strain rate in warp direction a) and distribution of effective strain rate on the upper skin ( $t=1$  mm,  $d=12.7$  mm,  $v=4$  m/s).**

Concerning Nomex core behavior, compressive crush strength, plateau stress and strain to compaction are also affected by loading rate [19]; consequently, in order to fully calibrate the dynamic behavior of the Nomex core, the Dynamic Increase Factor (ratio of the dynamic property value over the static one) DIF versus strain rate and relative volume for compaction have been assigned to the material model on the experimental results of [29], where dynamic compressive tests at different loading rates were conducted using a drop weight tower apparatus.

A good agreement between numerical and experimental results has been achieved with corrected skin material properties including 100% increase for maximum tensile strengths, 5% Elastic moduli (in warp and weft direction), 50% increase of strain to failure  $E_i T$  and 40% increase for the shear behavior. In particular, in Figure 4.47a the  $F-d$  curve for the baseline impact test is reported by using the calibrated material properties showing a satisfactory superposition, also for the Energy-displacement curve (in Figure 4.47b). The  $F-d$  curve in Figure 4.47 allows to identify the different damage stages during impact which are displayed in Figure 4.49: (1) the crushing of the core is pointed out by a small drop in the load and a slight changing in the slope of the  $F-d$  curve since the Nomex honeycomb structure attains its compressive strength. Successively, the core deflects with increasing the load and the skin locally fails until top skin perforation, (2)). The significant load drop caused by top skin failure, is followed by shear fracture in the Nomex core (3)), where the solid elements are eroded since they are too distorted. The compressive plastic deformation

in the Nomex core creates a small plug in the zone under the impactor (4)) which starts to deflect the lower skin in bending. In this way the load increases again and the final drop in the load curve is due to lower skin failure (5)) up to final perforation (6)).

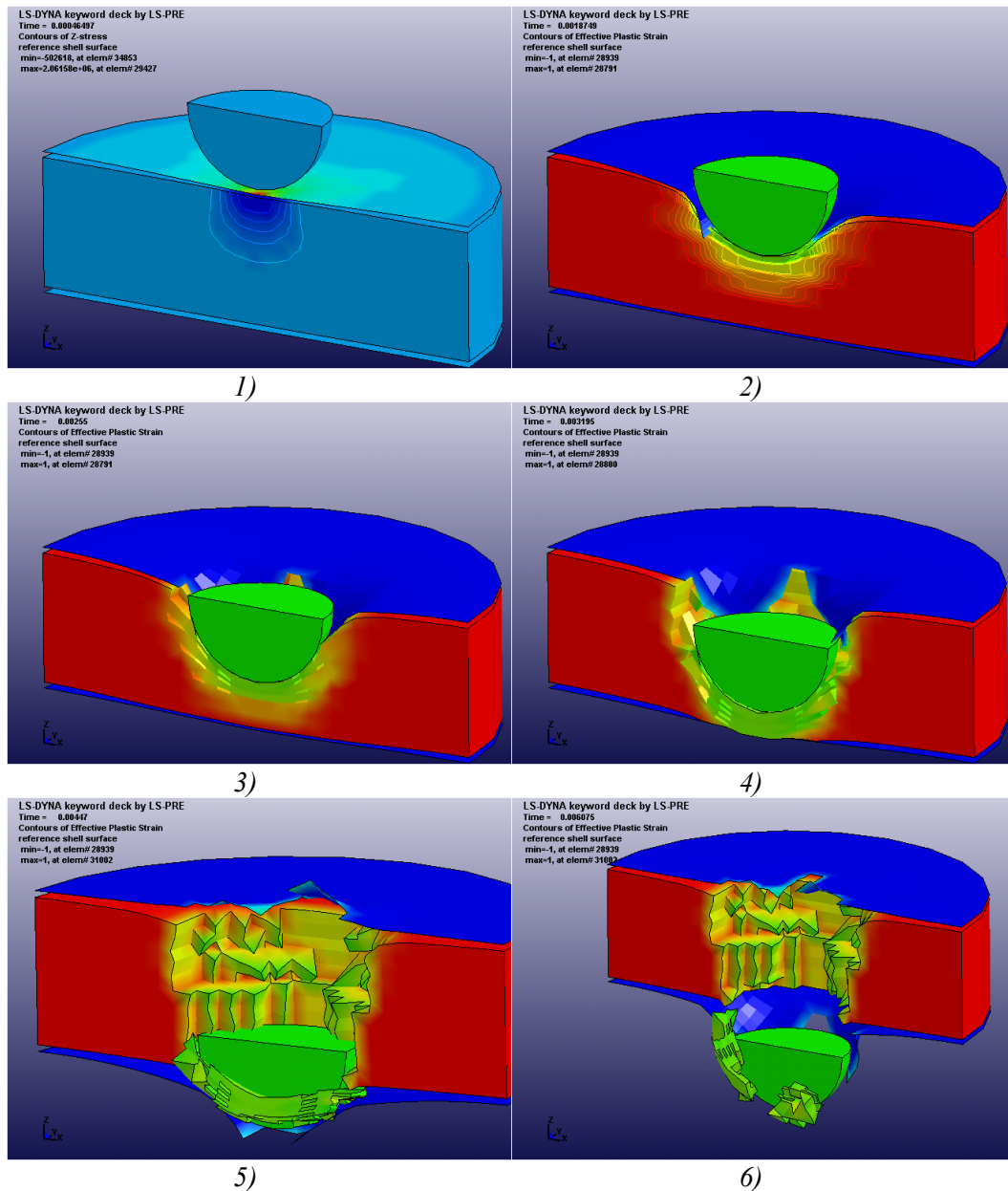


Figure 4.49: Simulated damage sequence occurring in the E-glass phenolic sandwich with  $t=1$  mm,  $d=12.7$  mm,  $v=4$  m/s (contour of plastic strain): 1) Nomex crushing, 2) Top skin

**failure, 3) Shear failure in the Nomex core, 4) Plug formation, 5) Bottom skin failure, 5) Complete penetration.**

Figure 4.50 and Figure 4.51a,b report the numerical results for the other impact tests. By increasing the impact velocity to 8 m/s for  $t=1$  mm and  $d=12.7$  mm the peak forces in the  $F-d$  curve remains almost constant and the agreement with experiments is good (Figure 4.50). In Figure 4.51a, the comparison between numerical and experimental results is reported for  $t=2$  mm,  $d=12.7$  mm and  $v=1$  m/s: the general trend of the contact force increases further up to the maximum load, where a significant load drop, suggesting major damage, is observed. After that, the  $F-d$  curve flattens out until the maximum displacement, corresponding to a zero velocity of the impactor, is achieved. During rebound, the elastic portion of the energy stored into the material is transferred back to the impactor, whereas another portion (represented by the area enclosed in the  $F-d$  curve) is irreversibly absorbed through material permanent damage, heat, and vibrations. The superposition shows good agreement in both loading and unloading phase. Compared with the case of  $t=1$  mm, the increasing of the skin thickness produces an increase of the energy absorbed given by a significant increase in the peak force (from 2.16 kN to 3.79 kN) indicating that skins represent a significant factor responsible for the energy absorption and the energy absorbed by each skin is almost constant. By increasing impact energy level, the numerical results slightly differs from the experimental ones. In particular, with increase the initial impact velocity to 4 m/s Figure 4.51b, the model is not able to predict with sufficient accuracy the increase of both peak forces occurring in the experimental test, probably due to the strain rate sensitivity on the phenolic skins and the through the thickness shear components which cannot be taken into account with sufficient accuracy in the adopted shell-based material model. The energy absorbed by the facesheets and honeycomb core grows by passing from 12.7 mm to 20.0 mm impactor diameter and in the corresponding  $F-d$  curve (Figure 4.52) both peak force (from around 2.5 kN to 3.10 kN) and central region governed by the core are increased whereas the overall shape of the curve is conserved. With the larger diameter impactor, larger contact-areas and contact-time are involved triggering more work for skin fracture and plastic deformation of the core.

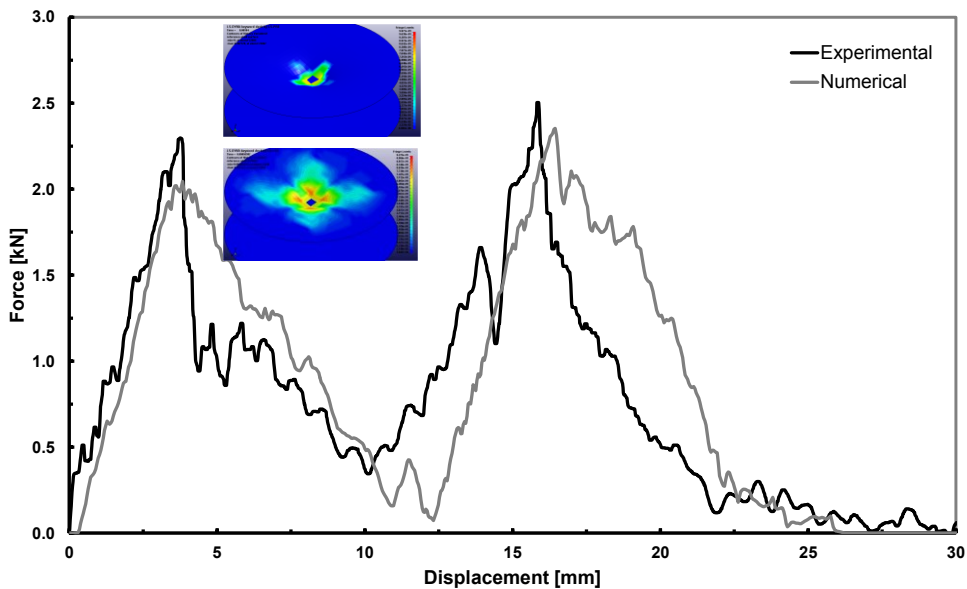


Figure 4.50: Comparison of experimental and numerical  $F-d$  curves for  $t=1\text{mm}$ ,  $d=12.7\text{mm}$ ,  $v=8\text{m/s}$  with evolution of damage variable  $\omega_1$  and  $\omega_{12}$ .

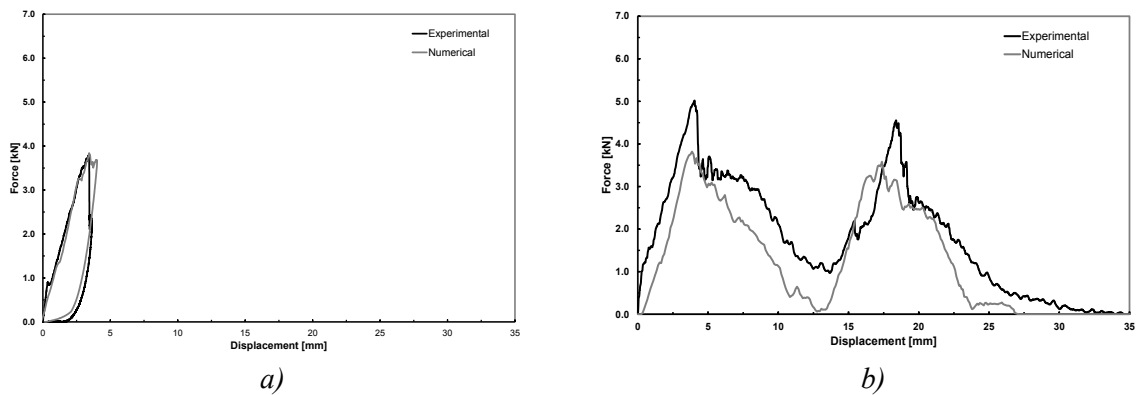


Figure 4.51: Comparison of experimental and numerical  $F-d$  curves for a)  $t=2\text{ mm}$ ,  $d=12.7\text{ mm}$ ,  $v=1\text{ m/s}$  and b)  $t=2\text{ mm}$ ,  $d=12.7\text{ mm}$ ,  $v=4\text{ m/s}$ .

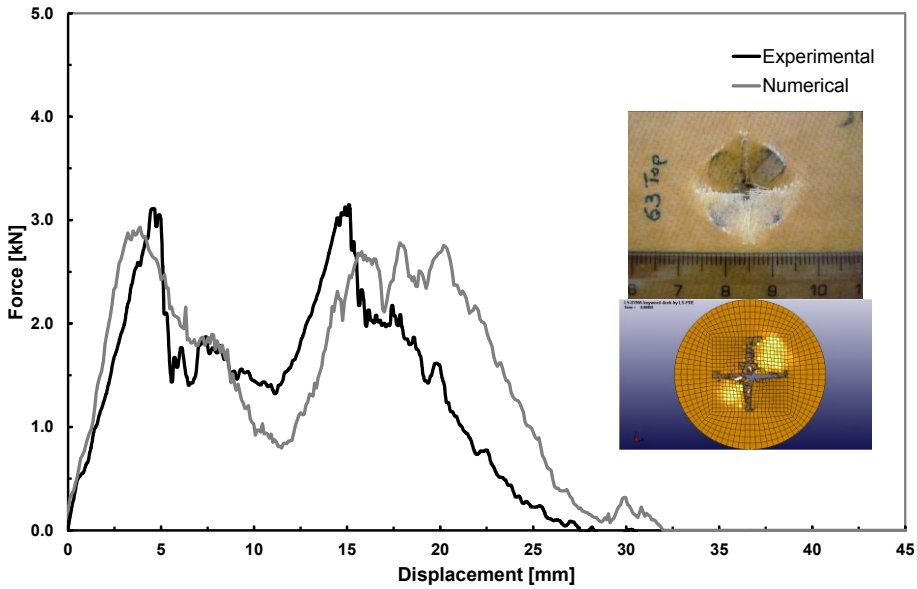
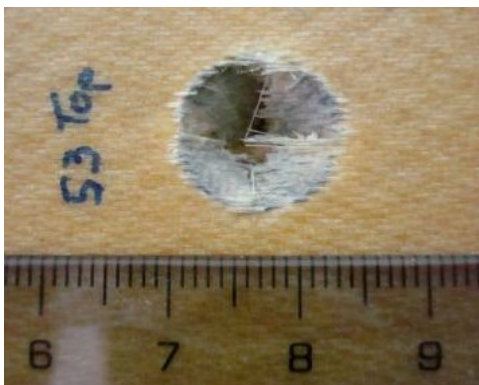


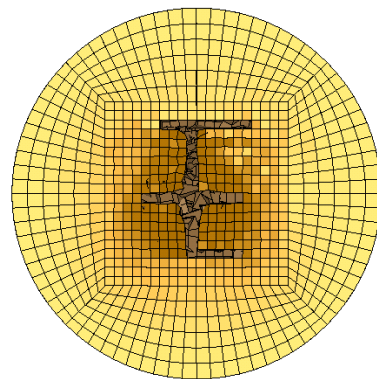
Figure 4.52: Comparison of experimental and numerical  $F-d$  curves for  $t=1$  mm,  $d=20.0$  mm,  $v=8$  m/s and corresponding top view of impacted specimens.

#### 4.7.1. Damage assessment

Damage resulted in the impact tests involves upper/lower skin failure and penetration, Nomex crushing, interface failure, delamination. The damaged specimens showed a very localized damaged area with a circular shape and with the dimensions approximately coincident with the impactor diameter (as reported in the case of complete penetration for  $t=1$  mm,  $d=12.7$  mm and  $v=8$  m/s in Figure 4.53a).



a)



b)

**Figure 4.53: Comparison of experimental a) and numerical b) top residual damage for E-glass phenolic sandwich with  $t=1$  mm,  $d=12.7$  mm,  $v=8$  m/s.**

The main failure mode in the composite skins is fiber breakage, which represents the basic energy absorption mechanism. In particular, the principal axes of skin failure coincide with the warp-weft directions of the surface fabric layers (horizontal and vertical directions in the Figure 4.53a, along which fiber fracture was found. The impactor of 20.0 mm of diameter produced similar damage and the involved damaged area extends in a circular region of diameter slightly higher than the impactor diameter (Figure 4.52). The numerical model showed a good agreement in terms of the damage occurred in the sandwich as a consequence of the impact load. The evolution of damage variable  $\omega_1$  and  $\omega_{12}$ , at the beginning of top skin perforation, is reported in the upper and lower inset of Figure 4.50 respectively, for  $t=1$  mm,  $d=12.7$  mm and  $v=8$  m/s: the irreversible damage due to fiber fracture develops along the warp direction where the element deletion occurs since more deformed elements lie along that directions. Moreover, the in plane shear deformation and permanent damage (with  $\omega_{12}$ ) spreads over a wide area under the impactor in contact with the top skin. The final residual damage of impacted sandwich specimens, in top view, is compared with the numerical results (Figure 4.53a,b) and in Figure 4.52 for the E-glass phenolic sandwich with  $t=1$  mm,  $d=12.7$  mm,  $v=8$  m/s and  $t=1$  mm,  $d=20.0$  mm,  $v=8$  m/s. The good agreement achieved confirmed the reliability of the model and the element deleted during the analysis correspond with the principal direction of fiber fracture; moreover, the numerical damaged area reproduces the circular shape with permanent deflection of damaged skin.

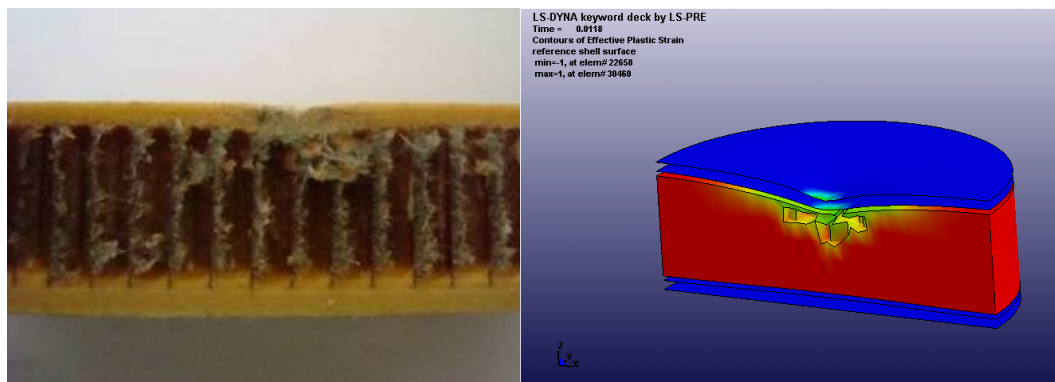


**Figure 4.54: Comparison of experimental a) and numerical b), through the thickness residual damage for E-glass phenolic sandwich with  $t=2$ mm,  $d=12.7$ mm,  $v=1$ m/s.**

Figure 4.54a,b display the experimental and numerical through the thickness residual damages for specimen with  $t=2\text{mm}$ ,  $d=12.7\text{mm}$ ,  $v=1\text{m/s}$  respectively. Permanent deflection occurs in the upper skin (slightly higher in the numerical case) while crushing and permanent plastic deformation affect the Nomex core.

## **4.8. Closing remarks**

In the present study, high energy impact tests were carried out on E-glass phenolic impregnated sandwich structures, adopting two skin thickness values, two different impact diameters and different impact velocities. The experimental tests were modeled through the explicit FE software LS-DYNA. Homogeneous equivalent solid elements have been adopted for the Nomex honeycomb core and shell elements for the phenolic facesheets in combination with an orthotropic nonlinear elasto-plastic and a CDM based constitutive behavior, respectively. A FE based procedure based on different experimental tests was presented in order to obtain and calibrate the basic properties for the adopted material model to take into account the main damage mechanisms occurring during the impact tests. A wide calibration of material properties based on static experimental tests resulted in a non-satisfactory reproduction of the impact behavior of examined sandwich structures since dynamic conditions affect some crucial material properties. A further investigation on the strain rate sensitive material properties allowed to calibrate a reliable sandwich model on a reference impact test. From the results obtained on the unknown cases, FE estimated with sufficient accuracy the overall force-displacement curves during the loading-rebound phases and complete penetration case as well as the sequence of damage related to the penetrating phases.

Satisfactory agreement between numerical predictions and experiments was also verified with reference to the extent and shape of damaged areas with a good correspondence in the onset and development of material damage. In particular, as confirmed by the analysis of the impacted sandwich panels, FE calculated considerable fiber fracture on top and bottom phenolic facesheets and plastic deformation of Nomex core. In general, the predicted results reproduce with a satisfactory accuracy the impact behavior of the analyzed sandwich structures; however a slight discrepancy was found when high impact velocities and thicker skins are involved. This circumstance probably depends on the possibility to accurately account for the dynamic behavior in the constitutive material model at different strain rates. So that, further developments will include a strain rate characterization of the GFRP in order to conduct reliable finite

element simulations. More work should be also done to investigate potential mechanisms and parameters involved in the dynamic behavior such as Nomex paper rate dependence, micro-inertial effects of the cellular structure, the influence of trapped air in case of stabilized compression.

## References

1. Abrate, S., *Impact on composite structures*. Cambridge: Cambridge University Press, 1998.
2. Bernard, M.L. and P.A. Lagace, *Impact Resistance of Composite Sandwich Plates*. Journal of Reinforced Plastics and Composites, 1989. **8**(5): p. 432-445.
3. Meo, M., R. Vignjevic, and G. Marengo, *The response of honeycomb sandwich panels under low-velocity impact loading*. International Journal of Mechanical Sciences, 2005. **47**(9): p. 1301-1325.
4. Anderson, T. and E. Madenci, *Experimental investigation of low-velocity impact characteristics of sandwich composites*. Composite Structures, 2000. **50**(3): p. 239-247.
5. Aktay, L., A.F. Johnson, and M. Holzapfel, *Prediction of impact damage on sandwich composite panels*. Computational Materials Science, 2005. **32**(3-4): p. 252-260.
6. Fatt, M.S.H. and K.S. Park, *Perforation of honeycomb sandwich plates by projectiles*. Composites Part a-Applied Science and Manufacturing, 2000. **31**(8): p. 889-899.
7. Raju, K.S., B.L. Smith, J.S. Tomblin, K.H. Liew, and J.C. Guarddon, *Impact damage resistance and tolerance of honeycomb core sandwich panels*. Journal of Composite Materials, 2008. **42**(4): p. 385-412.
8. Fan, X., *Investigation on Processing and Mechanical Properties of the Continuously Produced Thermoplastic Honeycomb*. PhD Thesis, Katholieke Universiteit Leuven, Belgium, 2006.
9. Gibson, L. and M. Ashby, *Cellular Solids*. Cambridge University Press, 1999.
10. Foo, C.C., G.B. Chai, and L.K. Seah, *Mechanical properties of Nomex material and Nomex honeycomb structure*. Composite Structures, 2007. **80**(4): p. 588-594.

11. Zinno, A., E. Fusco, A. Prota, and G. Manfredi, *Multiscale approach for the design of composite sandwich structures for train application*. Composite Structures, 2010. **92**(9): p. 2208-2219.
12. Heimbs, S., *Virtual testing of sandwich core structures using dynamic finite element simulations*. Computational Materials Science, 2009. **45**(2): p. 205-216.
13. Lebee, A. and K. Sab, *Transverse shear stiffness of a chevron folded core used in sandwich construction*. International Journal of Solids and Structures, 2010. **47**(18-19): p. 2620-2629.
14. Barre, S., T. Chotard, and M.L. Benzeggagh, *Comparative study of strain rate effects on mechanical properties of glass fibre-reinforced thermoset matrix composites*. Composites Part a-Applied Science and Manufacturing, 1996. **27**(12): p. 1169-1181.
15. Asprone, D., E. Cadoni, A. Prota, and G. Manfredi, *Strain-rate sensitiveness of a pultruded e-glass/polyester composite*. Journal of Composites for Construction, 2009. **13** p. 558-564.
16. Menna, C., D. Asprone, G. Caprino, V. Lopresto, and A. Prota, *Numerical simulation of impact tests on GFRP composite laminates*. International Journal of Impact Engineering, 2011. **38**(8-9): p. 677-685.
17. Zhao, H. and G. Gary, *Crushing behaviour of aluminium honeycombs under impact loading*. International Journal of Impact Engineering, 1998. **21**(10): p. 827-836.
18. Baker, W.E., T.C. Togami, and J.C. Weydert, *Static and dynamic properties of high-density metal honeycombs*. International Journal of Impact Engineering, 1998. **21**(3): p. 149-163.
19. Goldsmith, W. and J.L. Sackman, *An Experimental-Study of Energy-Absorption in Impact on Sandwich Plates*. International Journal of Impact Engineering, 1992. **12**(2): p. 241-262.
20. Heimbs, S., S. Schmeer, P. Middendorf, and M. Maier, *Strain rate effects in phenolic composites and phenolic-impregnated honeycomb structures*. Composites Science and Technology, 2007. **67**(13): p. 2827-2837.
21. Zinno, A., A. Prota, E. Di Maio, and C.E. Bakis, *Experimental characterization of phenolic-impregnated honeycomb sandwich structures for transportation vehicles*. Composite Structures, 2011. **93**(11): p. 2910-2924.

22. Matzenmiller, A., J. Lubliner, and R.L. Taylor, *A Constitutive Model for Anisotropic Damage in Fiber-Composites*. Mechanics of Materials, 1995. **20**(2): p. 125-152.
23. LS-DYNA, Keyword User's Manual, Livermore Software Technology Corporation, Version 971, 2007.
24. Yamashita, M. and M. Gotoh, *Impact behavior of honeycomb structures with various cell specifications - numerical simulation and experiment*. International Journal of Impact Engineering, 2005. **32**(1-4): p. 618-630.
25. Aktay, L., A.F. Johnson, and B.H. Kroplin, *Numerical modelling of honeycomb core crush behaviour*. Engineering Fracture Mechanics, 2008. **75**(9): p. 2616-2630.
26. Fischer, S., K. Drechsler, S. Kilchert, and A. Johnson, *Mechanical tests for foldcore base material properties*. Composites Part a-Applied Science and Manufacturing, 2009. **40**(12): p. 1941-1952.
27. DeTeresa, S.J., L.M. Allison, et al., *Experimental results in support of simulating progressive crush in carbon fiber textile composites* final report, Lawrence Livermore National Laboratory, 2001.
28. Heimbs, S., P. Middendorf, and M. Maier, *Honeycomb Sandwich Material Modeling for Dynamic Simulations of Aircraft Interior Components*. 9th International LS-DYNA Users Conference, Detroit, US, 2006.
29. Zinno, A., D. Asprone, A. Prota, and C.E. Bakis, *Experimental characterization of strain rate effects and impact behaviour of phenolic sandwich structures*. 9th International Conference on Sandwich Structures ICSS 9, , 2010.
30. St John, N.A. and J.R. Brown, *Flexural and interlaminar shear properties of glass-reinforced phenolic composites*. Composites Part a-Applied Science and Manufacturing, 1998. **29**(8): p. 939-946.
31. Fritzsche, P., M. Weder, I. Wyss, M. Hormann, and J. Muller, *A procedure for the simulation of failure in thermoplastic composites*. Composite Structures, 2008. **85**(4): p. 337-349.

## **CHAPTER V**

# ***FRACTURE TOUGHNESS OF MULTISCALE CARBON NANOTUBE REINFORCED COMPOSITES***

### **5.1. Introduction to framework**

In recent times, carbon nanotube (CNT)/polymer composites have emerged as a promising class of high performance materials because of extraordinary properties exhibited by CNTs, including: high specific modulus and strength, high electrical and thermal conductivity, low coefficient of thermal expansion. Due to these characteristics, the potential applications of these materials as structural and functional materials suitably comprise the aerospace, energy storage and electronic sector and other industries. However, even though experimental results have proved the high potential of such materials, the cost related to CNT production and the trial-and error approach used to develop suitable composites have made the complete control and modeling of effective properties of CNT reinforced polymer composites preferably desirable. The assessment and modeling of CNT based composite mechanical properties is rather complex and represents a challenging task. The main source of complexity is related to their hierarchical structure, which ranges from nano to macro length-scales. Therefore, it appears essential to address this issue according to a different approach from traditional ones, which is able to account for the characteristic phenomena of each length-scale and bridge their effects from the smaller scale to the macroscale [1].

Multiscale methods have recently gained an increasing attention to this field; the key feature of these methods is the possibility to combine simultaneously multiple modeling methods, from atomistic simulations to continuum theories, and span multiple time and length scales with the final goal of controlling and predicting the nanocomposite response. Within this modeling process, experimental characterization techniques play a major role for both understanding nanoscale mechanisms and determining modeling parameters. Within the discovery process of CNT-based composites, reliable modeling of nanocomposites properties allows a cheaper, faster and more efficient composite development when compared with pure experimental methods.

The activities presented in *Chapter V* are focused on multiscale modeling of Mode I interlaminar fracture toughness of CNT-based composites. The approach moves from the investigation of analytical models describing the CNT pullout mechanism, at the nanoscale, whose validation is based on available experimental data (Figure 5.55).

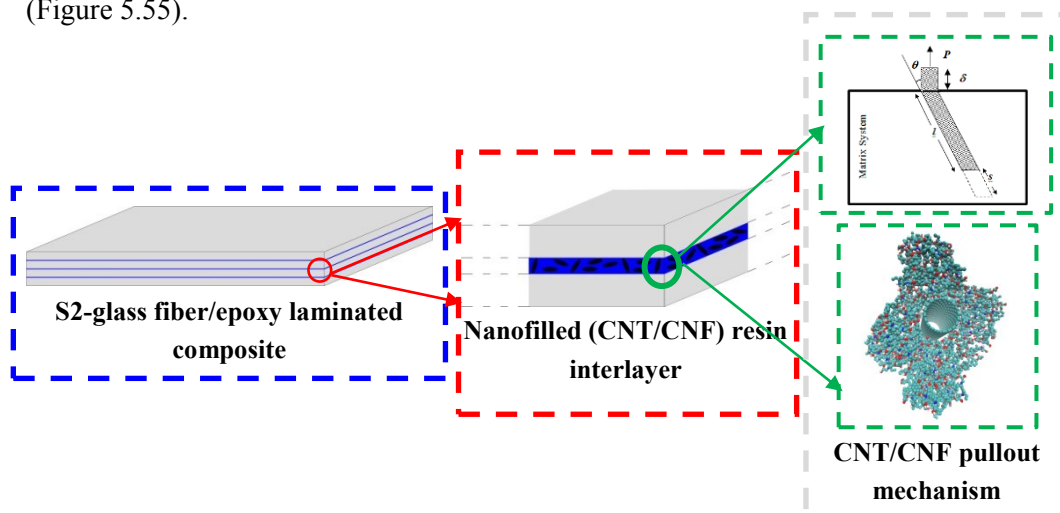


**Figure 5.55: Illustration of multiscale framework of damage analysis for Mode I interlaminar fracture toughness of CNT/CNF-based composites.**

In particular, these models are built to take into account the CNTs properties within the matrix at the nanoscale, i.e. length and orientation distribution, stress transfer. The first sections comprise a literature review on some critical CNT properties and experimental characterization techniques that are of fundamental concern for modeling purposes. Then, the literature review focuses on available models for CNT toughening mechanisms. A micromechanical model is then presented showing the

main assumptions, equations and some parametric analysis; finally the model is applied to a certain number of interlaminar Mode I fracture toughness experimental results.

## **5.2. Carbon Nanotubes – background and introduction**

Carbon nanotubes (CNTs) can be classified as mesoscale fillers having typical diameter values ranging between 1-100 nanometer and length values up to millimeters, resulting in high aspect ratios. The official CNT discovery dates back to 1991 with the publication of a research paper in which the author, Iijima [2], announced the preparation of “nanometre-size, needle-like tubes of carbon”. CNTs can exist into two main classes: single walled carbon nanotubes (SWCNTs) and multi-walled carbon nanotubes (MWCNTs). A SWCNT is a cylinder obtained by rolling up a portion of a graphite sheet with the tip of the roll-up vector (the chiral vector) connecting its tail, as shown in Figure 5.56. A MWCNT consists of concentric SWCNTs with different chirality and separated by a distance approximately coincident with the basal plane separation in graphite, i.e 0.36 nm [3]. These materials have increasingly attracted considerable attention because of their unique structure and remarkable mechanical, electrical, thermal and chemical properties [4, 5]. In fact, several research works have proved that Young’s modulus of single-walled nanotubes (SWNTs) is greater than 1TPa [6-8] and the tensile strength is of the order of 100GPa [9-11]. Moreover, CNTs are able to undergo large deformations without exhibiting fracture as well as recover their original, straight structure [12]. In addition, CNTs have very high thermal conductivities and good electrical properties [13, 14]. Due to CNT dimensions and morphology, it is believed that CNTs represent ideal fillers for polymers to enhance their mechanical properties. In fact, the incorporation of this kind of nanoscale constituents into polymer matrices leads to property enhancements greater than those attainable using conventional fillers.

Furthermore, such nanoscale reinforcements could make the resulting composites potentially suitable to be processed using traditional methods for plastic materials, which in general are more difficult or impossible with the larger, micron-scale conventional fibers. Despite these advantageous aspects, a large amount of work will have to be done in the field of CNT composites before we can exhaustively take advantage of the exceptional properties of CNTs for polymer matrix composite materials. In fact, the enhancements currently achieved by using CNT fillers are often significantly less than those predicted by simple micromechanical models.

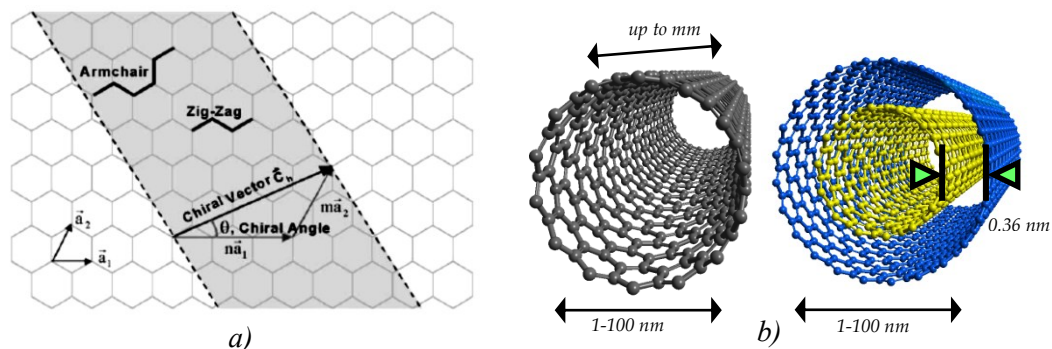


**Figure 5.56: Schematic representation of the SWCNT and MWCNT structure: a) definition of chiral vectors and chiral angle [5], b) three dimensional rendering.**

This is often caused by a variety of factors, including CNT dispersion within the polymer, size, shape and orientation of CNTs, interaction between the polymer and the CNT, type of CNT used and CNT agglomeration within the polymer system; all these factors are usually assumed to be “idealized” within a model, such as perfectly straight or aligned elongated tubes, perfect CNT-matrix bond, perfect dispersion, etc. For example, Morcom et al. [15] reported that a 66% Young’s modulus increment could be achieved by improving the dispersion of CNTs in a high density polyethylene matrix, whereas Bose et al. [16] showed that nature of pre-treatment and agglomeration were responsible for the Young’s modulus variation when increasing the filler loading. Du et al. [17] reported that the dispersion and orientation of CNTs indeed were the two crucial parameters to determine the reinforcement of the CNT/polymer composites. It can be concluded that although wide efforts have been conducted to achieve a good control of CNT/composite preparation, the key challenge still remains the efficient transferring of the superior properties of CNTs to the nanocomposites. In the following sections, the most important parameters affecting the final properties of CNT-based composites are described.

### 5.2.1. CNT length characterization

Due to their extraordinary properties, CNTs are increasingly being investigated for use in polymer composite applications. However, the mechanical and electrical and properties of such CNTs-based composites are strongly affected by the properties of the CNTs themselves. Even though effective CNT synthesis methods have been widely developed in the last decades, at the synthesis level it is very difficult to control CNT geometric configurations, including length, chirality, number of walls, orientation. For

this reason, one of the most important features of CNTs starting and dispersed material is that the tubes typically consist of diverse range of lengths, diameters and electronic properties, providing a widely heterogeneous initial system. As a consequence of this heterogeneity, the modeling of the effective properties of CNT-reinforced polymers is made complicated. The complex CNT micromechanical and nanoscale characteristics are mainly related to:

- variability of the structure and properties of the CNTs;
- dispersion and orientation of the CNTs within the polymer;
- characteristics of the interface and load transfer between the CNTs and the polymer;
- interphase between CNT and the polymer.

The accurate characterization and understanding of how these issues act at the nanoscale level represent a necessary step in order to optimize the fabrication phase and predict the effective properties of CNT-reinforced polymer systems.

Among these critical issues, a key step to optimize CNT industrial applications is the accurate measurement and characterization of CNT length, both during preparation and after composite processing. The exact determination of CNT lengths is difficult mainly due to a series of practical problems: CNT individualization without any damage, possibility to observe nanotubes as single tubes in microscopic techniques, entanglements of several nanotubes which restrict the individualization. In addition, due to the high CNT aspect ratio, it is a problem to follow long nanotubes in microscopic observations that may be also inclined with respect to the viewing plane. In general, dispersion characterization tools can be classified into two main types [18]: tools based on microscopy and tools based on spectroscopy. Four types of microscopy have been used to characterize CNT dispersion: transmission electron microscopy (TEM), scanning electron microscopy (SEM), atomic force microscopy (AFM), and optical microscopy, including confocal microscopy. Spectroscopic methods include Raman spectroscopy, UV–Vis spectroscopy, and scattering methods. All these methods can be applied to both low-viscosity liquids and polymers.

In addition to the issues related to CNT length characterization, the understanding of residual CNT length within a polymer matrix after dispersion and/or processing represent a further key step aimed at determining the effective mechanical properties of CNT-based composites. In fact, CNTs might be brittle and thus damaged during processing due to exertion of high external forces on CNTs. Several studies reported that nanotube length reduction could be due to composite method of

preparation, dispersion techniques, CNT chemical modification, as well as processing. In fact, CNTs as raw materials, obtained by bulk synthesis methods, are characterized by a strong interaction which tends to bond each other through van der Waals forces (mainly due to large surface areas of CNT tubes). This consequently leads them to primarily exist in large aggregates, such as ropes or bundles. In order to achieve systems with individualized CNTs, it has been observed that CNTs can be dispersed in a large number of different materials, including several surfactants and polymers [19, 20]. However, due to the fact that nanotubes are tightly bonded within a bundle, significant amount of energy may be required to detach nanotubes each other. For this reason, solutions of nanotubes are prepared through different dispersion procedures that usually include the use of sonication methods (comprising tip, bath, etc.), for which duration and intensity of ultrasound treatments are widely varied. Some dispersion procedures often employ a consecutive (ultra)centrifugation step to remove residual larger bundles, with the final aim of having primarily individual nanotubes and small bundles in the system. Several studies have reported that ultrasonic processing of CNTs may result in significant damage including buckling, bending and dislocations which affect the nanotube structure and become significant with longer periods of sonication [21]. In particular, these processes lead to a scission of the nanotubes into shorter segments with a rate of fragmentation that reduces with segment size. The mechanism that generates nanotube cutting is mostly related to fast collapsing cavitation bubbles which potentially produce a shear force able to exceed the tensile strength of the nanotube and thus cause its fragmentation [22]. The average length of the nanotubes has been shown to be reduced at a rate proportional to  $t^x$ , where  $t$  is the sonication time and  $x$  is determined experimentally [23]. For instance, in [23] the scission of nanotubes was found to follow a power law such that the average length of the ensemble decreased proportional to  $t^{-0.38}$  under continuous tip sonication. Other sonication parameters, such as frequency and power, influence the extent of nanotube scission as well, with lower frequencies producing forces of greater energy and high applied ultrasonication power increasing the defect density with a consequent reduction of the average length of the nanotubes.

Numerous studies demonstrated the feature of CNT fragmentation during dispersion. Saito et al. [24] found MWCNT fragmentation up to final lengths shorter than 1  $\mu\text{m}$  as a result of a sonication dispersion method in mixtures of sulfuric and nitric acid. CNT damage related to sonication time was investigated also by Hilding et al. [25] who reported that most length reduction occurred during the first few min of sonication, then, the rate of length reduction levels out. Blanch et al. [23] conducted a parametric

study in order to investigate the effect of the major controllable variables during CNT dispersion process. In particular, they considered the effect of ultracentrifugation temperature, duration and applied force on dispersion, using arc-discharge nanotubes in sodium dodecylbenzene sulfonate (0.5% mass percentage). Ultrasonication was performed using ultrasonic bath or alternatively with a probe sonicator. The solutions were characterized with UV–vis–NIR absorbance spectroscopy, Raman spectroscopy and atomic force microscopy AFM, with this latter analysis performed to determine the length and diameter distributions of each sample. As a result of the study, they reported that both length and diameter distribution of the populations of dispersed CNTs could be described by a log-normal distribution (Figure 5.57) with a greater number of nanotubes having shorter lengths and thinner diameters and a wide tail for longer dimensions. Moreover, they concluded that increasing sonication/centrifugation time, force and temperature, the fraction of individualized CNTs can be augmented, at the cost of a reduced CNT mean length.

CNT chemical modification may represent also a source of length reduction as reported by Gojny et al. [26] who observed a reduction of MWCNT lengths in MWCNT/epoxy composites prepared by mechanical mixing. In that study, length reduction was attributed to the amino-functionalization process on the MWCNTs.

Concerning CNT length reduction and distribution after nanocomposites processing, some authors reported that additional nanotube shortening can be experienced after melt processing. Fu et al. [27] investigated residual nanotube lengths after incorporation in an epoxy polymer matrix; the measurement of the MWCNT lengths was carried out using SEM and a shortening up to 1.4  $\mu\text{m}$  was found (with respect to initial nanotube lengths of 10–20  $\mu\text{m}$ ). Chen et al. [28] measured CNT lengths after sonication assisted composite preparation and a surface oxidation step using field-emission SEM. The comparison between the as-grown and processed CNTs indicated a strong shortening of MWCNTs, up to 90% of the initial length. Duncan et al. [29] investigated the fragmentation aspect ratio of differently functionalized MWCNTs in polycarbonate (PC) composites prepared by a solvent precipitation method. For the fractured composites, PC was dissolved in tetrahydrofuran and a sample was placed on a TEM grid from which aspect ratio distributions of the partially broken nanotubes was showed based on over 100 tubes.

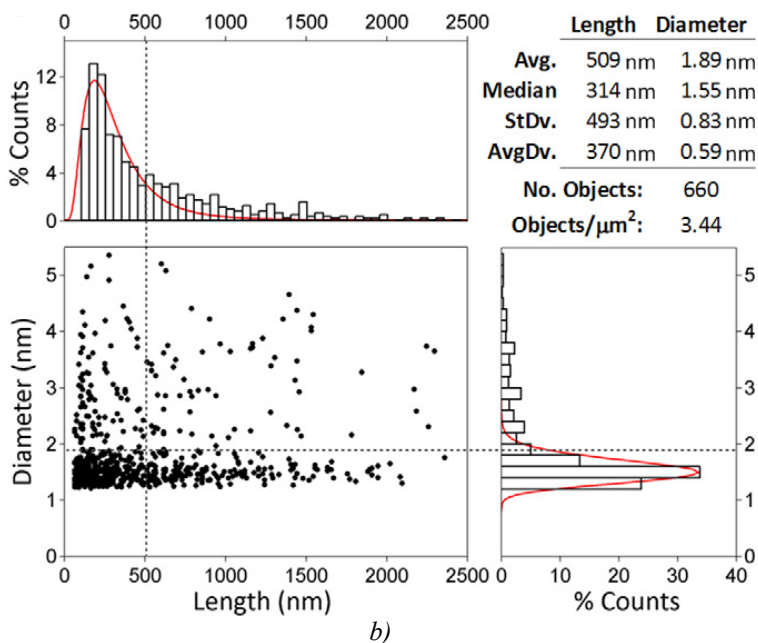
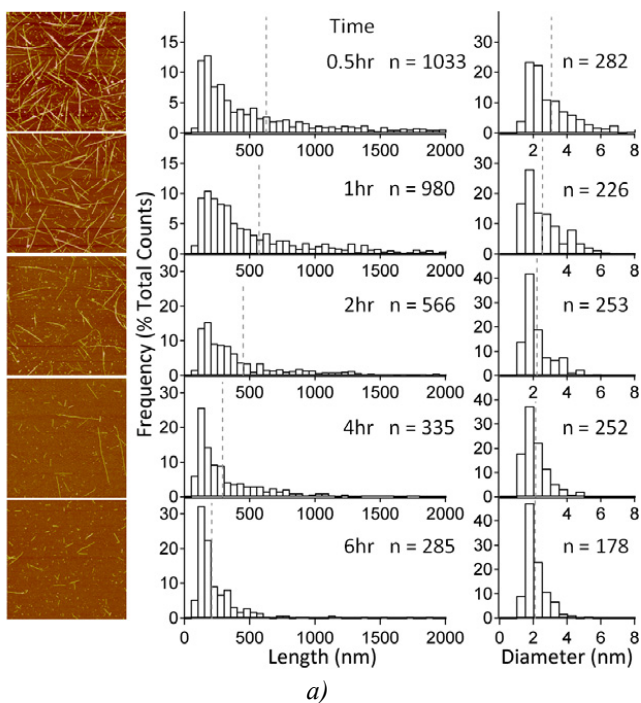
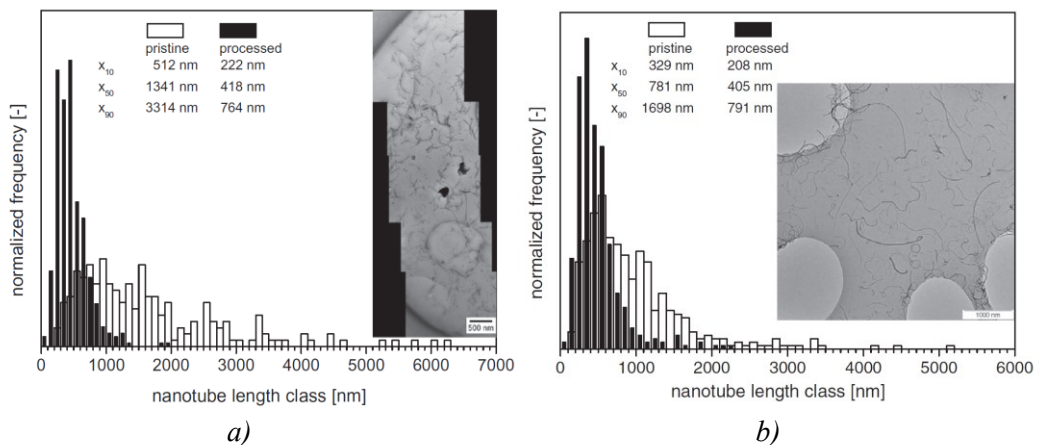


Figure 5.57: a) AFM analysis of dispersions of CNTs in 0.5% SDBS, b) simultaneous length and diameter measurements [23].

Zaragoza-Contreras et al. [30] synthesized MWCNT/polystyrene composites by using in situ bulk-suspension polymerization, with three different MWCNT (without any treatment) concentrations: 0.04, 0.08 and 0.16 wt%. With the assistance of ultrasound sonication and mechanical agitation to avoid nanotube re-aggregation, they achieved encapsulation and exfoliation of the nanotubes into the polymer host. The most important characteristic was the visible short length of the nanotubes, which was apparently below to 10  $\mu\text{m}$  attributed to the induction of strong cavitation due to the application of ultrasound during the synthesis. By solving some MWCNT-composite particles in THF and then performing SEM observations it was found that the nanotubes presented lengths in the range of 2–15  $\mu\text{m}$  which implicated a dramatic length reduction compared with the original size (120–140  $\mu\text{m}$ ) and average aspect ratio (around 1400). Thus, MWCNT degradation took place definitely as a consequence of the process of synthesis. In their study, Krause et al. [31] assessed the length distributions of pristine and processed MWCNTs using the same procedure, i.e. by dispersing them in a suitable solvent, applying TEM on individualized nanotubes and performing image analysis. This allowed them to evaluate the effects of processing dependent shortening in carbon nanotubes. In detail, two melt mixed composites based on PC with two kinds of commercially available MWCNTs were used, with 2 wt% and 1% wt MWCNTs.



**Figure 5.58: Comparison of length distributions before (pristine MWCNTs) and after processing of NanocylTM NC7000 a) and Baytubes b) C150HP MWCNTs [31].**

Figure 5.58 a) and b) show the comparison of length distributions of both nanotube materials before and after melt processing in the polycarbonate composites. The

authors found, for both cases, a significant nanotube shortening after melt processing of up to 30% of the initial mean length values.

The reduction of CNT length during processing inevitably causes a reduction of the effective mechanical properties of the composite and should be necessary taken into account when modeling the effective properties of CNT-based polymer composites. Inam et al. [32] investigated the mechanical properties of cured epoxy–0.1 wt% CNT/ nanocomposites having carbon nanotubes of different average lengths but same initial volume fraction. Carbon nanotubes were dispersed in the epoxy matrix using calendaring technique and then shortened by means of severe tip-sonication with different duration, i.e. 5, 8, 11 and 14 minutes of ultrasonication. This dispersion procedure produced batches of MWCNTs having average lengths of 2.09  $\mu\text{m}$ , 1.69  $\mu\text{m}$ , 1.33  $\mu\text{m}$ , 0.99  $\mu\text{m}$  and 0.50  $\mu\text{m}$ , respectively. Field-emission SEM was used to analyze the residual length of CNTs (at least 5000 CNTs for each case). They reported that higher aspect ratios of CNTs were responsible for achieving higher mechanical properties since the nanocomposites containing long carbon nanotubes (2.09  $\mu\text{m}$ , 1.69  $\mu\text{m}$ ) showed higher tensile strength, elastic modulus, fracture strain and fracture toughness as compared to nanocomposites containing short carbon nanotubes (1.33  $\mu\text{m}$ , 0.99  $\mu\text{m}$  and 0.50  $\mu\text{m}$ ). This was attributed to both larger surface areas offered by longer nanotubes and the effectiveness of dispersion method, i.e. calendaring.

As matter of fact, both length and diameter distribution of the populations of dispersed and/or processed CNTs are characterized by a greater number of nanotubes having shorter lengths and thinner diameters, with a wide tail for longer dimensions (for traditional short fiber composites it is the contrary). A wider variability in length rather than diameter has been observed experimentally; for instance, FE-SEM and HR-TEM analysis revealed almost no change in the diameters of CNTs after tip sonication [32]. Moreover, these distributions appear narrower with increasing dispersion time in the direction of shorter lengths and thinner diameters. It has been reported that this kind of sample data can be successfully described by a log-normal distribution as well as a Weibull distribution [25]. The probability density function of a Lognormal distribution for  $L_{CNT}$  is defined as:

$$f(L_{CNT}, \mu, \sigma) = \frac{1}{\sigma\sqrt{2\pi}} \cdot \frac{1}{L_{CNT}} \cdot e^{-\frac{(\log L_{CNT} - \mu)^2}{2\sigma^2}} \quad (5.1)$$

where the parameters  $\mu$  and  $\sigma$  denote the mean and standard deviation of the length's natural logarithm, respectively. On a logarithmic scale,  $\mu$  and  $\sigma$  can be defined as location and scale parameter, respectively. On the other hand, the probability density function of a Weibull distribution is formulated as follows:

$$f(L_{CNT}, \lambda, k) = \frac{k}{\lambda} \cdot \left(\frac{L_{CNT}}{\lambda}\right)^{k-1} e^{-\left(\frac{L_{CNT}}{\lambda}\right)^k} \quad (5.2)$$

where  $\lambda > 0$  is the scale parameter and  $k > 0$  is the shape parameter of the distribution. Ulrich et al. [33, 34] gave another form of Weibull distribution, expressed as follows:

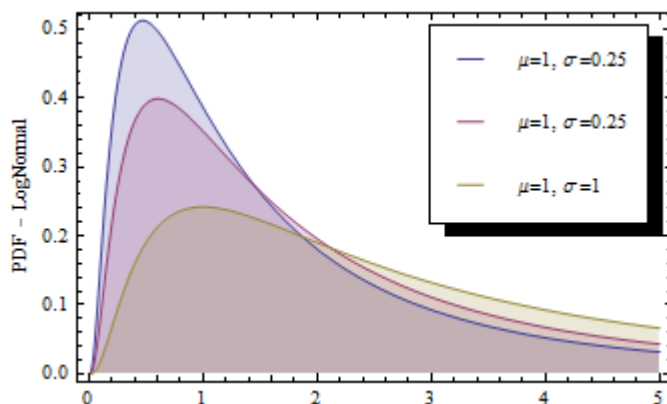
$$f(L_{CNT}, a, b) = abL_{CNT}^{b-1} e^{-aL_{CNT}^b} \quad (5.3)$$

where  $b = k$  is the shape parameter and  $a = \lambda^{-k}$  is the scale parameter. Different parameter values affect the shape of both Lognormal and Weibull distribution, as reported in Figure 5.59. Both scale and shape parameters can be estimated by maximum likelihood estimation (MLE); one alternative method is to estimate the shape and scale parameters through the cumulative distribution function using linear regression. This method counts the cumulated frequency of SWNT lengths from the experimental sample to create an empirical distribution.

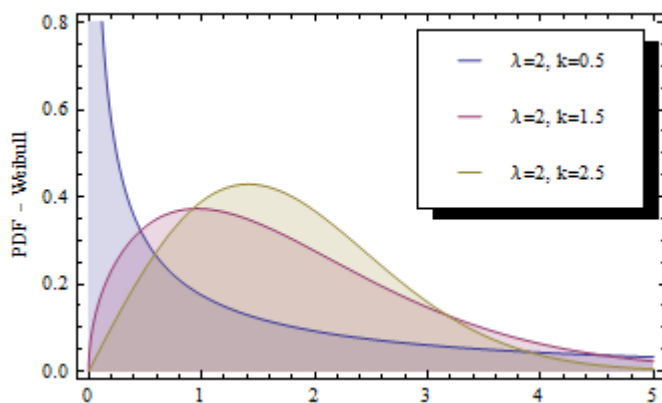
These distribution functions have been successfully used to describe CNT length distributions and implemented into closed formulation to predict CNT composite properties. In their work, Wang et al. [34] described an effective method for quantifying the length distribution of large populations of single-wall carbon nanotubes using atomic force microscopy and SIMAGIS software. The quantified lengths were extracted from software analysis and plotted into a histogram (Figure 5.60). They found that the Weibull probability plot could reasonably describe the experimental sample distribution. The fitted Weibull distribution was used to predict the length effect factor and elastic modulus of CNT/epoxy nanocomposites.

Jiang et al. [35] simultaneously considered the effects of orientation distribution and aspect ratio distribution on composite properties applying their model to predict the elastic properties of nanotube-reinforced composites. In their work CNT-reinforced composites were produced starting from performs obtained by passing a suspension of SWNTs through a porous membrane; a low viscosity Epon 862 resin solution was then infused through the thickness direction of the performs and cured to form. AFM was used to evaluate the aspect ratio distribution. The histogram of the aspect ratio distribution was successfully fitted by a lognormal distribution function,

with a resulting mean aspect ratio of the CNTs of about 140. They showed that, if the orientation and aspect ratio distribution does not have the symmetry of the normal distribution, the overall elastic properties of the composite may be significantly different varying in the range of 30% compared to the symmetric case.



a)



b)

**Figure 5.59: PDF for different scale and shape parameters: Lognormal a) and Weibull distribution b).**

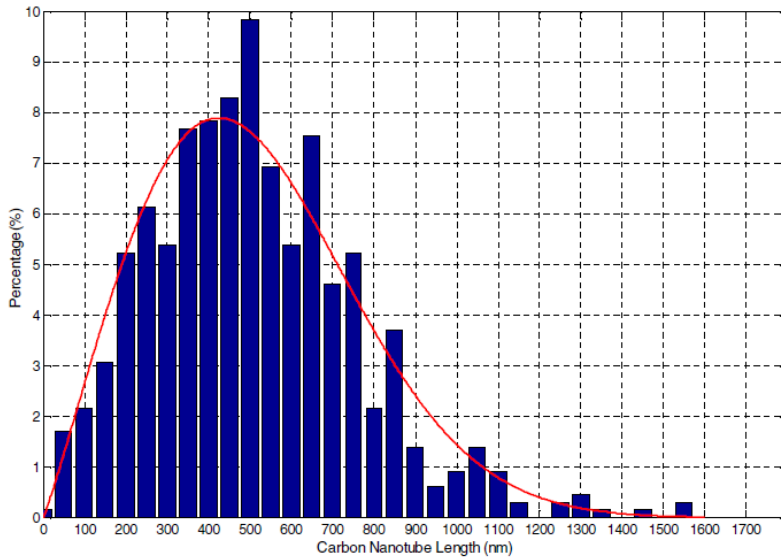


Figure 5.60: Histogram of dispersed SWNT lengths [34].

### 5.2.2. CNT orientation

The extraordinarily high stiffness and strength of nanotubes could potentially make them suited as a reinforcing phase in future generation of composite materials. One of the most remarkable problems related with their use as reinforcement in polymer matrices concerns the degree of control of their alignment within a polymer system. For instance, CNTs usually exist in the form bundles; so that individual nanotube orientations within a bundle can be identical even if the average orientation within the whole domain may be random. Moreover, since carbon nanotubes are anisotropic objects, orientation is a significant factor of dispersion playing an important role in determining numerous properties of CNT-based composites. Therefore, since the overall properties of a composite are very sensitive to the orientation distribution, the issue of the Orientation Distribution Function (ODF) has to be addressed in order to accurately estimate the properties of the composite and optimize processing conditions. Generally, the same mathematical approaches used for quantifying polymer orientation can be used for characterizing nanotube orientation. In particular, in a representative volume of a composite CNT orientation is generally expressed in terms of the orientation of the long axis of the tube with respect to a reference system and can be characterized by the Euler angles [36],  $(\alpha, \beta, \gamma)$ , as shown in Figure 5.61.

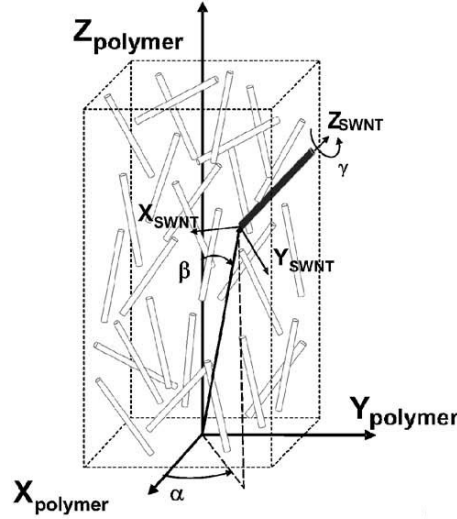


Figure 5.61: Definition of Euler angles in SWNT nanocomposites [36].

Then, the problem can be formulated analytically by the probability of finding nanotubes with orientations between angles  $(\alpha, \beta, \gamma)$  and  $(\alpha+d\alpha, \beta+d\beta, \gamma+d\gamma)$ , for which, the normalization condition is expressed as

$$\int_{\gamma=0}^{\gamma=2\pi} \int_{\alpha=0}^{\alpha=2\pi} \int_{\beta=0}^{\beta=\pi} f(\alpha, \beta, \gamma) \sin\beta d\beta d\alpha d\gamma = 1 \quad (5.4)$$

where  $f(\alpha, \beta, \gamma)$  is the ODF as a function of the three Euler angles  $(\alpha, \beta, \gamma)$ . However, due to the cylindrical geometry of the CNT inclusions, the dependence of  $\gamma$  may be removed. In this way, the orientation of a straight CNT is characterized by the two Euler angles  $\alpha$  and  $\beta$ ; the base vectors  $\mathbf{e}_i$  and  $\mathbf{e}'_i$  of the global  $(X_{polymer}, Y_{polymer}, Z_{polymer})$  and the local coordinate systems  $(X_{SWNT}, Y_{SWNT}, Z_{SWNT})$  are related via the transformation matrix  $\mathbf{g}$ :

$$\mathbf{e}_i = g_{ij} \mathbf{e}'_j$$

where  $\mathbf{g}$  is given by:

$$\mathbf{g} = \begin{bmatrix} \cos\alpha & -\cos\beta \sin\alpha & \sin\beta \sin\alpha \\ \sin\alpha & \cos\beta \cos\alpha & -\sin\beta \cos\alpha \\ 0 & \sin\beta & \cos\beta \end{bmatrix}$$

The orientation distribution of CNTs in a composite reduces to a probability density function  $f(\alpha, \beta)$  satisfying the normalization condition:

$$\int_{\alpha=0}^{\alpha=2\pi} \int_{\beta=0}^{\beta=\pi} f(\alpha, \beta) \sin\beta d\beta d\alpha = 1 \quad (5.5)$$

If CNTs are completely randomly oriented, the density function is  $f(\alpha, \beta) = 1/2\pi$ . Finally, for some loading conditions, it can be assumed that the CNT tube has no azimuthal dependence, and consequently the angle  $\alpha$  may be disregarded in the ODF expression.

Given the characteristics of the ODF, the methods used for the quantification of CNTs orientation are mainly based on three approaches: by measuring mechanical properties of the composite at different scale levels, image analysis, through physical-based measurements.

In the first approach, the dispersion and orientation of CNT fillers is derived from mechanical properties in a microstructural model [37]. The drawback of this method is related to the fact that the measured mechanical properties are usually the average value over large volumes, and sometimes do not effectively represent the local situation of individual CNTs.

Direct microstructure observations and subsequent image analysis have been demonstrated to be a satisfactory way to characterize the dispersion and orientation of CNTs in polymer composites [38-40]. However, some authors [40] pointed out that this technique suffers some limitations mainly related to: (i) the various morphologies and large amount of CNTs in one image that require automatic and accurate CNT identification tools; (ii) heterogeneity of the background brightness; (ii) CNT orientation relative to the observation plane. With regard this approach, Cooper et al. [41] prepared CNT based composites by using a poly(methyl methacrylate) (PMMA) matrix and polymer extrusion technique. The orientation distribution of nanotubes in the composite was determined by image analysis and found to be maximized in the extrusion flow direction. This result was similar to the result obtained by [42] using conventional fibers which were found to be closely aligned to the mold flow direction. Gao et al. [43] successfully developed an image analysis technique able to automatically and accurately analyze CNT/composite images. They used CNT/silicone composites with a filler loading of 15 wt% (dispersed in the silicon matrix by three roll mill) to validate the developed method and to correlate the obtained dispersion and orientation indices with composite processing conditions and CNT/composite electrical properties. By means of this technique, in a first step, CNTs with different dimensions and shapes are automatically identified and extracted from the SEM images; this is achieved by measuring the tube-shape characteristics with Hessian matrices for each pixel in the image. Thus, all the pixels from the same CNT are grouped into one

connected object and pixels from different CNTs are identified as different connected objects. On the basis of a statistics inference framework, in a second step, the spatial dispersion of the extracted CNTs is computed by taking the center of the mass of each CNT as the representative point of its spatial location. The orientational dispersion is consequently computed by fitting the pixel locations of each extracted CNT with a line section that is mathematically represented by a linear regression problem. In detail, the points in the  $j$ th CNT are denoted as  $[(x_i, y_i) : i=1, \dots, N_j]$ ; then the slope  $k_j$  and intercept  $b_j$  is found for the  $j$ th CNT with the minimum fitting error  $E_j$ :

$$E_j(k_j, b_j) = \sum_{i=1}^{N_j} (k_j x_i + b_j - y_i)^2 \quad (5.6)$$

Then, the angle  $\theta_j$  of this CNT is computed as:

$$\theta_j = \tan^{-1}(k_j) \quad (5.7)$$

The computation of the orientation angle for each CNT of the system produces an array of angles  $\theta_i, i:1, \dots, M$  which can be used to construct the histogram of the distribution of the  $\theta_i$ 's, giving the ODF the CNT orientations. By applying this technique, the authors found a substantial increase in the orientation index when the number of roll milling cycles increased, suggesting the alignment of CNTs due the strong and consistent shear force from the roll milling.

Physical-based methods used to measure orientation of CNTs in bulk polymers include [18]: neutron or X-ray scattering, light scattering and, recently, Raman spectroscopy. Neutron or X-ray scattering can be classified as a semi-quantitative method; in the case of perfect uniaxial orientation, the scattering due to nanotubes in the direction perpendicular to the orientation direction will be maximum, while that in the parallel direction will be zero over the angular range that can be probed. The resulting peak width has been used to characterize the relative orientation [44] in PVA-nanotube fibers: nanotube distributions were found to be significantly narrowed after nanocomposite drawing. Light scattering can also be used to measure nanotube orientation [18]; however, this technique can be limited due to the fact that individually dispersed carbon nanotubes as well as small bundles will not contribute to the signal perpendicular to the nanotube axis, because the wavelength of light is much larger than that of the diameter. Furthermore, anisotropy of the signal can be experienced due to nonhomogeneous variations in nanotube concentration on the micron scale.

The implementation of polarized Raman spectroscopy has been recently adopted as an effective and powerful quantitative tool to characterize the orientation of CNTs inclusions in polymer nanocomposites [18]. The common approach is to have the directions of the incoming and scattered polarized radiations parallel to one another (Figure 5.62). In nanotubes, all Raman-active vibrations can be assumed to be active only in the direction of the nanotube axis. This makes use of the fact that the observed Raman intensity depends on the angle between the nanotube axis and the electric field vector of the excitation beam [45]. This method has been recently adopted for ODF characterization. Wood et al. 2001 [46] observed that nanotubes can be aligned in a polymer matrix by flowing the polymer prior to curing, or by stretching the specimen in simple tension. They employed Raman spectroscopy to measure the degree of alignment of the tubes in the polymer for specimens cut both parallel and perpendicular to the flow direction finding them to be significantly different, as a function of mechanical strain. Blighe et al. [47] investigated the effect of CNT content and orientation on the mechanical properties of polyvinylalcohol (PVA) –nanotube composite fibers. The study was focused on the characterization of the orientational effects on Young’s modulus and strength of composites filled with rodlike fillers.

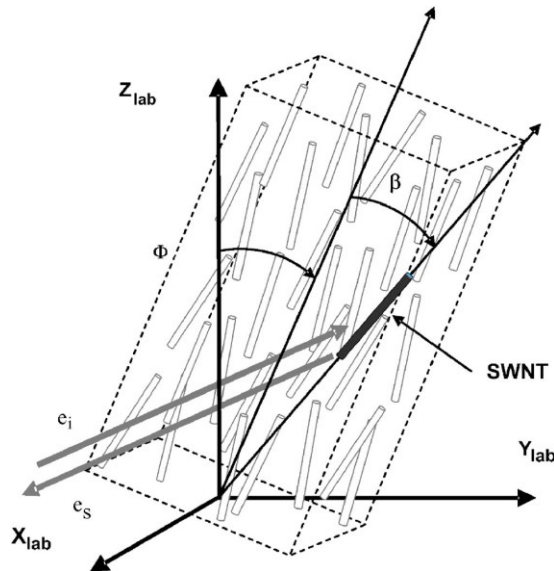


Figure 5.62: Incident and scattered intensities on the SWNT and related angles in the polymer and laboratory frames [36].

Nanotube orientation parameter and the nanotube effective modulus were monitored through Raman spectroscopy. They showed that continuum theory applies at the near-

molecular level that both the Herman's orientation parameter and the nanotube effective modulus increased with drawing, indicating that significant nanotube alignment occurred during composite fiber drawing. Pérez et al. [36] proposed a numerical methodology in order to derive the orientation distribution function ODF for a uniaxial-axially symmetric system using polarized Raman spectroscopy. In this way, the experimental information from the Raman intensity measurements were used to quantify the alignment of single wall nanotubes SWNTs in a urethane dimethacrylate/1,6 - hexanediol dimethacrylate UDMA/HDDMA polymer matrix, where  $\beta$  is the angle defined in equation 5.4. The numerical methodology was formulated in terms of Legendre polynomials and the principle of maximum information entropy [48]. The resulting ODF is a function of Legendre polynomials  $P_i(\cos\beta)$  as follows:

$$f(\beta) = \sum_{i=0}^{\infty} \frac{2i+1}{2} \langle P_i(\cos\beta) \rangle P_i(\cos\beta) \quad (5.8)$$

Where the average of the Legendre polynomial is defined according to:

$$\langle P_i(\cos\beta) \rangle = \frac{\int_{\beta=0}^{\beta=\pi} P_i(\cos\beta) f(\beta) \sin\beta d\beta}{\int_{\beta=0}^{\beta=\pi} f(\beta) \sin\beta d\beta} \quad (5.9)$$

Coefficients  $P_i(\cos\beta)$  are called order parameters and are determined experimentally. Only one or two order parameters may be determined experimentally depending on the adopted specific high resolution technique. One order parameter may be obtained from XRD or FTIR and two order parameters from polarized Raman spectroscopy. The same functions may be used to relate the scattered Raman intensity to the orientation of SWNTs in the polymer. The scattered Raman intensities in the polymer are functions of the poling direction angle and the averaged Legendre polynomials  $P_i(\cos\beta)$ , where  $i=2, 4$ . This is the reason why polarized Raman spectroscopy gives two order parameters of the ODF. The Raman spectroscopy technique allows determination of the average values of the Legendre polynomials leading to the definition of the distribution of all possible orientations:

$$f(\beta) = A \exp[-(\lambda_2 P_2(\cos\beta) + \lambda_4 P_4(\cos\beta))] \quad (5.10)$$

Order parameter  $P_2(\cos\beta)$  is also known as the Herman's orientation parameter. When the orientation is random the Herman's orientation parameter is 0. The Herman's orientation parameter is 1 when there is perfect orientation in a system where the alignment coincides with the angle  $0^\circ$ ; finally, when the alignment is at an angle of  $90^\circ$ , this value is equal to 0.5. Herman's orientation parameter  $P_2(\cos\beta)$  is the first term in the ODF equation containing the fundamental information related to the orientation of inclusions in the polymer. Order parameter  $P_4(\cos\beta)$  contributes with additional information to the ODF in terms of alignment.

### **5.2.3. CNT waviness**

Several experiments conducted on CNT-based composites revealed only modest improvements in the resulting composite strength and stiffness. In numerous cases, one reason could be attributed to the waviness and agglomeration effects which affect CNTs. In fact, many experimental observations have shown that CNTs exist in a curved and entangled state within a composite [49]; this is mainly attributed to their low bending stiffness (due to the small diameter of the tubes) and small elastic modulus in the radial direction. Since this kind of reinforcement morphology affects the stress transfer between the reinforcing CNTs and the matrix materials at the interface, it greatly influences the critical properties of nanocomposites, such as stiffness, toughness and strength. The effects of nanotube waviness on CNT polymer composite stiffness have been investigated by several authors [50]. Shao et al. [51] showed that the waviness can significantly reduce the stiffening effect of the CNTs. Different strategies have been adopted to model waviness of nanotubes in order to predict mechanical properties of CNT polymer composites. Yi et al. [52] and Berhan and Sastry [53] considered waviness in nanotubes approximating them with a sinusoidal shape whereas Li and Chou [54] simulated wavy nanotubes using polygons. By using a combined micromechanics approach and finite element simulation, Li et al. [55] found that the nanotube waviness tends to reduce the elastic modulus but increase the ultimate strain of a composite. Shi et al. [56] developed a micromechanics-based model where nanotubes were assumed to have a helical shape. In detail, they considered a curved CNT as a helical spring, with  $D$  being the spring diameter,  $\theta$  the spiral angle, and  $\varphi$  the polar angle. The length  $L$  of the curved CNT is related to these parameters by:

$$L = \frac{\varphi D}{2 \cos \theta} \quad (5.11)$$



**Figure 5.63: The spring model of a curved CNT [56].**

Within the model, the waviness of the CNT was governed by the spiral angle,  $\theta$ . The Mori-Tanaka [57] method was employed to estimate the stiffening effect of curved CNTs. Some important results came out: the waviness of CNTs does not influence the effective elastic moduli of composites reinforced with randomly oriented CNTs but when spatial and orientation distribution of CNTs in the matrix is nonuniform it was found that waviness may significantly reduce the stiffening effect of nanotubes.

In [32] the carbon nanotube was modeled as a continuum hollow cylindrical shape elastic material with some curvature in its shape. It was observed that waviness significantly reduces the effective reinforcement of the nanocomposites; moreover, through a parametric analysis conducted through finite element simulations it was found that by increasing the values of waviness indices, tensile strength of nanocomposites decreased. The influence of CNT waviness on ductility and fracture toughness was examined at different length scales by [58]; in their work, fiber curvature was added into a shear lag model to analyze the bonded stage in single curved-fiber pull-out. They observed that fibers with more curvature and longer embedded lengths can help toughen the composites since need higher debonding initiation force. Moreover in cases of large curvature, the matrix radial displacement should not be ignored compared with its axial displacement. Based on conventional fiber pull-out models, Yazdchi and Salehi [59] developed an analytical model to investigate the effects of nanotube waviness on interfacial stress transfer characteristics of single-walled carbon nanotubes (SWCNTs)/polymer composites. The wavy CNT was modeled with a solid cross-section and nanotube waviness was modeled by prescribing a sinusoidal CNT shape,  $y$ , of the form:

$$y = A \cos\left(\frac{2\pi z}{\lambda}\right) \quad (5.12)$$

where  $A$ ,  $k$  and  $z$  are the sinusoidal amplitude, sinusoidal wavelength and fiber longitudinal direction, respectively (Figure 5.64).

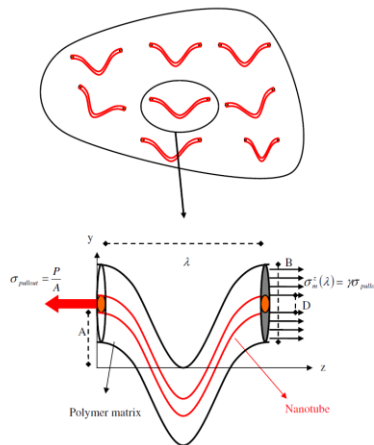


**Figure 5.64: RVE for wavy CNT embedded in polymer matrix [59].**

Their numerical results showed that the waviness of CNTs significantly influences the interfacial stress transfer characteristics of CNT/polymer composites which tend to reduce the stiffening effect of the CNTs. In addition, the maximum interfacial shear stress of a wavy CNT was higher than that of straight ones and increases with increasing the waviness.

#### 5.2.4. CNT-polymer interfacial shear stress (load transfer)

The load transfer effectiveness at the interfaces between nanotube and polymer is one of the most contributing factors for achieving superior mechanical performance in CNT-based nanocomposites. Generally, strong interfacial bonding gives rise to enhancements of Young's modulus and stiffness, while weak interfacial bonding may positively influence energy dissipation. Moreover, different filler and matrix pairs show different interfacial bonding. For example, the MWCNT-matrix stress transfer efficiency is estimated to be at least one order of magnitude larger than that of conventional fiber-based composites [60]. The factors affecting the interfacial adhesion between the nanotubes and the matrix are: dispersion, alignment, and surface treatment/functionalization of the nanotubes. For instance, Xu et al. [61] attributed the

excellent obtained mechanical properties of MWCNT/epoxy composites to the partial alignment of the MWNTs the matrix. Gojny et al. [62] reported that amine functionalization of MWNTs positively enhanced bonding with the epoxy matrix. Moreover, experimental measurements have reported that strong interaction between the nanotubes and polymer results in an increase of Young's modulus and toughness [63]. On the other hand, some authors observed that weak interactions between the nanotubes and polymer led to scarce improvement of composite properties [64].

Traditional methods for determining the interfacial shear strength between fiber and matrix systems may be problematic to apply for CNT-polymer measurements because of the extremely small dimensions of CNTs. Therefore, the number of experimental studies on the interfacial properties of CNT-dispersed polymer composites is limited. Barber et al. performed reproducible pullout experiments on individual MWCNT embedded in a polyethylene-butene polymer matrix using atomic force microscopy (AFM) [65, 66]. In that study, a MWNT was bonded on an AFM cantilever tip using amorphous carbon deposition and then embedded in molten polyethylene-butene. Results showed that the IFSS was in the range 10–90 MPa decreasing with CNT diameter. Cooper et al. detached individual SWNT bundles and MWNTs from an epoxy matrix using a scanning probe microscope [67]. The resulting IFSS values exhibited considerable scattering, as 35–380 MPa. Ding et al. [68] attempted to make in situ observations of single-CNT pulling out testing using a nano-manipulation system installed in a scanning electron microscope (SEM). They observed that the outer layer surface of pulled-out MWNTs was surrounded with epoxy polymer. Therefore, they concluded that the IFSS must be strong. Tsuda et al. [69] pulled out an individual MWNT from the fracture surface of a MWNT-dispersed/PEEK composite film using a nano-pullout testing system installed in an SEM. Tensile loading was measured using the elastic deformation of an AFM cantilever. In this test, the pullout length was controlled by making a through-thickness hole near the specimen edge. They reported that the IFSS of MWNT/PEEK composite was in the range of 3.5–7 MPa; in addition the IFSS of the specimen treated at 573 K under 1 MPa for 1 h increased to 6–14 MPa because of the recovery in interfacial bonding.

Even though experimental measurement of interfacial shear properties is a direct method, some technical problems may arise: resolution of the pull-out process observations; distinguishing CNT pull-out versus breakage; and measurement of the initial CNT embedded length. The alternative to these experimental methods is to perform atomic-scale modeling through molecular dynamics simulation. This approach

represents a valid tool to be employed at the small length scale of carbon nanotube, able to characterize the mechanical and thermal properties of CNT-based composites. Molecular dynamics simulations have been widely used on different CNT/polymer materials, including functionalized CNT. Frankland et al. [70] investigated polyethylene matrix with (10, 10) SWNTs. The estimated shear strength ranged from 0.7 MPa to 2.8 MPa for a crystalline matrix and amorphous matrix, respectively. Liao and Li [71] simulated SWNT and DWNT pullout from a polystyrene matrix; the resulting critical shear stress was 160 MPa, which is much higher than the data obtained for the polyethylene matrix above. This was attributed to the CNT-matrix binding energies of aromatic groups that are larger than those of polyethylene matrices. Wong et al. [72], obtained much higher IFSS ( $>100$  MPa) for polystyrene and epoxy matrix systems as well. Moreover, Lordi and Yao [73] suggested that helical polymer conformations in which chains can wrap around nanotubes might enhance nonbonded nanotube-polymer interactions. Yang et al. [74] performed MD simulations on MWCNT/epoxy system (Figure 5.65) in order to investigate the influence of diameter and length of a MWNT and the boundary and loading conditions on its pullout behavior from the polymer matrix. Even though MD can provide accurate local results, the accuracy is highly dependent on several factors [75]: initial boundary conditions, molecular model and adopted force field. In addition, the computation time might be very long for simulation of large systems of atoms. In [69], a list of experimental and MD simulation results concerning the critical interfacial shear stress for different CNT based composite systems is provided.

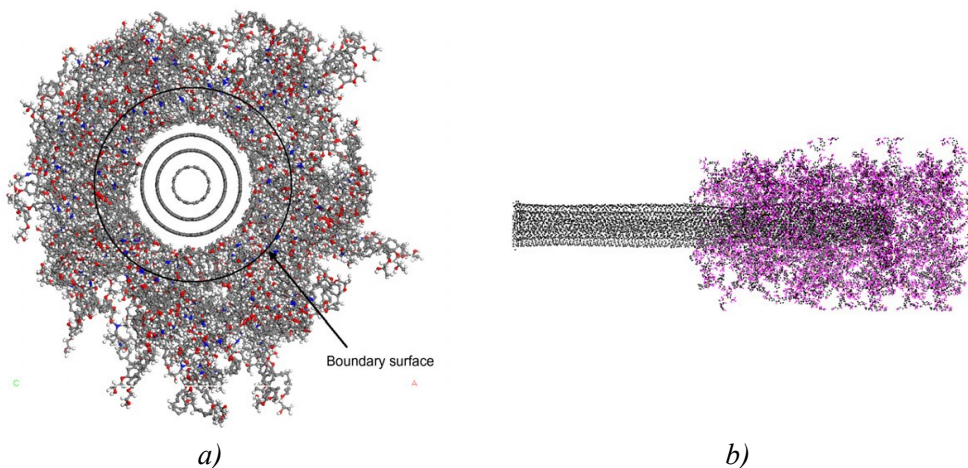


**Figure 5.65: Detail of an MD model: a) cross-sectional view of the model, b) CNT pull-out from polymer matrix [74].**

### **5.3. On nanocomposite toughness**

CNT/polymer composites have the potential to exhibit enhanced properties compared with composites containing conventional fillers. Numerous experimental measurements indicated that the fracture toughness of composite materials containing small amounts of nanotubes, properly dispersed in a polymer matrix, can be considerably enhanced. In addition, due to their small size, nanotubes overcome the problem of large local stress concentrations which often lead to a decrease of fracture toughness when microscale fillers are added to conventional composites. The potential applications of nanocomposites with high energy absorption capability mainly regard lightweight materials, protective armor, damping control, structural crashworthiness.

Concrete evidence of increased toughness of CNT composites includes some composite properties: interlaminar shear strength, fracture mechanics, energy release rate for different modes of delamination and impact test data [76]. Lubineau and Rahaman [77] performed a review of the current strategies for improving the degradation properties of laminated continuous-fiber/epoxy composites using carbon-based nanoreinforcements. From the analysis of their collected data, it was demonstrated that small loads of nanotubes (in the range of 0.5 – 1.0 wt%) were able to increase interlaminar shear strength and energy release rate for the different macroscopic delamination modes up to a hundred percent.

Even though there are several promising results in this field, some other authors found only slight improvements in CNT/polymer composite toughness properties. For instance, experiments performed by Gibson et al. [78] yielded no improvement in Mode I interlaminar fracture toughness of unidirectional carbon/epoxy laminates when MWNTs were sprinkled at ply interfaces during the layup process. Reclustering of the tubes during curing process was suggested to be the responsible of the unsatisfactory toughness performance. Results such that suggest that the toughening process at the nanoscale is rather complex since it involves a large number of variables, such as nanofiller dispersion, toughening mechanisms, CNT-matrix interfacial properties. For this reason, while for micro-reinforced composites the toughness mechanisms have been widely investigated for many years, for nanocomposites they are still an open issue mainly related to the nanoscopic dimensions.

The fracture toughness of a nanocomposite (but in general in a solid) is related to the amount of energy that needs to be spent to propagate a crack in the structure.

Different toughness mechanisms have been proposed to explain the increase of both stiffness and fracture toughness of nano-filler/polymer composites. Generally, these mechanisms depend on nanofiller shape, i.e. spherical, cylindrical or platelet shape. Table 5.1 reports the main toughening mechanisms for different type and size of nanofillers [79]:

**Table 5.6: Comparison of toughness mechanisms of micro- and nano-reinforced polymer matrix composites [79].**

	Particle			Fiber or tube		Patelet	
	<i>Micro (rigid)</i>	<i>Micro (rubber)</i>	<i>Nano (powder)</i>	<i>Micro (fibers)</i>	<i>Nanotube or fibers</i>	<i>Micro platelet</i>	<i>Nano-clay</i>
<i>Crack pinning</i>	Yes	Yes	Yes	Yes	Yes		No
<i>Crack deflection</i>	Yes	Yes	Yes	Yes	Yes	Yes	Yes
<i>Debonding or pullout</i>	Yes	Yes	Yes	Yes	Yes		No
<i>Matrix deformation or void nucleation</i>	Yes	Yes	Yes	Yes	Yes	Yes	No
<i>Fracture of fiber</i>		Yes		Yes	Yes		No
<i>Bridging</i>	Yes	Yes		Yes	Yes		Yes
<i>Microcracks</i>	Yes	Yes	Yes	Yes	Yes		Yes
<i>Shear banding</i>		Yes					

It can be observed that crack deflection, microcracks and matrix deformation or void nucleation may appear in all kinds of micro-scale or nano-scale filler-reinforced composites. Nanotube or nanofibers are potentially involved in all kinds of mechanisms; among these, bridging with local debonding occurs only when the tensile load is parallel to the axis of the CNTs (i.e., the crack path is perpendicular to the CNT). CNT bringing is mainly related to the remarkable nanotube extension capability, which generally is unimportant in traditional brittle fiber based composites. After CNT debonding from the matrix, classical pull-out mechanism is believed to be one of the most important sources of toughening in CNT polymer composites. Figure

5.66 illustrates a schematic representation of possible toughening mechanisms which are active for CNTs, whereas **Figure 5.67** reports concrete experimental evidence of this behavior.

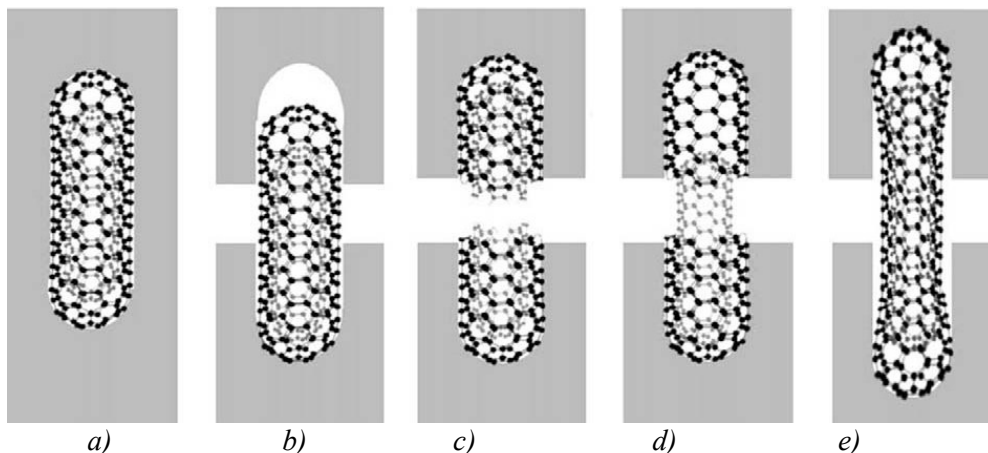


**Figure 5.66:** Schematic description of possible fracture mechanisms of CNTs [80]: (a) initial state of the CNT; (b) CNT pull-out due to CNT/matrix; (c) rupture of CNT ; (d) sword in sheath mechanism, i.e. fracture of the outer CNT layer and pull-out of the inner tube; (e) bridging and partial debonding of the interface.

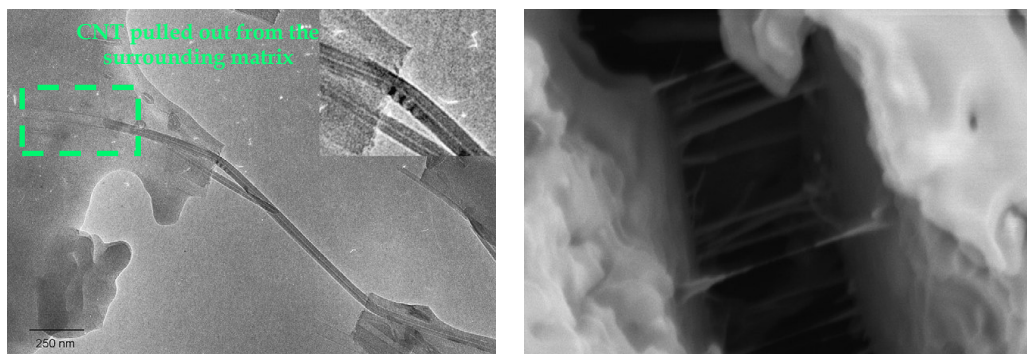


**Figure 5.67:** TEM micrographs of MWCNTs bridging a matrix crack; the inset highlights MWCNT pullout from the matrix [81].

Assuming that classical mechanics is valid at the nanoscale, the efficiency of the energy dissipation of nano sized fillers, such as nanotubes, can be evaluated if compared with microsized fibers for which filler pullout and filler fracture mechanisms are considered to be active. According to [76], a fair approach, to prove the CNT pullout energy dissipation capability, would consist in comparing the pull-out energy dissipated by a single microfiber of a given volume  $V_{mf}$  and critical length  $L_{cmf}$  with the

pull-out energy dissipated by a certain number  $n_{CNTs}$  of nanotubes having their own critical length  $L_{CNT}$ , volume of a single tube equal to  $V_{CNT}$  and a total volume equivalent to that of the microfiber,  $V_{mf}$ ; for both cases, the microfiber/nanotubes are perfectly aligned with the perpendicular direction to the crack plane (Figure 5.68) because for a fiber-based composite, the condition of maximum toughness (due to pullout) is achieved when fibers lie perpendicular to the plane of the crack. It can be observed that the total surface area of nanotubes is much larger than the area of the fiber having micrometer size. Other assumptions are: matrix material is rigid plastic, the micro-fiber or nanotube material behavior is linear elastic, all stress transfer from matrix to micro-fiber or nanotube occurs only by interfacial shear around the periphery of the fiber/tube when fiber/tube bonds with the matrix, the micro-fiber/matrix interfacial shear strength  $\tau_{mf}$  and the nanotube/matrix interfacial shear strength,  $\tau_{CNT}$  are constant values. The length of both types of filler has been chosen as the critical length since composite toughness is known to be maximized when the fiber length is equal to the critical length which separates the fibre pullout from the fiber fracture regime. In fact, within the cited assumptions, the micro fiber/nanotube fails under tension when a critical length condition is achieved [82]:

$$L_{cmf} = \frac{r_{mf}\sigma_{mf}}{\tau_{mf}} \quad \text{and} \quad L_{cCNT} = \frac{r_{CNT}\sigma_{CNT}}{\tau_{CNT}} \quad (5.13)$$

where  $r_{mf}$  and  $r_{CNT}$  are the fiber and nanotube radius, respectively and  $\sigma_{mf}$  and  $\sigma_{CNT}$  are the tensile strength of the microfiber and nanotube, respectively. Then, the upper limit for the pullout energy can be achieved by assuming that the volume of all CNTs is rearranged in the form of parallel tubes undergoing pull-out, as shown in Figure 5.68.

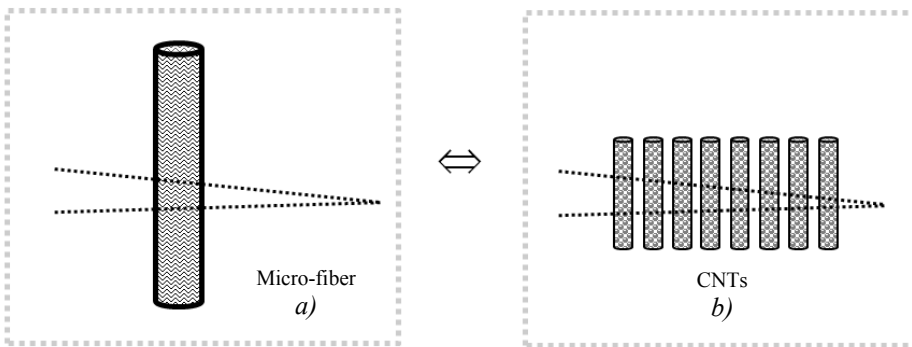


**Figure 5.68: Schematic representation of a crack propagating in a composite: through a micro-fiber a) and a certain number of CNTs b) having total volume equivalent to the volume of the microfiber.**

The required number of nanotubes having the same total volume  $V_{mf}$  in the same matrix is then:

$$n_{CNTs} = \frac{V_{mf}}{V_{CNT}} = \frac{r_{mf}^2 L_{cmf}}{r_{CNT}^2 L_{cCNT}} \quad (5.14)$$

The fiber length pulled out at fracture plane varies between 0 and  $L_c/2$ , as depicted in Figure 5.69. Being  $r_f$  and  $\tau_f$  the radius and the interfacial shear strength of a generic fiber, respectively, the average pullout energy (at fracture),  $G_{pf}$ , per fiber is then [76]:

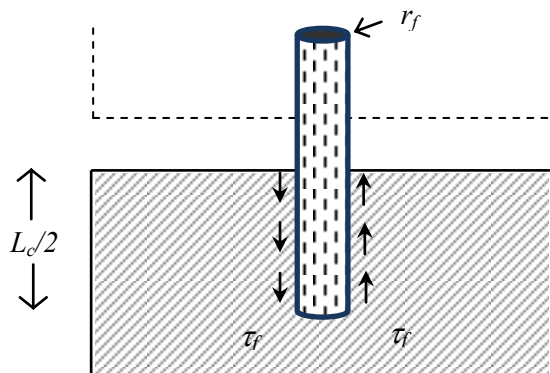


**Figure 5.69: Schematic illustration of a single fiber pullout.**

$$G_{pf} = \frac{1}{12} \pi r_f \tau_f L_c^2 \quad (5.15)$$

which corresponds to the work done in separating the specimen into two halves [82]. The ratio of the total pull-out energy for a set of  $n_{CNTs}$  nanotubes to the corresponding pullout energy for a single micro-fiber having the same volume  $V_{mf}$  is obtained using equation 5.14:

$$\frac{n_{CNTs} G_{pCNT}}{G_{pmf}} = \frac{n_{CNTs} r_{CNT} \tau_{CNT} L_{cCNT}^2}{r_{mf} \tau_{mf} L_{cmf}^2} = \frac{\sigma_{CNT}}{\sigma_{mf}} \quad (5.16)$$

where  $\sigma_{mf}$  and  $\sigma_{CNT}$  are the tensile strength of the microfiber and nanotube, respectively. Wichmann et al. [76] reported that the ratio  $\sigma_{CNT}/\sigma_{mf}$  is generally equal to

4–100 for typical CNTs and carbon micro-fibers (Carbon fibers have strengths of the order of 1–7 GPa, whereas CNTs have experimental strengths of the order of 30–100 GPa). Therefore, the energy absorption resulting from the pull-out mechanism for nanotubes is potentially much higher than that of conventional microfibers having an equivalent total volume.

A similar analysis can be conducted to compare the energies for breakage of a microfiber and a set of  $n_{CNTs}$  nanotubes having the same total volume, as assumed previously. The fracture energy of a generic fiber  $G_{ff}$  with linear elastic properties is [79]:

$$G_{ff} = \frac{\pi r_f^2 \sigma_f^2 L_c}{2E_f} \quad (5.17)$$

where  $E_f$  is the tensile modulus of the generic fiber. Then, the ratio of the fracture energy for a set of  $n_{CNTs}$  nanotubes to the corresponding fracture energy  $G_{fmf}$  for a single microfiber having the same total volume is:

$$\begin{aligned} \frac{n_{CNTs} G_{fCNT}}{G_{fmf}} &= \frac{n_{CNTs} r_{CNT}^2 \sigma_{CNT}^2 L_{cCNT}}{2E_{CNT}} \cdot \frac{2E_{mf}}{r_{mf}^2 \sigma_{mf}^2 L_{cmf}} \\ &= \frac{L_{cmf}}{L_{cCNT}} \cdot \frac{E_{mf}}{E_{CNT}} \cdot \left( \frac{\sigma_{CNT}}{\sigma_{mf}} \right)^2 \end{aligned} \quad (5.18)$$

where  $G_{fCNT}$ ,  $G_{fmf}$  and  $E_{CNT}$ ,  $E_{mf}$  are the maximum fracture energy and the tensile modulus of a single nanotube/single micro fiber, respectively. In [79], the numerical value of this ratio is estimated to be at least 1000 for typical CNTs and carbon-fibers.

This analysis suggests that the potential energy absorption in both fiber pull-out and fiber fracture is expected to be much greater for a set of nanotubes than for a corresponding micro-fiber having an equivalent volume. However, this straightforward model provides an ideal quantification as well as an upper limit for CNT energy dissipation since a great number of limiting factors may significantly reduce the toughening capability of CNTs. For instance, the possibility of CNT agglomeration reduces this potentiality due to the decrease of available interface area between matrix and CNT; the orientation of tubes with respect the loading direction usually is rather than perpendicular to the crack tip and not uniform within the whole composite and along the length of the CNT; moreover, the high level of stress around nanotubes may cause matrix failure, increasing the absorbed energy contribution from micro cracking. There is also another important issue related to the characterization of the effect of

CNT aspect-ratio on energy absorption because of the difficulty in accurately control this ratio in the experiments. All these factors may contribute to the limited success and the wide range of experimentally observed results. These circumstances request a better understanding of the deformation mechanisms and CNT variables governing nanocomposite fracture in order to optimize the design of the nanocomposite microstructure (nanotube–polymer interface, nanotube volume fraction, etc.) for enhanced toughness.

### **5.3.1. CNT fracture toughness modeling**

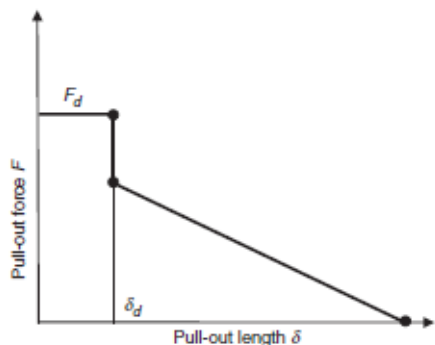
Although MD simulations appear very suitable to describe interactions at CNT-matrix atomic level, they are sometimes limited by length and time scales when larger systems have to be analyzed, requiring very long simulation time. These limitations often make continuum micromechanics approaches more effective for analyses at length scales in the micron range. For this reason, in numerous past studies, CNT toughening mechanisms have been first identified and then modeled according to micromechanical approaches that were generally used for micro-fiber based composites. Particular emphasis has been given to the analytical shear lag model originally proposed by Cox [83], which was aimed at estimating of the stresses in the fiber transferred from the matrix through the interface; or to the modeling of single straight fiber pullout on the basis of the approach proposed by Kelly [82]. These micromechanical models may represent a valid starting point for understanding and modeling nanocomposites toughness.

As mentioned in previous sections, at micromechanical level the fracture energy of CNT polymer composites is related to the energy dissipated by different toughening mechanisms: crack pinning, crack deflection, debonding or pullout, matrix deformation or void nucleation, CNT fracture, bridging, microcracks. Nevertheless, these mechanisms are influenced by several parameters, such as, volume fraction of CNTs, CNT size and shape, interfacial bonding, CNT orientation and are often difficult to distinguish. In addition, it is not necessary for all these contributions to act simultaneously for a certain nanocomposite system; in fact, in some cases, one of these toughness contributions may dominate the total fracture toughness of CNTs reinforced composites. It has been also proved that the most important toughness mechanism in CNT polymer composites are represented by nanotube pullout and nanotube fracture. As well as in conventional fiber pullout mechanism, there are three main stages

characterizing nanotube pullout. The first stage is called the bonded stage, in which the nanotube and the matrix are well bonded. As the pull-out force reaches a certain threshold value, the debonding stage begins. During this stage, part of the nanotube moves along the debonded interface resisted by a friction force, while the rest of the nanotube remains well bonded to the matrix. Nanotube sliding from the matrix occurs when debonding extends to the entire interface. In this final stage, the entire nanotube slides through the matrix resisted by frictional forces. The proper modeling of this mechanism is a fundamental concern since it is used to determine the effective traction law for the CNT bridging stress as well as the steady state bridging toughness increment.

Different models have been proposed to describe the pullout behavior of CNTs, mainly based on continuum mechanics (including shear lag approach and  $J$ -integral computation) with the final aim of predicting toughness enhancement of both CNT polymer composites and laminate composites.

Gao and Li [84] developed a shear lag model for CNT/polymer composites by modeling a capped nanotube as an effective fiber based on molecular structure mechanics. The ‘free ends’ boundary conditions, reported in the original Cox [83] model, were modified to account for a fully embedded nanotube. They found that the large aspect ratio of nanotubes is responsible for an increase of interfacial stress transfer, improving the reinforcing effects of nanotubes. Tong et al. [85] developed two continuum-mechanics-based mechanistic models to characterize the pull-out behavior of a long MWCNTs from its surrounding matrix. Both models were employed to describe the bridging tractions provided by MWCNTs perpendicularly embedded in the matrix between the two adjacent layers of a laminated composite in a double cantilever beam (DCB) test specimen. In detail, one model was proposed to reproduce the mechanism of debonding and its propagation along the MWCNT–matrix interface due to weak interfacial shear strength; the simplified pull-out force,  $F_{MWCNT}$ , and displacement,  $\delta$ , relationship was assumed as in equation (5.19), where  $F_d$  is the constant applied pull-out force for the whole debonding propagation process,  $\delta_d$  is the maximum pull-out displacement at the onset of a MWCNT fully debonded from its surrounding matrix,  $\tau_f$  is the friction shear stress between the MWCNT and the matrix,  $d_c$  and  $l$  are the MWCNT diameter and length, respectively.

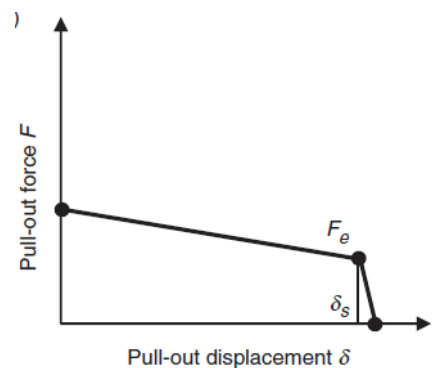


$$F_{MWCNT} = \begin{cases} F_d & 0 \leq \delta \leq \delta_d \\ \tau_f \pi d_c (l - \delta) & \delta_d \leq \delta \leq l \end{cases}$$

(5.19)

**Figure 5.70: Relationship between the pull-out force and pull-out displacement for a MWCNT being pulled out from its surrounding matrix [85].**

The other model took into account the sword-in-sheath mechanism after the breakage of the outermost layer in a MWCNT. The pull-out force for the case of the inner layer of MWCNTs being pulled out from the outermost nanotube after the outermost layer breaks, was assumed as follow:



$$F_{MWCNT} = \begin{cases} \tau_{fW} \pi d_c (l - \delta) & 0 \leq \delta \leq \delta_s \\ \frac{\bar{l} - \delta}{\bar{l} - \delta_s} F_e & \delta_s \leq \delta \leq \bar{l} \leq l \end{cases}$$

(5.20)

**Figure 5.71: Pull-out force and displacement curve MWCNT sword in sheath mechanism [85].**

where  $\tau_{fW}$  is the frictional stress between the outermost CNT of the MWCNT and the rest of the inner layers,  $F_e = \tau_{fW} \pi d_c (l - \delta)$ ,  $\bar{l}$  is chosen as  $l$  for approximation and  $\delta_s$  is the displacement limit for complete sliding between tubes. These relationships were applied to quantify the retard to the delamination crack propagation and the consequent enhanced delamination toughness. Their numerical results showed that an increase in the MWCNTs density, length, and interfacial shear stress as well as maximum pull-out displacement of MWCNTs, could lead to a higher mode I delamination toughness of composite laminates.

Blanco et al. [86] presented an analytical model for the Mode I interlaminar fracture of laminated composites reinforced with aligned carbon nanotubes (CNTs). The model was based on the crack-closure technique for fiber bridging, where the toughening mechanisms of the aligned CNTs were either pullout (frictional sliding) from the matrix or sword-in-sheath sliding. Particularly, to capture bridging due to pullout, the Dugdale model (a homogenized bridging zone law of continuously distributed nonlinear springs) was used, resulting in a linear and softening form of the bridging stress  $p(x)$  on the crack face as reported in equation 5.21, where  $\tau_c$  is the interfacial shear stress of the CNT being pulled out from the matrix,  $r$  and  $L_{CNT}$  are the radius and the length of the CNTs, respectively,  $v_{CNT}$  is the volume fraction of the CNTs and  $u(x)$  is the crack opening of the bridged zone.

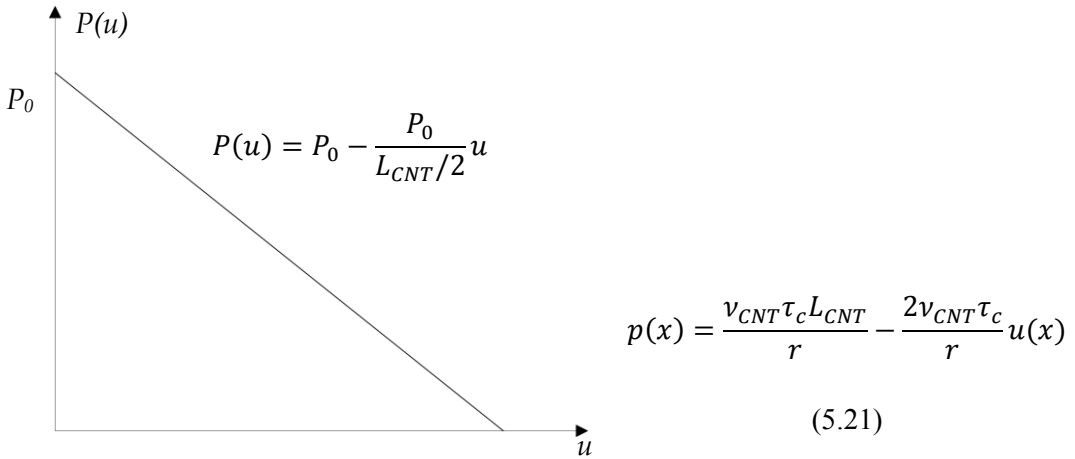


**Figure 5.72: Linear bridging law for pullout of CNTs [86].:**

Concerning the sword-in-sheath mechanism, the mathematical formulation of the bridging stress  $p(x)$  law was expressed as:

$$p(x) = \begin{cases} \frac{2\tau_{in,out}v_{CNT}}{r} \left( \frac{L_{CNT}}{2} - u(x) \right) & 0 \leq u(x) \leq \delta_1 \\ \frac{2\tau_{in,out}v_{CNT}}{r} \left( \frac{\frac{L_{CNT}}{2} - \delta_1}{\delta_2 - \delta_1} \right) (\delta_2 - u(x)) & \delta_1 \leq u(x) \leq \delta_2 \\ 0 & \delta_2 \leq u(x) \end{cases} \quad (5.22)$$

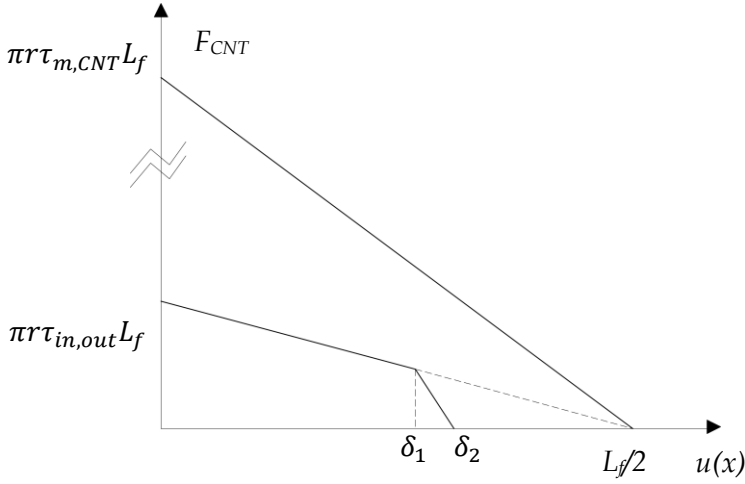


**Figure 5.73: Mathematical illustration of equations 5.21 and 5.22 (MWCNT pullout and sword in sheath mechanism) [86].**

where  $\tau_{in,out}$  is the interfacial shear strength between the outer and the inner CNT and  $\delta_1$  and  $\delta_2$  are taken from characteristic experimental values. By using these laws, Blanco et al. [86] obtained the normalized expression for the delamination resistance improvement in the steady-state regime, i.e. with  $u(x) = \tilde{u} = L_{CNT}/2$ :

$$\frac{G_{ss}}{G_0} = \begin{cases} 1 - \frac{\alpha_p^2}{\beta_p G_0} = 1 + \frac{1}{2} \left( \frac{L_{CNT}}{r} \right) \frac{\nu_{CNT} \tau_c L_{CNT}}{G_0} & \text{due to pullout} \\ 1 + \frac{1}{G_0} (2\alpha_{ss} \delta_1 + \beta_{ss} \delta_1^2 + \beta \Omega_{ss} (\delta_2 - \delta_1)) & \text{due to sword in sheath} \end{cases} \quad (5.23)$$

with:

$$\alpha_p = \frac{\tau_c \nu_{CNT} L_{CNT}}{r}$$

$$\beta_p = -\frac{2\tau_c \nu_{CNT}}{r}$$

$$\alpha_{ss} = \frac{\tau_{in,out} \nu_{CNT} L_{CNT}}{r}$$

$$\beta_{ss} = -\frac{2\tau_{in,out}v_{CNT}}{r}$$

$$\Omega_{ss} = \frac{\tau_{in,out}v_{CNT}L_{CNT}}{r} \left(1 - \frac{\delta_1}{L_{CNT}/2}\right)$$

Then, the balance of energy when the crack propagates was expressed to the application of  $J$  integral introducing the previous bridging stress models. The authors demonstrated that fiber aspect ratio is critical in the bridging process, with longer stitching fibers allowing a better bridging of the crack. In addition, even though the pullout mechanism dissipates more energy than the sword-in-sheath mechanism, CNT fracture is a limiting factor on toughness enhancement when reducing fiber diameter.

Chen et al. [87] proposed a CNT toughening model based on three levels of failure analysis: atomistic, meso and macroscale level. An atomistic-level failure model was used for characterizing CNT/matrix interfacial bond breaking whereas a mesoscopic-level model, based on shear leg theory, was adopted to study CNT-fiber failure and obtain the force–displacement relation of equivalent nonlinear springs; finally a macroscopic-level model, based on fracture mechanics, was used to express equivalent bridging nonlinear springs. The results of the study suggested that both longer CNTs and strong CNT/matrix interface do not definitely confer better fracture toughness on composites because the failure mode is converted from CNT pull-out to CNT breakage. The cited models were developed considering a unique (average) value for CNT length and fixed CNT orientation (i.e. aligned with respect to the loading direction).

However, in actual CNT reinforced composites, CNTs are rather misaligned within the matrix, following an orientation distribution. In this condition, the crack surfaces are bridged by inclined CNTs which are pulled out at various angles. Hence, CNT pullout models which include these characteristics are desirable in order to correctly predict the mechanical properties CNT reinforced composite systems. Grimmer et al. [88] considered CNT orientation in their model; in particular, they developed an energy-based model (based on previous work in fracture of ceramic composites) to evaluate the expected losses due to CNT pull-out and CNT fracture with regard to the delamination fatigue resistance in carbon nanotube reinforced glass fiber/polymer composites. The CNT orientation was taken into account by considering a random distribution of CNTs within the matrix system. Mirjalili and Hubert [89] modeled CNTs bridging effect on the toughening of polymers by taking into account the orientation of CNTs with respect to the crack front and the nanotube rupture

contribution to the CNT bridging energy computation. Particularly, the fracture toughness of polymers was modeled considering two dominant toughening mechanisms acting within CNT-modified polymers, i.e. CNT pull-out and CNT rupture. The contributions to the bridging stress were calculated using the definition of the  $J$ -integral and taking into account the effect of aligned (with respect to the crack growth plane) and randomly oriented CNTs on the fracture toughness of CNT/polymer composites. This model is described next for comparison purposes that will be addressed in the subsequent paragraphs. The following assumptions have been made by Mirjalili and Hubert:

- CNTs are straight with cylindrical geometry;
- CNTs are assumed inextensible and sufficiently strong to enable complete pullout without rupture up to a critical length value;
- CNT length is given as a unique value as an average length (rather than a length distribution);
- CNT-matrix bond is assumed to be frictional and the interfacial shear stress between the nanotube and the polymer is assumed constant;
- the pullout energy contribution is computed for CNT lengths less than a critical length value;
- the value of  $J_{rupture}$  ( $J$  integral) representing the contribution of broken CNTs is computed as the area under the stress vs. displacement curve for rupturing a CNT. For this purpose a linear stress–strain curve for the CNTs is assumed.

Within these assumptions, the total contribution of aligned CNTs to the bridging energy is:

$$J_{pull-out}^{Aligned} = \frac{1}{12} V_{CNT} \left( \frac{\tau L_{CNT}^2}{r} \right) \quad L_{CNT} \leq l_c \quad (5.24)$$

$$J_{pull-out}^{Aligned} + J_{rupture}^{Aligned} = \frac{1}{12} V_{CNT} \frac{l_c}{L_{CNT}} \left( \frac{\tau l_c^2}{r} \right) + \frac{1}{2} V_{CNT} \left( 1 - \frac{l_c}{L_{CNT}} \right) \sigma_u L_{CNT} \varepsilon_{max} \quad L_{CNT} > l_c \quad (5.25)$$

where:

- $J_{pull-out}$  is the CNT pullout energy contribution;
- $J_{rupture}$  is the energy associated with CNT failure;
- $V_{CNT}$  is the CNT volume fraction;
- $r$  is CNT radius;
- $L_{CNT}$  is the average CNT length;

- $\tau$  is the (constant) interfacial shear stress between the nanotube and the polymer;
- $\sigma_u$  is the nanotube ultimate strength;
- $\varepsilon_{max}$  is the CNT elongation before failure;
- $l_c$  is the CNT critical length which represents the limit for CNT pullout and is defined in equation 5.13.

The  $J$  contribution in case of  $L > l_c$  is derived assuming that CNTs are fully dispersed; this implies that only  $V_f \frac{l_c}{L_{CNT}}$  portion of the CNTs will be pulled-out, and the rest of the CNTs,  $V_f \left(1 - \frac{l_c}{L_{CNT}}\right)$ , will fracture. It should be noted that according to the value of  $l_c$  for CNTs, the pull-out portion of the nanotubes can be very small. The bridging effect of randomly oriented CNTs is then estimated assuming that CNTs have uniform orientation distribution. The contribution of randomly oriented CNTs is estimated through  $J_b(\theta)$ , which represents the energy contribution of a CNT bridging a crack with an angle  $\theta$ , and is expressed by means of a known orientation distribution function  $f(\theta)$ . The equation is then simplified assuming a critical angle,  $\theta_c$ , which divides the bridging contribution of randomly oriented nanotubes into those that do not contribute. From a mathematical point of view,  $\theta_c$  represents the angle for which the area underneath the curve  $(\theta) = \sin^2\theta(\cos^3\theta + \sin^3\theta)$ , over  $0-90^\circ$ , is equal to the area of the hatched rectangle over  $\theta_c-90^\circ$ . The corresponding computed critical angle is  $\theta_c = 50^\circ$ . Thus, the CNT bridging effect for randomly oriented CNTs in a 3D space can be found by multiplying the  $J$  expressions (equations 5.24 and 5.25) by the probability of having CNTs oriented between  $50^\circ$  and  $90^\circ$ . This probability is the area of a spherical cap having a height of  $L_{CNT}/2 * (1-\sin 50)$ , divided by the area of a half sphere with diameter  $L_{CNT}$ ; the computed value corresponds to 0.23. This means that only 23% of randomly oriented CNTs will contribute to the bridging process. Finally, the CNT bridging effect for randomly oriented CNTs in a 3D space can be written by multiplying  $J$  expressions by 23%:

$$\begin{aligned}
 J_b^{random} &= 23\% \cdot J_{pull-out}^{Aligned} = \\
 &= 0.23 \cdot \left[ \frac{1}{12} V_{CNT} \left( \frac{\tau L_{CNT}^2}{r} \right) \right] L_{CNT} \leq l_c
 \end{aligned} \tag{5.26}$$

$$J_b^{random} = 23\% \cdot (J_{pull-out}^{Aligned} + J_{rupture}^{Aligned}) = \tag{5.27}$$

$$= 0.23 \left[ \frac{1}{12} V_{CNT} \frac{l_c}{L_{CNT}} \left( \frac{\tau l_c^2}{r} \right) + \frac{1}{2} V_{CNT} \left( 1 - \frac{l_c}{L_{CNT}} \right) \sigma_u L_{CNT} \varepsilon_{max} \right] \quad L_{CNT} > l_c$$

From the description of these pullout models, it can be observed that even though CNT effective length has been demonstrated to be highly variable within a polymer composite system (see section 5.2.1), generally only an average length is used to describe the nanotube characteristic length. Moreover, CNT orientation is often handled considering CNT random distribution. The lack of this information (i.e. length and orientation distribution) may lead to poor effectiveness of theoretical modeling and final product performance analysis. In fact, it is well known that the final mechanical properties of CNT reinforced composites, such as tensile strength, elastic modulus, and fracture toughness, are strongly dependent on the whole nanotube length distribution rather than an average length and/or angle. An example of micromechanical model accounting for both CNT length and orientation distribution, can be found in [27] in case of prediction of CNT composite strength. In that study, CNT length after processing of composites was measured and then characterized using a two-parameter Weibull distribution function. The CNT strength was evaluated by means of the CNT reinforcing efficiency factor ( $\lambda$ ) for the composite strength, which was estimated from the information about CNT length distribution and critical CNT length for randomly distributed CNT reinforced polymer composites. Recently, Chowdury et al. [90] developed a nano-mechanical model to calculate the tensile modulus and the tensile strength of randomly oriented short CNT reinforced nanocomposites considering the statistical variations of diameter and length of the CNTs. According to this model, the entire composite was assumed to be composed of a certain number of composite segments which contain CNTs of almost the same diameter and length. The tensile modulus and tensile strength of the composite were then calculated by the weighted sum of the corresponding modulus and strength of each composite segment.

The last two aforementioned examples, consider both CNT length and orientation statistical variability (Fu work, [27]) and CNT length and diameter statistical variability (Chowdury [90] work) to predict CNT composite tensile elastic modulus and strength. As matter of fact, no analytical model, which includes statistical variability for both CNT length and orientation, has been proposed to predict fracture toughness of CNT based composites. The micromechanical model presented in the following section is based on these assumptions, i.e. CNT length and orientation variability, and is used to predict interlaminar mode I fracture toughness of nanofilled S2-glass fiber/epoxy laminated composites.

## 5.4. Current CNT pullout model

In this section, a micromechanical-based model is presented in order to model interlaminar mode I fracture toughness of S2-glass fiber/epoxy laminated composites, modified using nanofillers (Carbon NanoTubes, CNTs, and Carbon NanoFibers, CNFs) with/without surface functional groups and with different ranges of aspect ratio [91].

The present model was originally developed by Jain et al. [92] (in turn derived by the work on fiber pullout mechanics provided by Li et al. [93]) and successively formulated, in a more general form, by Fu and Lauke [94]; both models have been successfully used for quantifying the fracture energy of short fiber-brittle matrix composites due to pullout. In particular, Fu and Lauke model is suitable for evaluating the fiber pull-out energy (but no fracture energy of broken fibers) of short fiber composites and takes into account fiber length variability as well as fiber orientation variability. The main scope of using Fu and Lauke model is firstly to implement, for CNT based composites, a formulation that includes both length and orientation distribution to predict interlaminar mode I fracture toughness of nanofilled S2-glass fiber/epoxy laminated composites. Moreover, further issues will be addressed by comparing Fu and Lauke model with a formulation suitably developed for CNT based composites (rather than short fibers), for quantifying the enhancement of fracture toughness in CNT-modified polymers i.e. the Mirjalili model [89], illustrated in Section 5.3.1.

In detail, Fu and Lauke [94] is used to determine the steady state bridging toughness increment when CNTs are added into a matrix interlayer between two adjacent glass fiber reinforced composite plies. The nanofilled interlayer is the region encompassing the CNTs and excluding the glass fibers, denoted with thickness  $T_{max}$ , as reported in Figure 5.74b.

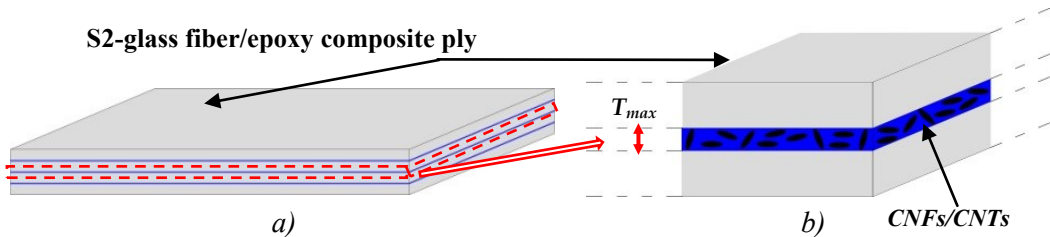


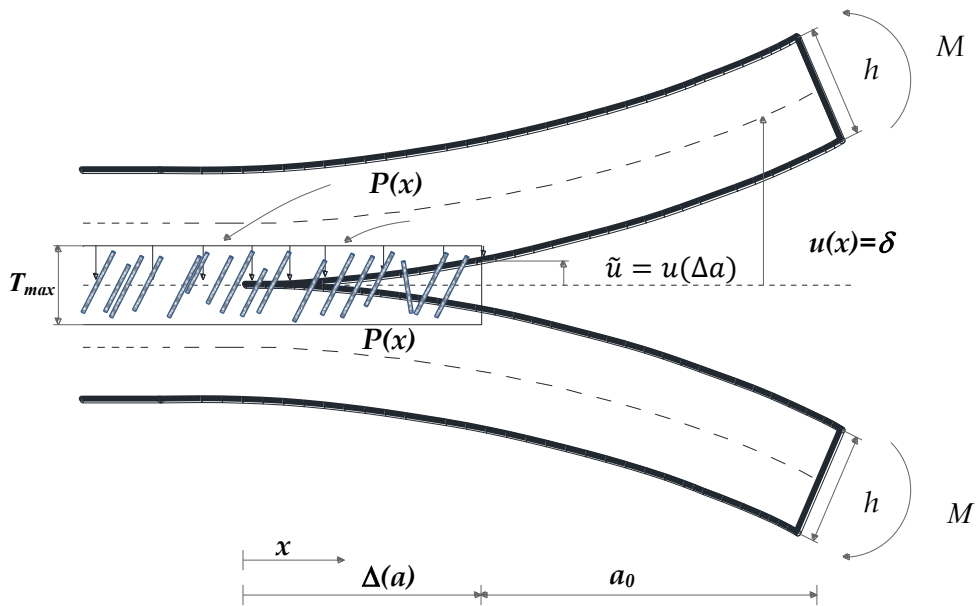
**Figure 5.74: Schematic representation of CNF/CNT filled epoxy resin interlayer placed at the midplane of the composite laminate (highlighted in red); a) S2-glass fiber/epoxy laminated composite, b) focus on the nanofilled epoxy interlayer placed at the midplane of the laminate.**

Consider a double cantilever beam (DCB) specimen with the CNTs of the matrix interlayer bridging the crack opening in a Mode I interlaminar shear test. The CNT orientation is assumed to be variable within the interlayer. Figure 5.75a depicts a schematic representation of the problem whereas Figure 5.75b illustrates the bridging action of CNTs/CNFs within the resin interlayer while crack propagates at the midplane of the laminate.

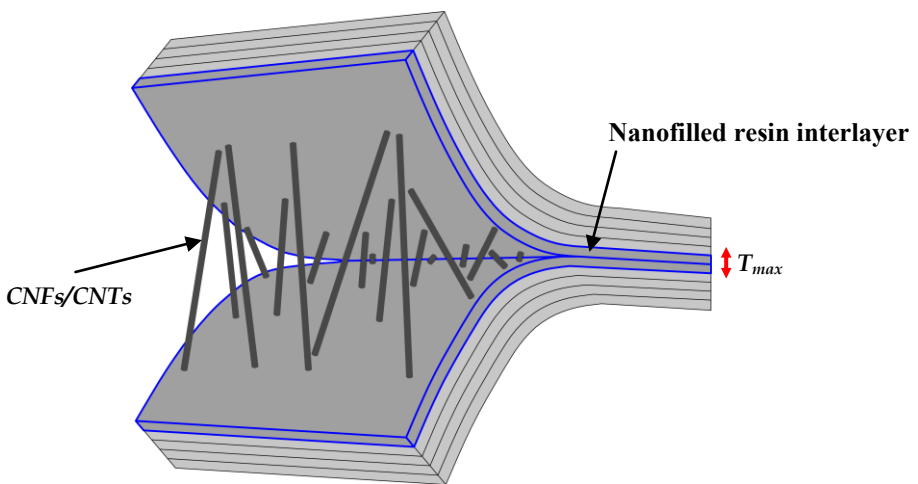
In terms of Mode I interlaminar fracture energy as a function of crack opening, some characteristic stages can be identified during a Mode I test involving CNT reinforced composite laminates (which are assumed to be homogeneous orthotropic). The first energy limit that is reached,  $G_0$  (initial toughness), is due to fracture of neat resin; this energy contribution is assumed, as hypothesis, unchanged when the nanoreinforced layer is produced; afterwards, interlaminar fracture energy increases as crack opening proceeds as a consequence of bridging crack closure exerted by CNTs in the interlayer. In fact, for stable extension of the crack, the crack opening force must equal the resistance to crack propagation. The resistance to crack extension is the non-recoverable work done per unit area in propagating the crack. This condition can be expressed through the balance of energy when crack propagates along the middle plane of the interlaminar matrix layer by the application of  $J$ -integral [86, 95]:

$$G_R(\Delta a) = G_0 + 2 \int_0^{\tilde{u}} P(x) du \quad (5.28)$$

where  $G_R$  is the propagation fracture toughness as a function of crack growth,  $\Delta a$ ,  $\tilde{u}$  is the crack opening at the mouth of the bridged zone ( $x=\Delta a$ ) and  $P(x)$  is closure traction stress due to the action of the CNTs; this action is provided by the CNT toughening mechanisms described in Section 5.3. However, it is not necessary for all these mechanisms to act simultaneously for a given nanocomposite system, and in some of them, one of these toughness contributions may dominate the total fracture toughness of CNTs reinforced composites. Within the present model, the bridging traction  $P(x)$  is assumed to be due to simple CNT pullout from the matrix. For the steady state crack growth condition, the upper limit of the integral is known, i.e.  $\tilde{u} = \frac{T_{max}}{2}$ , and the increase in fracture toughness due to bridging of CNTs,  $G_b$ , can be computed. Once the bridging traction stress  $P(x)$  acting on an infinitesimal element  $bxdx$  at a distance  $x$  from the crack tip is made explicit, a possible method to compute  $G_b$  is by finding the area under the effective crack opening-traction curve.



a)



b)

Figure 5.75: Illustration of the CNT-bridged Mode I IFT specimen, a); focus on the CNF/CNT bridging action during crack propagation, b).

An alternative method to compute the nanocomposite steady-state fracture energy increment from bridging of CNTs is by using the energy absorbed by the pullout of a single CNT and then integrating to incorporate contributions from all the CNTs bridging the crack [92]. Following the second method, Fu and Lauke [94] derived the expression for the nanocomposite steady-state fracture energy increment due to fiber pullout (we will assume CNT instead of a generic fiber). The computation has been conducted considering arbitrary CNT orientation and variable CNT length. The assumptions made within the model can be summarized as follows:

- A mode I delamination crack propagates along the middle plane of the interlaminar matrix layer containing the CNTs, i.e. the load direction is normal to the face of the crack as in Figure 5.76;
- Matrix crack is planar and CNTs will bridge this matrix crack;
- CNTs are straight with cylindrical geometry;
- CNTs are assumed inextensible and sufficiently strong to enable complete pullout without rupture up to a critical length value of the fiber;
- the CNT embedded length may vary due both a length distribution and to the different orientation of the CNTs with respect to the loading direction;
- CNT-matrix bond is assumed to be frictional and the elastic bond is neglected;
- there will be a bridging traction only if the crack opening is less than the value of  $L_{CNT}/2$ ;
- issues related to bundles of multiple CNTs are not addressed;
- the effect of snubbing friction between CNTs and matrix at the CNT exit point during CNT pull-out is taken into account;
- fracture stress of CNTs obliquely crossing the fracture plane (i.e. the equivalent case of inclined strength of micro-fibers) is considered;
- the energy required for CNT breakage is not quantified.

A schematic view of CNT pullout within the interlayer is reported in Figure 5.76a whereas the scheme of the CNT pullout problem is shown in Figure 5.76b where  $s$  is the slippage distance of the embedded end of the CNT,  $l$  is the CNT embedded length,  $\delta$  is the crack opening displacement and  $\theta$  is the CNT inclination angle with respect to the load direction,  $P$ .

When the CNT is embedded between the two halves of the crack, only the shorter embedded length,  $l$ , undergoes pull out while the longer segment length ( $L_{CNT} - l$ ) will not pull out. This implies that the CNT bridging action due to pullout will be active only if crack opening is less than the value of  $L_{CNT}/2$ .

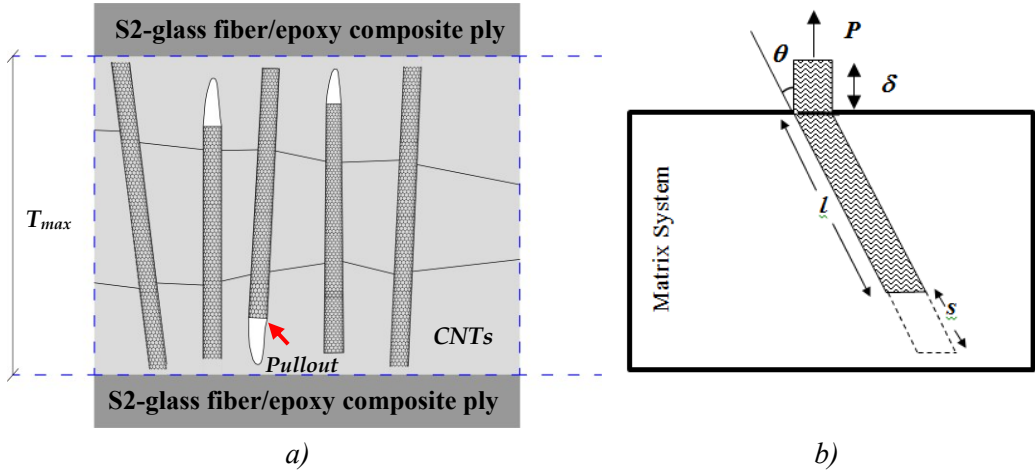


**Figure 5.76: Scheme of CNT pullout problem: a) pullout of different CNTs within the resin interlayer; b) CNT pullout schematization where  $l$  is the CNT embedded length,  $\delta$  is the crack opening displacement and  $\theta$  is the CNT inclination angle with respect to the load direction,  $P$ .**

Moreover, the embedded length varies due to the CNT orientation (with respect to the loading direction) and to the position of the center of mass of each tube through the thickness of the interlayer. As previously mentioned, the model treats CNTs by taking into account the statistical variation of CNT lengths and orientation. CNT length distribution and the CNT orientation distribution are assumed to be independent. Concerning CNT length distribution  $f(L)$  is the length probability density function, defined as:

$$f(L_{CNT}) = abL_{CNT}^{b-1}e^{-aL_{CNT}^b} \quad (5.28)$$

that is another form of a two parameter Weibull distribution, with  $a, b$  size and shape parameters, respectively (as reported in equation 5.2). From this distribution, the mean CNT length and the most probable length (mode length) are, respectively:

$$\bar{L}_{CNT} = \int_0^{\infty} L_{CNT}f(L_{CNT})dL = a^{-\frac{1}{b}}\Gamma\left[\frac{1}{b} + 1\right] \quad (5.29)$$

$$L_{CNT}^{mod} = \left[\frac{1}{a} - \frac{1}{ab}\right]^{\frac{1}{b}} \quad (5.30)$$

where  $\Gamma$  is the gamma function. In Section 5.2.1 this distribution was demonstrated to be suitable for describing CNT length sample data. The CNT orientation distribution is then described by means of the probability density function,  $g(\theta)$ , defined as [94]:

$$g(\theta) = \frac{[\sin\theta]^{2p-1}[\cos\theta]^{2q-1}}{\int_{\theta_{min}}^{\theta_{max}} ([\sin\theta]^{2p-1}[\cos\theta]^{2q-1})d\theta} \quad (5.31)$$

where  $\theta_{min} \leq \theta \leq \theta_{max}$  and  $p$  and  $q$  are the shape parameters which can be used to determine the shape of the distribution curve, and  $p \geq 1/2$  and  $q \geq 1/2$ . Figure 5.77 reports different CNT orientation distribution curves for different values of  $p$  and  $q$ . The mean CNT orientation and the most probable CNT orientation angle can be expressed in the following form, respectively:

$$\bar{\theta} = \int_{\theta_{min}}^{\theta_{max}} \theta g(\theta) d\theta \quad (5.32)$$

$$\theta_{mod} = \arctan \left\{ \left[ \frac{2p-1}{2q-1} \right]^{\frac{1}{2}} \right\} \quad (5.33)$$

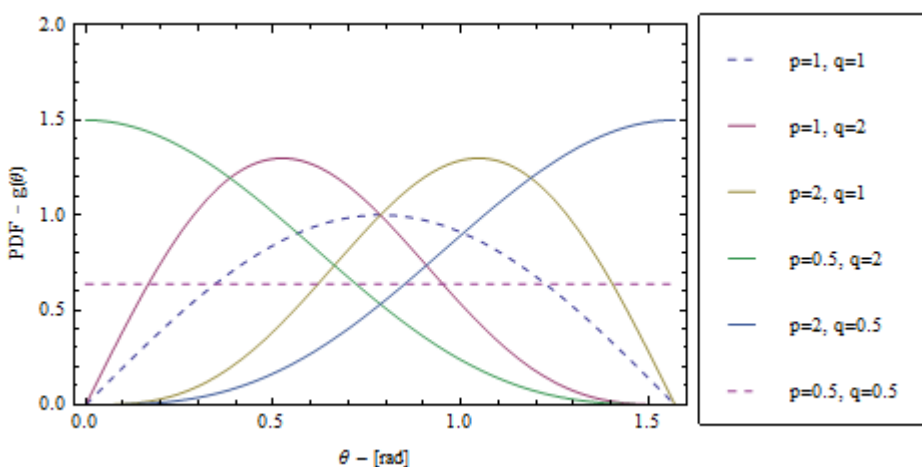


**Figure 5.77: PDF for CNT orientation distribution: equation 5.31 reported for different scale and shape parameters.**

If  $V_f$  is the volume fraction of CNTs, the CNT length distribution allows determination of the average (total) number of CNTs within the matrix interlayer specimen. However, this number has to be modified in order to account for the probability for a CNT (with shorter embedded length between  $l$  and  $dl$  and an angle from  $\theta$  to  $\theta + d\theta$ ) to cross the crack plane. To compute this probability, a uniform distribution of CNT center of gravity along the specimen thickness direction is assumed. Within these assumptions, the CNT pull-out energy is derived in a general

form as a function of CNT length distribution and CNT orientation distribution, as well as interfacial properties. Particularly, according to the Fu and Lauke model [94], the following expression can be used to evaluate the CNT pull-out energy:

$$G_b^{po} = \frac{8V_{CNT}a_0}{d_{CNT}\bar{L}_{CNT}} \left[ \int_{\theta=0}^{\bar{\theta}_{max}} \int_{L=L_{CNT}^{min}}^{L_{c\theta}} \int_{l=0}^{L/2} \left( \frac{l^2}{2} + \frac{a_1 l^3}{6a_0} + \frac{a_2 l^4}{12a_0} \right) f(L)g(\theta) \cos \theta e^{\mu\theta} dl dL d\theta + \int_{\theta=0}^{\theta_{max}} \int_{L=L_{c\theta}}^{L_{CNT}^{max}} \int_{l=0}^{L_{c\theta}/2} \left( \frac{l^2}{2} + \frac{a_1 l^3}{6a_0} + \frac{a_2 l^4}{12a_0} \right) f(L)g(\theta) \cos \theta e^{\mu\theta} dl dL d\theta \right] \quad (5.34)$$

where:

- $G_b^{po}$  is nanocomposite steady-state fracture energy increment due to CNT pullout and computed by taking into account CNT length distribution and CNT orientation distribution;
- $V_{CNT}$  is the CNT volume fraction compared to the matrix in the interlayer region;
- $d_{CNT}$  is CNT diameter (assumed as a unique value rather than on a statistical base);
- $\bar{L}_{CNT}$  is the mean CNT length;
- $a_0, a_1, a_2$  are constants determined empirically that characterize the interfacial friction shear stress providing the relationship between pull-out load and crack-opening displacement. In detail, the interfacial frictional shear stress  $\tau_{CNT}$ , is assumed to have the following form [93]:

$$\tau_{CNT}(s) = a_0 + a_1 s + a_2 s^2 \quad (5.35)$$

with  $s$  being the slippage distance of the embedded end of the CNT. Within the assumption of inextensibility of the tube representing the CNT, the slippage distance corresponds to the crack opening displacement  $\delta$ , thus:

$$\tau_{CNT}(\delta) = a_0 + a_1 \delta + a_2 \delta^2 \quad (5.36)$$

This expression accounts for a possible slip hardening-softening behavior at the CNT-matrix interface. In case of constant interfacial shear stress,  $\tau_{CNT}(\delta) = \bar{\tau}_{CNT}$ . Moreover, it is possible to account for an additional “snubbing” frictional stress supplied to misaligned fibers as the exit from the matrix, according to a snubbing coefficient, as proposed by [93]. Hence, the pullout can be written as:

$$\begin{aligned}
 P(l, \delta, \theta) &= \tau_{CNT}(\delta)\pi d_{CNT}(l - \delta)e^{\mu\beta} \quad \text{for } l \geq \delta \\
 P(l, \delta, \theta) &= 0 \quad \text{for } l < \delta
 \end{aligned}
 \tag{5.37}$$

where  $\mu$  is the snubbing friction between fibers and matrix at the fiber exit point;

-  $\theta_{min}, \theta_{max}$  are the lower and upper limit of the integration over the angles which contribute to pullout energy;

-  $L_{CNT}^{min}, L_{CNT}^{max}$  are the lower and upper limit of the CNT length distribution, respectively;

-  $L_{c\theta}$  is the critical CNT length for an oblique CNT pulled out at an angle,  $\theta$ , with the loading direction. In the case  $l \geq L_{c\theta}/2$  the fiber will break instead of being pulled out.  $L_{c\theta}$  can be expressed as:

$$L_{c\theta} = \frac{\sigma_{fu\theta} d_{CNT}}{2\bar{\tau}_{CNT} e^{\mu\theta}}
 \tag{5.38}$$

where  $\sigma_{fu\theta}$  is the fracture stress of oblique CNT equivalent to the so-called fiber inclined strength for short fiber composites. For brittle fibers the fracture stress of oblique fibers is given by:

$$\sigma_{fu\theta} = \sigma_{fu}(1 - A \tan\theta)
 \tag{5.39}$$

where  $\sigma_{fu}$  is the tensile strength of fibers which align in the loading direction,  $\tau_i$  the interfacial shear stress and  $A$  is a constant determining the fiber inclined strength. If  $L_c$  is the critical transfer length of aligned fibers, therefore  $L_{c\theta}$  can be rewritten as:

$$L_{c\theta} = L_c \frac{(1 - A \tan\theta)}{e^{\mu\theta}}
 \tag{5.40}$$

-  $\theta_{max}$  is the limit of fiber orientation angle defined by  $\sigma_{fu\theta} \geq 0$ :

$$\theta_{max} = \arctan(1/A)
 \tag{5.41}$$

When the inclined fiber strength effect is neglected, i.e.  $A=0$ , then the equation is reduced to the sum of three contributions (not reported here, see [94]). When the interfacial shear stress is assumed as a constant value  $\bar{\tau}_{CNT}$  (i.e. not depending on the crack opening displacement with  $a_1=a_2=0$ ) equation 5.34 reduces to:

$$G_b^{po} = \frac{8V_{CNT}\bar{v}_{CNT}}{d_{CNT}\bar{L}_{CNT}} \left[ \int_{\theta=0}^{\bar{\theta}_{max}} \int_{L=L_{CNT}^{min}}^{L_{c\theta}} \int_{l=0}^{L/2} \frac{l^2}{2} f(L)g(\theta) \cos \theta e^{\mu\theta} dl dL d\theta + \int_{\theta=0}^{\theta_{max}} \int_{L=L_{c\theta}}^{L_{CNT}^{max}} \int_{l=0}^{L_{c\theta}/2} \frac{l^2}{2} f(L)g(\theta) \cos \theta e^{\mu\theta} dl dL d\theta \right] \quad (5.42)$$

For aligned CNTs (i.e.  $\theta=0$ ) having a unique value of length  $L_{CNT} < L_c$  (i.e. the hypotheses of CNT length and orientation statistical variations are removed), all CNTs undergo pullout; in this condition, for  $A=\mu=0$ , the steady state pullout energy reduces to:

$$G_b^{po} = \frac{V_{CNT}\bar{v}_{CNT}L_{CNT}^2}{6d_{CNT}} \quad (5.43)$$

This result corresponds to the pullout energy term  $J_{pullout}$  of equation 5.24 reported by Mirjalili and Jain [89, 92] within the same assumptions, including the variation of the embedded length along the interlayer thickness. If we do not assume a statistical variation of the CNT center of gravity along the direction of thickness interlayer, then the energy due to pullout becomes:

$$G_b^{po} = \frac{V_{CNT}\bar{v}_{CNT}L_{CNT}^2}{d_{CNT}} \quad (5.44)$$

i.e. six times higher than the previous case (equation 5.43). This expression corresponds to the pullout energy term computed by Blanco et [86] (reported in equation 5.23) and is derived considering the hypothesis of having all CNTs bridging the crack plane. Therefore, the aspect related to the CNT center of gravity position along the thickness of the nanoreinforced layer appears very important since it affects the final value of pullout energy.

### 5.4.1. Experimental validation

The model presented in the previous section, has been implemented on the basis of the experimental data available from [91, 96] for validation purposes. This experimental campaign adopted, as baseline material, S2-glass fiber/epoxy laminated composite made by the filament winding method. The baseline material system was modified using nanofillers with different surface functional groups (for the investigated

cases, the functionalization is made of carboxyl and glycidylxypropyltrimethoxysilane, GPS) and with different ranges of aspect ratio by adding fillers in the interlayer region between plies. The experimental program concerned Mode I and Mode II interlaminar fracture toughness (IFT) tests and was originally designed to study the effect of nanofiller functionality, filler size or aspect ratio, filler placement method and filler alignment direction in order to achieve optimal improvement in the interlaminar fracture resistance of multi-scale reinforced composites. For the scope of the present study, only Mode I IFT tests will be analyzed.

#### **5.4.2. Materials and experimental results [91]**

##### ***Materials***

The baseline composite material was made of unidirectional fiber reinforced laminates made by wet filament winding method using type 449AA-750 S-2 Glass® fiber (AGY, Aiken, SC) and an epoxy resin matrix system.

The nanofillers added to the epoxy resin were the following:

- un-functionalized heat treated carbon nanofibers (UF-CNFs)
- short carboxyl-functionalized CNTs (COOH-CNTs)
- short hydroxyl-functionalized CNTs (OH-CNTs)
- un-functionalized vertical grown CNTs (VGCNTs)

VGCNTs, UF-CNFs, and OH-CNTs were used as raw material for the in-house production of silane-functionalized nanofillers. The silane coupling agent used to functionalize the oxidized VGCNTs and CNFs and the as-received OH-CNTs is 3-glycidylxypropyl-trimethoxysilane, referred to as GPS. Short GPS-CNTs, long GPSCNTs, and GPS-CNFs were used for manufacturing multi-scale reinforced composites. Additionally, multiscale composites were also manufactured using COOH-CNTs and UF-CNFs in the as-received condition. All of the functionalized nanofillers used to manufacture the multiscale composites are summarized in Table 5.2.

A total of seven types of CNT- or CNF-filled resin along with the baseline resin with no nanofiller have been considered and reported in the Table 5.8. The nanofiller concentrations were established on the basis of a previous studies where the nanofillers were dispersed using the bath sonication method; nanofiller concentrations used for the investigation were selected for each type of filler based on the resulting

maximum filler concentration for which no visual aggregate was detected and a uniform dispersion state was typically seen using the optical microscope.

**Table 5.7: Functionalized nanofillers used for making multi-scale reinforced composites**

<i>Name in this investigation</i>	<i>Functional group</i>	<i>Raw material for functionalization</i>
Short COOH-CNT	COOH-, OH-	Used as-received
Short GPS-CNT	3-Glycidyloxypropyl silane	Short OH-CNTs
Long GPS-CNTs	3-Glycidyloxypropyl silane	VGCNTs
GPS-CNFs	3-Glycidyloxypropyl silane	UF-CNFs

This condition may be useful for the assumption that not too many CNT bundles are present in the resin system after sonication. The particle-filled epoxide was sonicated in an ultrasonic bath operating at 45 W and 38.5 kHz for 2-8 hours as specified in Table 5.3.

Unidirectional reinforced composite sheets were manufactured by wet-winding method. The composite consisted of 20 plies and cured in a hot press held under a pressure of 240 kPa at 80°C for 2 hours and then 125°C for 3 hours.

**Table 5.8: Multiscale nanofiler-composite composition and sonication time**

Case	Resin system	Composition		Bath Sonication	
		CNFs	CNTs	Time (h)	Temperature (°C)
1	0.5 wt% UF-CNF epoxy	0.5 wt%		4	60
2	0.5 wt% GPS-CNF epoxy	0.5 wt%		2	60
3	0.5 wt% short GPS-CNT epoxy		0.5 wt%	8	60
4	0.25 wt% long GPS-CNT epoxy		0.25 wt%	8	60

The resulting fiber volume fraction of the cured composite was determined to be  $62\pm 2\%$ . The multiscale reinforced composites that will be considered within this study were made by adding a calculated amount of nanofilled resin (equivalent to the weight of resin in two plies of cured composite plate,  $\sim 14$  grams) to the surfaces of both sheets facing the midplane to serve as a nanofilled interlayer region on the fracture plane. The nanofilled interlayer was uniformly spread onto the wet prepreg using a Nylon roller. Mode I IFT tests were conducted using double-cantilever beam (DCB) specimens (prepared according to ASTM standard D5528-01) having length, width, and thickness of approximately  $150 \times 25 \times 3.5$  mm.

### ***IFT Test results***

By adding CNF- or CNT-filled resin at the fracture plane of IFT specimens (made without any nanofillers in the prepregged matrix material) led to significant enhancement of fracture toughness, see Table 5.9 and Figure 5.78. The most relevant experimental outcome that will be considered for the purposes of the study, is the increment in critical strain energy release rate,  $G_{I0}$ , for the mode I IFT test. This value represents the CNTs contribution to toughen the polymer matrix. In detail, a significant improvement in  $G_{I0}$  was obtained by adding either the UF-CNF or GPS-CNF resin interlayer (30-39% relative to the baseline). However, GPS functionalization of CNFs showed relatively little improvement in all toughness measures in comparison to material made with a UF-CNF interlayer. The effects of interlayer nanofiller length on toughness were evaluated using short GPS-CNTs and long GPS-CNTs. The addition of the short GPS-CNT interlayer increased  $G_{I0}$  by 52% compared to the baseline material. An even higher increase was obtained by using longer GPS-CNTs in the interlayer, i.e. 80%. These results demonstrated that using high aspect ratio, small diameter and functionalized nanofillers in the interlayer produced the highest fracture toughness of the S2- Glass/epoxy composite.

SEM observations revealed that for all composite samples made with or without a nanofilled interlayer, the glass fibers were uniformly packed throughout the entire thickness, showing no discrete resin-rich interlayer. This feature was attributed the resin in the interlayer that plausibly bled out during the consolidation process due to the low viscosity of the epoxy resin system used to manufacture the composites.

**Table 5.9: Mode I IFT test results**

MATERIAL INTERLAYER		Mode I Strain Energy Release Rate							
		Onset				Propagation			
		$G_{Io}$ (J/m <sup>2</sup> )	C.o.V. (%)	Increm. (%)	$G_{Io}$ incr. (J/m <sup>2</sup> )	$G_{Ip}$ (J/m <sup>2</sup> )	C.o.V. (%)	Increm. (%)	$G_{Ip}$ incr. (J/m <sup>2</sup> )
	Baseline Composite	127	4.2	0	-	616	1.9	0	-
Case 1	0.5 wt% UF-CNF epoxy	165	14	30	38	903	1.5	47	315
Case 2	0.5 wt% GPS-CNF epoxy	176	8.4	39	49	968	4.1	57	282
Case 3	0.5 wt% short GPS-CNT epoxy	193	8.6	52	66	1025	1.3	66	585
Case 4	0.25 wt% long GPS-CNT epoxy	228	8.4	80	101	1201	1.5	95	742

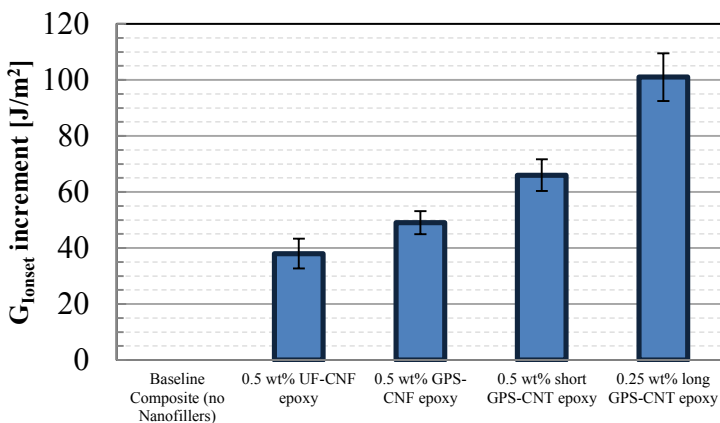


**Figure 5.78: Increment of the onset of damage  $G_{Io}$  for the mode I IFT test**

**Nanofiller toughening mechanisms**

SEM images of fracture surfaces of IFT specimens allowed Zhu [91, 97] to analyze the effects of CNTs or CNFs on the fracture behavior of the multi-scale reinforced composites. Results from SEM observations can be summarized as follows:

- When nanofiller particles were added in the interlayer a high number of CNTs/CNFs was found on the fracture surface, Figure 5.79a;
- Although the long GPS-CNTs were not long enough to prevent glass fiber pullout, SEM images showed many long GPS-CNTs pulled from the matrix Figure 5.79b and bridging matrix cracks;
- Concentration of filler was found in close proximity to the glass fibers at the fracture plane; during the material consolidation process, the epoxy in the interlayer was plausibly bled out and the fillers were entrapped by glass fibers, Figure 5.79a;
- Long CNTs can bridge the matrix crack in the narrow gaps between the glass fibers;
- Based on the increased toughness of the composites with an interlayer, it appeared that dense concentrations of CNTs and CNFs trapped in between the glass fibers inhibited delamination propagation.
- In case of functionalized CNTs/CNFs, an epoxy layer bonded to CNTs or CNFs was observed, (Figure 5.79d). Since this behavior was not typically observed for unfunctionalized fillers, plausibly a better adhesion between CNTs or CNFs with the epoxy matrix was obtained after functionalization.

Apart from the previous results, some other issues were pointed out by Zhu [91]. During the composite consolidation, due to the low viscosity, the resin in a liquid state flowed both along the glass fiber length direction and across the glass fiber length direction before specimen cure. However, while the resin can flow freely in all directions within a composite, the nanofillers may not. Moreover, the high glass fiber volume fraction (>60%) within the composite reduces the free space between glass fibers, which is, in a cross-section of glass fiber bundles, approximately 0-10  $\mu\text{m}$  (typically even smaller than the average length of long CNTs/CNFs). Hence, the glass fiber can restrict long CNTs/CNFs from migrating with the resin transverse to the fibers (leading to high concentration of filler in the interlayer) and favor the CNT migration along the fiber direction. Different CNT placement locations were investigated by Zhu [91] in order to understand the direction of CNT/matrix flow during the consolidation process. The results indicated that, during composite consolidation and cure, the short CNTs migrated along the fiber direction and towards the mid-plane when placed away from it.

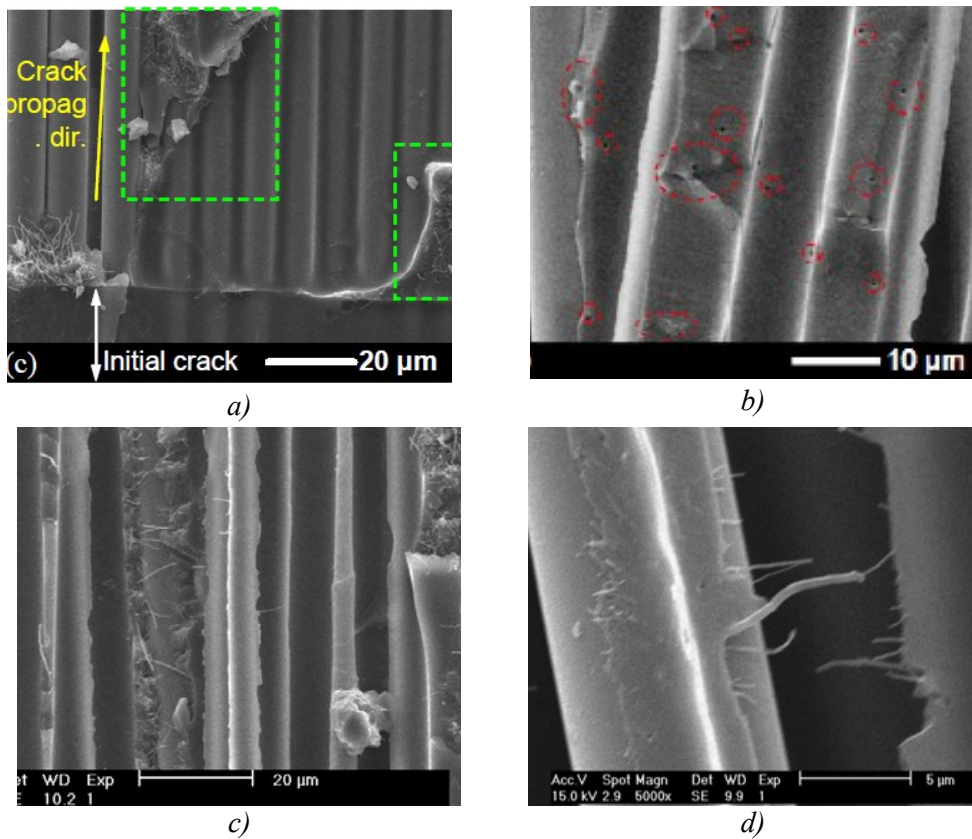


Figure 5.79: SEM images of mode I fracture surfaces [91]: a) composite with a long GPS-CNT epoxy interlayer; b) long GPS-CNTs in the interlayer: cavities in circles were possibly created by CNT pull-out; c) composite with a GPS-CNF interlayer; d) GPS-CNFs with epoxy layers bonded to the CNF surface.

### 5.4.3. CNT Pullout model application

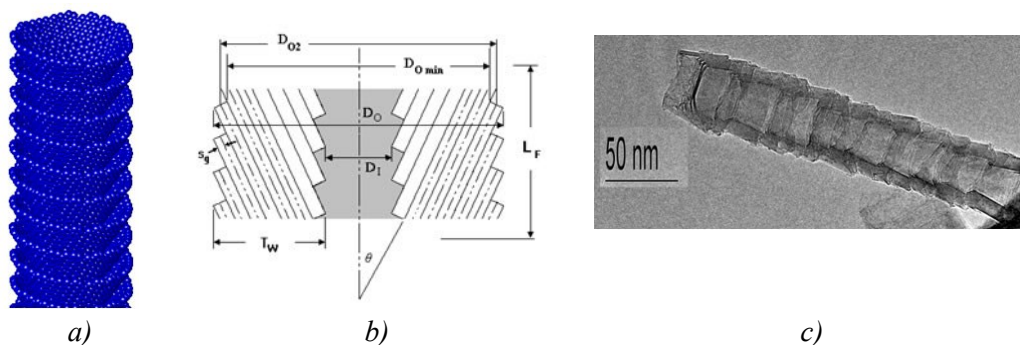
#### *Input material data acquisition*

The fracture toughening model described in Section 5.4 requires several types of material input data. For CNT and CNF fillers, the most difficult issue is related to the variability of physical (e.g. diameter, length, multiple walls etc.) and mechanical properties (e.g. tensile strength, elastic modulus), that sometimes are properly described in the form of a statistical distribution. Moreover, some changes of the initial system (e.g. volume fraction, CNT length etc.) can be induced during functionalization, dispersion processes, manufacturing processes. In the following paragraphs the acquisition of CNT/CNF material input data is illustrated, based on vendor datasheets,

experimental measurements, and literature data. The experimental cases are divided into *cases 1-2* and *cases 3-4* for material properties concerning CNFs and CNTs, respectively.

**CNF material properties**

CNFs used in cases 1-2 were supplied by Applied Sciences Inc. (Cedarville, OH) in the form of Vapor-Grown Carbon NanoFibers (CNFs).



	<i>PR-24-XT</i>
Production	<b>Full scale</b>
Diameter, nanometers	<b>60 to 150</b>
Length, nanometers	<b>30,000 to 100,000</b>
Comments	<b>As grown material essentially free of CVD carbon</b>

**Figure 5.80: CNF details: a) 3D rendering; b) longitudinal section; c) TEM image and material characteristics - (from Applied Sciences Inc. (Cedarville, OH) [http://apsi.com/?page\\_id=19](http://apsi.com/?page_id=19)).**

Three grades of VGNCFs (with the commercial name Pyrograf-III) are available by Applied Sciences: (I) as-grown VGCNFs subjected to post-fabrication pyrolytic stripping to remove polyaromatic hydrocarbon residues (commercially designated as PR-24-XT-PS), (II) high temperature heat treated VGCNFs with smooth surfaces (PR-24-XT-HHT-LD), and (III) surface functionalized VGCNFs (PR-24-XT-HHT-LD-OX) produced by subjecting the high temperature heat treated fibers to an oxidative treatment in a wet chemical process that changes the surface oxygen and nitrogen contents and promotes bonded interactions with organic matrices. PR-24-XT-HHT-LD CNFs were used to manufacture multiscale reinforced composites.

Concerning the mechanical properties of PR-24-XT-HHT-LD CNFs, Ozkan et al. [98] measured the mechanical strength and the elastic modulus of individual nanofibers of pyrolytically stripped, high temperature heat-treated and oxidized VGCNF by a MEMS (Microelectromechanical Systems tool) nanomechanical property characterization method. In another experimental work, Ozkan et al. [99] conducted nanoscale pull-out experiments in order to obtain the Interfacial Shear Strength (ISS) of individual VGCNF embedded in Epon 828™ difunctional bisphenol A/epichlorohydrin compounded with EPIKURE™ 3140 polyamide curing agent.

It is well known that dispersion processes reduce the length of nanotubes/nanofibers, as described in Section 5.2.1. For this reason, it is very important to know the CNF length distribution after sonication. From Zhu's work [91] the measurements of length distribution after different bath sonication time were reported. The CNF-filled resin mixtures were sonicated in an ultrasonic bath operating at 45 W and 38.5 kHz for 4 and 2 hours for CNFs and GPS functionalized CNFs, respectively (before the placement of the interlayer). The results of 4 hours bath sonication were considered as length distribution input data for both CNFs and GPS-CNFs cases. It should be noticed that in that case, the mass fraction of CNFs was equal to 0.05% wt whereas a weight percentage of 0.5% wt was used in the CNF reinforced interlayer for the reinforced composites Figure 5.81 reports experimental data (a) and fitted curves (b), according to the length distribution of equation 5.28. The resulting CNF average length was 3.7  $\mu\text{m}$ , almost one order of magnitude less than the minimum initial value of CNF length according to the manufacturer.

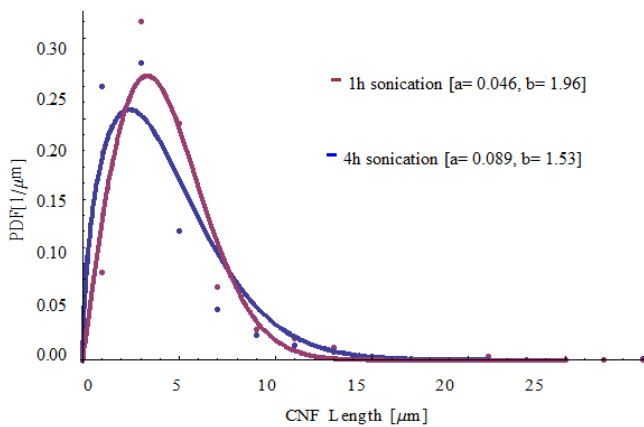


**Figure 5.81: UF-CNF length distribution after 1 and 4 hours of bath sonication dispersion time according to the length distribution of equation 5.28.**

### ***CNT material properties***

CNTs used in *cases 3-4* are were short hydroxyl-functionalized CNTs (OH-CNTs) and un-functionalized vertical grown CNTs (VGCNTs), both supplied by Cheaptubes (Brattleboro, VT). VGCNTs grown aligned to each other in the length direction with minimal entanglement. The information reported in Figure 5.82 have been gathered from the datasheet of the vendor.

Outer Diameter: 10-20nm  
Inside Diameter: 3-5nm  
Ash: <1.5 wt%  
Purity: >95 wt%  
Length: 0.5-2.0  $\mu\text{m}$   
Specific Surface Area: 233  $\text{m}^2/\text{g}$   
Electrical  
Conductivity: >100 S/cm  
Bulk density: 0.22  $\text{g}/\text{cm}^3$   
True density:  $\sim 2.1 \text{ g}/\text{cm}^3$

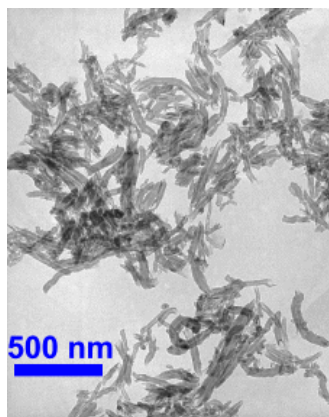


**Figure 5.82: Short OH Functionalized material properties and Short OH TEM image; provided by <http://www.cheaptubesinc.com/shortohcnts.htm#ixzz2HkbOislo>**

Outer Diameter: 8-15nm  
MWNTs Inside Diameter: 3-5nm  
Ash: <1.5 wt%  
Purity: >95 wt%  
Length: 10-50  $\mu\text{m}$   
Specific Surface Area: 233  $\text{m}^2/\text{g}$   
Electrical Conductivity: >100 S/cm  
Bulk density: 0.15  $\text{g}/\text{cm}^3$   
True density:  $\sim 2.1 \text{ g}/\text{cm}^3$

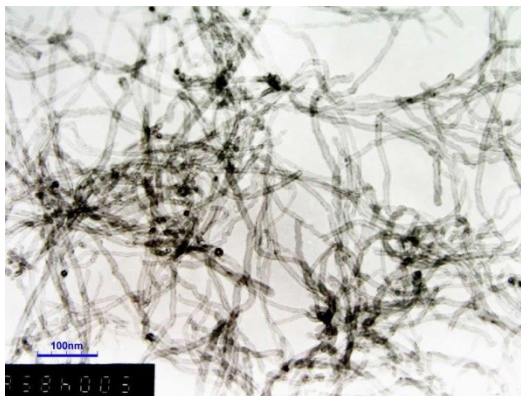


**Figure 5.83: VGCNTs material properties and VGCNTs TEM image; provided by <http://www.cheaptubesinc.com/shortohcnts.htm#ixzz2HkbOislo>**

Concerning the mechanical properties of OH-CNTs and VGCNTs, the values reported in Table 5.5 were implemented in the model, on the basis of the available experimental values.

**Table 5.10: Mechanical properties of CNTs used within the present study**

Reinforcement	Diameter (nm)	Young's Modulus (GPa)	Tensile Strength (GPa)	Failure strain (%)
MWCNT [10, 11]	10–40	800	20–50	2–12
SWNT [100]	0.6–3	1000	10–52	5–10

With regard to length distribution of CNTs, the CNT-filled resin mixtures (short GPS-CNT epoxy and long GPS-CNT epoxy) were sonicated in an ultrasonic bath operating at 45 W and 38.5 kHz for 8 hours at 60°C. Actually no length distribution data were available from Zhu's work [91]. However, in case of long GPS-CNT epoxy, it is assumed in the current investigation that the residual length distribution after sonication roughly corresponds to the length distribution reported in [96] where residual lengths of a-MWCNTs (the same VGCNTs as in Zhu's work) after 5 minutes of sonication in the mixture of epoxide and acetone were measured with the aim of predicting the modulus of MWCNT/epoxy composites. The weight fraction of a-MWCNTs in epoxide/acetone mixture was equivalent to 0.5 wt% in resin. The resulting average length was 0.77µm, almost one order of magnitude less than the initial value of VGCNT length (Figure 5.84).

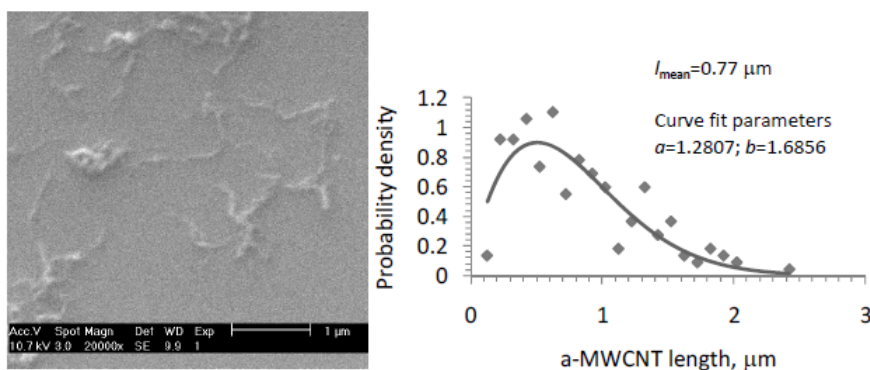


**Figure 5.84: Probability density distribution of a-MWCNTs (i.e. VGCNTs) after 5 minutes of sonication in epoxide/acetone mixture [96].**

### Volume Fraction of CNFs/CNTs

The CNF/CNT volume fraction of, i.e.  $V_{CNF}$ ,  $V_{CNTs}$  was calculated according to the rule of mixture:

$$V_f = \frac{W_f/\rho_f}{W_f/\rho_f + (1 - W_f)/\rho_m}$$

where  $W_f$  is the CNF/CNT mass fraction and  $\rho_f$  and  $\rho_m$  are the CNF/CNT and matrix density, respectively. However, this value may be affected by uncertainty. For example, fracture toughness specimens were fabricated starting from 356 by 305 mm impregnated sheets and consolidated in a press at room temperature. When the resin rich interlayer was placed, a calculated amount of nanofilled resin, equivalent to the weight of resin in two plies of cured composite plate, was added to the surfaces of both sheets facing the midplane to serve as a nanofilled interlayer region on the fracture plane. This amount was estimate as ~14 grams. By considering the following values:

$$\left\{ \begin{array}{l} \rho_{matrix}^{Epon} = 1.1 \frac{g}{cm^3} \\ \rho_{CNF}^{bulk} = 0.90 \frac{g}{cm^3} \\ V_{CNF} = 0.61\% \\ \rho_{CNF}^{NanoComp} \approx 1.098 \frac{g}{cm^3} \end{array} \right.$$

Obviously, a reasonable amount of interlayer material was “lost” during the manufacturing process (for instance 2 grams). The “expected” thickness of the nanofilled resin interlayer would be:

$$t_{interlayer} = \frac{14(g)[or\ 12(g)]}{356 \cdot 305(mm \cdot mm) \cdot 1.098 \cdot 10^{-3} \left(\frac{g}{mm^3}\right)} \approx$$

$$\approx 0.117mm [or\ 0.100mm] \approx 120\mu m [or\ 100\mu m]$$

However, since SEM observations revealed that the interlayer corresponded approximately to the space between glass fiber bundles (i.e. 0-20  $\mu m$ ), it is plausible that the epoxy in the interlayer was mostly bled out and the fillers were entrapped by glass fibers, leading to concentrated nanofillers at the fracture plane. This hypothesis is particularly true in case of CNFs, whose lengths (after sonication) are in the range of 2-

10  $\mu\text{m}$  limiting the CNF migration process. In the light of this consideration, the “true” (or “local”) CNF/CNT volume fraction in the interlayer could be comprised between 6-10 times greater than the “initial” one.

### ***Experimental comparison***

After collecting available material data, the only unknown for *cases 1-2* (UF-CNFs and GPS-CNFs) was the interfacial shear stress  $\tau$  (assumed as constant) of GPS-functionalized CNFs. For *case 4* the length distribution of the VGCNTs was derived from [91] whereas the interfacial shear stress  $\tau$  for both *cases 3* and *4* was unknown. In order to understand the dependence of the main variables adopted in the models and verify the assumptions made about the initial system, some parametric analyses have been conducted starting from a baseline nanocomposite system. Concerning the orientation, random distribution is assumed in the baseline nanocomposite system even though a partial alignment (with respect to glass fibers and through the thickness directions) may be experienced by nanofillers due to the composite consolidation process.

### ***Cases 1-2: 0.5 wt% UF-CNF epoxy and 0.5 wt% GPS-CNF epoxy***

Mode I IFT tests showed that the onset of mode I fracture toughness increased (on the average) of 38 and 49  $\text{J/m}^2$  with respect to the baseline material (neat epoxy resin) when 0.5 wt% UF-CNFs and 0.5 wt% GPS-CNFs were added to the epoxy resin, respectively. This increase can be reasonably attributed to the toughening mechanisms induced by the nanofillers. Among them, the most relevant can be identified as CNF pullout and CNF breakage. In addition, assuming that the CNF length distribution is the same for both cases (i.e. that the CNF length distribution after 2 and 4 hours of sonication is the same), the GPS functionalization most likely improved the interfacial shear strength of CNFs resulting in a slight increase of fracture energy. For this reason, a reasonable way to compare theoretical-experimental results was to report the pullout energy (or bridging energy) as a function of the unknown GPS-based interfacial shear strength. In this way a reasonable value of  $\tau$  for GPS-CNFs can be estimated. The material properties for the baseline UF-CNF system are provided in Table 5.11. The baseline material data are implemented into the Fu and Lauke model [94], and the Mirjalili model [89], with the assumption of random orientation distribution of CNFs and a fixed CNF length distribution.

**Table 5.11: Input material data for case 1, 0.5 wt% UF-CNF epoxy, baseline material properties.**

<i>Pullout model by Fu and Lauke [94]</i>	<i>Bridging (pullout + CNF fracture) model by Mirjalili [89]</i>
<p>Orientation = Random;</p> <p><math>A = 0.083</math>; [27]</p> <p><math>\mu = 0.15</math>; [27]</p> <p><math>d_{CNF} = 105</math> nm; (average outer CNF diameter from Applied Sciences DataSheet)</p> <p><math>\sigma_{ult} = 2.85</math> GPa; (average) Table 5.6</p> <p><math>V_{CNF} = 0.61\%</math>; [91]</p> <p><math>p = 0.5</math>; (random orientation distribution)</p> <p><math>q = 0.5</math>; (random orientation distribution)</p> <p>CNF center of gravity is assumed to be distributed uniformly through the thickness direction of the interlayer</p> <p><math>b = 1.830</math>; (fit of experimental CNF length distribution data, [91] computed with units of length: meters)</p> <p><math>a = 0.704 \cdot 10^{10}</math>; (fit of experimental CNF length distribution data, [91] computed with units of length: meters)</p> <p><math>L_{ave} = 3.73</math> <math>\mu\text{m}</math>; (fit of experimental CNF length distribution data, [91] as reported in Figure 5.81)</p>	<p>Orientation = Random;</p> <p><math>f_{\theta} = 0.23</math>;</p> <p><math>L_{ave} = 3.73</math> <math>\mu\text{m}</math>; [91]</p> <p><math>r_{CNF} = 0.5 \cdot 105</math> nm; (average outer CNF diameter from Applied Sciences DataSheet)</p> <p><math>V_{CNFs} = 0.61\%</math>; [91]</p> <p><math>\sigma_{ult} = 2.85</math> GPa; (average) Table 5.6</p> <p><math>E_{CNF} = 245</math> GPa; [98]</p> <p><math>\varepsilon_{max} = \sigma_{ult} / E_{CNF} = 0.0116327</math></p>

Figure 5.85 reports the increment of fracture energy as a function of interfacial shear strength when the two theoretical models are implemented by using baseline material properties. Red dashed line and black dashed line denote the interfacial shear strength value (experimentally determined by Ozkan et al. [99]) and the average experimental increment of mode I fracture energy (onset), respectively. For both

models, the increment of fracture energy rises up to the value of interfacial shear strength that determines the attainment of a critical CNF length. After this point, the fracture energy decreases since it is due only to the pullout of CNFs having under-critical length. Basically, within the assumptions made for the baseline systems, both models significantly underestimated the enhancement of fracture energy, whatever is the value for the CNF interfacial shear strength. Moreover, in correspondence of the CNF interfacial shear strength value provided by Ozkan et al. [99], the fracture energy enhancement is very small since a critical length condition is attained for smaller shear strength values.

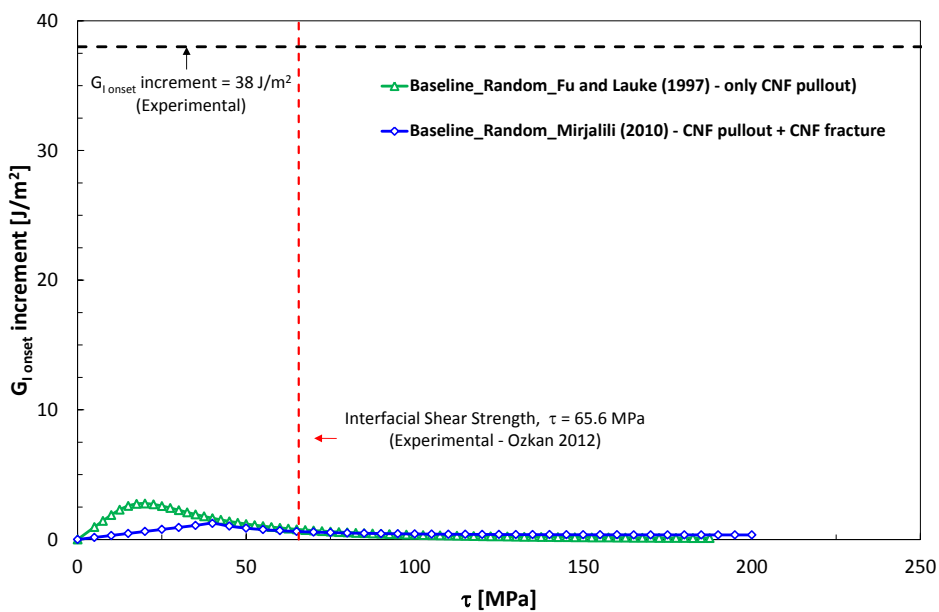
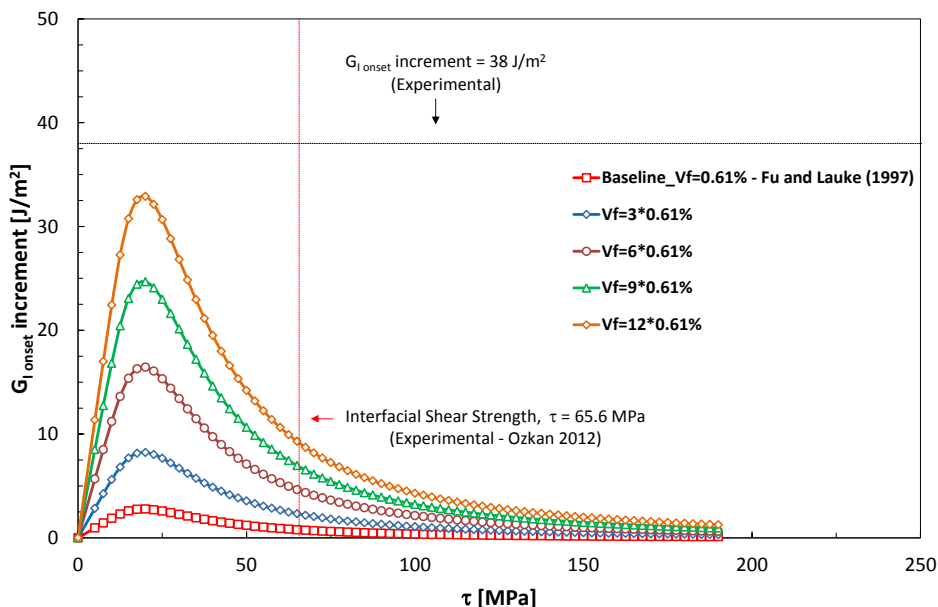


**Figure 5.85: Increment of fracture energy ( $G_{Ionset}$  increment) as a function of interfacial shear strength  $\tau$ . Case 1 (baseline material properties, Table 5.11).**

It should be pointed out that the Fu and Lauke model (green line) appears very effective compared with the Mirjalili model (blue line) since it computes the pullout contribution of CNFs according to a length distribution instead of a unique value of length. In fact, before reaching a critical length condition, the pullout contribution is much higher when the Fu and Lauke model is adopted. Following, some graphs obtained through parametric analysis implementing the Fu and Lauke model are reported. In these graphs, the red dashed line and black dashed line denote the interfacial shear strength value (experimentally determined by Ozkan et al. [99]) and the average experimental increment of mode I fracture energy (onset), respectively.

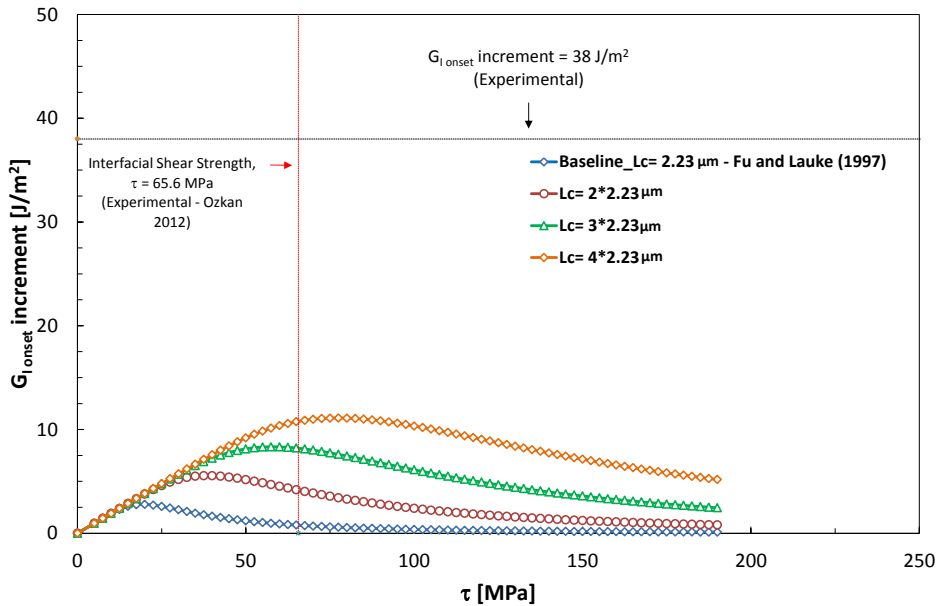
The CNFs length distribution was fixed as the experimental one (as reported in [91] and Table 5.11).

Figure 5.86 reports the increment of mode I fracture energy for different “initial” values of  $V_{CNF}$ . The experimental “initial” value is 0.61% derived by adding 0.5wt% of UF-CNFs to the resin system. The 5 curves are obtained by multiplying the “initial” volume fraction by a factor 1, 3, 6, 9, 12, respectively, trying to take into account that the “true” CNF volume fraction can be higher than the initial one since dense concentrations of CNFs were observed after consolidation process.



**Figure 5.86: Increment of fracture energy ( $G_{I_{onset}}$  increment) as a function of interfacial shear strength  $\tau$ : Case 1 (variation of  $V_{CNF}$ ).**

Figure 5.87 reports the increment of mode I fracture energy for different values of critical length. The initial critical length (i.e. the one obtained using baseline material properties) corresponds to  $2.23\mu\text{m}$ . The four cases are obtained by multiplying the initial critical length by 1-4 (for instance, this can be achieved by increasing the ultimate CNF tensile strength). This may take into account uncertainties on tensile strength, diameter values or, in a more general way, on the analytical expression for the critical length. It can be observed that when critical length is longer, the pullout energy contribution increases due to the fact that more fibers (within the CNF length distribution) contribute to pullout. Simultaneously, the critical length condition is reached for higher interfacial shear strength values.



**Figure 5.87: Increment of fracture energy ( $G_{Ionset}$  increment) as a function of interfacial shear strength  $\tau$ : Case 1 (variation of  $L_C$ ).**

Figure 5.88 reports the increment of mode I fracture energy for different values of CNF outer diameter. In a system with constant  $V_{CNFs}$ , CNFs with smaller diameter values increase the available CNF surface to be pulled out (since a greater number of CNFs is required in order to fulfill the volume fraction constraint). However the critical length condition is reached for smaller values of interfacial shear strength when the CNF diameter is small. This can be observed for  $d_{min} = 60$  nm (blue line) whose pullout energy contribution is the highest if the interfacial shear strength is less than 12.5 MPa.

Figure 5.89 reports the increment of mode I fracture energy for different values of average CNF orientation angle,  $\theta_{ave}$ . Four cases are analyzed: random distribution ( $p = 0.5$  and  $q = 0.5$ ), CNFs almost aligned with respect to the trough the thickness load direction (i.e.  $\theta_{ave} = 5^\circ$  with  $p = 0.5$  and  $q = 50$ ),  $\theta_{ave} = 20^\circ$  ( $p = 1$  and  $q = 7$ ) and  $\theta_{ave} = 65^\circ$  ( $p = 30$  and  $q = 7$ ). This parametric analyses try to account for the possibility that CNF orientation in the consolidated composite system may be affected by the matrix flow during curing process, resulting in a partial alignment of the CNFs into the through the thickness direction and/or glass fiber direction. When CNFs are almost aligned with  $\theta_{ave} = 5^\circ$ , the pullout energy contribution is roughly doubled respect to the random case distribution; on the contrary, CNFs with an average orientation which tends to the glass fiber direction, reduce the pullout energy of one half if compared to the random case.

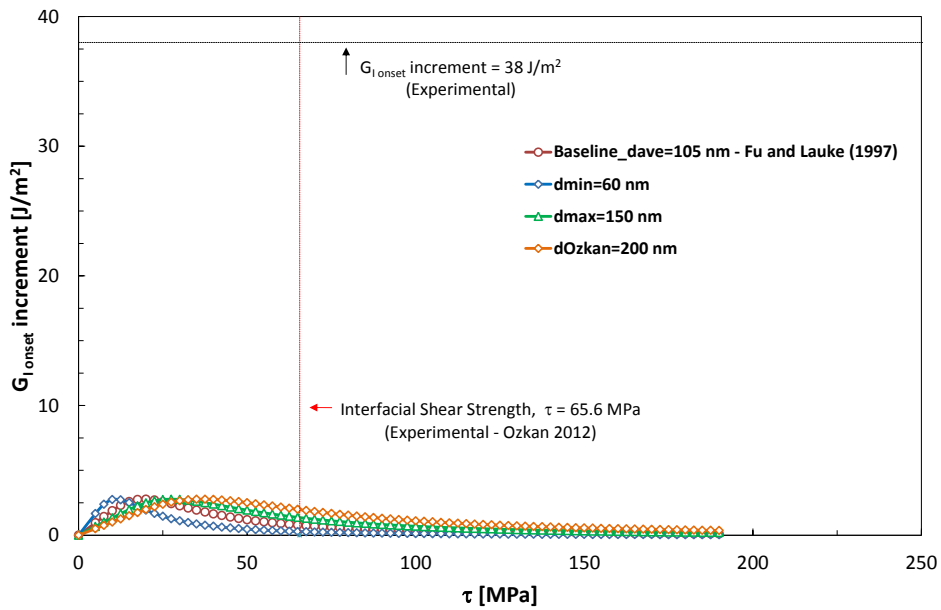


Figure 5.88: Increment of fracture energy ( $G_{I\text{onset}}$  increment) as a function of interfacial shear strength  $\tau$ : case 1 (variation of  $d_{CNT}$ ).

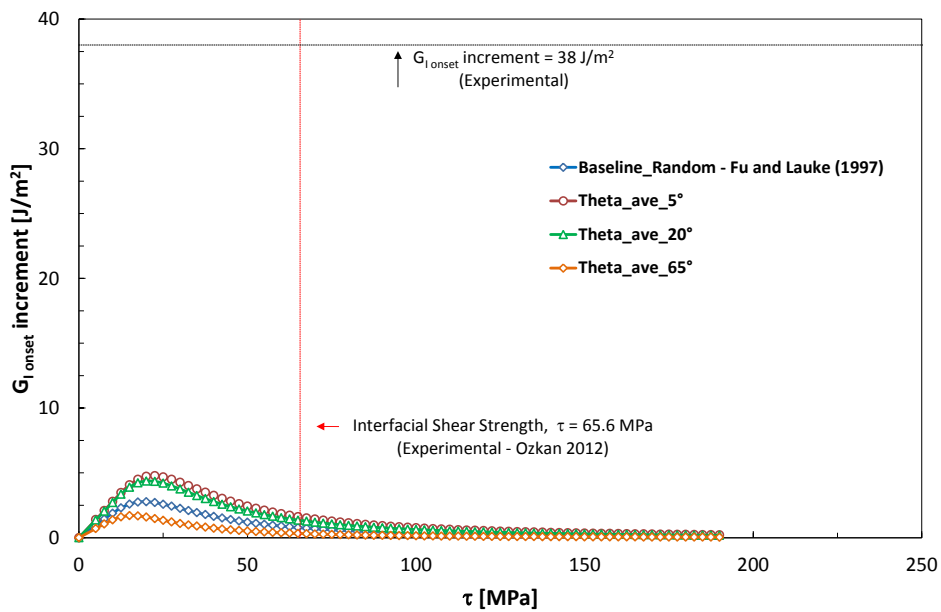


Figure 5.89: Increment of fracture energy ( $G_{I\text{onset}}$  increment) as a function of interfacial shear strength  $\tau$ : case 1 (variation of  $\theta_{CNT}$ ).

Moreover, when the alignment with the loading direction is achieved, the CNF critical length condition is reached for higher values of interfacial shear strength (in the Fu and Lauke model the critical length value takes into account the CNF orientation).

From these parametric analyses, some critical issues needing to be addressed in order to properly use the presented fracture toughening model were identified:

- the volume fraction of nanofiller in the zone of crack propagation can be significantly affected by the manufacturing process; in the experimental work used in with the present analysis, the CNF volume fraction in the resin prior to consolidation of the composite laminate may be lower than actual and lead to an underestimation of the pullout energy.
- The critical length of CNFs/CNTs should be carefully determined, especially when different length values exist in the system. The exact value is strongly related to the CNF/CNT tensile strength that sometimes is reported in a wide range of values. The correct value of the critical length is also reasonably related to the assumptions of considering fibers/tubes as “inextensible”.
- The average CNF/CNT orientation angle is, in some way dependent on the matrix flow during the consolidation or manufacturing process. This was confirmed by the tests performed by Ye Zhu [91]. It is plausible that short CNFs/CNTs “travel” through the thickness direction resulting in partial vertical alignment. On the contrary, long CNFs/CNTs are reasonably unable to cross glass fibers, resulting in a 2D-random orientation distribution mostly in the interlaminar plane.

Based on these considerations and experimental evidences, some modifications to the baseline system input values have been made with the aim of considering a system closer to the actual one.

$V_{CNF}$ : A  $V_{CNF}$  value of roughly eight times than the “initial” one is adopted in order to simulate the dense concentration of CNFs at the fracture plane. Basically, the initial amount of nanofilled modified epoxy resin was 14 grams (to produce the interlayer) containing 0.5 wt% of CNFs. If we assume that approximately 3-4 grams were lost during placement operations, the initial interlayer would be made of 10-11 grams of 0.5 wt% CNF modified resin. Due to the length of CNFs, it is plausible to assume that only matrix bled out from the interlayer system, as a consequence of consolidation process. If we assume that around 5-6 grams of (sole) epoxy resin bled out from the CNF modified interlayer, the resulting  $V_{CNF}$  of “trapped” CNFs would be between 6 and 12 times higher than the initial  $V_{CNF}$  value of 0.610%. Within this assumption, the

resulting interlayer thickness would be between 25 and 35  $\mu\text{m}$  (closer to the SEM observations). Moreover, due to the fact that CNT lengths (for case 3-4) are smaller than CNFs ones, CNTs would easily “follow” the resin flow with a resulting “true” volume fraction less than the CNF one.

$d_{ave}$  : in his experimental campaign, Ozkan [99] performed pullout tests on PR-24-XT-LHT-OX also varying the CNF diameter. Actually, the range of investigated outer diameter values was 200-450 nm. Instead of using an average value from datasheet (i.e. 105 nm),  $d_{ave}$  was selected as 250 nm.

$L_c$  : in case of GPS-CNFs, if we attribute the fracture energy increment (from 39 to 49  $\text{J}/\text{m}^2$ ) to an ISS increase due to GPS functionalization, the  $G_{I\ onset}(\tau)$  curve for UF-CNF should cross the lined corresponding to the experimental ISS value of 65.6 MPa (by Ozkan [99], see Figure 5.87) before the peak, i.e. before reaching a critical length condition. In this way, additional increases of ISS values,  $\tau$ , compared to the UF-case (as an example, due to functionalization) would result in an increment of fracture energy. For this reason, a reasonable value of 1.5\*initial critical length (i.e.  $\cong 3.3\ \mu\text{m}$ ) was used.

$\theta_{ave}$  : in Section 5.4.2, it was pointed out that the resin flow may partially align the CNTs. Reasonably, it can be assumed, as hypothesis, that the average orientation angle is less than  $45^\circ$  (i.e. the average angle of the random distribution) with respect to the interlaminar normal direction..

The result of Fu and Lauke model, obtained implementing the above discussed “modified” material data, is reported in Figure 5.90, along with the result of Mirjalili model in order to appreciate the differences. In correspondence to the ISS value provided by Ozkan [99], the Mirjalili model always underestimates the average experimental increment of fracture energy both for aligned and especially for random orientation distribution. On the contrary, Fu and Lauke model provides an increment of fracture energy very close to the average experimental result when ISS is assumed equal to the one provided by Ozkan [99], i.e. 65.6 MPa (red dashed line in the graph). This result also indicates that when ISS rises up to  $\approx 90\ \text{MPa}$ , the fracture energy can be increased up to  $52\ \text{J}/\text{m}^2$ . This value is very close to the experimental increment of mode I fracture energy obtained with the GPS-CNF epoxy system (grey dashed line in the graph). Further improvement of CNF interfacial properties may lead to a reduction of pullout energy due to the CNF fracture that involves more and more CNFs.

Figure 5.92 reports the increment of mode I fracture energy for different “initial” values of  $V_{CNT}$ . The experimental “initial” value is 1.805% and was derived by the addition of 0.25 wt% of long GPS-CNTs to the resin system.

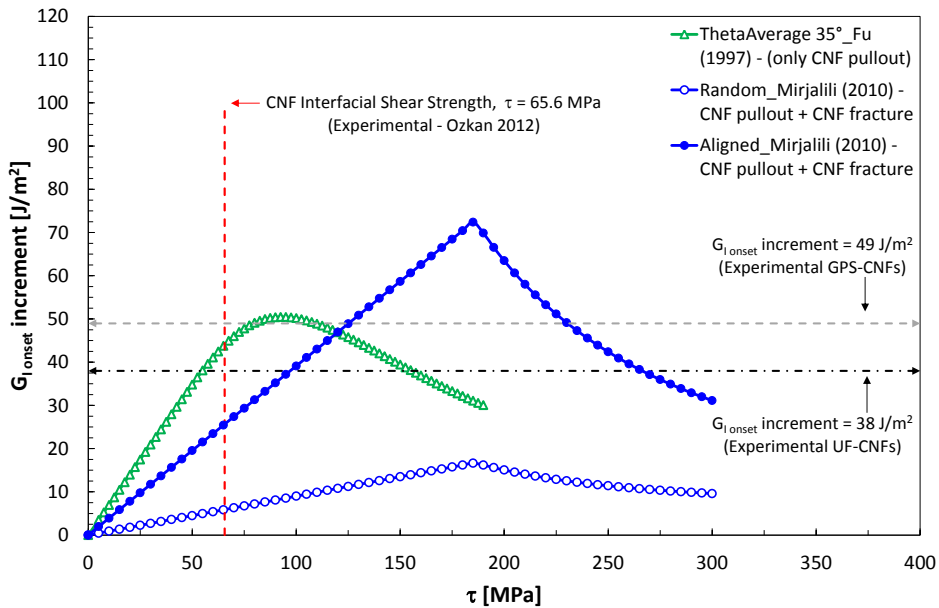


**Figure 5.90: Increment of fracture energy ( $G_{Ionset}$  increment) as a function of interfacial shear strength  $\tau$ : case 1-2, comparison of Fu and Lauke model and Mirjalili model by assuming modified input material data.**

**Cases 3-4: 0.5 wt% short GPS-CNTs epoxy and 0.25 wt% long GPS-CNTs epoxy**

In order to predict the onset of mode I fracture energy of short and long GPS-CNT based composites, the material properties for the baseline system of long GPS-CNT (with a known length distribution) have been firstly defined. The data are reported in Table 5.12 and implemented into the Fu and Lauke model and the Mirjalili model with the initial assumption of random orientation distribution of CNTs and a fixed length distribution.

Figure 5.91 reports the results concerning the two theoretical models, implemented by using baseline material properties. Black dashed line denotes the average experimental increment of mode I fracture energy (onset) obtained in Case 4 (long GPS-CNTs). Within the assumptions made for the baseline system, both models significantly underestimated the enhancement of fracture energy, regardless of the value of GPS-CNT interfacial shear strength. Again in this case, the Fu and Lauke model (green line) provides a higher energy contribution for pullout energy, mainly

due to the fact that it is computed on the basis of a length distribution instead of a unique value of length.

**Table 5.12: Input material data for case 4, 0.25 wt% long GPS-CNTs epoxy, baseline material properties.**

<i>Pullout model by Fu and Lauke [94]</i>	<i>Bridging (pullout + CNT fracture) model by Mirjalili [89]</i>
Orientation = Random;	Orientation = Random;
$A = 0.083$ ; [27]	$f_{\theta} = 0.23$ ;
$\mu = 0.15$ ; [27]	$L_{ave} = 0.77 \mu\text{m}$ ; [96]
$d_{CNT} = 11.5 \text{ nm}$ ; (average outer CNT diameter from Cheaptubes DataSheet)	$r = 0.5 * 11.5 \text{ nm}$ ; (average outer CNT diameter from Cheaptubes DataSheet)
$\sigma_{ult} = 35 \text{ GPa}$ ; [86, 89]	$V_{CNF} = 1.805\%$ ; [91]
$V_{CNF} = 1.805\%$ ; [91]	$\sigma_{ult} = 35 \text{ GPa}$ ; [86, 89]
$p = 0.5$ ; (random orientation distribution)	$E_{CNF} = 800 \text{ GPa}$ ; [86, 89]
$q = 0.5$ ; (random orientation distribution)	$\varepsilon_{max} = \sigma_{ult} / E_{CNF} = 0.04375$
$b = 1.6856$ ; [96] fit of experimental CNF length distribution data computed with units of length: meters	
$a = 1.6607 * 10^{10}$ ; [96] fit of experimental CNF length distribution data computed with units of length: meters	
$L_{ave} = 0.77 \mu\text{m}$ ; [96]	

As was done for CNF-based cases, some parametric analyses implementing only the Fu and Lauke model are following reported. However, for GPS-CNT cases, we do not have an experimental value for the GPS-CNT ISS. The black dashed line in the graphs will always denote the average experimental increment of mode I fracture energy (onset) obtained in case of 0.25 wt% long GPS-CNTs epoxy. The VGCNTs length distribution was fixed as the experimental one reported in [96].

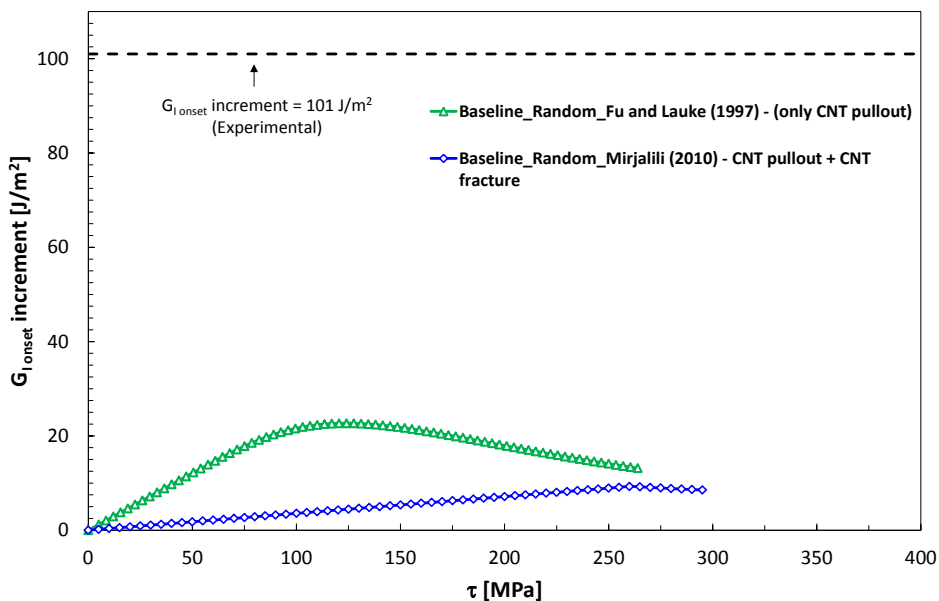


Figure 5.91: Increment of fracture energy ( $G_{I_{onset}}$  increment) as a function of interfacial shear strength  $\tau$ : Case 4 (baseline material properties, Table 5.12).

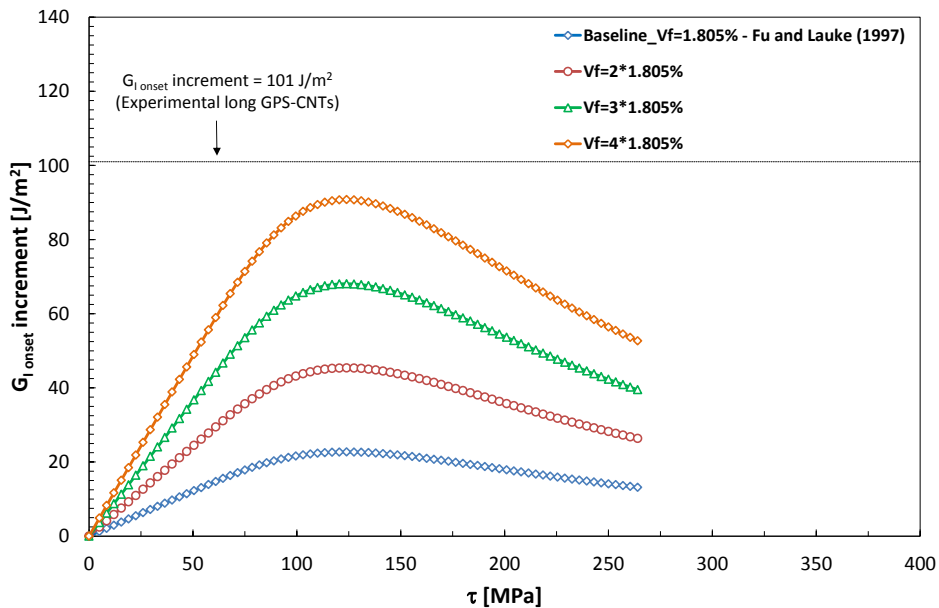
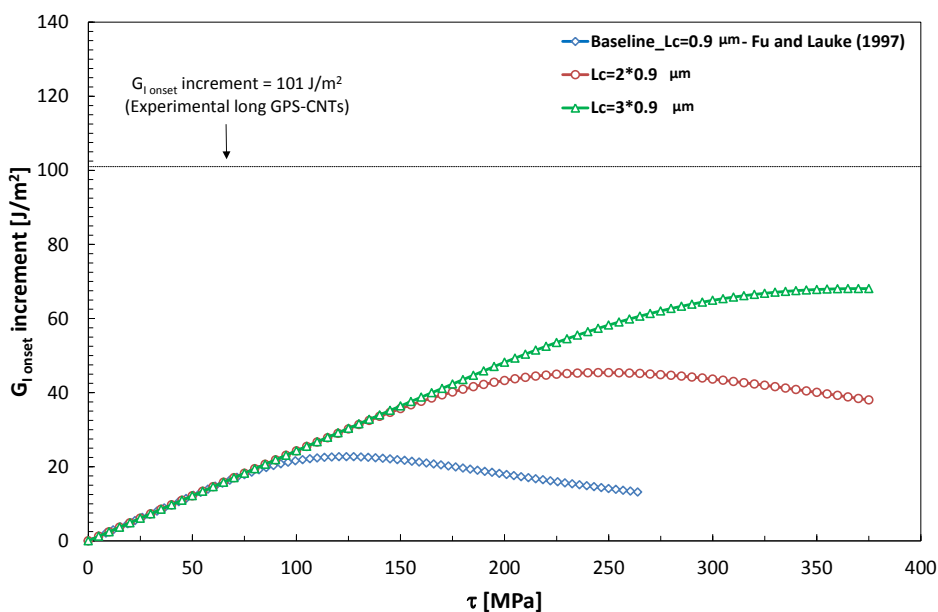


Figure 5.92: Increment of fracture energy ( $G_{I_{onset}}$  increment) as a function of interfacial shear strength  $\tau$ : Case 4 (variation of  $V_{CNF}$ ).

The four curves are obtained by multiplying the “initial” volume fraction by 1-4, trying to consider that the “true” CNF volume fraction can be higher than the “initial” one since dense concentrations of CNTs most likely arose during consolidation process.

Figure 5.93 reports the increment of mode I fracture energy for different values of critical length. Three cases obtained by multiplying the initial critical length by 1-3 (by increasing the ultimate CNT tensile strength) are reported. It can be observed that, the critical length condition is reached for higher interfacial shear strength values (between 100 and 370 MPa) if compared with the CNF cases.



**Figure 5.93: Increment of fracture energy ( $G_{I_{onset}}$  increment) as a function of interfacial shear strength  $\tau$ : Case 4 (variation of  $L_C$ ).**

Figure 5.94 reports the increment of mode I fracture energy for different values of CNT outer diameter. If CNT diameter is 15 nm (the maximum value taken from the datasheet) the critical length condition is reached for higher ISS values, i.e. around 150 MPa.

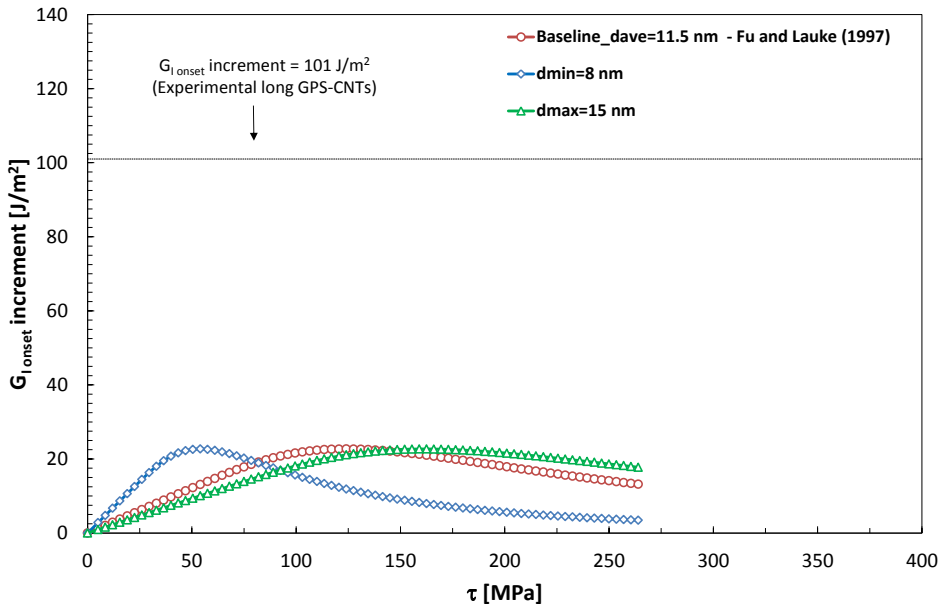


Figure 5.94: Increment of fracture energy ( $G_{ionset}$  increment) as a function of interfacial shear strength  $\tau$ : Case 4 (variation of  $d_{CNT}$ ).

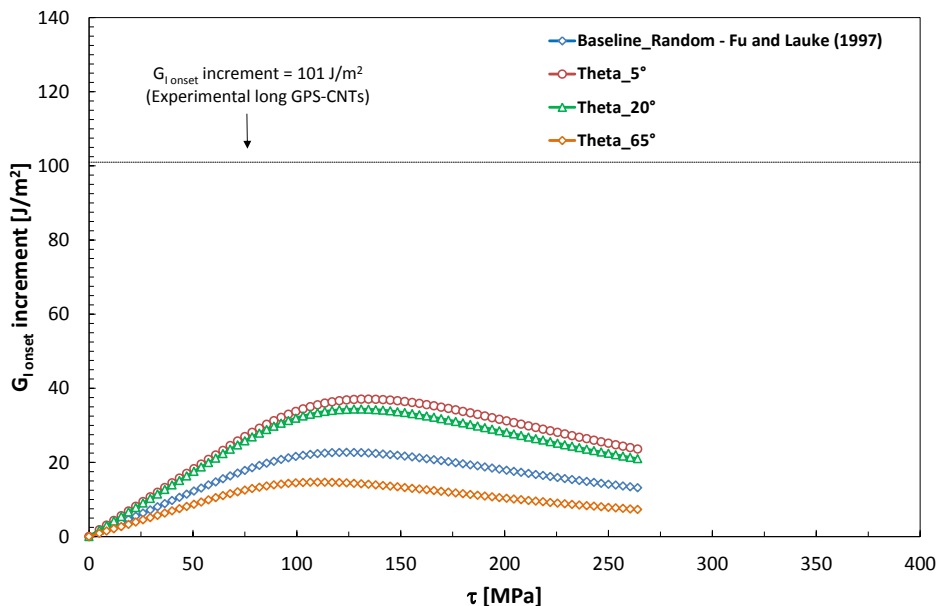


Figure 5.95: Increment of fracture energy ( $G_{ionset}$  increment) as a function of interfacial shear strength  $\tau$ : Case 4 (variation of  $\theta_{CNT}$ ).

Figure 5.95 reports the increment of mode I fracture energy for different values of average CNF orientation angle,  $\theta_{ave}$ . Four cases were analyzed, as reported in the previous paragraph: random distribution, CNTs almost aligned with respect to the interlaminar normal (i.e.  $\theta_{ave}=5^\circ$ ),  $\theta_{ave}=20^\circ$  and  $\theta_{ave}=65^\circ$ . When CNTs are almost aligned with the through-thickness direction, i.e.  $\theta_{ave}=5^\circ$ , the pullout energy contribution is almost doubled with respect to the random case distribution.

The results of the parametric analysis revealed that, for the baseline material properties, the increment of fracture energy is always underestimated. Hence, the following “modified” values have been implemented in the model:

$V_{CNT}$  : the  $V_{CNT}$  value was roughly doubled with respect to the “initial” one in order to simulate the dense concentration of long CNTs at the fracture plane. This value is smaller than the  $V_{CNFs}$  used for CNF cases due to the hypothesis that longer CNFs are more likely to be trapped into the interlayer.

$d_{ave}$  : left as 11.5 nm as the average outer diameter provided by the manufacturer.

$L_c$  : as for CNT-based cases, a reasonable value of 1.5\*initial critical length, was adopted.

$\theta_{ave}$  : also for CNT-based epoxy systems the assumption of  $\theta_{ave}=35^\circ$  was made.

Figure 5.96 reports the results of the application of the Fu and Lauke model and the Mirjalili model with the modified material properties. It can be observed that the Mirjalili model predicts the correct increment of mode I fracture energy (i.e.  $10 \text{ J/m}^2$ ) only if a perfectly alignment is assumed for CNTs and for a ISS value of roughly 280 MPa (more than two times higher than ISS value estimated for GPS-CNFs). A more realistic prediction is provided when the Fu and Lauke model is implemented with “modified” material data. In fact, it predicts the average experimental increment of mode I fracture energy for ISS values around 145 MPa, as it can be observed in Figure 5.96 in correspondence to the intersection between green line (Fu and Lauke model with modified material properties) and black dashed line (experimental  $G_{I\text{onset}}$  increment).

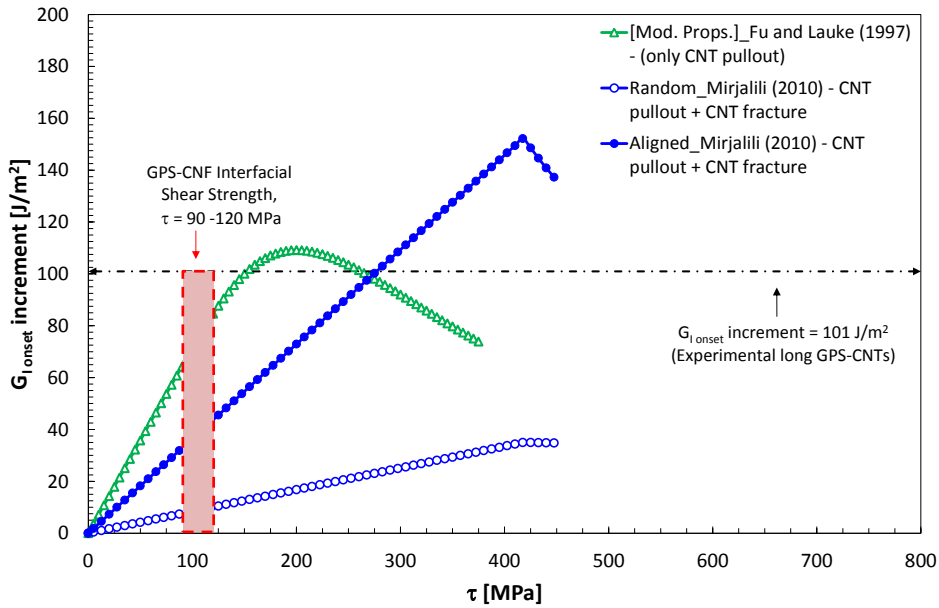


**Figure 5.96: Increment of fracture energy ( $G_{Ionset}$  increment) as a function of interfacial shear strength  $\tau$ : Case 4, comparison of the Fu and Lauke model and the Mirjalili model by assuming modified input material data.**

In order to validate the previous result, the increment of mode I fracture energy obtained for *Case 3* (i.e. adding short GPS-CNTs in the epoxy system) has been predicted by using the same modified values of those established for *Case 4*, in terms of:  $V_{CNT}$ ,  $L_c$  and  $\theta_{ave}$ . The main difference with *Case 4* is the CNT length, whereas the resulting ISS should be approximately the same. However, no information on short CNT length distribution data was available. Nonetheless, using the hypothesis that sonication reduced the initial CNT length, the following input material data were used for *Case 3*, Table 5.13:

**Table 5.13: Input material data for case 3, 0.5 wt% short GPS-CNTs epoxy, baseline material properties.**

<i>Pullout model by Fu and Lauke [94]</i>	<i>Bridging (pullout + CNT fracture) model by Mirjalili [89]</i>
<p>Orientation : <math>\theta_{ave}=35^\circ</math>;</p> <p><math>A = 0.083</math>; [27]</p> <p><math>\mu = 0.15</math>; [27]</p> <p><math>d_{CNT} = 10</math> nm; (outer CNT diameter from Cheaptubes DataSheet)</p> <p><math>\sigma_{ult} = 1.5*35</math> GPa; [86, 89]</p> <p><math>V_{CNT} = 2.2*2.451\%</math>; [91]</p> <p><math>p = 0.5</math>;</p> <p><math>q = 2</math>;</p> <p><math>b = 1.6356</math>; (hypothesis) with units of length: meters</p> <p><math>a = 2.2807*10^{10}</math>; (hypothesis) with units of length: meters</p> <p><math>L_{ave} = 0.4</math> <math>\mu\text{m}</math>; (hypothesis)</p>	<p>Orientation = both random and aligned;</p> <p><math>f_\theta = 0.23</math>;</p> <p><math>L_{ave} = 0.4</math> <math>\mu\text{m}</math>; (hypothesis)</p> <p><math>r = 0.5*10</math> nm; (outer CNT diameter from Cheaptubes DataSheet)</p> <p><math>V_{CNT} = 2.2*2.451\%</math> ; [91]</p> <p><math>\sigma_{ult} = 1.5*35</math> GPa; [86, 89]</p> <p><math>E_{CNF} = 800</math> GPa; [86, 89]</p> <p><math>\varepsilon_{max} = \sigma_{ult} / E_{CNF} = 0.04375</math></p>

Figure 5.97 reports the results of the application of the Fu and Lauke model and the Mirjalili model to the short GPS-CNT system with the “modified” material properties. It can be observed that the Mirjalili model predicts the correct increment of mode I fracture energy (i.e.  $66 \text{ J/m}^2$ ) only if a perfect alignment through the thickness is assumed for CNTs and for a ISS value of roughly 450 MPa that is approximately two times higher than ISS value estimated for long GPS-CNT. A more realistic prediction is provided when the Fu and Lauke model is implemented with “modified” material data. In fact, assuming a CNT average orientation angle distribution of  $35^\circ$  (, the model predicts the average experimental increment of mode I fracture energy for

ISS values of around 180 - 200 MPa (the highlighted red area in the graph), which are higher than long GPS-CNTs.

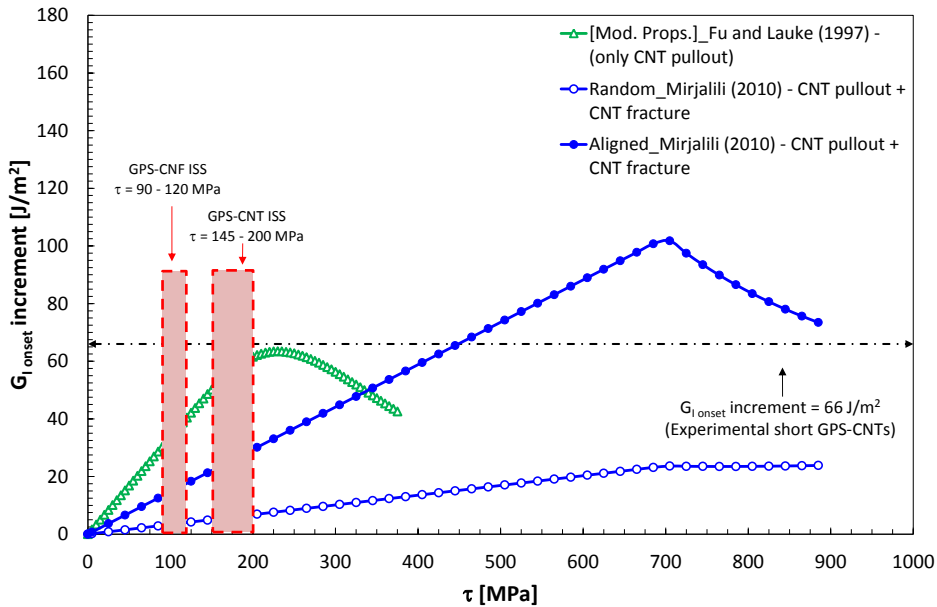


**Figure 5.97: Increment of fracture energy ( $G_{I_{onset}}$  increment) as a function of interfacial shear strength  $\tau$ . Case 3, comparison of Fu and Lauke model and Mirjalili model by assuming modified input material data.**

The previous assumption on short GPS-CNT length distribution (i.e., with  $L_{ave} = 0.4 \mu\text{m}$ ) was verified by plotting the pullout energy as a function of average CNT length. In detail, the mode length of the CNT length distribution (i.e. the peak of the probability density function), i.e. equation 5.30, was fixed as 1/4 of the minimum CNT length value provided by the manufacturer (i.e.  $0.5 \mu\text{m}$ ), resulting in  $L_{mod} = 0.125 \mu\text{m}$ . With this constraint, the CNT length distribution of equation 5.28 can be changed by varying the values of the parameters  $a$  and  $b$ , resulting in different values of  $L_{ave}$  (equation 5.29). Figure 5.98 reports the fracture energy due to pullout as a function of CNT average length in case of ISS equal to: 150, 200, 250 MPa. The smallest value of ISS permits the highest increment in mode I strain energy release rate (up to  $180 \text{ J/m}^2$ ) since it provides the highest critical length condition. It is interesting to note that the

average experimental increment of mode I fracture energy is correctly predicted when the CNT average length is approximately between 0.30 – 0.50  $\mu\text{m}$ .

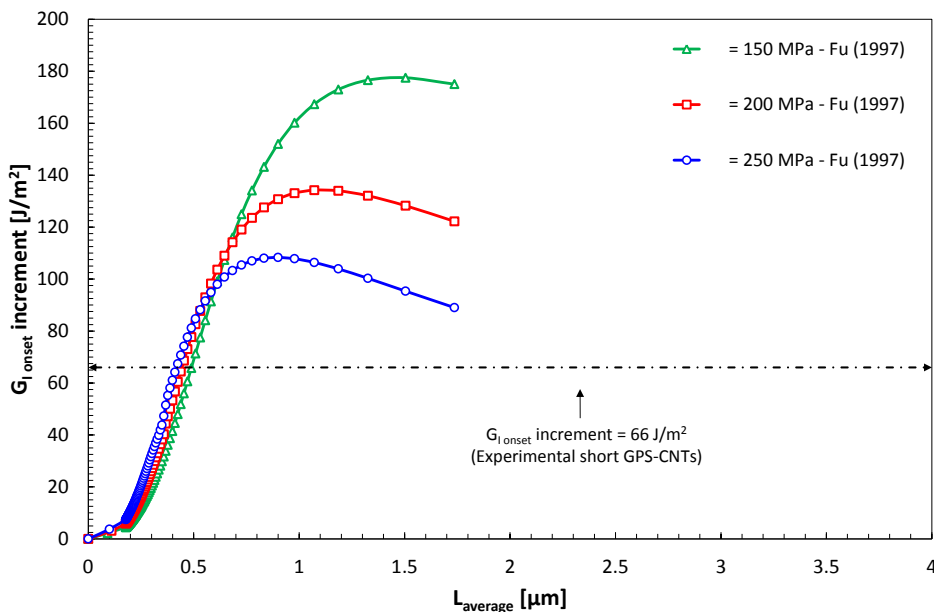


**Figure 5.98:** Increment of fracture energy  $G_{\text{Ionset}}$  as a function of average CNT length,  $L_{\text{average}}$ : Case 3, comparison of the Fu and Lauke model varying interfacial shear strength,  $\tau$ , values.

## 5.5. Concluding remarks

In this chapter, an overview on the main issues related to CNT polymer composites has been firstly presented. Among them, aspects related to CNT length and orientation characterization, as well as geometry and stress transfer to the matrix, have been reviewed. A general overview on CNT/polymer fracture toughening behavior has been then provided focusing on CNT toughening mechanisms and their modeling. A micromechanical model, based on the work by Fu and Lauke [94] work (suitably developed for short fiber composites), has been presented in order to model mode I interlaminar fracture toughness of multiscale CNT- or CNF-filled S2-Glass/epoxy composites. Model predictions were compared to Mode I interlaminar fracture toughness test experimental data obtained by using different nanofiller types, lengths,

and functionalization. The analyses aimed to link the available experimental data to the micromechanical model. Different effects on CNT fracture toughness have been evaluated, including filler functionalization and length. When experimental available inputs for CNFs and CNTs are implemented in the Fu and Lauke model, the predicted onset of interlaminar fracture energy did not match the experimental one. A satisfactorily prediction was achieved by making further adjustments to the parameters like CNT/CNT critical length rather orientation distribution.

The results obtained by Zhu's experimental investigation [91] along with the use of theoretical models by Fu and Lauke [94] and Mirjalili [89], allowed the identification of some critical problems related to the modeling of toughening mechanisms of nanofilled epoxy materials:

- the Fu and Lauke model appeared more appropriate than Mirjalili model due to the possibility of using a nanofiller length distribution. According to this approach the resulting ISS value for GPS-CNF based systems was around 90 MPa, whereas for long GPS-CNT systems it was around 150 MPa; this latter value was almost confirmed in case of short GPS-CNTs for which a statistical length distribution was hypothesized and then verified;
- it appears essential to know the true length distribution of nanofillers mainly for two reasons: nanofillers lengths are inevitably reduced when a dispersion process is used; the use of a unique value of nanofiller length in a model may lead to significant underestimation or overestimation of the results;
- when a resin rich interlayer is used to obtain a multiscale reinforced composite, a proper definition of a "true" nanofiller volume fraction should be provided. Nanofillers migration due to resin flow and composite fiber obstruction can represent a source of strong variation of "local" nanofiller volume fraction that triggers possible variations in toughening efficacy. Moreover, the composite manufacturing process may influence the nanofiller orientation.
- another issue is probably related to the critical length value. When CNT are pulled out from the matrix, the critical length value could be longer than the theoretical one. This may be due to a sort of "underestimation" of the true CNF/CNT tensile strength or to the fact that within the assumptions of these theoretical models, we are considering fibers/tubes as "inextensible". In

addition, CNT waviness could have some influence on the determination of effective CNT critical length.

In the light of these considerations, molecular dynamics (MD) simulations are ongoing in order to suitably enhance the presented micromechanical model (Figure 5.99a,b). In fact, MD simulations of CNT pulled out at different angles would provide an accurate estimation of the pullout law to be implemented in the fracture energy micromechanical model. Moreover, further information concerning snubbing friction between CNT and matrix as well as critical CNT length definition could be provided.

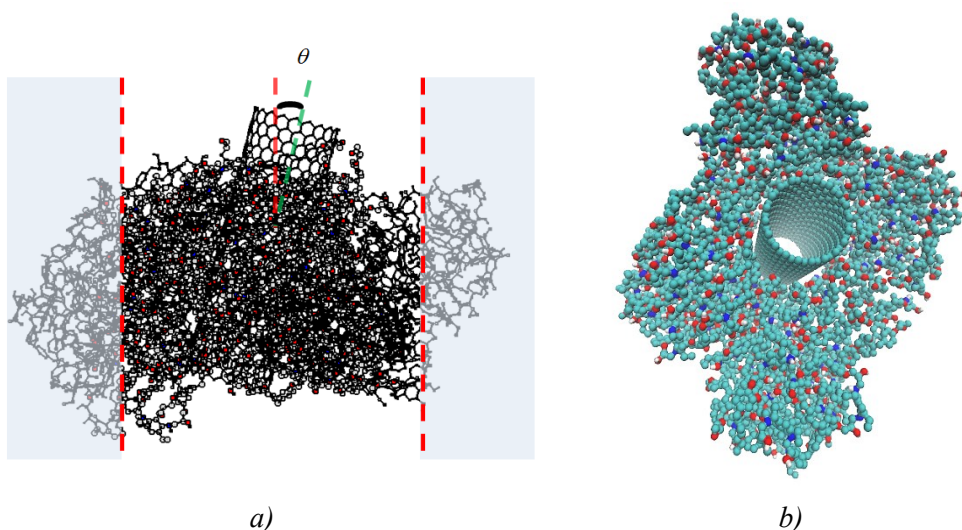


**Figure 5.99:** a) MD initial system for CNT pullout at an angle  $\theta$  from an epoxy matrix; b) three dimensional rendering.

### References

1. Quaresimin, M., M. Salviato, and M. Zappalorto, *Strategies for the assessment of nanocomposite mechanical properties*. Composites Part B-Engineering, 2012. **43**(5 ): p. 2290-2297.
2. Iijima, S., *Helical Microtubules of Graphitic Carbon*. Nature, 1991. **354**(6348): p. 56-58.
3. Forro, L. and C. Schonenberger, *Physical properties of multi-wall nanotubes*. Carbon Nanotubes, in: Topics in Applied Physics, Springer, 2001. **80**: p. 329-390.

4. Endo, M., M.S. Strano, and P.M. Ajayan, *Potential applications of carbon nanotubes*. Carbon Nanotubes, in: Topics in Applied Physics, Springer, 2008. **111**: p. 13-61.
5. Thostenson, E.T., Z.F. Ren, and T.W. Chou, *Advances in the science and technology of carbon nanotubes and their composites: a review*. Composites Science and Technology, 2001. **61**(13): p. 1899-1912.
6. Salvetat, J.P., G.A.D. Briggs, et al., *Elastic and shear moduli of single-walled carbon nanotube ropes*. Physical Review Letters, 1999. **82**(5): p. 944-947.
7. Hernandez, E., C. Goze, P. Bernier, and A. Rubio, *Elastic properties of C and BxCyNz composite nanotubes*. Physical Review Letters, 1998. **80**(20): p. 4502-4505.
8. Cooper, C.A., R.J. Young, and M. Halsall, *Investigation into the deformation of carbon nanotubes and their composites through the use of Raman spectroscopy*. Composites Part a-Applied Science and Manufacturing, 2001. **32**(3-4): p. 401-411.
9. Yakobson, B.I., M.P. Campbell, C.J. Brabec, and J. Bernholc, *High strain rate fracture and C-chain unraveling in carbon nanotubes*. Computational Materials Science, 1997. **8**(4): p. 341-348.
10. Yu, M.F., O. Lourie, M.J. Dyer, K. Moloni, T.F. Kelly, and R.S. Ruoff, *Strength and breaking mechanism of multiwalled carbon nanotubes under tensile load*. Science, 2000. **287**(5453): p. 637-640.
11. Demczyk, B.G., Y.M. Wang, J. Cumings, M. Hetman, W. Han, A. Zettl, and R.O. Ritchie, *Direct mechanical measurement of the tensile strength and elastic modulus of multiwalled carbon nanotubes*. Materials Science and Engineering a-Structural Materials Properties Microstructure and Processing, 2002. **334**(1-2): p. 173-178.
12. Falvo, M.R., G.J. Clary, R.M. Taylor, V. Chi, F.P. Brooks, S. Washburn, and R. Superfine, *Bending and buckling of carbon nanotubes under large strain*. Nature, 1997. **389**(6651): p. 582-584.
13. Ebbesen, T.W., H.J. Lezec, H. Hiura, J.W. Bennett, H.F. Ghaemi, and T. Thio, *Electrical conductivity of individual carbon nanotubes*. Nature, 1996. **382**(6586): p. 54-56.
14. Biercuk, M.J., M.C. Llaguno, M. Radosavljevic, J.K. Hyun, A.T. Johnson, and J.E. Fischer, *Carbon nanotube composites for thermal management*. Applied Physics Letters, 2002. **80**(15): p. 2767-2769.

15. Morcom, M., K. Atkinson, and G.P. Simon, *The effect of carbon nanotube properties on the degree of dispersion and reinforcement of high density polyethylene*. Polymer, 2010. **51**(15): p. 3540-3550.
16. Bose, S., R.A. Khare, and P. Moldenaers, *Assessing the strengths and weaknesses of various types of pre-treatments of carbon nanotubes on the properties of polymer/carbon nanotubes composites: A critical review*. Polymer, 2010. **51**(5): p. 975-993.
17. Du, J.H., J. Bai, and H.M. Cheng, *The present status and key problems of carbon nanotube based polymer composites*. Express Polymer Letters, 2007. **1**(5): p. 253-273.
18. Grady, B.P., *Dispersion, Orientation, and Lengths of Carbon Nanotubes in Polymers*. Carbon Nanotube-Polymer Composites: Manufacture, Properties, and Applications, John Wiley & Sons, Inc., Hoboken, NJ, USA., 2011.
19. Moore, V.C., M.S. Strano, E.H. Haroz, R.H. Hauge, R.E. Smalley, J. Schmidt, and Y. Talmon, *Individually suspended single-walled carbon nanotubes in various surfactants*. Nano Letters, 2003. **3**(10): p. 1379-1382.
20. Blanch, A.J., C.E. Lenehan, and J.S. Quinton, *Optimizing Surfactant Concentrations for Dispersion of Single-Walled Carbon Nanotubes in Aqueous Solution*. Journal of Physical Chemistry B, 2010. **114**(30): p. 9805-9811.
21. Lu, K.L., R.M. Lago, Y.K. Chen, M.L.H. Green, P.J.F. Harris, and S.C. Tsang, *Mechanical damage of carbon nanotubes by ultrasound*. Carbon, 1996. **34**(6): p. 814-816.
22. Hennrich, F., R. Krupke, et al., *The mechanism of cavitation-induced scission of single-walled carbon nanotubes*. Journal of Physical Chemistry B, 2007. **111**(8): p. 1932-1937.
23. Blanch, A.J., C.E. Lenehan, and J.S. Quinton, *Parametric analysis of sonication and centrifugation variables for dispersion of single walled carbon nanotubes in aqueous solutions of sodium dodecylbenzene sulfonate*. Carbon, 2011. **49**(15): p. 5213-5228.
24. Saito, T., K. Matsushige, and K. Tanaka, *Chemical treatment and modification of multi-walled carbon nanotubes*. Physica B-Condensed Matter, 2002. **323**(1-4): p. 280-283.
25. Hilding, J., E.A. Grulke, Z.G. Zhang, and F. Lockwood, *Dispersion of carbon nanotubes in liquids*. Journal of Dispersion Science and Technology, 2003. **24**(1): p. 1-41.

26. Gojny, F.H., M.H.G. Wichmann, B. Fiedler, I.A. Kinloch, W. Bauhofer, A.H. Windle, and K. Schulte, *Evaluation and identification of electrical and thermal conduction mechanisms in carbon nanotube/epoxy composites*. *Polymer*, 2006. **47**(6): p. 2036-2045.
27. Fu, S.Y., Z.K. Chen, S. Hong, and C.C. Han, *The reduction of carbon nanotube (CNT) length during the manufacture of CNT/polymer composites and a method to simultaneously determine the resulting CNT and interfacial strengths*. *Carbon*, 2009. **47**(14): p. 3192-3200.
28. Chen, L.M., R. Ozisik, and L.S. Schadler, *The influence of carbon nanotube aspect ratio on the foam morphology of MWNT/PMMA nanocomposite foams*. *Polymer*, 2010. **51**(11): p. 2368-2375.
29. Duncan, R.K., X.Y.G. Chen, J.B. Bult, L.C. Brinson, and L.S. Schadler, *Measurement of the critical aspect ratio and interfacial shear strength in MWNT/polymer composites*. *Composites Science and Technology*, 2010. **70**(4): p. 599-605.
30. Zaragoza-Contreras, E.A., E.D. Lozano-Rodriguez, M. Roman-Aguirre, W. Antunez-Flores, C.A. Hernandez-Escobar, G. Flores-Gallardo, and A. Aguilar-Elguezabal, *Evidence of multi-walled carbon nanotube fragmentation induced by sonication during nanotube encapsulation via bulk-suspension polymerization*. *Micron*, 2009. **40**(5-6): p. 621-627.
31. Krause, B., R. Boldt, and P. Pötschke, *A method for determination of length distributions of multiwalled carbon nanotubes before and after melt processing*. *Carbon*, 2011. **49**.
32. Fawad Inam, T.V., Jonathan P Jones and Xu Lee, *Effect of carbon nanotube lengths on the mechanical properties of epoxy resin: An experimental study*. *Journal of Composite Materials*, 2012. **29**: p. 10.
33. Ulrych, F., M. Sova, J. Vokrouhlecky, and B. Turcic, *Empirical Relations of the Mechanical-Properties of Polyamide-6 Reinforced with Short Glass-Fibers*. *Polymer Composites*, 1993. **14**(3): p. 229-237.
34. Wang, S.R., Z.Y. Liang, B. Wang, and C. Zhang, *Statistical characterization of single-wall carbon nanotube length distribution*. *Nanotechnology*, 2006. **17**(3): p. 634-639.
35. Jiang, B., C. Liu, C. Zhang, B. Wang, and Z. Wang, *The effect of non-symmetric distribution of fiber orientation and aspect ratio on elastic properties of composites*. *Composites Part B-Engineering*, 2007. **38**(1): p. 24-34.

36. Perez, R., S. Banda, and Z. Ounaies, *Determination of the orientation distribution function in aligned single wall nanotube polymer nanocomposites by polarized Raman spectroscopy*. Journal of Applied Physics, 2008. **103**(7).
37. Moniruzzaman, M. and K.I. Winey, *Polymer nanocomposites containing carbon nanotubes*. Macromolecules, 2006. **39**(16): p. 5194-5205.
38. Ciecierska, E., A. Boczkowska, and K.J. Kurzydowski, *Quantitative description of the spatial dispersion of carbon nanotubes in polymeric matrix*. Journal of Materials Science, 2010. **45**(9): p. 2305-2310.
39. Pegel, S., P. Potschke, T. Villmow, D. Stoyan, and G. Heinrich, *Spatial statistics of carbon nanotube polymer composites*. Polymer, 2009. **50**(9): p. 2123-2132.
40. Li, Z., Y. Gao, K.S. Moon, Y.G. Yao, A. Tannenbaum, and C.P. Wong, *Automatic quantification of filler dispersion in polymer composites*. Polymer, 2012. **53**(7): p. 1571-1580.
41. Cooper, C.A., D. Ravich, D. Lips, J. Mayer, and H.D. Wagner, *Distribution and alignment of carbon nanotubes and nanofibrils in a polymer matrix*. Composites Science and Technology, 2002. **62**(7-8): p. 1105-1112.
42. Choy, C.L., W.P. Leung, K.W. Kowk, and F.P. Lau, *Elastic-Moduli and Thermal-Conductivity of Injection-Molded Short-Fiber Reinforced Thermoplastics*. Polymer Composites, 1992. **13**(2): p. 69-80.
43. Gao, Y., Z. Li, Z.Y. Lin, L.J. Zhu, A. Tannenbaum, S. Bouix, and C.P. Wong, *Automated dispersion and orientation analysis for carbon nanotube reinforced polymer composites*. Nanotechnology, 2012. **23**(43).
44. Pichot, V., P. Launois, M. Pinault, M. Mayne-L'Hermite, and C. Reynaud, *Evidence of strong nanotube alignment and for iron preferential growth axis in multiwalled carbon nanotube carpets*. Applied Physics Letters, 2004. **85**(3): p. 473-475.
45. Duesberg, G.S., I. Loa, M. Burghard, K. Syassen, and S. Roth, *Polarized Raman spectroscopy on isolated single-wall carbon nanotubes*. Physical Review Letters, 2000. **85**(25): p. 5436-5439.
46. Wood, J.R., Q. Zhao, and H.D. Wagner, *Orientation of carbon nanotubes in polymers and its detection by Raman spectroscopy*. Composites Part a-Applied Science and Manufacturing, 2001. **32**(3-4): p. 391-399.
47. Blighe, F.M., K. Young, et al., *The Effect of Nanotube Content and Orientation on the Mechanical Properties of Polymer-Nanotube Composite*

- Fibers: Separating Intrinsic Reinforcement from Orientational Effects*. Advanced Functional Materials, 2011. **21**(2): p. 364-371.
48. Vangurp, M., *The Use of Rotation Matrices in the Mathematical-Description of Molecular Orientations in Polymers*. Colloid and Polymer Science, 1995. **273**(7): p. 607-625.
49. Vigolo, B., A. Penicaud, et al., *Macroscopic fibers and ribbons of oriented carbon nanotubes*. Science, 2000. **290**(5495): p. 1331-1334.
50. Bradshaw, R.D., F.T. Fisher, and L.C. Brinson, *Fiber waviness in nanotube-reinforced polymer composites-II: modeling via numerical approximation of the dilute strain concentration tensor*. Composites Science and Technology, 2003. **63**(11): p. 1705-1722.
51. Shao, L.H., R.Y. Luo, S.L. Bai, and J. Wang, *Prediction of effective moduli of carbon nanotube-reinforced composites with waviness and debonding*. Composite Structures, 2009. **87**(3): p. 274-281.
52. Yi, Y.B., L. Berhan, and A.M. Sastry, *Statistical geometry of random fibrous networks, revisited: Waviness, dimensionality, and percolation*. Journal of Applied Physics, 2004. **96**(3): p. 1318-1327.
53. Berhan, L. and A.M. Sastry, *Modeling percolation in high-aspect-ratio fiber systems. II. The effect of waviness on the percolation onset*. Physical Review E, 2007. **75**(4).
54. Li, C.Y. and T.W. Chou, *Continuum percolation of nanocomposites with fillers of arbitrary shapes*. Applied Physics Letters, 2007. **90**(17).
55. Li, C.Y. and T.W. Chou, *Failure of carbon nanotube/polymer composites and the effect of nanotube waviness*. Composites Part A-Applied Science and Manufacturing, 2009. **40**(10): p. 1580-1586.
56. Shi, D.L., X.Q. Feng, Y.G.Y. Huang, K.C. Hwang, and H.J. Gao, *The effect of nanotube waviness and agglomeration on the elastic property of carbon nanotube-reinforced composites*. Journal of Engineering Materials and Technology-Transactions of the ASME, 2004. **126**(3): p. 250-257.
57. Mori, T.a.T., K. , *Average Stress in Matrix and Average Elastic Energy of Materials With Misfitting Inclusions*. Acta Metallurgica et materialia, 1973. **21**: p. 571-574.
58. Chen, X.Y., I.J. Beyerlein, and L.C. Brinson, *Curved-fiber pull-out model for nanocomposites. Part I: Bonded stage formulation*. Mechanics of Materials, 2009. **41**(3): p. 279-292.

59. Yazdchi, K. and M. Salehi, *The effects of CNT waviness on interfacial stress transfer characteristics of CNT/polymer composites*. Composites Part A- Applied Science and Manufacturing, 2011. **42**(10): p. 1301-1309.
60. Wagner, H.D., O. Lourie, Y. Feldman, and R. Tenne, *Stress-induced fragmentation of multiwall carbon nanotubes in a polymer matrix*. Applied Physics Letters, 1998. **72**(2): p. 188-190.
61. Xu, X.J., M.M. Thwe, C. Shearwood, and K. Liao, *Mechanical properties and interfacial characteristics of carbon-nanotube-reinforced epoxy thin films*. Applied Physics Letters, 2002. **81**(15): p. 2833-2835.
62. Gojny, F.H., J. Nastalczyk, Z. Roslaniec, and K. Schulte, *Surface modified multi-walled carbon nanotubes in CNT/epoxy-composites*. Chemical Physics Letters, 2003. **370**(5-6): p. 820-824.
63. Qian, D., E.C. Dickey, R. Andrews, and T. Rantell, *Load transfer and deformation mechanisms in carbon nanotube-polystyrene composites*. Applied Physics Letters, 2000. **76**(20): p. 2868-2870.
64. Schadler, L.S., S.C. Giannaris, and P.M. Ajayan, *Load transfer in carbon nanotube epoxy composites*. Applied Physics Letters, 1998. **73**(26): p. 3842-3844.
65. Barber, A.H., S.R. Cohen, and H.D. Wagner, *Measurement of carbon nanotube-polymer interfacial strength*. Applied Physics Letters, 2003. **82**(23): p. 4140-4142.
66. Barber, A.H., S.R. Cohen, S. Kenig, and H.D. Wagner, *Interfacial fracture energy measurements for multi-walled carbon nanotubes pulled from a polymer matrix*. Composites Science and Technology, 2004. **64**(15): p. 2283-2289.
67. Cooper, C.A., S.R. Cohen, A.H. Barber, and H.D. Wagner, *Detachment of nanotubes from a polymer matrix*. Applied Physics Letters, 2002. **81**(20): p. 3873-3875.
68. Ding, W., L. Calabri, K.M. Kohlhaas, X. Chen, D.A. Dikin, and R.S. Ruoff, *Modulus, fracture strength, and brittle vs. plastic response of the outer shell of arc-grown multi-walled carbon nanotubes*. Experimental Mechanics, 2007. **47**(1): p. 25-36.
69. Tsuda, T., T. Ogasawara, F. Deng, and N. Takeda, *Direct measurements of interfacial shear strength of multi-walled carbon nanotube/PEEK composite using a nano-pullout method*. Composites Science and Technology, 2011. **71**(10): p. 1295-1300.

70. Frankland, S.J.V., A. Caglar, D.W. Brenner, and M. Griebel, *Molecular simulation of the influence of chemical cross-links on the shear strength of carbon nanotube-polymer interfaces*. Journal of Physical Chemistry B, 2002. **106**(12): p. 3046-3048.
71. Liao, K. and S. Li, *Interfacial characteristics of a carbon nanotube-polystyrene composite system*. Applied Physics Letters, 2001. **79**(25): p. 4225-4227.
72. Wong, M., M. Paramsothy, X.J. Xu, Y. Ren, S. Li, and K. Liao, *Physical interactions at carbon nanotube-polymer interface*. Polymer, 2003. **44**(25): p. 7757-7764.
73. Lordi, V. and N. Yao, *Molecular mechanics of binding in carbon-nanotube-polymer composites*. Journal of Materials Research, 2000. **15**(12): p. 2770-2779.
74. Yang, L., L.Y. Tong, and X.D. He, *MD simulation of carbon nanotube pullout behavior and its use in determining mode I delamination toughness*. Computational Materials Science, 2012. **55**: p. 356-364.
75. Lau, K.T., C. Gu, and D. Hui, *A critical review on nanotube and nanotube/nanoclay related polymer composite materials*. Composites Part B-Engineering, 2006. **37**(6): p. 425-436.
76. Wichmann, M.H.G., K. Schulte, and H.D. Wagner, *On nanocomposite toughness*. Composites Science and Technology, 2008. **68**(1): p. 329-331.
77. Lubineau, G. and A. Rahaman, *A review of strategies for improving the degradation properties of laminated continuous-fiber/epoxy composites with carbon-based nanoreinforcements*. Carbon, 2012. **50**(7): p. 2377-2395.
78. Gibson, R.F., V. Anumandla, X. Wu, and D. Bettinger, *Experimental characterization of delamination in unidirectional carbon/epoxy laminates featuring a carbon nanotube-enhanced ply interface*. Proceedings of the SEM Annual Conference & Exposition on Experimental and Applied Mechanics 2005: p. 71-79.
79. Sun, L.Y., R.F. Gibson, F. Gordaninejad, and J. Suhr, *Energy absorption capability of nanocomposites: A review*. Composites Science and Technology, 2009. **69**(14): p. 2392-2409.
80. Gojny, F.H., M.H.G. Wichmann, B. Fiedler, and K. Schulte, *Influence of different carbon nanotubes on the mechanical properties of epoxy matrix composites - A comparative study*. Composites Science and Technology, 2005. **65**(15-16): p. 2300-2313.

81. Fiedler, B., F.H. Gojny, M.H.G. Wichmann, M.C.M. Nolte, and K. Schulte, *Fundamental aspects of nano-reinforced composites*. Composites Science and Technology, 2006. **66**(16): p. 3115-3125.
82. Kelly, A., *Interface Effects and the Work of Fracture of a Fibrous Composite*. Proceedings of the Royal Society London A, 1970. **319**: p. 22-95.
83. Cox, H., *The elasticity and strength of paper on other fibrous materials*. British Journal of Applied Physics, 1952. **3**: p. 72.
84. Gao, X.L. and K. Li, *A shear-lag model for carbon nanotube-reinforced polymer composites*. International Journal of Solids and Structures, 2005. **42**(5-6): p. 1649-1667.
85. Tong, L., X. Sun, and P. Tan, *Effect of Long Multi-walled Carbon Nanotubes on Delamination Toughness of Laminated Composites*. Journal of Composite Materials, 2008. **42**(5): p. 5-23.
86. Joaquín Blanco, E.J.G., Roberto Guzmán de Villoria and Brian L. Wardle, *Limiting Mechanisms of Mode I Interlaminar Toughening of Composites Reinforced with Aligned Carbon Nanotube*. Journal of Composite Materials, 2009. **43**: p. 825-841.
87. Chen, Y.L., B. Liu, X.Q. He, Y. Huang, and K.C. Hwang, *Failure analysis and the optimal toughness design of carbon nanotube-reinforced composites*. Composites Science and Technology, 2010. **70**(9): p. 1360-1367.
88. Grimmer, C.S. and C.K.H. Dharan, *Enhancement of delamination fatigue resistance in carbon nanotube reinforced glass fiber/polymer composites*. Composites Science and Technology, 2010. **70**(6): p. 901-908.
89. Mirjalili, V. and P. Hubert, *Modelling of the carbon nanotube bridging effect on the toughening of polymers and experimental verification*. Composites Science and Technology, 2010. **70**(10): p. 1537-1543.
90. Chowdhury, S.C., B.Z. Hague, T. Okabe, and J.W. Gillespie, *Modeling the effect of statistical variations in length and diameter of randomly oriented CNTs on the properties of CNT reinforced nanocomposites*. Composites Part B-Engineering, 2012. **43**(4): p. 1756-1762.
91. Zhu, Y., *Carbon nanofiller modified multifunctional glass/fiber epoxy laminated composites*. PhD dissertation - Penn State University, 2011.
92. Jain, L.K. and R.C. Wetherhold, *Effect of Fiber Orientation on the Fracture-Toughness of Brittle Matrix Composites*. Acta Metallurgica et Materialia, 1992. **40**(6): p. 1135-1143.

93. Li, V.C., Y.J. Wang, and S. Backer, *A Micromechanical Model of Tension-Softening and Bridging Toughening of Short Random Fiber Reinforced Brittle Matrix Composites*. Journal of the Mechanics and Physics of Solids, 1991. **39**(5): p. 607-625.
94. Fu, S.Y. and B. Lauke, *The fibre pull-out energy of misaligned short fibre composites*. Journal of Materials Science, 1997. **32**(8): p. 1985-1993.
95. Suo, Z., G. Bao, and B. Fan, *Delamination R-Curve Phenomena Due to Damage*. Journal of the Mechanics and Physics of Solids, 1992. **40**(1): p. 1-16.
96. Sharma, A., *Controlling dispersion and electric-field-assisted alignment of carbon nanotubes and nanofibers for multifunctional epoxy composites*. PhD dissertation - Penn State University, 2010.
97. Zhu, Y., C.E. Bakis, and J.H. Adair, *Effects of carbon nanofiller functionalization and distribution on interlaminar fracture toughness of multi-scale reinforced polymer composites*. Carbon, 2012. **50**(3): p. 1316-1331.
98. Ozkan, T., M. Naraghi, and I. Chasiotis, *Mechanical properties of vapor grown carbon nanofibers*. Carbon, 2010. **48**(1): p. 239-244.
99. Ozkan, T., Q. Chen, and I. Chasiotis, *Interfacial strength and fracture energy of individual carbon nanofibers in epoxy matrix as a function of surface conditions*. Composites Science and Technology, 2012. **72**(9): p. 965-975.
100. Coleman, J.N., U. Khan, W.J. Blau, and Y.K. Gun'ko, *Small but strong: A review of the mechanical properties of carbon nanotube-polymer composites*. Carbon, 2006. **44**(9): p. 1624-1652.



## **CONCLUSIONS**

The work conducted in the present thesis concerns the damage modeling of composite materials by means of a multiscale approach. The most critical issues related to the failure mechanisms acting at different length scales of composites have been explored and discussed. The procedures proposed to evaluate the damage behavior of such materials involved both experimental, analytical and numerical tools. In detail, damage modeling has been performed for different case studies: GFRP composite laminates, phenolic impregnated skins/honeycomb Nomex core sandwich structures, Carbon Nanotube/Nanofiber modified S2-Glass/epoxy composites.

The first level of analysis concerned the damage occurred in case of low-velocity impact tests (*Chapter I*), carried out on glass fabric/epoxy laminates, adopting two panel thicknesses and different impact energy values. In this case, the multiscale modeling is conducted including both intralaminar and interlaminar levels of damage occurring within a composite laminate, as a consequence of impact events. This has been possible through the definition of suitable finite element models for the composite plies and interlaminar connections, by means of the explicit finite element software LS-DYNA. This allowed to characterize the critical parameters acting at the smaller (interlaminar) scale and affecting the macroscopic impact response of the composite laminate. In detail, from the obtained results, finite element simulations estimated with sufficient accuracy the overall force-displacement curves during the loading and rebound phases, as well as the irreversibly absorbed energy. Numerical predictions and experiments revealed satisfactory agreement with reference to the extent of fiber breakage as well as extent and shape of projected and ply-by-ply delaminated areas. Particularly, numerical simulations predicted considerable delamination at the interface located at the mid-plane of the specimens (characterized by two layers having same orientation), as found in the impact tests. The modeling method adopted within this

study revealed that both level of composite damage should be taken into account for reliable numerical simulations able to interpret the macroscopic composite impact behavior. Following this strategy much effort should be made in terms of accurate models of ply connections and ply damage constitutive model. In fact, within the study, the predicted delamination extent between laminae of identical orientation was found to be larger than the actual one. Probably, this depended on the interlaminar strengths used for the calculations, which were assumed independent of the relative orientations on adjacent plies. Another limit was found when the impact energy was closer to penetration limit; in this case constitutive models based on damage accumulation will be desirable for future analysis.

With reference to honeycomb sandwich structures, investigated in *Chapter II* and *Chapter III*, due to their hierarchical structure, a multiscale approach was necessary in order to suitably capture damage mechanisms occurring to the composite skins and Nomex honeycomb core. With the scope to move from the meso scale level, the analysis presented in *Chapter III* was aimed at accurately addressing some important aspects related to the out-of-plane Nomex honeycomb compressive response, such as linear elastic response, onset of instability, collapse limit and progressive folding during crushing. In order to evaluate the influence of imperfection variability on the compressive response of Nomex honeycomb structure, a statistics-based approach testing has been proposed and applied to a detailed finite element model of a single representative Nomex honeycomb cell. The proposed method dealt with the random sampling of the elements of the mesh in a finite element numerical analysis, on the basis of a normal distribution of thickness and Young modulus values of the cell wall material. All the simulations have been run through both ABAQUS/Standard and ABAQUS/Explicit. The analyses of the results revealed that the compressive behavior of the Nomex honeycomb is more sensitive to thickness imperfections rather than Young's modulus variation: a large coefficient of variation (CV) on wall thickness values tends to underestimate the compressive strength of the honeycomb if compared to the experimental values, whereas the Young's modulus variation provides compressive strength values always in the range of the experimental ones, even though the statistical variation on the numerical results resulted more limited. A very good correlation, in terms of experimental and numerical compressive stress–strain relationships, has been achieved when both the imperfections are included in the model in the range of CV=10-15%. The simulation of the crushing regime allowed to assess the cell wall folding mechanism, which is the responsible for the energy absorbing capability of honeycomb sandwich structures. The final folded pattern has been

demonstrated very close to the experimental one. It has been also shown that the repeated contact between adjacent folded walls led to a characteristic trend in the compressive strain curve. However, the simulation of this deformational stage drew the attention to the constitutive behavior assigned to the paper Nomex material. The assumption of linear elastic perfectly plastic behavior led to a pronounced increase of residual stress during wall contact that was slightly different from the more brittle actual one. It should be emphasized that the detailed representation of the cell allowed for a deep investigation of the cell wall deformation patterns and failure modes. For this reason, as future recommendation, the present method could be potentially extended for the cases of complex loading conditions, such as in the case of tension and shear loading in both in-plane and out-of-plane directions achieving reliable predictions of the mechanical behavior of honeycomb structures.

A different multiscale modeling strategy was used in *Chapter IV* to model high energy impact tests carried out on E-glass phenolic Nomex honeycomb sandwich structures, adopting two skin thickness values, two different impact diameters and different impact velocities. The virtual testing approach was implemented through the explicit finite element software LS-DYNA by using homogeneous equivalent solid elements for the Nomex honeycomb core and shell elements for the phenolic facesheets. The method was based on different experimental tests and numerical simulation performed at both the sandwich constituent scale (skins and Nomex honeycomb core) and assembly scale. When calibrated material properties coming from static experimental tests were used in the sandwich assembly model, the energy absorption capability (in terms of force displacement curves) resulted underestimated, since dynamic conditions affected some crucial material properties. A further calibration based on strain rate sensitiveness of skins and honeycomb core allowed to satisfactorily estimate the overall force-displacement curves. Satisfactory agreement between numerical predictions and experiments was also found referring to the damage extent and shape including the onset and development of material damage. In detail, numerical analyses predicted wide fiber fracture on top and bottom phenolic facesheets and plastic deformation of Nomex core. The proposed multiscale procedure allowed to point out the issue of strain rate sensitiveness, when high impact velocities are considered. For this reason, future developments will include the possibility to achieve strain rate characterization of the phenolic skins and Nomex paper material as well as micro-inertial effects of the cellular structure with the aim of conducting more reliable finite element simulations.

When CNT/polymer composites were investigated (*Chapter V*), the multiscale damage modeling procedure was focused on aspects related to CNT scale, including length and orientation characterization, stress transfer to the matrix as well as CNT toughening mechanisms. A micromechanical model, taking into account CNT length and orientation distribution, was implemented in order to model mode I interlaminar fracture toughness of multiscale CNT/CNF S2-Glass/epoxy composites. The analyses aimed at investigating different effects on CNT fracture toughness, including CNT length and filler functionalization. The analysis of the results revealed some important issues. First of all, the use of CNT length distribution in the micromechanical model appeared to be a suitable way to consider the actual dispersion of CNTs within a polymer matrix. When a unique value of CNT length was used in the model, strong fracture energy underestimation was experienced. A proper computation of CNT volume fraction was needed when a resin rich interlayer is added between fiber reinforced composite plies. In fact, both resin flow and microsized fibers obstruction are responsible for CNT migration and agglomeration. Moreover, the consolidation process could be responsible for partial alignment of CNTs; these features were found to be a source of strong variation of “local” nanofiller volume fraction triggering possible variations of toughening energy. According to the proposed approach the resulting interlaminar shear strength value for GPS-CNF based systems was around 90 MPa, whereas approximately 150MPa for long GPS-CNT systems; this latter value was also confirmed in case of short GPS-CNTs for which a statistical length distribution was hypothesized and then verified. A further issue was pointed out concerning the CNT critical length value to be considered in the model. A wrong estimation of this parameter (for instance due to the determination of CNF/CNT tensile strength rather the assumptions of inextensibility of tubes) would lead to possible underestimation of pullout energy. In order to overcome this issue, a molecular dynamics modeling approach was suggested for future developments, based on oriented CNT pullout virtual tests.